Measurement of 8B Solar Neutrinos above 2 MeV Threshold Using Novel Background Reducion in KamLAND

博士論文

Measurement of ^{8}B Solar Neutrinos above 2 MeV Threshold Using Novel Background Reduction in KamLAND

KamLANDでの革新的なバックグラウンド低減による閾値2 MeVでの^{8}B太陽ニュートリノ測定

B6SD2021

Takahiko Hachiya
蜂谷 尊彦

東北大学大学院理学研究科物理学専攻

2021
令和3年

Abstruct

Since its the first real-time measurement by Kamiokande in 1989 through the electron scattering (ES), the ^{8}B solar neutrino has been studied to understand the neutrino oscillation. Based on the LMA-MSW solution which was determined by the reactor $\overline{\nu}_e$ measurement, the survival probability of ν_e on the earth (P_{ee}) is expected to increase towards lower E_ν from 30% ($E_\nu \sim 10$ MeV, the matter effect dominant) to 50% ($E_\nu < 1$ MeV, the vacuum oscillation dominant). To observe this *upturn* behavior, neutrino experiments have been lowering their detection thresholds. The current lowest thresholds are, in the recoil-electron kinetic energy ($E_{\rm kin}$), 3.5 MeV for water cherenkov (WC) detectors (SK and SNO) and 3 MeV for a liquid scintillator (LS) detector (Borexino). The backgrounds which limit the thresholds are the Rn descendant in the water for WC detectors and γ-rays from detector components like photo-detectors for Borexino. KamLAND, which is a larger LS detector than Borexino, can suppress the γ-ray BGs by the self-shielding. Thus, if other BGs are sufficiently reduced, it can detect ^{8}B solar ν events below 3 MeV.

In this study, with the introduction of the new BG reduction methods, *n-tag* and *shower-tag* for muon-spallation products and *Day-scale* tag and BiTl tag for ^{208}Tl, the sensitivity to single events above 2 MeV energy in KamLAND has significantly improved. It resulted the first measurement of ^{8}B solar ν ES signals at 2–3 MeV ($E_{\rm kin}$) region at 3.4σ level. The observed rate was $0.62^{+0.21}_{-0.20}$ of the unoscillated model expectation, which is consistent with the LMA-MSW. An analysis with the entire energy spectrum lowered the allowance of the flat P_{ee} model from 84% (SK+SNO) to 64% (SK+SNO+KamLAND).

Acknowledgments

I would like to thank my adviser Prof. Kunio Inoue for always allowing me to carry on my study without any restrictions. I want to thank Prof. Itaru Shimizu for his guidance mainly in analytical aspects for the past 9 years since I was an undergraduate student.

The KamLAND data for this work were obtained thanks to all the current and former KamLAND collaborators and RCNS members. I would especially like to express my appreciation to those who joined the purification campaign in 2007–2009. I thank Prof. Masayuki Koga and Prof. Kengo Nakamura for their helps in my on-site shifts.

The analytical parts of this work were helped by Dr. Sei Ieki for the muon-spallation, Seisho Abe for atmospheric neutrinos, Prof. Koichi Ichimura and Dr. Nanami Kawada for the fiducial volume uncertainty, and Dr. Haruo Ikeda for general programing-things. I thank Yuki Karino for the fundamental invention of the new spallation background reduction tool and appreciate Dr. Yuto Kamei, Kazumi Hata, and Minori Eizuka who helped me to solidify the tool.

I am grateful for the daily physics discussions I have been able to have with Prof. Koji Ishidoshiro, Prof. Yasuhiro Kishimoto, Dr. Azusa Gando, Dr. Hideyoshi Ozaki, Dr. Atsuto Takeuchi, and Haruhiko Miyake.

The KamLAND-Zen 800 related works, which were in the first 3 years of my doctor course, were great experiences for me. I thank the head of the mini-balloon construction, Prof. Yoshihito Gando, for guiding me in various works especially in the welding of the balloon film. I thank the mini-balloon experts, (names already shown here plus) Dr. Kota Ueshima, Dr. Hiroko Watanabe, Dr. Keishi Hosokawa, Dr. Shuhei Obara, and Dr. Shingo Hayashida, and all members involved to the KamLAND-Zen 800 works (of course) including the failed ballon works in 2015–2016.

Finally I would like to thank my parents and friends for making me who I am today.

Contents

1 Introduction

The first real-time measurement of ^{8}B solar neutrinos was achieved by Kamiokande (KM) II experiment in 1989 [1]. Since then the ^{8}B ν has been a useful tool to understand the nature of neutrinos and the Sun.

In 2001, the difference of the fluxes measured through the electron scattering (ES) channel by Super-Kamiokande (SK) [2] and charged current (CC) channel by SNO [3] provided an indication of the flavor conversion of neutrinos, which is currently described as the three flavor neutrino oscillation.

The oscillation in the solar ν sector is controlled by a mixing angle θ_{12} and a mass square difference Δm^2_{21}. There were several combinations of (θ_{12}, Δm^2_{21}) as possible solutions for the SK+SNO result. The first result from KamLAND [4], which measured disappearance of reactor $\bar{\nu}_e$'s, excluded the solutions except the Large Mixing Angle (LMA) MSW solution [5].

In the LMA-MSW scenario, an increase of the survival probability of ν_e on the Earth (P_{ee}) is expected in lower energy region ($E_\nu \sim 1$ MeV) than higher energy region ($E_\nu \sim$ 10 MeV). The *upturn* feature was indirectly confirmed by comparing different types of solar neutrinos (*pp*, ^{7}Be, *pep*, and ^{8}B). However it hasn't been confirmed in a continuous spectrum of a single neutrino source. Moreover the spectral shape of P_{ee} at the transition region is expected to have an ability to prove new physics. For the precise measurement of the transition region, (^{8}B) solar neutrino experiments have been lowering their analysis thresholds. This study aims to achieve the lowest energy threshold of 2 MeV using KamLAND and novel background reduction techniques.

Solar neutrino events at 2–3 MeV energy region are an ultimate background for neutrinoless double-beta decay search experiments which use liquid scintillator such as KamLAND-Zen [6, 7] and SNO+ [8]. The 2–3 MeV data from this study can be thought the double-beta-isotope-less background spectrum.

2 Solar Neutrinos and Neutrino Oscillation

2.1 ^{8}B Solar Neutrinos

2.1.1 Standard Solar Model

A standard solar model (SSM) is a portrait of a main-sequence star in the process of evolution [9]. Basic assumptions of the model are

- the Sun is in a hydrostatic equilibrium, where the radiative and particle pressures balance gravity.
- the radiative energy is provided by nuclear fusions and changes of the abundances of isotopes are caused only by nuclear fusions.

Computation of the evolution process is started from a chemically homogeneous sphere. The inputs are the mixing length parameter and the initial helium and metal mass fractions. They are calibrated to match today's solar luminosity $L_\odot$, radius $R_\odot$, and abundances of isotopes on the surface. Figure 2.1 shows the density profile of the Sun obtained from the latest SSM calculation [10].

2.1.2 Nuclear Reactions in the Sun

The overall nuclear fusion reactions in the Sun can be described as

$$4p \rightarrow \alpha + 2e^+ + 2\nu_e + 26.7 \text{ MeV}. \tag{2.1}$$

The main energy generating process is called proton-proton (*pp* chain) and another process which is achieved with helps from carbon, nitrogen, and oxygen is called CNO cycle. Neutrino producing reactions in the two processes are summarized in Table 2.1 and 2.2. Figure 2.2 and 2.3 show flux and production position in the Sun, respectively, of solar neutrinos predicted by the SSM (B16-GS98) [10].

^{8}B solar neutrinos have widely ranged energy ($\sim$1–10 MeV) and are produced deep inside ($r/R_\odot < 0.15$) the Sun. These properties are suitable for proving the transition region of P_{ee}.

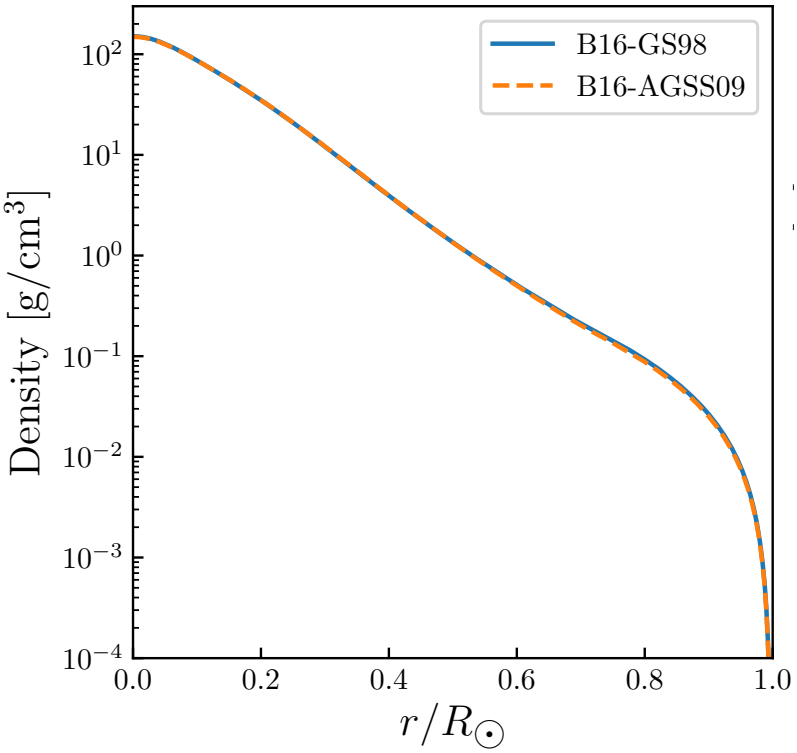

Figure 2.1: Position dependence of the density of the Sun calculated in [10]. Two models of solar abundances (GS98 [11] and AGSS09 [12]) are assumed. Figure from Ref. [13].

Table 2.1: Neutrino producing reactions in *pp* chain

Name	Reaction	Fraction in *pp* chain	E_ν [MeV]
pp	$p + p \to {}^2\mathrm{H} + e^+ + \nu_e$	0.9976	< 0.42
pep	$p + e^- + p \to {}^2\mathrm{H} + \nu_e$	0.0024	1.44
^{7}Be	$^7\mathrm{Be} + e^- \to {}^7\mathrm{Li} + \nu_e$	0.154×0.9989	0.86 or 0.38
^{8}B	$^8\mathrm{B} \to {}^8\mathrm{Be}^* + e^+ + \nu_e$	0.154×0.0011	< 16
hep	$^3\mathrm{He} + p \to {}^4\mathrm{He} + e^+ + \nu_e$	2.5×10^{-7}	< 18.8

Table 2.2: Neutrino producing reactions in CNO cycle

Reaction	E_ν [MeV]
$^{13}\mathrm{N} \to {}^{13}\mathrm{C} + e^+ + \nu_e$	< 1.199
$^{15}\mathrm{O} \to {}^{15}\mathrm{N} + e^+ + \nu_e$	< 1.73
$^{17}\mathrm{F} \to {}^{17}\mathrm{O} + e^+ + \nu_e$	< 1.74

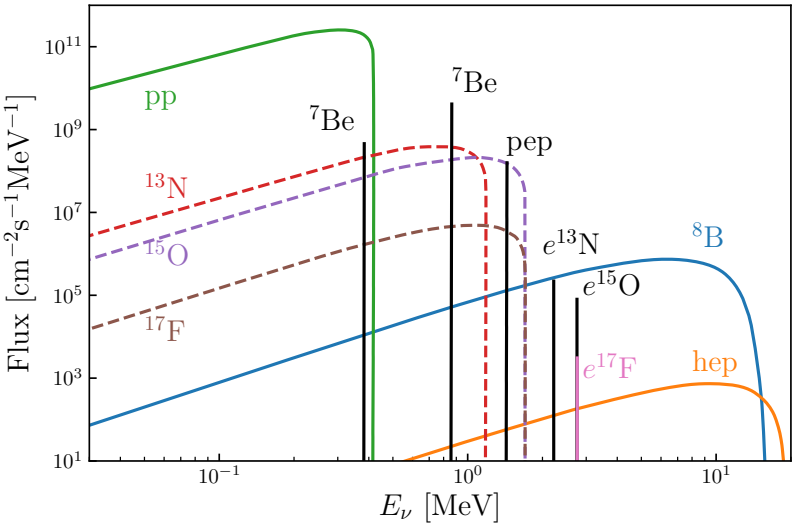

Figure 2.2: Flux of solar neutrinos predicted from the SSM (B16-GS98) [10]. Figure from Ref. [13].

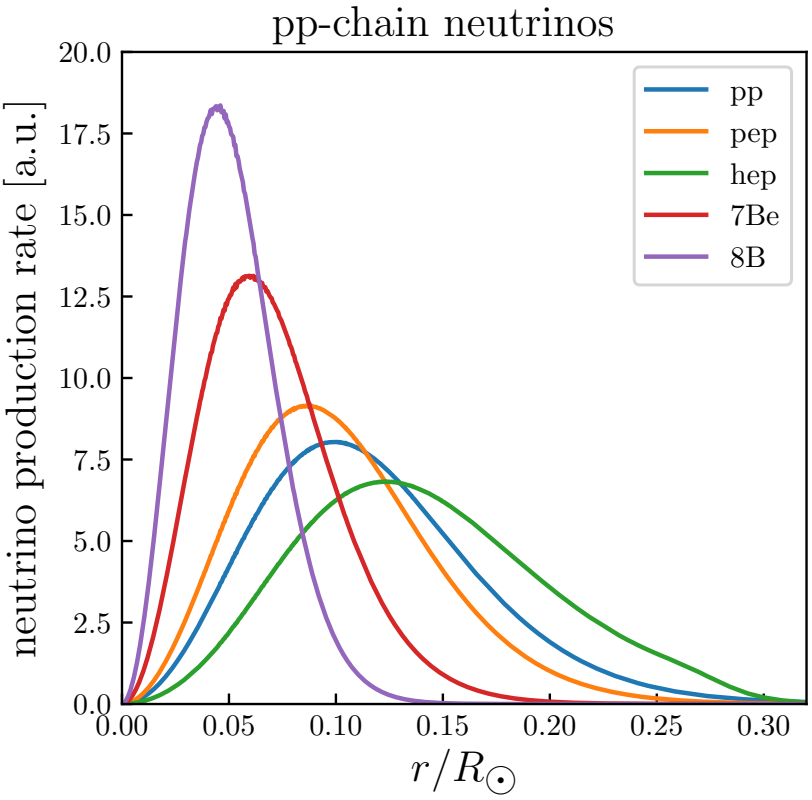

Figure 2.3: Production position distribution of *pp* chain neutrinos predicted from the SSM (B16-GS98) [10]. Figure from Ref. [13].

2.2 Neutrino Oscillation

2.2.1 Oscillation in Vacuum

Neutrino oscillation [14, 15] is a phenomenon in which neutrinos change their flavor during flight. It is caused by the existence of mass eigenstates ($\nu_{i=1,2,3}$) apart from flavor eigenstates ($\nu_{\alpha=e,\mu,\tau}$). The relation between the two types of eigenstates is described as

$$\begin{pmatrix}\nu_e\\ \nu_\mu\\ \nu_\tau\end{pmatrix} = U_{\mathrm{PMNS}} \begin{pmatrix}\nu_1\\ \nu_2\\ \nu_3\end{pmatrix}, \tag{2.2}$$

where U_{PMNS} is the Pontecorvo-Maki-Nakagawa-Sakata (PMNS) matrix with three mixing angles ($\theta_{ij=12,23,13}$) and a CP-violating phase (δ)

$$U_{\mathrm{PMNS}} = \begin{pmatrix}1 & 0 & 0\\ 0 & c_{23} & s_{23}\\ 0 & -s_{23} & c_{23}\end{pmatrix} \begin{pmatrix}c_{13} & 0 & s_{13}e^{-i\delta}\\ 0 & 1 & 0\\ -s_{13}e^{i\delta} & 0 & c_{13}\end{pmatrix} \begin{pmatrix}c_{12} & s_{12} & 0\\ -s_{12} & c_{12} & 0\\ 0 & 0 & 1\end{pmatrix}, \tag{2.3}$$

$$c_{ij} = \cos\theta_{ij}, \tag{2.4}$$

$$s_{ij} = \sin\theta_{ij}. \tag{2.5}$$

The time evolution of the mass eigenstate follows the Schrödinger equation

$$i\frac{\partial}{\partial t}\left|\nu_i\right\rangle = E_i\left|\nu_i\right\rangle, \tag{2.6}$$

$$\left|\nu_i(t)\right\rangle = \exp(-iE_it)\left|\nu_i(t=0)\right\rangle. \tag{2.7}$$

Using 2.2 and 2.7 we obtain

$$\left|\nu_\alpha(t)\right\rangle = \sum_i U^*_{\alpha i}\exp(-iE_it)\left|\nu_i(t=0)\right\rangle. \tag{2.8}$$

The transition probability is given as

$$P(\nu_\alpha\to\nu_\beta) = \left|\left\langle\nu_\beta\middle|\nu_\alpha(t)\right\rangle\right|^2 \tag{2.9}$$

$$= \sum_i\sum_j U_{\beta i}U^*_{\alpha i}U_{\alpha j}U^*_{\beta j}\exp\bigl(-i(E_i-E_j)t\bigr) \tag{2.10}$$

$$\sim \sum_i\sum_j U_{\beta i}U^*_{\alpha i}U_{\alpha j}U^*_{\beta j}\exp\left(-i\frac{(m_i^2-m_j^2)}{2E}t\right) \tag{2.11}$$

$$= \delta_{\alpha\beta} - 4\sum_{i>j}\mathrm{Re}(U_{\beta i}U^*_{\alpha i}U_{\alpha j}U^*_{\beta j})\sin^2\left(\frac{\Delta m^2_{ij}}{4E}t\right) \tag{2.12}$$

$$+ 4\sum_{i>j}\mathrm{Im}(U_{\beta i}U^*_{\alpha i}U_{\alpha j}U^*_{\beta j})\sin\left(\frac{\Delta m^2_{ij}}{4E}t\right)\cos\left(\frac{\Delta m^2_{ij}}{4E}t\right), \tag{2.13}$$

$$\Delta m^2_{ij} = m^2_i - m^2_j, \tag{2.14}$$

where the relativistic condition ($m_i \ll p$, $p \sim E$) is used as follows

$$E_i = \sqrt{p^2 + m_i^2} \tag{2.15}$$

$$\sim E + \frac{m_i^2}{2E}. \tag{2.16}$$

The phase can be written as

$$\frac{\Delta m^2_{ij}}{4E} t \sim \frac{1.27 \Delta m^2_{ij}[\mathrm{eV}^2] L[\mathrm{m}]}{E[\mathrm{MeV}]}, \tag{2.17}$$

where $L = ct$ is the flight distance.

In a simplified 2×2 mixing case with a mixing angle θ and a mass difference Δm^2, the transition probability is given by

$$P^{(2)}(\nu_\alpha \to \nu_\beta) = \sin^2 2\theta \sin^2 \left(\frac{1.27 \Delta m^2[\mathrm{eV}^2] L[\mathrm{m}]}{E[\mathrm{MeV}]} \right). \tag{2.18}$$

The scale of Δm^2 that can be explored differs depending on the combination of (E, L). Long baseline reactor neutrinos ($E \sim 4$ MeV, $L \sim 100$ km) are sensitive to $\Delta m^2 \sim 10^{-5}$–10^{-4} eV^2. Atmospheric neutrinos ($E \sim 10^2$–10^4 MeV, $L \sim 10^3$–10^4 km) are sensitive to $\Delta m^2 \sim 10^{-5}$–10^{-2} eV^2. Observation of those neutrinos led to measurements of Δm^2_{21} [16] and $\Delta m^2_{31} (\sim \Delta m^2_{31})$ [17], respectively.

The oscillation parameters have been measured using various types of neutrinos such as solar [18, 19, 20], atmospheric [21, 22], reactor [23, 24, 25, 26], and accelerator [27, 28, 29] neutrinos. Table 2.3 shows the results of a global analysis [30, 31]. Current allowed region of the combination $(\theta_{12}, \Delta m^2_{21})$, which governs the solar neutrino oscillation, is called large mixing angle (LMA) solution.

2.2.2 Oscillation in Matter

Propagation of neutrinos in matter is affected by potentials. It is called Mikheyev-Smirnov-Wolfenstein (MSW) effect [32, 33] or simply the matter effect. The NC potential (V_N) is relevant to all flavors of neutrinos, while the CC one ($V_C = \sqrt{2} G_F N_e$, where G_F is Fermi's constant and N_e is the electron density) is only to ν_e. In the 2×2 case, the Hamiltonian which governs the propagation is expressed as

$$H = U \begin{pmatrix} E_1 & 0 \\ 0 & E_2 \end{pmatrix} U^\dagger + V_C \begin{pmatrix} 1 & 0 \\ 0 & 0 \end{pmatrix} + V_N \tag{2.19}$$

$$= \left(E + \frac{m_2^2 + m_1^2}{4E} \right) + \frac{\Delta m^2}{4E} \begin{pmatrix} -\cos 2\theta & \sin 2\theta \\ \sin 2\theta & \cos 2\theta \end{pmatrix} + \frac{V_C + V_N}{2} + \frac{V_C}{2} \begin{pmatrix} 1 & 0 \\ 0 & -1 \end{pmatrix}. \tag{2.20}$$

Ignoring oscillation-non-related terms, we get

$$H = \begin{pmatrix} -\left(\frac{\Delta m^2}{4E} \cos 2\theta - V_C/2 \right) & \frac{\Delta m^2}{4E} \sin 2\theta \\ \frac{\Delta m^2}{4E} \sin 2\theta & \frac{\Delta m^2}{4E} \cos 2\theta - V_C/2 \end{pmatrix}. \tag{2.21}$$

Table 2.3: The neutrino oscillation parameters obtained from a global fit to experimental data. $\Delta m^2_{3l} = \Delta m^2_{31} > 0$ for normal mass ordering ($m_1 < m_2 < m_3$) and $\Delta m^2_{3l} = \Delta m^2_{32} < 0$ for inverted mass ordering ($m_3 < m_1 < m_2$). Table from Ref. [31].

NuFIT 5.1 (2021)

		Normal Ordering (best fit)		Inverted Ordering ($\Delta\chi^2 = 2.6$)	
		bfp $\pm 1\sigma$	3σ range	bfp $\pm 1\sigma$	3σ range
without SK atmospheric data	$\sin^2\theta_{12}$	$0.304^{+0.013}_{-0.012}$	$0.269 \to 0.343$	$0.304^{+0.012}_{-0.012}$	$0.269 \to 0.343$
	$\theta_{12}/^\circ$	$33.44^{+0.77}_{-0.74}$	$31.27 \to 35.86$	$33.45^{+0.77}_{-0.74}$	$31.27 \to 35.87$
	$\sin^2\theta_{23}$	$0.573^{+0.018}_{-0.023}$	$0.405 \to 0.620$	$0.578^{+0.017}_{-0.021}$	$0.410 \to 0.623$
	$\theta_{23}/^\circ$	$49.2^{+1.0}_{-1.3}$	$39.5 \to 52.0$	$49.5^{+1.0}_{-1.2}$	$39.8 \to 52.1$
	$\sin^2\theta_{13}$	$0.02220^{+0.00068}_{-0.00062}$	$0.02034 \to 0.02430$	$0.02238^{+0.00064}_{-0.00062}$	$0.02053 \to 0.02434$
	$\theta_{13}/^\circ$	$8.57^{+0.13}_{-0.12}$	$8.20 \to 8.97$	$8.60^{+0.12}_{-0.12}$	$8.24 \to 8.98$
	$\delta_{\rm CP}/^\circ$	194^{+52}_{-25}	$105 \to 405$	287^{+27}_{-32}	$192 \to 361$
	$\frac{\Delta m^2_{21}}{10^{-5}\ \text{eV}^2}$	$7.42^{+0.21}_{-0.20}$	$6.82 \to 8.04$	$7.42^{+0.21}_{-0.20}$	$6.82 \to 8.04$
	$\frac{\Delta m^2_{3\ell}}{10^{-3}\ \text{eV}^2}$	$+2.515^{+0.028}_{-0.028}$	$+2.431 \to +2.599$	$-2.498^{+0.028}_{-0.029}$	$-2.584 \to -2.413$
		Normal Ordering (best fit)		Inverted Ordering ($\Delta\chi^2 = 7.0$)	
		bfp $\pm 1\sigma$	3σ range	bfp $\pm 1\sigma$	3σ range
with SK atmospheric data	$\sin^2\theta_{12}$	$0.304^{+0.012}_{-0.012}$	$0.269 \to 0.343$	$0.304^{+0.013}_{-0.012}$	$0.269 \to 0.343$
	$\theta_{12}/^\circ$	$33.45^{+0.77}_{-0.75}$	$31.27 \to 35.87$	$33.45^{+0.78}_{-0.75}$	$31.27 \to 35.87$
	$\sin^2\theta_{23}$	$0.450^{+0.019}_{-0.016}$	$0.408 \to 0.603$	$0.570^{+0.016}_{-0.022}$	$0.410 \to 0.613$
	$\theta_{23}/^\circ$	$42.1^{+1.1}_{-0.9}$	$39.7 \to 50.9$	$49.0^{+0.9}_{-1.3}$	$39.8 \to 51.6$
	$\sin^2\theta_{13}$	$0.02246^{+0.00062}_{-0.00062}$	$0.02060 \to 0.02435$	$0.02241^{+0.00074}_{-0.00062}$	$0.02055 \to 0.02457$
	$\theta_{13}/^\circ$	$8.62^{+0.12}_{-0.12}$	$8.25 \to 8.98$	$8.61^{+0.14}_{-0.12}$	$8.24 \to 9.02$
	$\delta_{\rm CP}/^\circ$	230^{+36}_{-25}	$144 \to 350$	278^{+22}_{-30}	$194 \to 345$
	$\frac{\Delta m^2_{21}}{10^{-5}\ \text{eV}^2}$	$7.42^{+0.21}_{-0.20}$	$6.82 \to 8.04$	$7.42^{+0.21}_{-0.20}$	$6.82 \to 8.04$
	$\frac{\Delta m^2_{3\ell}}{10^{-3}\ \text{eV}^2}$	$+2.510^{+0.027}_{-0.027}$	$+2.430 \to +2.593$	$-2.490^{+0.026}_{-0.028}$	$-2.574 \to -2.410$

Based on this, a new mixing angle θ_M and mass eigenstates $\nu_{1M,2M}$ can be defined as

$$\begin{pmatrix} \nu_\alpha \\ \nu_\beta \end{pmatrix} = \begin{pmatrix} \cos\theta_M & \sin\theta_M \\ -\sin\theta_M & \cos\theta_M \end{pmatrix} \begin{pmatrix} \nu_{1M} \\ \nu_{2M} \end{pmatrix}, \tag{2.22}$$

where

$$\tan 2\theta_M = \frac{(\Delta m^2/(2E))\sin 2\theta}{(\Delta m^2/(2E))\cos 2\theta - \sqrt{2}G_F N_e}. \tag{2.23}$$

The new Δm^2_M is

$$\Delta m^2_M = 4E\sqrt{A^2 + B^2}, \tag{2.24}$$

$$A = \frac{\Delta m^2}{4E}\cos 2\theta - V_C/2, \tag{2.25}$$

$$B = \frac{\Delta m^2}{4E}\sin 2\theta. \tag{2.26}$$

The oscillation effect gets maximum at the critical density

$$N_{e,c} = \frac{\Delta m^2 \cos 2\theta}{2\sqrt{G_F}E}. \tag{2.27}$$

For example, density at the core of the Sun is 6×10^{25} /cm^3. A ν_e with an energy of 1.4 MeV satisfies the condition.

Oscillation in the Sun

For the solar neutrino oscillation, the adiabatic approximation[1] can be applied. Then the survival probability of a ν_e produced in the Sun and comes to the Earth in the three-flavor form is given by [34]

$$P_{ee} = P^{(2)}_{ee}\cos^4\theta_{13} + \sin^4\theta_{13}, \tag{2.28}$$

$$P^{(2)}_{ee} = \frac{1}{2}(1 + \cos 2\theta_{12M}\cos 2\theta_{12}). \tag{2.29}$$

High energy (> 10 MeV) ν_e's cross the $N_{e,c}$ during the propagation from the production point to the surface of the Sun and fully affected by the matter effect

$$P_{ee} \sim \sin^2\theta_{12} \sim 0.3. \tag{2.30}$$

The low energy (< 1 MeV) behavior is almost same as the vacuum solution

$$P_{ee} \sim 1 - \frac{1}{2}\sin^2 2\theta_{12} \sim 0.56. \tag{2.31}$$

The increase of P_{ee} toward lower energy is called *upturn*, see Figure 2.4.

Until the early 2000s, several combinations of $(\Delta m^2_{21}, \theta_{12})$ are allowed as the MSW solutions. The first result of KamLAND excluded all of them except the large-mixing-angle (LMA) solution [4].

[1] It assumes that the change of the density of the matter is enough slow that ν_{iM} stays in the same mass eigenstate during propagation. A high energy ($E \sim 10$ MeV) ν_e produced near the core of the Sun is almost ν_{2M} and it becomes ν_2 at the surface of the Sun.

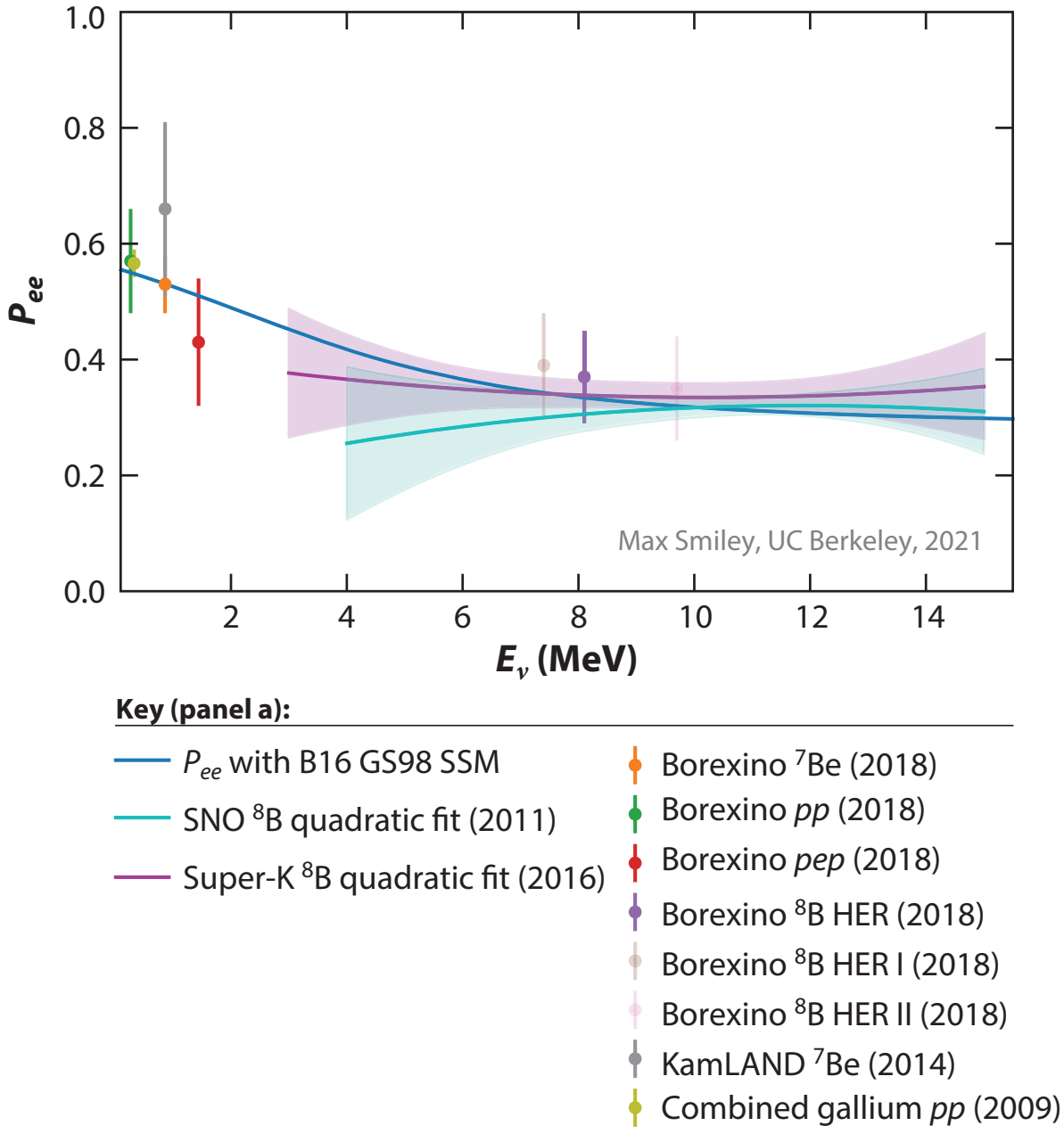

Figure 2.4: Survival probability of the solar ν_e on the Earth. Figure from Ref. [35].

Oscillation in the Earth Matter

Propagation of solar neutrinos is affected by the Earth matter. The effect appears as the increase of ν_e flux in the night. See Ref. [36, 37] for the detailed calculation of the Earth matter effect. Based on the current estimation of $(\Delta m^2_{21}, \theta_{12})$, a few % level of the day/night asymmetry for the ^{8}B solar neutrinos ($E \sim 10$ MeV) is expected. The result from Super-Kamiokande shows the indication [38]

$$A_{DN} = -A_{ND} = -\frac{P_{ee}^{\rm night} - P_{ee}^{\rm day}}{(P_{ee}^{\rm night} + P_{ee}^{\rm day})/2} = (-2.1 \pm 1.1)\%.$$

Matter Effect by New Physics

As can be seen from the conversion of the formulae 2.19, 2.20, and 2.21, any flavor (or mass) asymmetric potentials among the eigenstates affect the matter effect and change the energy dependence of P_{ee} from the standard MSW-LMA solution.

For example, in the so called non-standard interaction (NSI), Hamiltonian in the matter has additional term

$$V_e \begin{pmatrix} \varepsilon_{ee} & \varepsilon_{e\mu} & \varepsilon_{e\tau} \\ \varepsilon^*_{e\mu} & \varepsilon_{\mu\mu} & \varepsilon_{\mu\tau} \\ \varepsilon^*_{e\tau} & \varepsilon^*_{\mu\tau} & \varepsilon_{\tau\tau} \end{pmatrix}, \tag{2.32}$$

$$\varepsilon_{\alpha\beta} = \sum_f \frac{N_f}{N_e} (\varepsilon^{f,L}_{\alpha,\beta} + \varepsilon^{f,R}_{\alpha,\beta}), \tag{2.33}$$

where

- f: matter fermions (e, u, d)
- ε: neutrino interaction strength with f

Another example is sterile neutrinos ν_s which don't participate in NC and CC. In this case, the fourth (or more) mass eigenstate ν_4 is considered and the NC part of the Hamiltonian becomes asymmetric

$$V_N \begin{pmatrix} 1 & & & \\ & 1 & & \\ & & 1 & \\ & & & 0 \end{pmatrix} = V_N \left[1 + \begin{pmatrix} 0 & & & \\ & 0 & & \\ & & 0 & \\ & & & -1 \end{pmatrix} \right]. \tag{2.34}$$

See Ref. [13] for a general review of these new physics and their impacts on the matter effect. Figure 2.5 shows how P_{ee} changes with sterile neutrinos. The shape of the MSW-LMA transition region ($E_\nu \sim$2–5 MeV) is sensitive to such new physics.

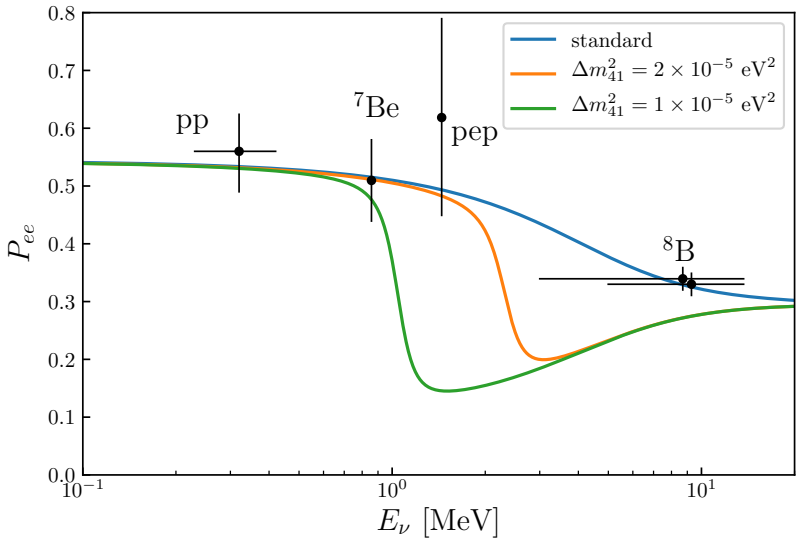

Figure 2.5: P_{ee} in the scenario of the existence of ν_4. $\sin^2 2\theta_{41} = 0.01$ is assumed. Figure from Ref. [13].

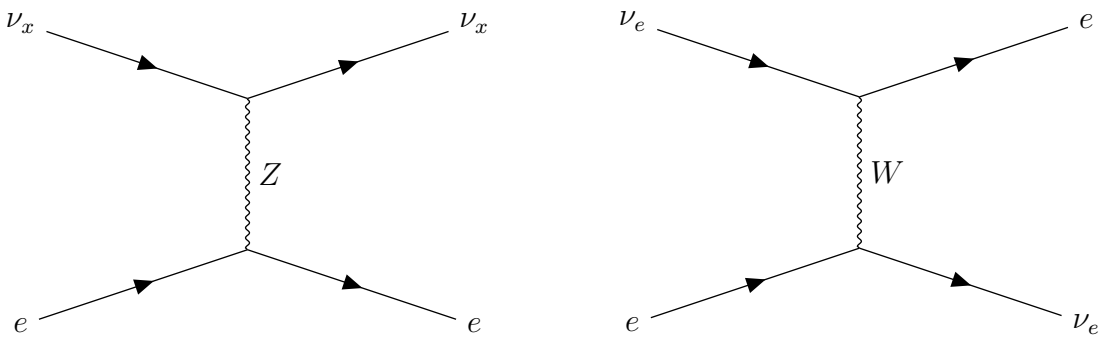

(a) NC (b) CC

Figure 2.6: Neutrino-electron ES

2.3 Detection Methods and Cross Sections

Neutrinos from the Sun can be detected through neutrino-electron elastic scattering (ES), charged current (CC) reactions, or neutral current (NC) reactions. Main focus of the solar neutrino analysis of this thesis will be on ES. CC and NC events will be treated as backgrounds for the ES signals.

2.3.1 Neutrino-Electron ES

ES is actually NC for $\nu_{\mu,\tau}$ and CC+NC for ν_e, see Figure 2.6. The cross section is calculated as follows:

$$\frac{d\sigma}{dT} = \frac{2G_F^2 m_e}{\pi}\left[g_L^2 + g_R^2\left(1-\frac{T}{E_\nu}\right)^2 - g_L g_R \frac{m_e T}{E_\nu^2}\right], \tag{2.35}$$

$$g_L|_{\nu_e} = \left(\frac{1}{2}+\sin^2\theta_W\right), g_L|_{\nu_{\mu,\tau}} = \left(-\frac{1}{2}+\sin^2\theta_W\right), \tag{2.36}$$

$$g_R = \sin^2\theta_W \sim 0.23, \tag{2.37}$$

where T is the kinetic energy of the recoil-electron. In Ref. [39], radiative corrections for solar neutrinos were calculated. The impact on the recoil-electron energy spectrum of ^{8}B ν at 2–15 MeV is 0–4% level.

In an experiment, T is the observable. Depending on the scattering angle of the neutrino, it can be any value less than

$$T_{\max} = \frac{E_\nu}{1+m_e/(2E_\nu)}. \tag{2.38}$$

The recoil-electron is mostly forwardly scattered. Water cherenkov detectors use the directional information to identify the solar ν ES events.

2.3.2 CC and NC

SNO [40] used heavy water (D_2O) to detect CC and NC separately:

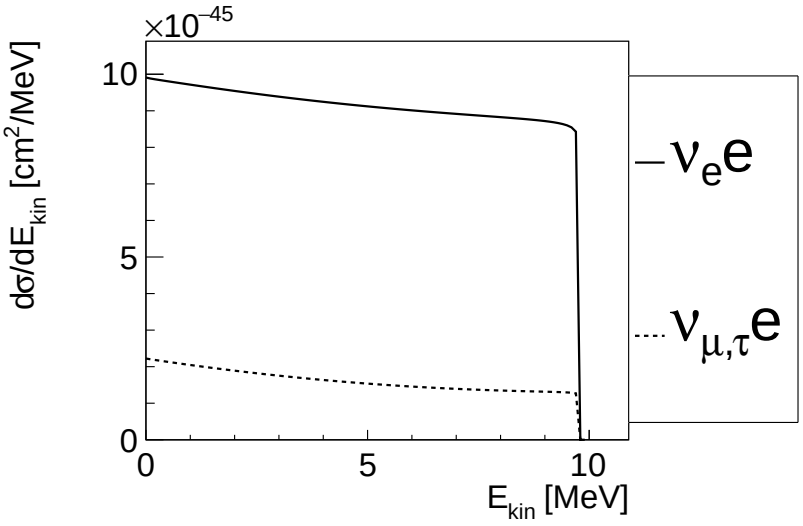

Figure 2.7: Differential cross section of ES with an incident neutrino with 10 MeV energy.

- CC: $\nu_e + d \to p + p + e^-$
- NC: $\nu_x + d \to n + p + \nu_x$

In an organic liquid scintillator detector, whose main component is carbon, ^{13}C ($\sim 1\%$ natural abundance) is sensitive to CC and NC reactions. Those with larger cross sections are as follows:

- CC (ground): $\nu_e + ^{13}\mathrm{C} \to e^- + ^{13}\mathrm{N}(1/2^-_{\mathrm{g.s.}})$
  - ^{13}N ($Q_{\beta+} = 2.22$MeV, $\tau = 862$ sec)
  - $E_\nu = T_e + Q(2.22$ MeV)
  - Signal property: possible delayed coincidence
- CC (excited): $\nu_e + ^{13}\mathrm{C} \to e^- + ^{13}\mathrm{N}(3/2^-)$
  - $^{13}\mathrm{N}(3/2^-) \to ^{12}\mathrm{C}(0^+) + p + 1.56$ MeV
  - $E_\nu = T_e + Q(2.22$ MeV$) + E_x(3.5$ MeV$)$
  - Signal property: just a single event
- NC : $\nu_x + ^{13}\mathrm{C} \to \nu_x + ^{13}\mathrm{C}(3/2^-)$
  - $^{13}\mathrm{C}(3/2^-) \to ^{13}\mathrm{C}(1/2_{\mathrm{g.s.}}) + \gamma(3.69$ MeV$)$
  - Signal property: mono-energetic γ

Detailed calculation of the cross sections were performed in Ref. [41, 42, 43, 44]. The difference between the NC cross section models are relatively large ($\sim 40\%$). Figure 2.8 shows the three cross sections calculated in Ref. [43].

CC is good at measuring the $P_{ee}(E_\nu)$ spectrum because the recoil-electron energy has 1-to-1 relation with E_ν. NC is useful to measure the total solar neutrino flux independently of the oscillation effect.

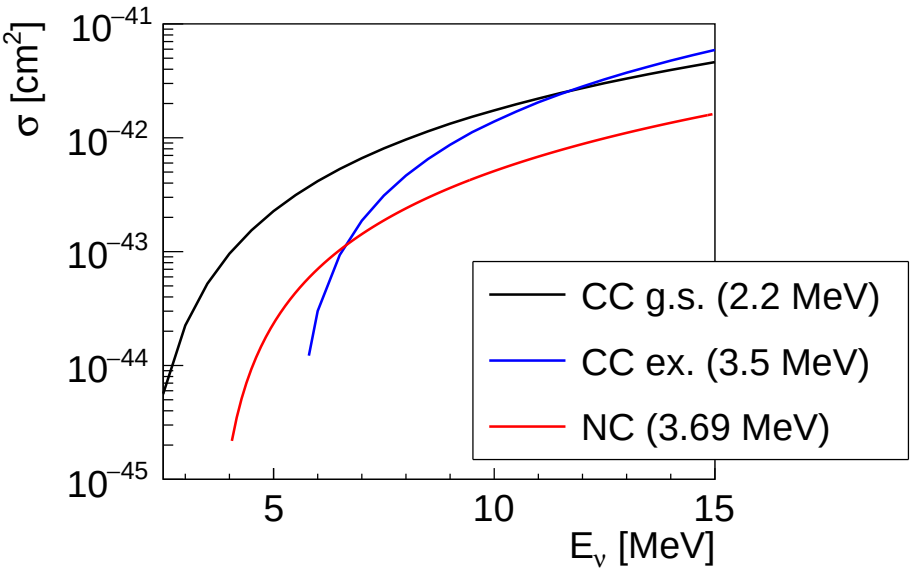

Figure 2.8: Cross sections of the neutrino capture on ^{13}C based on Ref. [43].

2.4 Experiments

Measurement of the energy spectrum of ^{8}B solar ν_e has been performed by water cherenkov (WC) detectors (Super-Kamiokande [SK] [18, 38], SNO [19], and SNO+ [45]) and liquid scintillator (LS) detectors (Borexino [46, 47] and KamLAND [48]). The latest constraint on the P_{ee} is derived by the combination of SNO's NC total flux [2] and SNO's CC and SK's ES shapes, see Figure 2.9. In the ^{8}B only results, a flat $P_{ee} \sim 0.32$ is still allowed and *upturn* is not confirmed. Note that SK recently reported upward change in the lower energy event rate in their latest preliminary analysis [38] (2020) as compared to Ref. [18] (2016).

Basically ^{8}B solar ν signals in WC and LS detectors are just single electron. No delayed-coincidence tagging technique is available. That is there are many kinds of backgrounds for the signal such as external γ-rays, decays of muon-spallation products, and LS (water) intrinsic radioactivities. Figure 2.10 shows the summary of the backgrounds. WC detectors (SK and SNO) achieved $E_{\rm kin}$ threshold of 3.5 MeV. This limit is set by water-intrinsic ^{214}Bi. In a LS detector, better purification than water and coincidence tagging (^{214}Bi–^{214}Po) are available. As a result, Borexino, a 300-ton LS detector, achieved the lowest energy threshold of 3 MeV [46]. Below 3 MeV, Borexino suffers from external γ rays from ^{208}Tl and ^{214}Bi which are in photo-detectors[3]. Another LS detector, KamLAND, performed its ^{8}B solar ν analysis with a 5 MeV energy threshold due to LS-intrinsic ^{208}Tl.

[2] $\left[5.25 \pm 0.16(\text{stat.}) \pm^{+0.11}_{-0.13} (\text{syst.})\right] \times 10^{6}$ /cm^2/s

[3] A 2 MeV threshold analysis is tried with an energy-radius simultaneous fitting method in Ref. [49]. However the 2–3 MeV energy spectrum shown in the work was dominated by 100x more external backgrounds than solar ν signals. The detection significance of solar ν signals at the energy region is not clear.

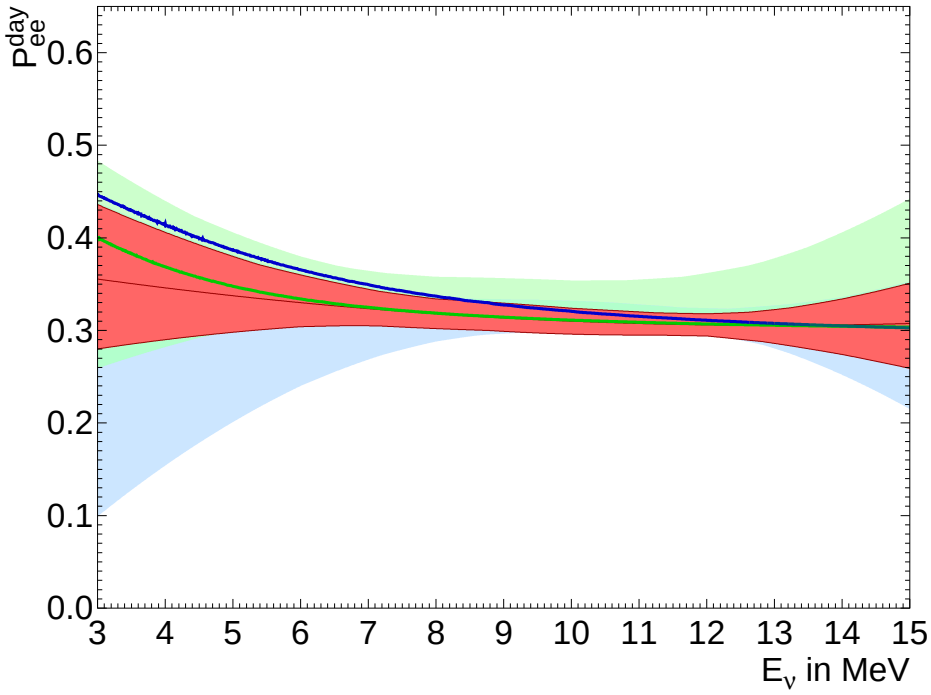

Figure 2.9: 1σ constraint on P_{ee}. Blue band is SNO [19]. Green band is SK. Red band is SK+SNO. Blue line corresponds to $\Delta m^2_{21} = 7.41 \times 10^{-5}$ eV^2 (solar+KamLAND[$\bar{\nu}_e$]). Green line corresponds to $\Delta m^2_{21} = 4.9 \times 10^{-5}$ eV^2 (solar). Figure from Ref. [18].

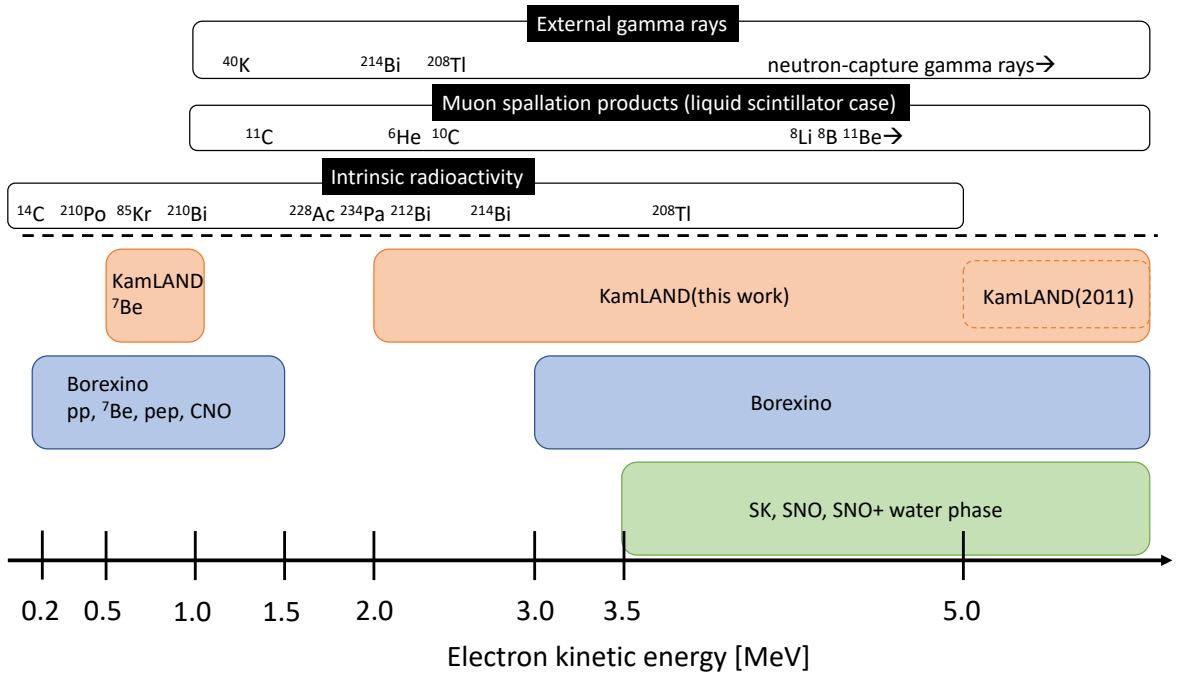

Figure 2.10: Summary of experimental measurements and backgrounds for several-MeV single events.

3 KamLAND

Kamioka Liquid scintillator Anti-Neutrino Detector (KamLAND) is a multi-purpose detector initially designed to observe anti-neutrinos coming from Japanese reactors. Physics data taking of KamLAND started in 2002 and the detector has been running for 20 years with some updates and modifications. Various physics analyses have been performed using it such as neutrino oscillation parameters measurement[23], geo-neutrino measurement[50], solar neutrino measurements[48, 51], astrophysical neutrino searches[52, 53, 54], neutrinoless double-beta decay search[7], and so on.

3.1 Detection Method

Liquid scintillators emit photons when excited by energy deposits of charged particles. Thus KamLAND can detect all of charged particle interactions brighter than a threshold by detecting the photons using photomultiplier tubes.

3.1.1 Neutrinos

The neutrino-electron elastic scattering (ES) is used for the solar neutrino analysis of this thesis. See Section 2.3 for the detail. The recoil-electron is just detected as a *single event*. No coincidence technique is available for this detection method.

3.1.2 Electron Anti-Neutrinos

KamLAND detects electron anti-neutrinos using inverse beta-decay:

$$\bar{\nu_e} + p \rightarrow e^+ + n. \tag{3.39}$$

The energy threshold of this reaction in the laboratory frame, where the proton is at rest, is calculated as follows:

$$E_{\text{th}} = \frac{(m_n + m_e)^2 - m_p^2}{2m_p} = 1.806 \text{ MeV}, \tag{3.40}$$

where m_n is the mass of a neutron, m_e the mass of an electron, and m_p the mass of a proton.

The pair of the positron and the neutron produced in the reaction creates a delayed coincidence (DC) signal as follows:

- Prompt signal: Energy deposit of e^+ (T_{e^+}) and annihilation γ's ($2m_e$)
- Delayed signal: γ from n-capture on p: $n + p \rightarrow d + \gamma$ (2.22MeV).

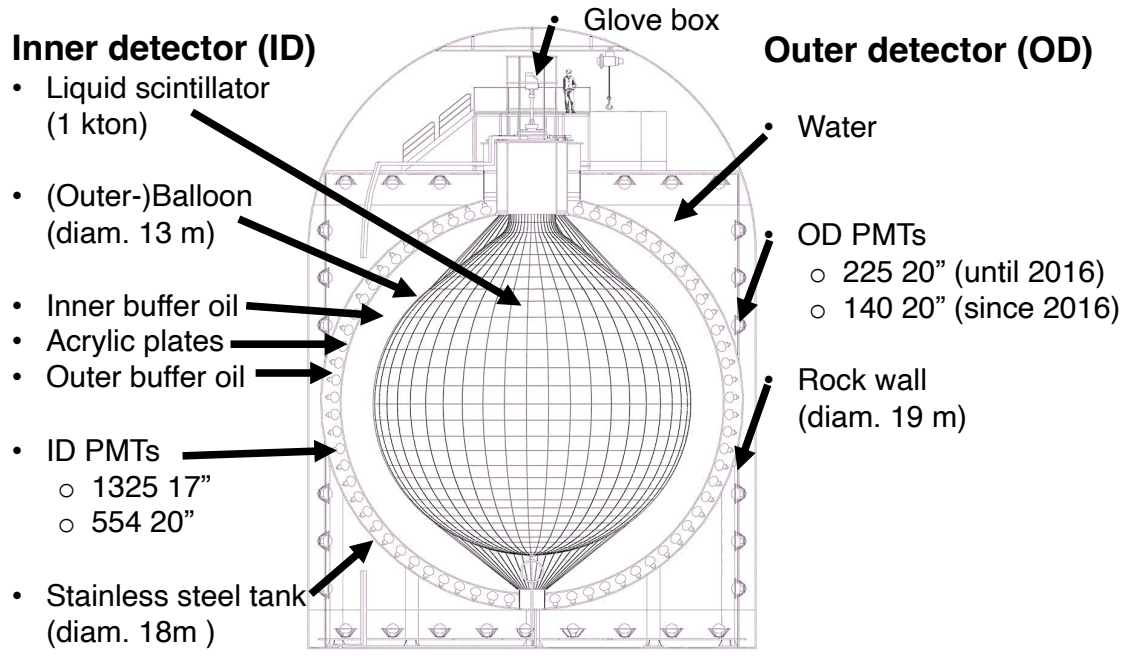

Figure 3.1: Schematic view of the KamLAND detector

The energy of the prompt signal ($E_{\rm p}$) has connection with the neutrino energy (E_ν) as follows:

$$E_{\rm p} = T_{e^+} + 2m_e \tag{3.41}$$
$$= (E_\nu + m_p - m_e - m_n - T_n) + 2m_e \tag{3.42}$$
$$= E_\nu - T_n - 0.78 \text{ MeV}, \tag{3.43}$$

where T_n is the kinetic energy of the neutron. T_n is $\mathcal{O}(10)$ keV for an MeV-neutrino. Thus it is almost negligible and E_p and E_ν are in 1-to-1 relation.

The mean capture time of neutrons in the KamLAND liquid scintillator was measured as 207.5 ± 2.8 μs [55].

The DC has strength in accidental background reduction; hence it can be characterized by the following parameters:

- Energy of the delayed signal ($E_{\rm d}$)
- Distance between the reconstructed vertices of the prompt and delayed signals (dR)
- Time difference between the prompt and delayed signals (dT)

3.2 Overview of the Detector

Figure 3.1 shows the schematic view of the KamLAND detector. The detector is located in Kamioka mine, Gifu, Japan. The experimental site is 1,000 m beneath Mt. Ikenoyama and it corresponds to 2,700 m.w.e. Cosmic-ray muon rate is 0.34 Hz in the detector[4], which is 10^{-5} of ground surface level. The components of the detector are divided into two parts: inner detector (ID) and outer detector (OD).

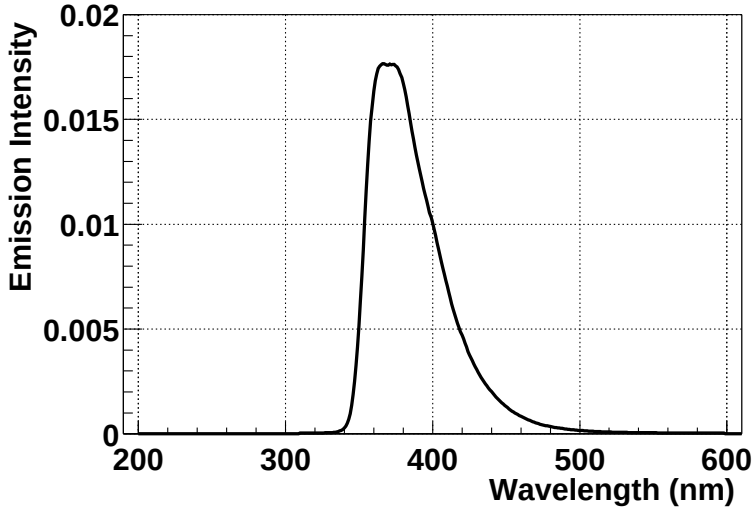

Figure 3.2: Emission spectrum of outer-LS. Figure from [56].

3.2.1 Inner Detector

The main component of ID is 1-kton liquid scintillator (LS). The LS is the target and the detector for neutrino interactions. Scintillation photons are produced by charged particles from the interactions. The photons are monitored by photomultiplier tubes (PMTs) mounted on stainless steel (SS) tank. The layered structure of the liquids, LS, inner buffer oil, and outer buffer oil, is designed to prevent Rn from coming inside the LS.

In KamLAND-Zen (see Section 3.3) periods, Xe-loaded LSs (a few 10-tons) are installed in the center of ID. In this text, I call Xe-loaded LS as Xe-LS (or inner-LS) and the original KamLAND LS as Kam-LS (or outer-LS). Similarly, I call the inner-LS container as inner-balloon and the outer-LS container as outer-balloon.

Liquid Scintillator (Outer-LS)

The liquid scintillator of KamLAND consists of 80.2% of pseudo-cumene (PC), 19.8% of dodecane, and 1.36 g/L of 2,5-diphenyloxazole (PPO). Fluorescence emission peak of PC is at ∼290 nm. PPO works as a wavelength shifter for its absorption peak is at ∼300 nm and its emission peak is at ∼360 nm, which is the sensitive region for PMTs (see Figure 3.4). Figure 3.2 shows the emission spectrum of outer-LS. Properties of outer-LS are summarized in Table 3.1.

Radiopurity of outer-LS is discussed in Section 3.5.3 and the number of targets is discussed in Section 3.8.

Balloon (Outer-balloon)

Outer-LS is contained in a plastic film vessel, (outer-)balloon, whose diameter is 13 m. The film has a 5-layered structure which consists of EVOH (25 μm thick) + Nylon (15 μm) $\times 3$ + EVOH (25 μm) (= 135 μm thick in total). EVOH has a high ability to prevent Rn permeation. The permeability of outer-balloon film is 1.95×10^{-10}cm^2/sec [58]. Kevlar

Table 3.1: Properties of outer-LS

Parameter	Value
Density at 11.5 °C	0.780 g/cm^3
Optical parameters from tuned MC simulation (T2KLG4sim-g4.9.6)	
Before purif.	
Light output	10,600 photons/MeV
Absorption length at 400 nm	15 m
Scintillation decay time	7.7 ns
After purif.	
Light output	8,600 photons/MeV
Absorption length at 400 nm	12.5 m
Scintillation decay time	8.2 ns
Light yield [57]	
Before purif.	
17" PMTs only	300 p.e./MeV
17" + 20" PMTs	500 p.e./MeV
After purif.	
17" PMTs only	200 p.e./MeV
17" + 20" PMTs	330 p.e./MeV
Refractive index at 400 nm	1.46

braid ropes, 44-longitudinal and 30-lateral, support the outer-balloon. ^{40}K activity in the Kevlar is 21.6 Bq (2.5 Bq of 1.46 MeV gamma-ray) [58].

Buffer Oil

The outer-balloon is surrounded by non-scintillating mineral oil, buffer oil. The buffer oil is a mixture of Normalparaffin ($C_{12}H_{26}$) and Isoparaffin (C_nH_{2n+2}, n$\sim$14). Acrylic plates (3 mm thick) separate buffer oil into two parts. Inner buffer oil and outer buffer oil. The outer buffer oil is exposed to PMTs and SS-tank wall, which provide Rn through emanation.

Photomultiplier Tubes (PMTs)

1325 PMTs with 17"-diameter photocathode (17" PMTs) and 554 PMTs with 20"-diameter photocathode (20" PMTs) detect scintillation photons from neutrino interactions. They were produced by Hamamatsu Photonics K.K. (HPKK). Figure 3.3 shows the schematic view of the PMTs.

The 17" PMT (HPKK R7250) was specially developed for better energy resolution and timing resolution based on the 20" PMT (HPKK R3600) [59]. The dynode type was changed from line-focus type to venetian-blind type and the photocathode size was limited to 17" diameter by masking while keeping the same physical size as 20" PMT. Thanks to these changes, the peak-to-valley (P/V) ratio against 1 p.e. signal and the

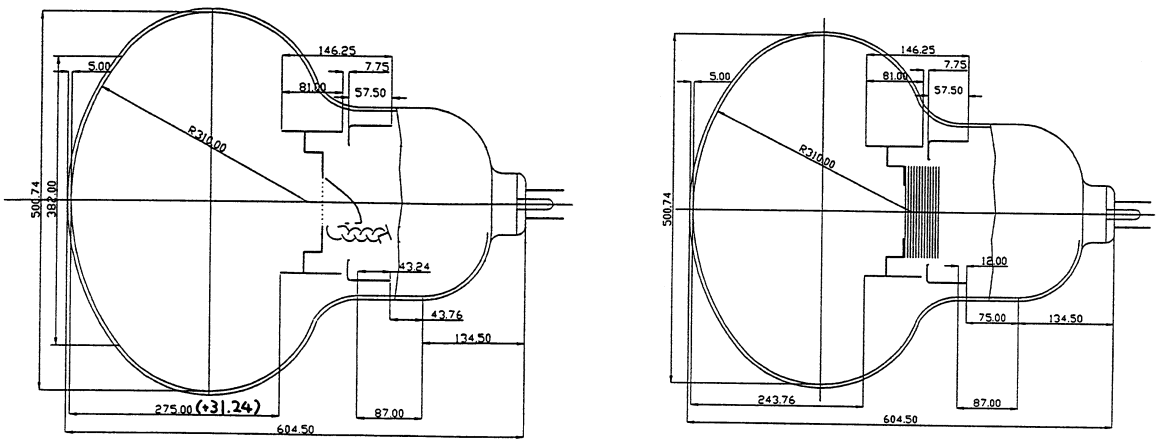

Figure 3.3: Schematic view of the PMTs. (Left) 17" PMT. (Right) 20" PMT. Figure from [56]

Table 3.2: Comparison of KamLAND PMTs. TTS and P/V ratio were measured by HPKK.

Parameter	17"	20"
Production ID	R7250	R3600
Dynode type	Line-focus	Venetian-blind
Physical size (diam.)	20"	
Photocathode size (diam.)	17"	20"
TTS (FWHM)	3.07 ns	5.39 ns
P/V ratio	3.40	1.74

transit time spread (TTS) were improved as compared to the 20" PMT. The differences of the PMTs are summarized in Table 3.2.

The quantum efficiency (Q.E.) of the KamLAND PMT is ∼20% at ∼350 nm (see Figure 3.4). The sensitive region ranges from 300 nm to 500 nm.

Geo magnetic compensation coils were installed in the KamLAND cavern to cancel the magnetic field of the earth (∼500 mG). It was measured that ±50 mG magnetic field changes the output of the 17" PMT by $< 20\%$ [60].

Thermometer [61]

Three thermometers were hung near the central axis of the detector in the beginning of KamLAND. They were removed on Apr. 19th, 2004.

The thermometers were made of platinum, MgO, and stainless steel. The size of them was 4 cm long and 0.5 cm in diameter. The cable for hanging them was teflon-coated copper. The three were positioned at z = -5.5 m, 0 m, and +5.5 m, where z is the height from the center of the detector.

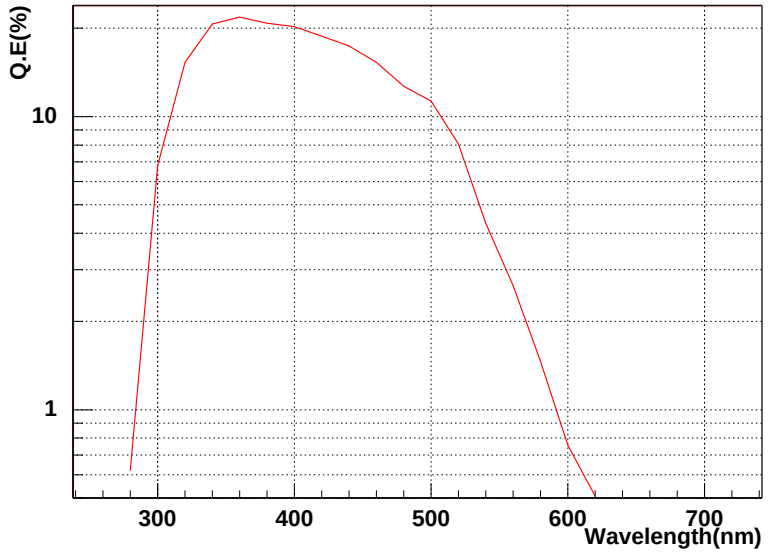

Figure 3.4: Q.E. of KamLAND PMTs measured by HPKK. Figure from [58].

3.2.2 Outer Detector

OD is 3.2 kton water-Cherenkov detector. It is used for cosmic-ray muon veto and acts as a shield against gamma-rays and fast neutrons from the rock cavern. At the start of the KamLAND experiment, 225 20" PMTs, which were formerly used for the Kamiokande experiment, were installed. Later in 2016, these were replaced by 140 20" PMTs (OD refurbishment campaign) [62]. Of the 140 PMTs, 40 are high quantum efficiency PMTs and were mounted to the detector equator region. There were Tyvek sheets at ±8.5 m from the detector equator, which optically separated the OD into 3 parts, top, middle, and bottom. They were removed at the refurbishment campaign. OD hardware trigger configuration was also changed at the campaign as follows:

- Before the campaign: 4 sectioned (top, upper middle, lower middle, bottom) triggers
- After the campaign: 3 sectioned (top, middle, bottom) and 1 global (total) triggers

In KamLAND physics analyses, the number of total-hit-OD-PMTs-in-200ns (N200OD) of 5 is commonly used for muon veto condition before the campaign and 9 after the campaign.

Purified water is continuously supplied from the bottom of the detector at a rate of $\sim 8\ \mathrm{m}^3$/hr. The targeted radiopurities are 0.22 mBq/L for ^{222}Rn (^{238}U series) and < 0.001 mBq/L for ^{224}Ra (^{232}Th series) [62].

3.3 KamLAND-Zen

KamLAND Zero neutrino double-beta decay experiment (KamLAND-Zen) searches for neutrinoless double-beta decay of ^{136}Xe ($Q_{\beta\beta}$=2.458 MeV) using xenon gas dissolved (∼3wt%) LS (Xe-LS). The xenon gas is enriched with ∼91% of ^{136}Xe. The Xe-LS is held by a 25-μm-thick nylon film vessel (Inner-balloon), which is put at the center of

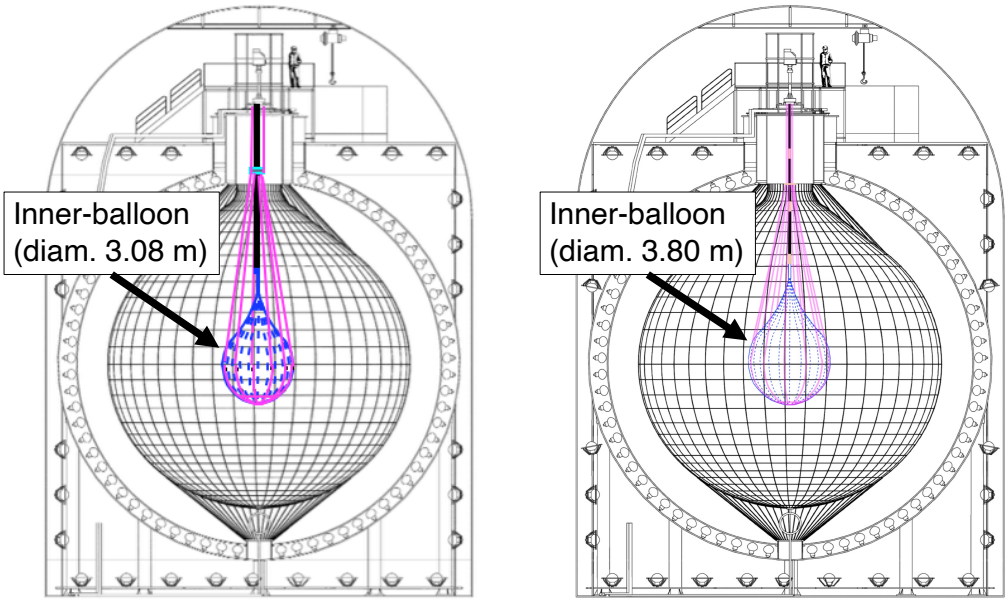

Figure 3.5: Schematic view of the KamLAND-Zen detector setup. (Left) KamLAND-Zen 400. (Right) KamLAND-Zen 800. The OD configuration is changed after the OD refurbishment campaign.

KamLAND ID (see Figure 3.5). The inner-balloon consists of 24 gores, which are heat-welded together.

3.3.1 KamLAND-Zen 400

Data taking of KamLAND-Zen 400 (Zen400) started in 2011 with the 3.08-m-diameter inner-balloon and 320 kg of xenon (Zen400 1st phase). After a purification campaign for ^{110m}Ag reduction, the xenon amount was increased to 380 kg (Zen400 2nd phase). The inner-balloon of Zen400 was un-installed in Dec. 2015.

3.3.2 KamLAND-Zen 800

Broken Inner-Balloon

Upgrade to KamLAND-Zen 800 (Zen800) with an almost doubled amount of xenon (745 kg) was first tried in 2016 (Failed Zen800). Inner-balloon with 3.80-m-diameter was installed to KamLAND ID and expanded with xenon-less LS in Aug. 2016. After a few months of monitoring before xenon loading, the KamLAND collaboration confirmed LS leakage from the inner-balloon and uninstalled it in Nov. 2016. The uninstalled balloon was inspected and several broken points (holes) were found at the welding line edges.

Data Taking with the New Inner-Balloon

A new inner-balloon for Zen800 was produced in 2017 with the revised welding method [63] and installed to KamLAND in May 2018. Data taking of Zen800 started in Jan. 2019

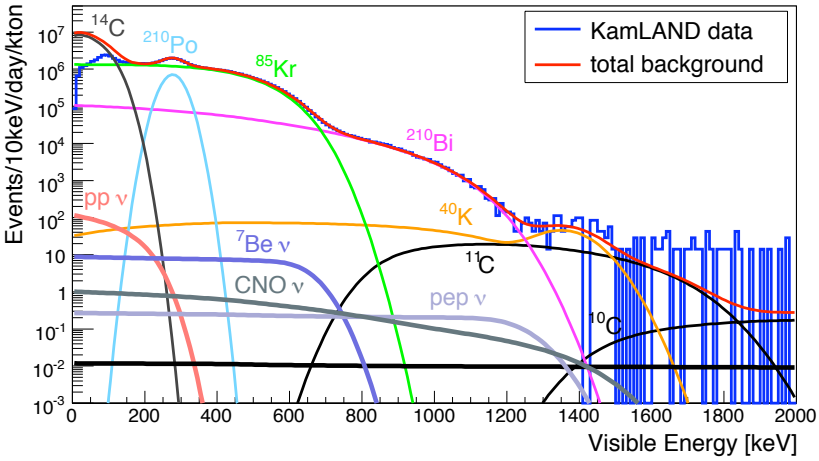

Figure 3.6: Single events energy spectrum of KamLAND until 2006. Figure from [64].

after some LS purification works.

3.4 History of KamLAND

The history of KamLAND is summarized in Table. 3.3. In the ^{8}B solar neutrino analysis of this thesis, the following periods are used:

- Period before the purification campaign: BeforePuri

  Analytical energy threshold > 5 MeV

- Period after the purification campaign and before Zen400: SolarPhase

  Analytical energy threshold > 2 MeV

- Period after Zen400 and before Zen800: AfterZen

  Analytical energy threshold > 2 MeV

Analytical energy thresholds are set lower for SolarPhase and AfterZen. Hence, in those periods, the activity of ^{232}Th in the LS is lower and nothing other than the LS is inside the ID.

3.5 Purification of Outer-LS

Decays of natural radioisotopes in outer-LS are background events for all physics analyses. At the beginning of KamLAND, for reactor anti-neutrino measurement, the focus of purification was on the reduction of ^{238}U (^{214}Bi), ^{232}Th (^{212}Bi and ^{208}Tl), and ^{40}K. They were removed by water extraction and nitrogen purge (the 1st purification system).

The low energy (< 2 MeV) event rate of KamLAND was, however, too high to detect ^{7}Be solar neutrinos. Background sources in this energy region were dominated by ^{85}Kr, ^{210}Bi, ^{210}Po, and ^{40}K (see Figure 3.6). To remove them, a circulation purification campaign was performed twice (2007 May.–2007 Aug. and 2008 Jun.–2009 Feb.) with distillation and high purity nitrogen purge (the 2nd purification system).

Table 3.3: History of KamLAND. Periods used for the ^{8}B solar neutrino analysis are highlighted with the bold font.

Period name	Date yyyy/mm/dd	Run#	Inside ID
Before purification (BeforePuri)			
Period 1	**2002/03/09–2004/04/19**	**000220–003611**	**Thermometer**
Period 2	**2004/04/19–2007/05/12**	**003612–006801**	**-**
(4π calibration)	(2007/01/04–2007/01/11)	(006474–006535)	Calibration
Outer-LS purification campaign			
1st purification	2007/05–2007/08		
After 1st purif.	2007/08–2008/06		
2nd purification	2008/06–2009/02		
After purification (SolarPhase)			
Period 1	**2009/04/07–2011/06/21**	**008502–010485**	**-**
(w $CdWO_4$)	(2011/05/27–2011/05/31)	(010447–010451)	$CdWO_4$
4π calibration	2011/06/21–2011/07/08	010486–010620	Calibration
Period 2	2011/07/08–2011/08/13	010621–010675	-
KamLAND-Zen 400 1st phase			
Preparation	2011/08–2011/10		Inner-balloon
Data set (DS) 1	2011/10/12–2012/02/09	011000–011212	Inner-balloon
Xe-LS filtration	2012/02/09–2012/03/01	011213–011253	Inner-balloon
DS 2	2012/03/01–2012/06/14	011254–011409	Inner-balloon
Xe-LS purification campaign			
	2012/06/14–2013/12/11		
KamLAND-Zen 400 2nd phase			
Period 1	2013/12/11–2014/11/17	012247–012770	Inner-balloon
Period 2	2014/11/17–2015/10/27	012771–013297	Inner-balloon
Xe-LS calibration	2015/10/27–2015/10/28		Inner-balloon
After calibration	2015/11–2015/12		Inner-balloon
	Inner-balloon un-installation 2015/12/23		
OD refurbishment campaign			
	2016/01/04–2016/06/22		
Between Zen400 and Zen800 (AfterZen)			
Period 1	**2016/06/22–2016/08/03**	**013720–013785**	**-**
Failed KL-Zen 800	2016/08–2016/11		Inner-balloon
	Inner-balloon un-installation 2016/11/22		
Period 2	**2016/12/05–2018/04/16**	**013991–014958**	**-**
KamLAND-Zen 800			
Preparation	2018/05–2019/01		Inner-balloon
Period 1	2019/01/22–ongoing	015404–ongoing	Inner-balloon

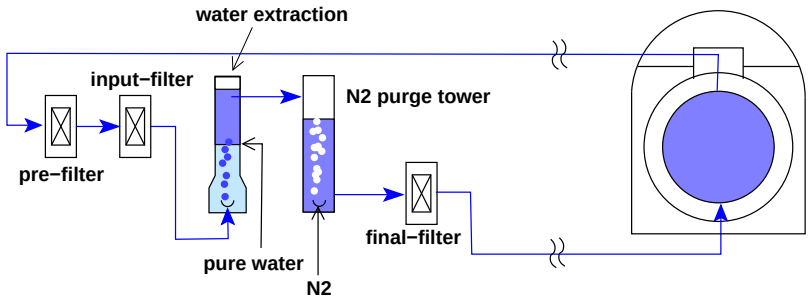

Figure 3.7: Schematic view of the 1st purification system. Figure from [58].

3.5.1 1st Purification System

1st purification system consists of water extraction towers, nitrogen purge towers, and three filters (Figure 3.7). Radioactive elements in the form of ions in oils are extracted by pure water. Nitrogen purge is effective for removing water, ^{222}Rn gas, and oxygen which affects the light yield of the LS. The finenesses of the filters are as follows:

- Pre-filter: 1 μm.
- Input-filter: 0.1 μm.
- Final-filter: 0.05 μm.

Problem of the 1st Purification System [64]

Nitrogen gas used for the 1st purification system was recycled in the system. It is suspected that ^{222}Rn, which turns into ^{210}Bi and ^{210}Po, and ^{85}Kr from a small leak in the system were accumulated as the filling process going.

3.5.2 2nd Purification System

2nd purification system, which was constructed in 2006, consists of distillation systems and high purity nitrogen purge systems as shown in Figure 3.8. See [64] for more detailed information. The LS drained from the KamLAND detector is distilled and divided into the original 3 components, PC, normalparaffin (NP), and PPO (Figure 3.9). They meet again in the mixing tank and the mixture is purged by nitrogen and sent back to KamLAND.

In order to reduce ^{210}Bi event rate, removal of its long-lived parent, ^{210}Pb ($T_{1/2} = 22.3$ yr), is necessary. Distillation is found to be the most efficient method to do it with the reduction factor of 10^3–10^4 [65].

Nitrogen purge towers of the 2nd purification system (Figure 3.10) achieves a high efficiency of ^{222}Rn removal thanks to low pressure and a large flow of nitrogen gas. A high purity nitrogen generator was constructed in KamLAND site. Radioactivities of the produced nitrogen gas are as follows:

- ^{222}Rn: 5 μBq/m^3.
- ^{85}Kr: $\ll 1$ μBq/m^3.

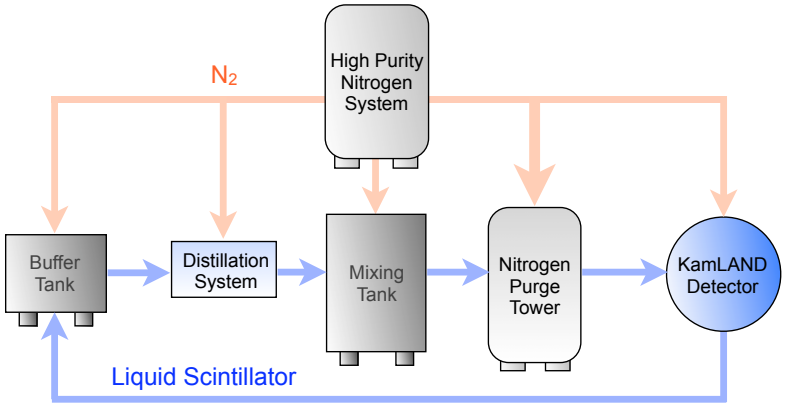

Figure 3.8: Schematic view of the 2st purification system. Figure from [64].

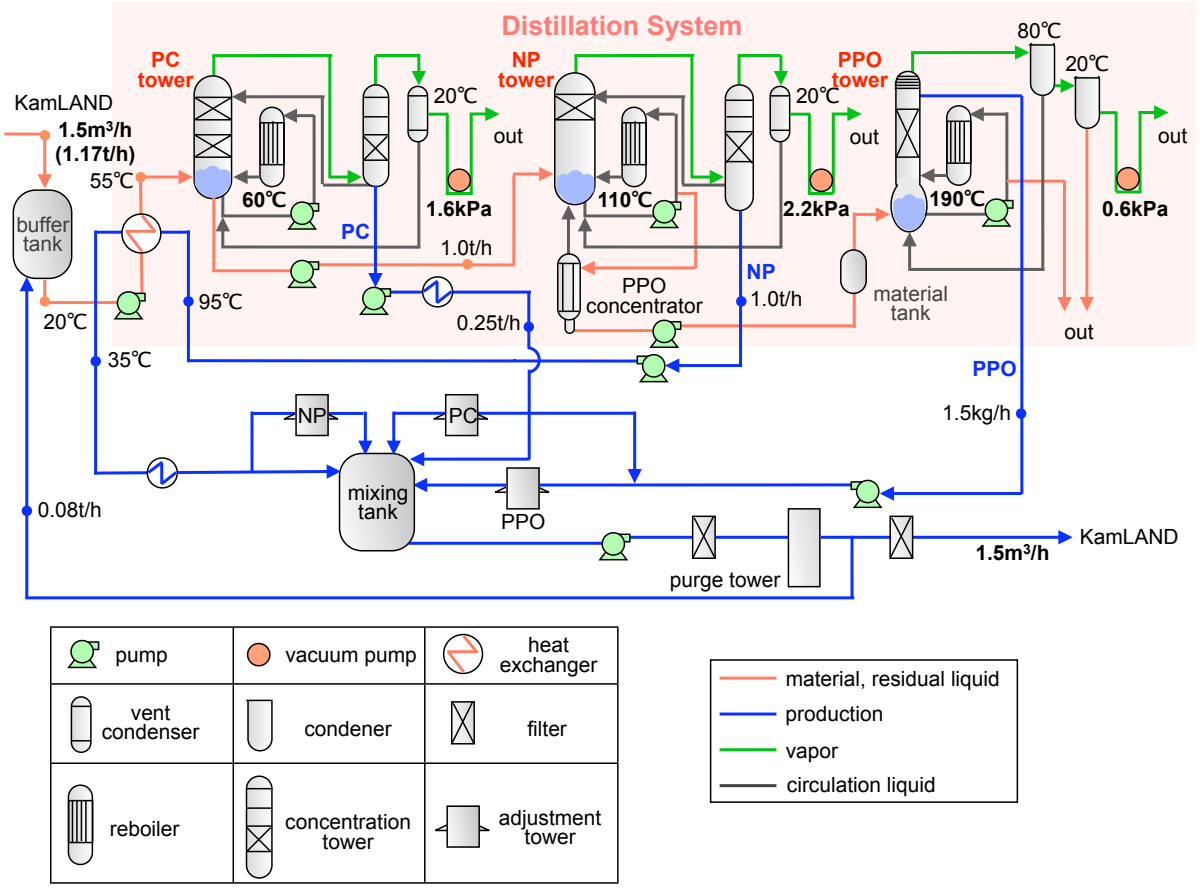

Figure 3.9: Schematic of the distillation system. Figure from [64].

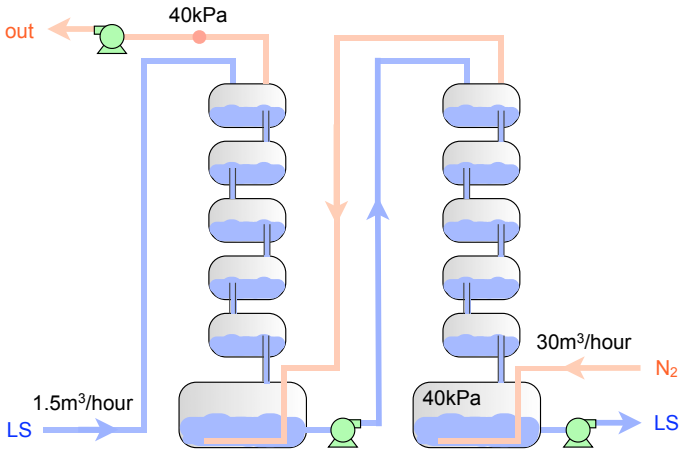

Figure 3.10: Nitrogen purge towers of the 2nd purification system. Figure from [64].

Table 3.4: Radioactivities in the LS. Before vs after processed by the 1st purification system.

Isotope	Raw LS	LS processed by the 1st purif. syst. [58]
^{238}U	2×10^{-13} g/g	$(3.5 \pm 0.5) \times 10^{-18}$ g/g
^{232}Th	$< 6 \times 10^{-12}$ g/g	$(5.2 \pm 0.2) \times 10^{-17}$ g/g
^{40}K	$< 1.2 \times 10^{-12}$ g/g	$< 2.7 \times 10^{-16}$ g/g

- ^{39}Ar: < 0.2 μBq/m^3.

3.5.3 Results of the Purifications

Performance of the 1st purification system

Radioactivities of the LS before applying any purification were measured by ICP-MS, and those of the LS processed by the 1st purification system were measured by KamLAND. ^{238}U (^{232}Th) concentration in KamLAND was evaluated from a delayed-coincidence-tagged event rate of ^{214}Bi–^{214}Po (^{212}Bi–^{212}Po) assuming secular equilibrium. See Table 3.4 for the summary.

Performance of the 2nd Purification System

^{238}U/^{232}Th/^{40}K concentrations in the LS processed by the 2nd purification system are summarized in Table. 3.5. A factor of ∼3 reduction in the ^{232}Th concentration as compared to the one achieved by the 1st purification system is important for the main topic of this thesis, a measurement of elastic scattering events of ^{8}B solar neutrinos. Daughters of ^{232}Th, ^{212}Bi–^{212}Po and ^{208}Tl, are background events for the analysis.

Event rate reduction in the < 2 MeV energy region is evident in Figure 3.11. Thanks to the reduction, KamLAND succeeded in a measurement of ^{7}Be solar neutrinos [51]. The reduction factors dependent on the energy region are as follows:

- 0.3 MeV (^{210}Po peak): 50.

Table 3.5: Radioactivities in the LS. After processed by the 2nd purification system [51]. For ^{232}Th and ^{40}K, the concentration values written in [51] are not directly used in this table. Instead, the ^{232}Th concentration is calculated from the event rate of 59 nBq/m^3 and the ^{40}K concentration is calculated from the event rate of 181/day/kton.

Isotope	Value
^{238}U	$(5.0 \pm 0.2) \times 10^{-18}$ g/g
^{232}Th	$(1.8 \pm 0.1) \times 10^{-17}$ g/g
^{40}K	$(8.2 \pm 1.3) \times 10^{-18}$ g/g

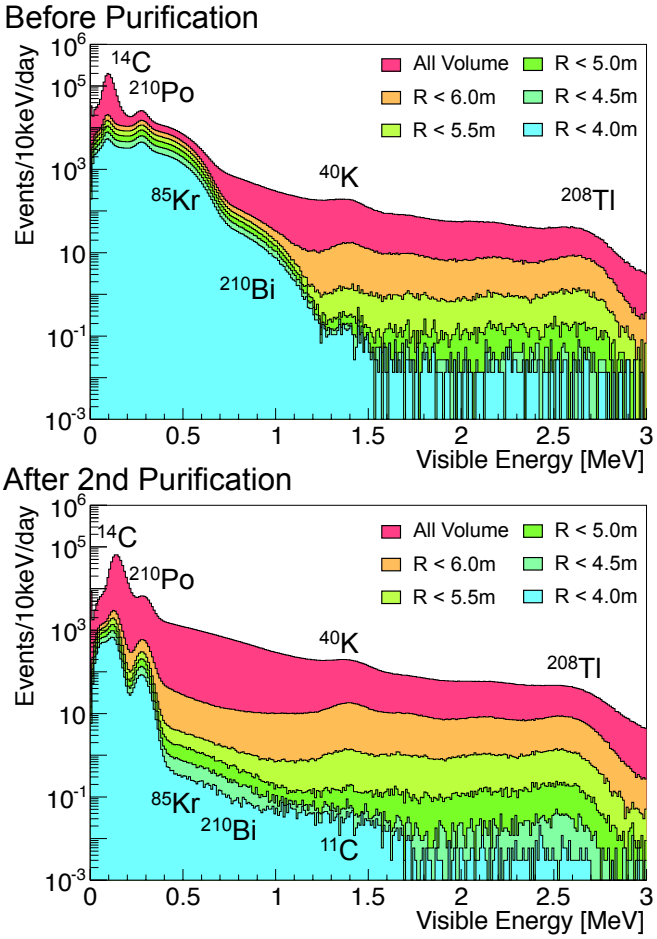

Figure 3.11: Single events energy spectra of KamLAND with various radius from the center of the detector (R) selections. (Upper) "Before Purification" means before processed by the 2nd purification system. (Lower) "After 2nd Purification" means after 2 times of the purification campaign with the 2nd purification system. Figure from [66].

Table 3.6: ^{210}Bi, ^{210}Po, and ^{85}Kr in Outer-LS [66].

Isotope	Before puri.	After 1st puri.	After 2nd puri.
		[mBq/m^3]	
^{210}Bi	37.2 ± 3.6	9.5 ± 0.3	0.43 ± 0.17
^{210}Po	44.3 ± 1.5	12.1 ± 0.1	3.0 ± 0.1
^{85}Kr	580.5 ± 3.6	169.6 ± 0.3	0.11 ± 0.13

- 0.5 MeV: 5,000.
- 1.0 MeV: 100.

Measured radioactivities of ^{210}Bi, ^{210}Po, and ^{85}Kr are summarized in Table. 3.6.

The lowered event rate allowed KamLAND to change the energy (prompt trigger) threshold from ∼0.6 MeV to ∼0.3 MeV. This plays a crucial role in 2–5 MeV analysis of ^{8}B solar neutrino analysis for 2 following reasons:

1. Tagging efficiency for the delayed coincidence of ^{214}Bi–^{214}Po ($T_{1/2}$ = 164 μs) is improved from ∼98% to >99.99%. The visible energy of the alpha ray from ^{214}Po decay is ∼0.55 MeV in KamLAND. Before the purification campaign, KamLAND could detect it using the delayed trigger (∼0.4 MeV threshold, 920 μs window). The time window, however, was the limitation of the tagging efficiency. With the lowered prompt threshold of 0.3 MeV, ^{214}Po is detectable without depending on the delayed trigger.

2. Quenched scintillation signals of alpha decay of ^{232}Th daughters, ^{220}Rn, ^{216}Po and ^{212}Bi, can be detected in the 0.3–0.5 MeV visible energy region in KamLAND. They are used to tag ^{212}Bi–^{212}Po and ^{208}Tl (see Section addRefLater).

Decrease of the Light Yield

Light yield of outer-LS decreased in the purification campaign with the 2nd purification system. Changes from the value of the before purification are −8% for after 1st purification campaign and −25% for after 2nd purification campaign [66].

3.6 Data Acquisition (DAQ)

KamLAND has 2 DAQ systems. One is KamDAQ which consists of front-end electronics (KamFEE) boards and a trigger module. The other is Module for General-Use Rapid Application (MoGURA) DAQ, which has been usable since 2013 (Zen400 2nd phase). Signals from 17" PMTs are divided into two and sent to both systems. 20" PMTs and OD PMTs are connected to KamDAQ only. KamDAQ data is used for general event reconstruction, and MoGURA is used for neutron events produced by cosmic-ray muons.

3.6.1 KamDAQ

KamFEE

KamFEE records signals from PMTs. 12 PMTs are connected to a KamFEE board. Its main component is Analog Transient Waveform Digitizer (ATWD) chip. ATWD holds an analog waveform of a PMT and digitizes it on request. The digitized waveform data consists of 128 of 10-bit samples. The sampling interval is set to 1.5 ns. Resulting time length of 192 ns (= 128 × 1.5 ns) is enough longer than 18-m-flight-time of a photon in LS (∼90 ns) + scintillation time width (∼50 ns) = 140 ns. The digitization takes ∼25 μs. To avoid deadtime during the digitization, one PMT is connected to two ATWDs, A channel and B channel, and the channels are cyclically used one by one.

It is required for FEE to process both signals from low energy events (1 p.e./PMT) and from high energy events like muon (>1000 p.e./PMT). There are three amplifiers on the KamFEE board as follows:

- High (H) gain: ×20
- Middle (M) gain: ×4
- Low (L) gain: ×0.5

The combination of 10-bit depth and the amplifiers realizes a dynamic range of 40,000.

Trigger

Trigger decision is made based on the number of hit PMTs. When a PMT signal exceeds the threshold of the discriminator, a digitized signal is issued for 125 ns. It is summed up within a board (up to 12) and the hit-sum is sent to the trigger board. A sum of the hit-sums from all KamFEE boards is called NSum, which is used for a trigger decision. The trigger board has a 40 MHz clock which is synchronized to GPS time.

There are some trigger types. Those related to analysis in this thesis are explained as follows:

- ID Prompt: Most basic one. A global acquisition command is sent to KamFEE cards when NSum exceeds the ID Prompt threshold.
- ID Delayed: During delayed-window[1] after an ID Prompt trigger issuance, a global acquisition command is sent to KamFEE cards when NSum exceeds ID Delayed threshold.
- 1 PPS: A global acquisition command is sent to KamFEE cards every second. (No acquisition command had been sent until Feb. 15, 2004 [67].)
- ID Prescale: During the prescale-window (0.01024 sec) after a 1-PPS trigger issuance, a global acquisition command is sent to KamFEE cards when NSum exceeds the ID Prescale threshold.

[1] The delayed window is set to 1000 μs in the trigger script. In 2018, it was found that the realized value was ∼920 μs, and the script was updated to make the realized value ∼1230 μs.

Table 3.7: History of the trigger threshold settings.

Period	NSumMax threshold (corresponding ∼50% eff. E_{vis}) Prompt	Delayed
BeforePuri	200 (0.75 MeV)	120 (0.35 MeV)
SolarPhase	70 (0.25 MeV)	70 (0.25 MeV)
AfterZen	70 (0.35 MeV)	50 (0.2 MeV)
Zen800 (until Jan. 19, 2020)	60 (0.3 MeV)	50 (0.25 MeV)
Zen800 (since Jan. 20, 2020)	47 (0.2 MeV)	45 (0.2 MeV)

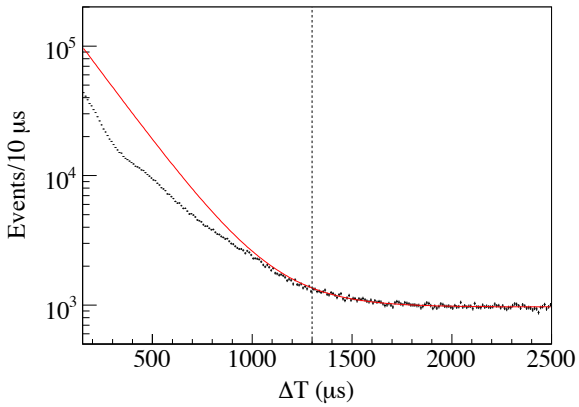

Figure 3.12: Time-difference-from-muon (ΔT) distribution of the neutron candidate events ($1.8 < E_{\mathrm{vis}} < 2.6$ MeV) of the KamDAQ data. Red line shows the best fit result of (exponential + constant) fitting to the data (fit range is ΔT >1300 μs). Figure from [55].

Trigger thresholds are different depending on the periods. Table 3.7 shows the summary. Prescale trigger is used for the efficiency evaluations of the prompt and delayed triggers. In the before purification period, sequential decays of ^{214}Bi–^{214}Po ($\tau = 237$ μs, $E_{\mathrm{vis}} \sim 0.55$ MeV) were taggable only through the delayed trigger. Since the after purification period, the prompt trigger threshold has been low enough to detect ^{214}Po in LS. In KamLAND-Zen periods, it is required to detect quenched ^{214}Po signal from the inner-balloon film. Thus the delayed trigger threshold was lowered at the start of Zen400. When comparing SolarPhase and AfterZen, the reason for the worsening energy thresholds despite the same NSumMax thresholds is that the number of bad PMTs began to increase rapidly around the end of SolarPhase. In the Zen800 period, the KamLAND collaboration further lowered the threshold after the finding that ^{220}Rn and ^{216}Po events ($E_{\mathrm{vis}} = 0.25$–0.6 MeV) can be used to tag the events of ^{212}Bi–^{212}Po and ^{208}Tl [68].

3.6.2 Problem of the Data Taking After High Energy Events

After high energy events like cosmic-ray muons, overshoots and after pulses of PMTs happen. Due to them, for about ∼1ms, KamDAQ is not so good at detecting low energy events such as neutron capture gamma-rays (capture time in LS ∼200 μs) produced by cosmic-ray muons (Figure 3.12).

Overshoot

KamLAND PMTs have overshoot after muons, and the baseline goes up by a few mV, which is higher than the pulse height of 1 p.e. signal ($\sim$1 mV). The recovery time constant is $\sim$470 μs [69]. The Cause of the overshoot is at the AC coupling part in the PMT's bleeder circuit.

After Pulse

After pulse is caused by residual gas in a PMT. Photo electrons created by incident light ionize the gas while heading to dynode and produce cations. The cations tackle photo cathode and produce photo electrons again.

After pulse of a KamLAND PMT occurs $\mathcal{O}$(1–10) μs after the main pulse, and the fraction is $\sim$3% of the main pulse [60].

3.6.3 MoGURA DAQ

MoGURA DAQ is basically an improved system from KamDAQ especially aiming for deadtime-free data collection. It is currently used only for neutron events after muons. Its high performance of data taking after muons is made possible by the MoGURA board, baseline restorer (BLR), and special trigger logic (Adaptive trigger).

MoGURA

MoGURA has 8-bit FADCs, which can digitize analog signals within only $\sim$1 ns (cf. 25 μs by KamFEE). There are 4 amplifiers on MoGURA:

- Precise (P) gain: $\times$120
- High (H) gain: $\times$24
- Middle (M) gain: $\times$2.4
- Low (L) gain: $\times$0.24

Sampling rate of P gain is as high as 1 GHz and those of other gains are 200 MHz.

BLR

BLR stabilizes the baseline of the PMT signal by deriving and subtracting low-frequency components in the signal. It enables the baseline recovery within $\sim$1 μs.

Adaptive Trigger

Adaptive trigger is a differential trigger decision mechanism to mitigate NHit-baseline shift. The mode is enabled after a high energy event (NHit >950) which issues a Launch trigger.

Original MoGURA DAQ configuration without the Adaptive trigger (in 2009–2012) had suffered from overflow of data after muons. As a result, the detection efficiency of spallation neutrons was only $\sim$70%. After the Adaptive trigger installation, it was improved to $\sim$90% [69]. The improvement is visible in Figure 3.13.

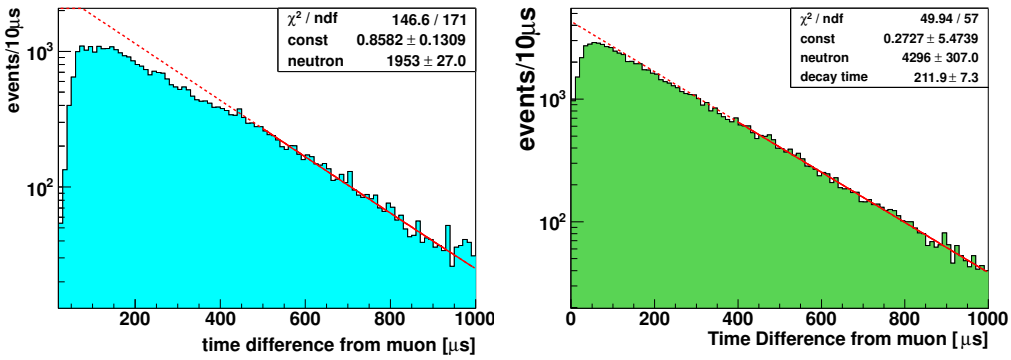

Figure 3.13: Time-difference-from-muon distribution of the neutron candidate events of the MoGURA DAQ data. Non-showering muons (residual charge $<10^6$ p.e.) are selected. (Left) Without Adaptive trigger. (Right) With Adaptive trigger. Figure from [69].

Table 3.8: Calibration sources used in KamLAND

Source	Visible Particle	Energy (MeV)
^{203}Hg	γ	0.279
^{137}Cs	γ	0.622
^{68}Ge	e^+ annihilation γ	0.511×2
^{65}Zn	γ	1.116
^{60}Co	γ	$1.133 + 1.173$
^{241}Am^{9}Be	de-excitation γ, n-capture γ	4.438, 2.223
^{210}Po^{13}C	de-excitation γ, n-capture γ	4.438, 2.223

3.7 Calibration Systems

Detector calibrations are essential to understand the response of the LS and PMTs. KamLAND has a z-axis calibration system and an off-axis (4π) calibration system. These are mounted in a glovebox in the chimney section of KamLAND, which is over-pressured with nitrogen gas to prevent radon gas contamination. Figure 3.14 shows the schematic view of the glovebox. The diameter of the detector access flange at the bottom of the glovebox is 8 inches. Various radioactive sources (see Table 3.8) and a diffusion ball (for lasers) have been deployed using the systems.

3.7.1 z-axis Calibration System

The central z-axis calibration in KamLAND is performed by simply bringing the source down from the glovebox since the glovebox is located at $(x, y) = (0, 0)$ position, where x and y are the distances from the detector center. The z-axis calibration system was installed in 2002 and upgraded once in 2009. Here I call the old system as v1 z-axis system and the new one as MiniCal.

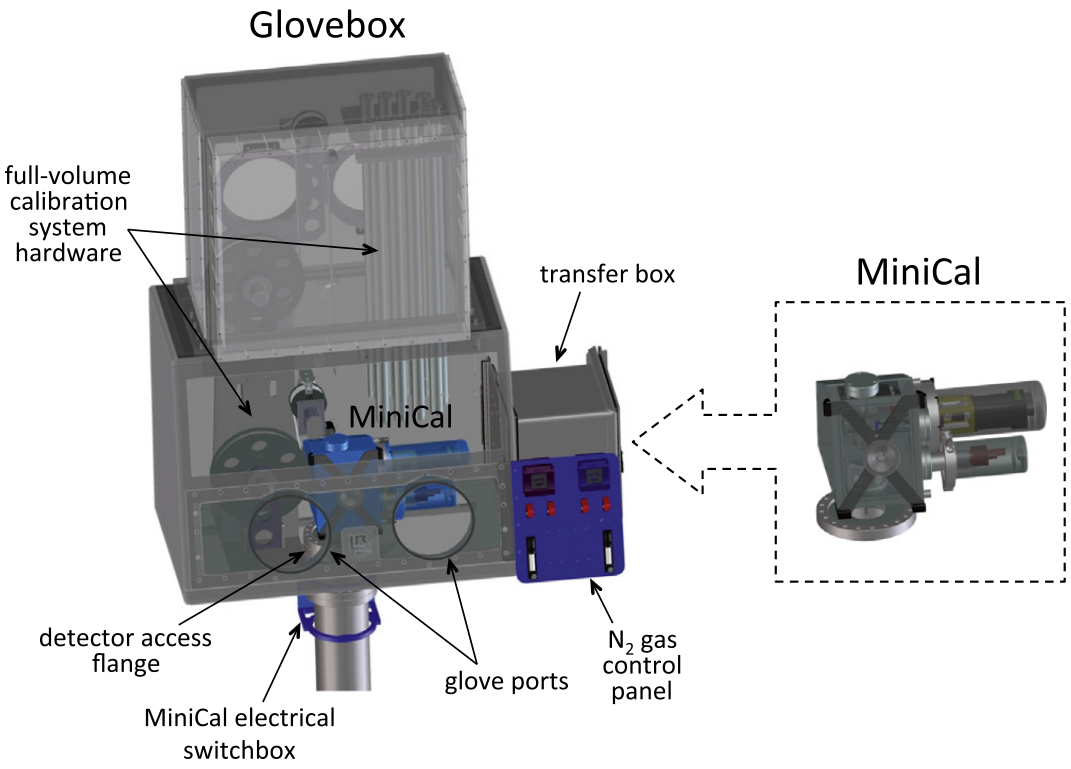

Figure 3.14: Schematic view of the glovebox of KamLAND. Figure from [70].

Problem of the V1 z-axis System

In the BeforePuri period with the v1 z-axis system, sometimes increase in the activity of ^{222}Rn was observed after the operations. Figure 3.15 shows the one-year trend of ^{222}Rn activity in KamLAND on a log-scale and Figure 3.16 shows the trend in a shorter period and on a linear scale. About 70 μBq ($= 0.1$ μBq/m^3 increase in the figure $\times$Volume$_{r<5.5\text{ m}}$) of the activity was introduced with each operation. It is suspected that the cable used to bring down the source collected radon while the system was not in use [70]. The cable was exposed to the air in the glovebox.

MiniCal

MiniCal [70] is a compact and ultra-clean z-axis calibration system. Figure 3.17 shows the schematic view of MiniCal. The compactness of the system was designed to fit within the existing glovebox. MiniCal itself is hermetically sealed and both volumes of MiniCal and the glovebox are flushed with nitrogen gas to prevent radon contamination when operating.

Figure 3.18 shows the ^{222}Rn activity in the SolarPhase with MiniCal. The global trend is formed by radon carried from the outer-balloon by convection. $\mathcal{O}(0.1)$ μBq/m^3 spikes seen in Figure 3.16 are not evident in Figure 3.18, see around Jul. 2009 for example.

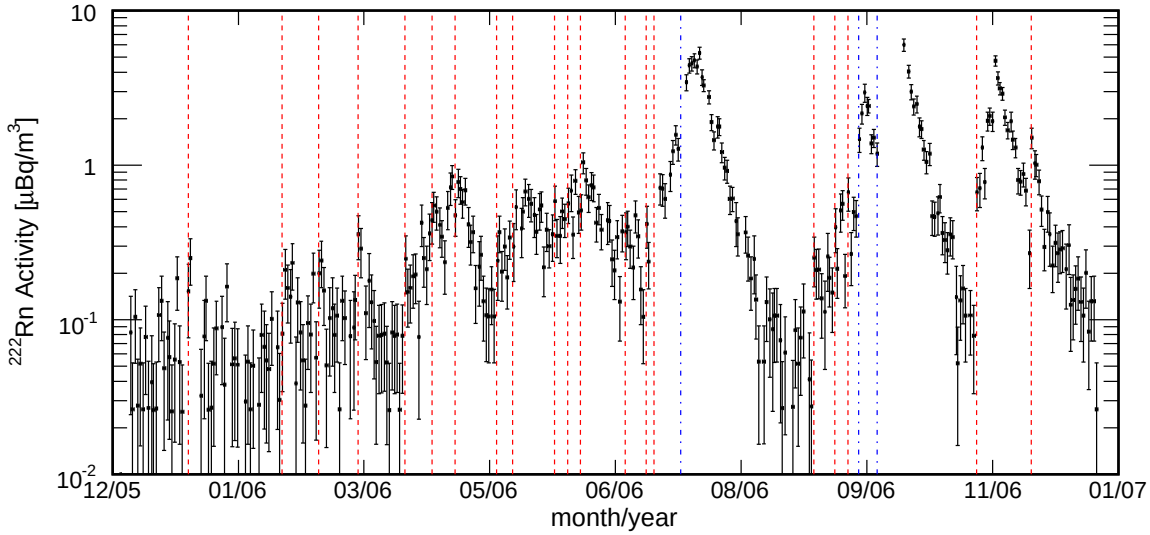

Figure 3.15: Rn activity in the BeforePurii inside a 5.5-m-radius fiducial volume. Red lines indicate the v1 z-axis calibration timings. Blue lines indicate the off-axis calibration timings. Figure from [71].

3.7.2 Off-axis Calibration System

The off-axis (4π) calibration system [71] has an articulated pole (see Figure 3.19) that can be angled with two cables to place sources in various positions. Figure 3.20 shows the illustration of the system.

The KamLAND collaboration performed the 4π calibration campaign twice. One was in the BeforePuri period and another was at the end of SolarPhase. As a result of the first campaign, the uncertainty of a 5.5-m-radius fiducial volume was reduced by a factor of two [71].

3.7.3 Calibration with Radioactive Sources

Radioactive sources are used for calibrating reconstructed energy and understanding the time variation of relative PMT hit-timings, which is caused by KamFEE board replacements. The sources are housed in an LS-resistant Teflon or stainless steel container, paired with a weight, and introduced into the detector. Figure 3.21 shows the example deployments.

3.7.4 Calibration with Lasers

KamLAND has two laser calibration systems. One is called the Japan Laser System and has a 500-nm dye-laser. The wavelength is longer than the absorption wavelength of the LS. Therefore it is useful for the timing calibration. Another is called the U.S. Laser System and has a 337-nm nitrogen laser. Photons with this wavelength are absorbed by the LS and re-emitted with a longer wavelength. Hence the system is useful for understanding the light propagation process [61]. Figure 3.22 shows the setup of the Japan Laser System.

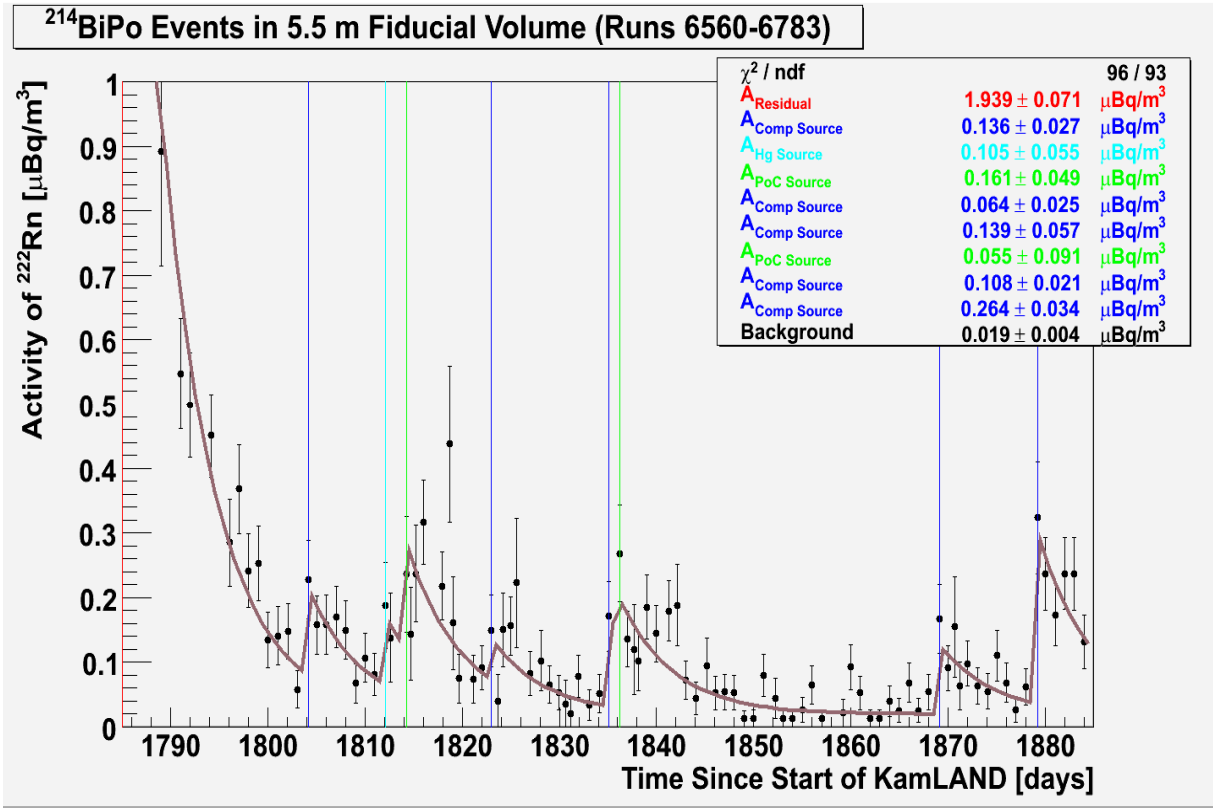

Figure 3.16: Rn activity in the BeforePuri inside a 5.5-m-radius fiducial volume. Colored vertical lines indicate the v1 z-axis calibration timings. The gray line shows the model (background + activities introduced during calibrations) fitted to the data. Figure from [72].

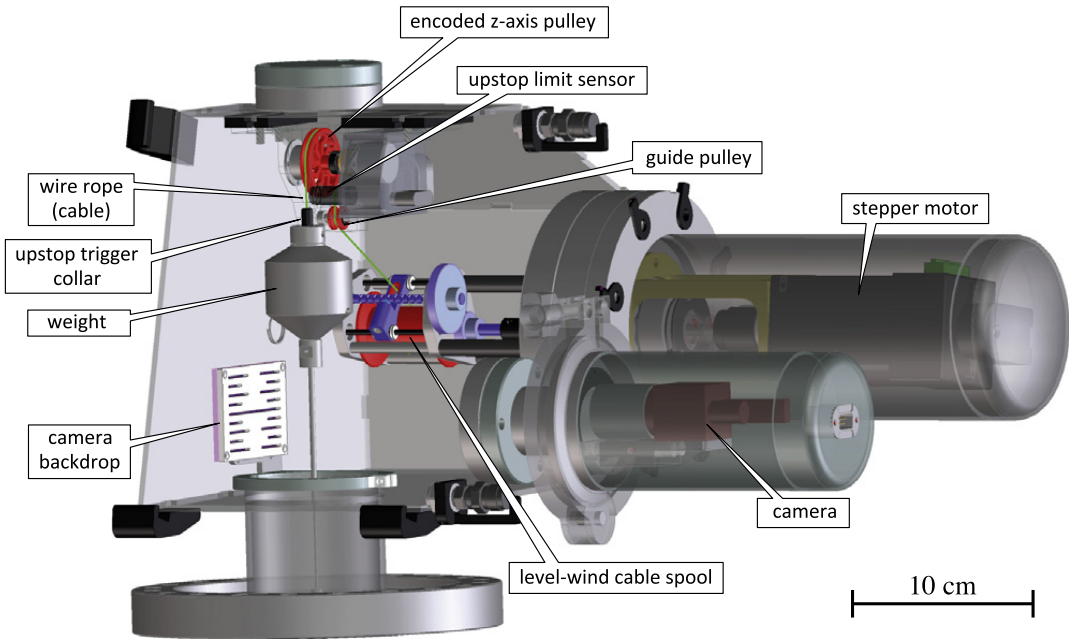

Figure 3.17: Schematic view of MiniCal. Red lines indicate the MiniCal calibration timings. Figure from [70].

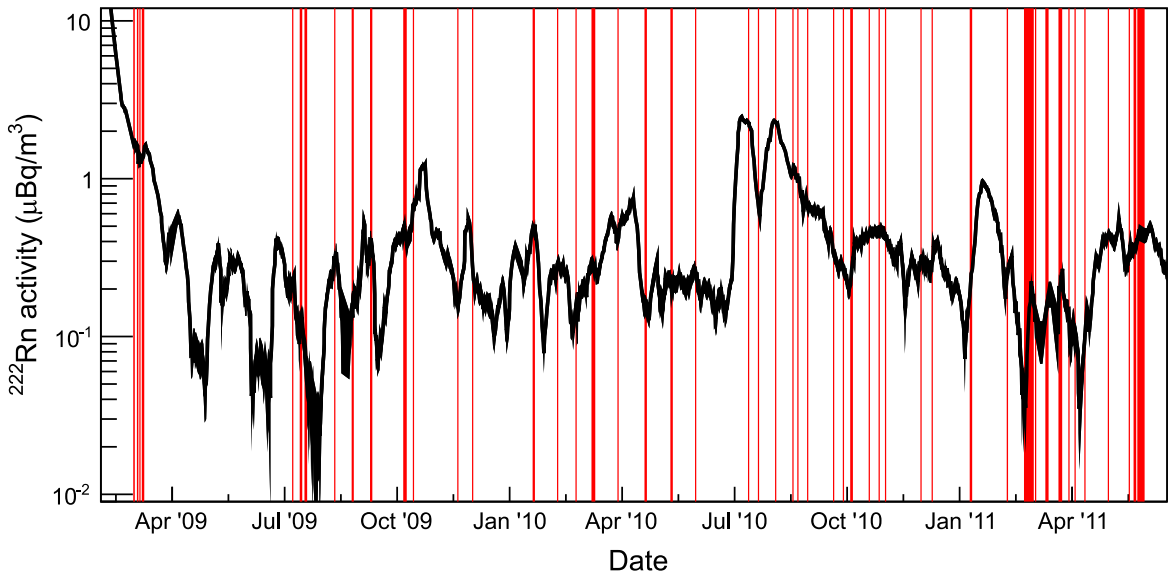

Figure 3.18: Rn activity in the SolarPhase inside a 5.5-m-radius fiducial volume. Red lines indicate calibration operations using MiniCal. Figure from [70].

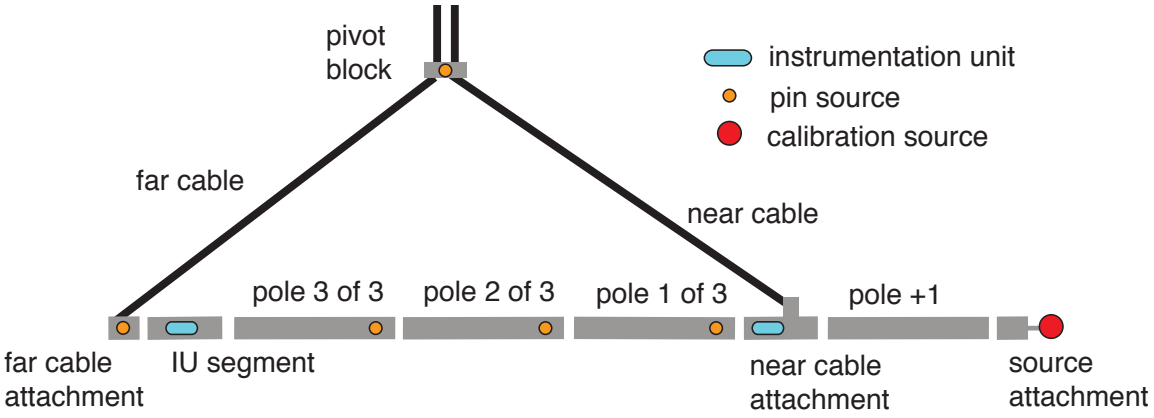

Figure 3.19: Schematic view of the 4π calibration pole. Figure from [71].

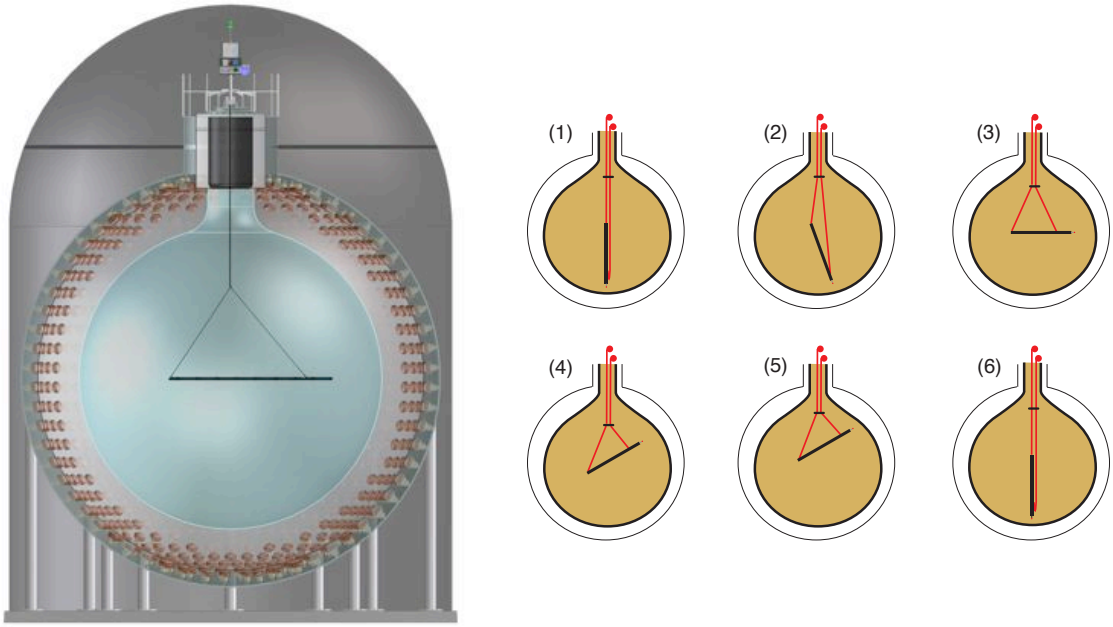

Figure 3.20: Illustration of the 4π calibration system. Figure from [71].

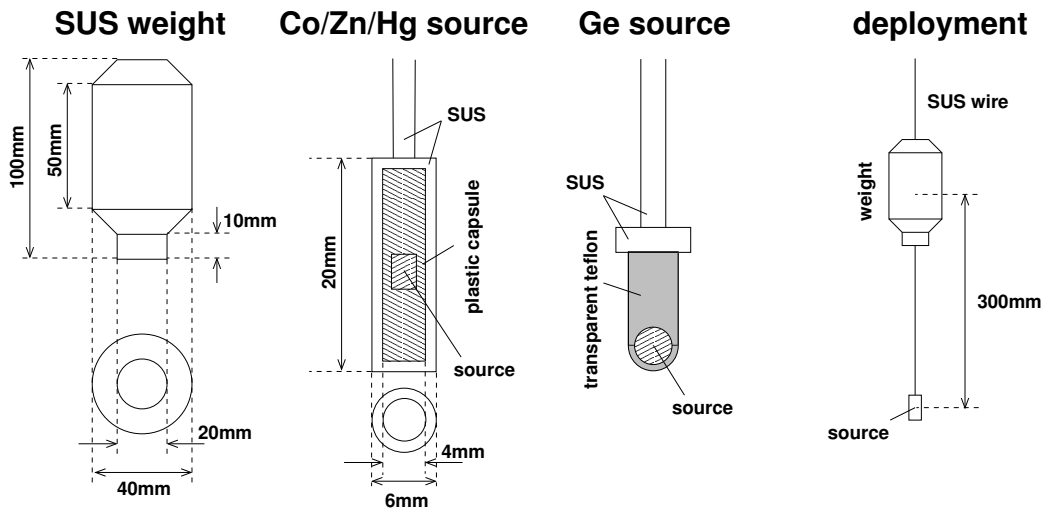

Figure 3.21: Schematic view of the radioactive sources. Figure from [58].

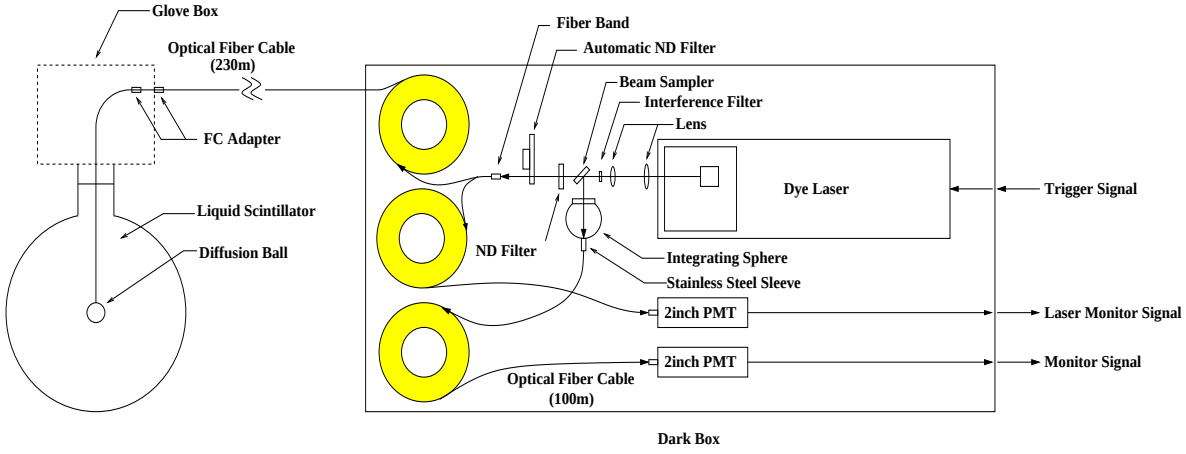

Figure 3.22: Schematic view of the Japan Laser System. Figrure from [56].

3.8 Number of Targets

3.8.1 Targets per LS Mass

The Outer-LS consists of dodecane (80.2%$_{\text{volume}}$), PC (19.8%$_{\text{volume}}$), and PPO (1.36 ± 0.02 g/L$_{\text{Dodecane+PC}}$). The dodecane versus PC ratio is calculated from the input amount of each component at the detector construction [73]. The PPO concentration is the measured value of the LS sampled from KamLAND [74].

Specific densities of dodecane and PC at 15°C are 0.7526 g/cm^3 and 0.8796 g/cm^3, respectively. Based on these values, the mass ratios of the LS components including PPO are calculated as follows:

$$\text{Dodecane} : \text{PC} : \text{PPO} = 77.471\% : 22.354\% : 0.175\%.$$

Molar masses of the three components are as follows:

- Dodecane ($C_{12}H_{26}$): 170.34 g/mol
- PC (C_9H_{12}): 120.195 g/mol
- PPO ($C_{15}H_{11}NO$): 221.259 g/mol

Here, the following atomic weights [75] are used for the calculation:

- H: 1.008
- C: 12.011
- N: 14.007
- O: 15.999

Numbers of the molecules per 1 g of LS are calculated to be as follows:

- Dodecane: 0.77471 / 170.34 = 4.5480×10^{-3} mol/g
- PC: 0.22354 / 120.195 = 1.8598×10^{-3} mol/g
- PPO: 0.00175 / 221.259 = 0.00791×10^{-3} mol/g

Thus numbers of the elements per 1 kton of LS are calculated to be as follows:

- H: 8.4708×10^{31}
- C: 4.3018×10^{31}
- N: 4.76×10^{27}
- O: 4.76×10^{27}
- e^-: 3.4289×10^{32}

The ^{13}C/C ratio of the LS was measured as $(1.0923 \pm 0.0001)\%$ [76]. Based on this, number of ^{13}C targets per 1-kton of LS is calculated to be

$$4.6990 \times 10^{29}.$$

Table 3.9: Number of targets from water and gasses in the LS.

element	number from water [/kton$_{\mathrm{LS}}$]	number from gasses [/kton$_{\mathrm{LS}}$]
H	2.0×10^{27}	-
N	-	$< 6.7 \times 10^{27}$
O	1.0×10^{27}	$< 1.1 \times 10^{26}$

Possibility of the Change of the Composition

The input amounts of dodecane and PC were measured before the processing of the water extraction and nitrogen purge. The amounts may change in the processes. Though a change of the volume by mixing dodecane and PC is not measured, the measured LS density, $(777.54 \pm 0.2) \times 10^{-3}$ g/cm^3, is lower than the simple weighted average of dodecane (80.2%) and PC (19.2%), 777.746×10^{-3} g/cm^3.

Based on the following things

- measured LS density: $(777.54 \pm 0.2) \times 10^{-3}$ g/cm^3
- measured PPO concentration: 1.36 ± 0.02 g/L$_{\mathrm{dodecane+PC}}$
- assumption: no volume change by mixing the components ($\mathrm{Vol}_{\mathrm{dodecane}} + \mathrm{Vol}_{\mathrm{PC}} + \mathrm{Vol}_{\mathrm{PPO}} = \mathrm{Vol}_{\mathrm{LS}}$)
- density of PPO: 1.1 ± 0.1 g/cm^3 [77, 78]

the density of the dodecane and PC mixture is estimated to be 777.144×10^{-3} g/cm^3. The composition is also estimated to be dodecane : PC = 80.67 : 19.33. The impacts of the change in the composition are 0.2% for H, 0.03% for C, and 0.02% for e^-. In the solar neutrino analysis of this thesis, only C and e^- matter and the impacts are negligibly small.

Contributions from Water and Gasses

The water contamination in the LS before the purification campaign was measured as 30 ppm [56]. Oxygen dissolved in the LS was measured as < 3 ppm [79]. Nitrogen dissolved in the LS is estimated to be < 156 ppm based on the discussion on the nitrogen solubility for dodecane and PC [61]. The numbers of targets calculated from these values are summarized in Table 3.9. These contributions are negligible in the calculation of the numbers of H, C, and e^-.

3.8.2 Temperature and Density of the LS

The averaged temperature of the LS is 11.5 °C. Figure 3.23 shows the temperature distribution in KamLAND. It ranges from 10.5 to 14 °C in the volume within the radius from the center of the detector (r) of 4 m. Thus the LS temperature can be conservatively expressed as 11.5 ± 2.5 °C.

The measured Outer-LS density is $(777.54 \pm 0.20) \times 10^{-3}$ g/cm^3 at 15 °C. The temperature dependence of the density of the LS was measured as 7.41×10^{-4} g/cm^3/K. Therefore

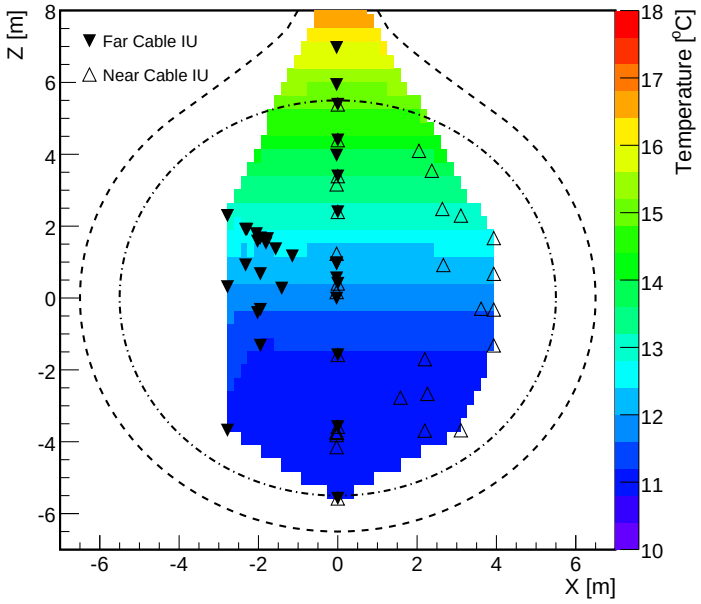

Figure 3.23: Temperature distribution in KamLAND. Figure from [71]

the density of the LS in the volume of $r < 4$ m is estimated to be $(780.13 \pm 1.86) \times 10^{-3}$ g/cm^3.

3.8.3 Impact of the Purification Campaign

At the last cycle of the LS filling of the purification campaign, the density of the LS was maintained to be $(777.5 \pm 0.5) \times 10^{-3}$ g/cm^3 at 15 °C, see Figure 3.24. The PPO concentration was also maintained to be $1.36^{+0.01}_{-0.04}$ g/L [80]. Based on these values, the impact of the purification campaign on the number of target electrons is estimated to be less than 0.1% and negligible.

3.8.4 Summary of This Section

In summary, the numbers of targets per LS volume are as follows:

- e^-: $(2.6750 \pm 0.0064) \times 10^{29}$ /m^3
- ^{13}C: $(3.6658 \pm 0.0087) \times 10^{26}$ /m^3

The uncertainties are dominated by the temperature (density) distribution.

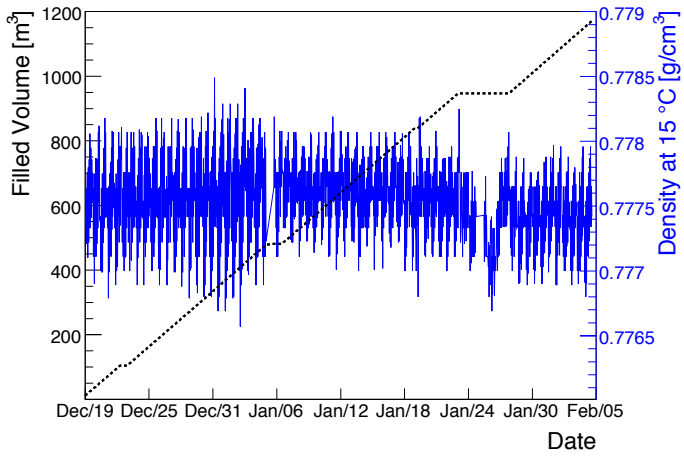

Figure 3.24: Time variation of the density of the LS filled at the last cycle of the purification campaign. Figure from [64]

4 Event Reconstruction

This chapter describes general event reconstruction process of KamLAND data. Figure 4.1 shows the schematic diagram. The data is processed as follows:

1. The most primitive data in KamLAND is the collection of digitized signals of PMTs, which is called *kdf*. *kdf* has trigger and timestamp information.
2. An event builder reads the *kdf*, sorts the data fragments using the timestamp, and stores the sorted data to a serial file (*sf*).
3. Waveform analyses are applied to the *sf* events and hit-timings and charge information are derived. They are stored to a raw-TQ file (*rtq*).
4. Several correction (constant) tables are created based on the *rtq*.
5. Finally, using the tables, events are reconstructed from the *rtq*. Point like events have vertex and energy information. Track like events have entrance and exit position information. The stored file format is called (general) vector file (*[g]vf*).

4.1 Waveform Analysis

Hit-timings and charges of photons are derived by finding peaks in the waveform after pedestal subtraction.

At the beginning of each run, pedestal data is taken using random triggers and sampling interval calibration is performed using a 25-ns clock pulse.

Figure 4.2 shows example waveforms after pedestal subtraction. The vertical red lines indicate identified peak timings. In Figure 4.2 (Left), the vertical line left side of the peak indicates the leading edge and one right side of the peak indicates the trailing edge. The hit-timing is defined as the leading edge timing. The charge is defined as the sum of ATWD channel numbers from the leading edge to the trailing edge.

See Ref. [58] for the detail of the peak finding algorithm.

4.2 Creation of Correction (Constant) Tables

4.2.1 Timing Correction

Hit-timings of PMTs are basically calibrated using a laser (T_{laser}). Additional corrections are considered for some periods as follows:

- T_{time}: time variation of the detector condition after a laser calibration
- T_{cable}: delay due to the cable extension for the BLR installation in 2009

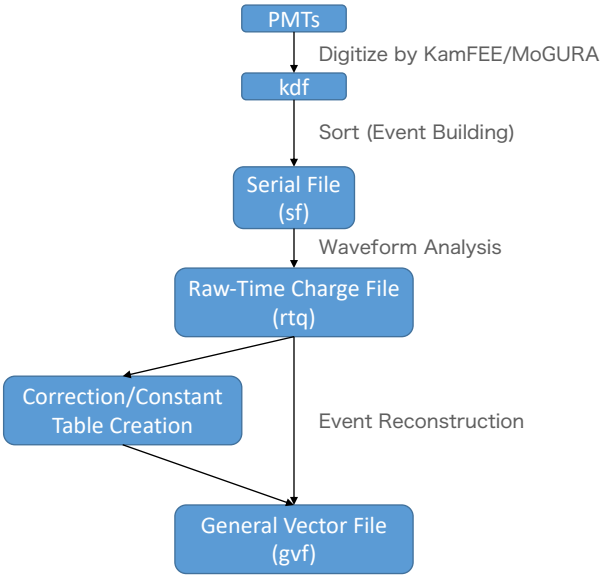

Figure 4.1: Schematic diagram of the event reconstruction in KamLAND

Therefore, the timing correction (offset) for a PMT is given by

$$T_{\text{offset}} = T_{\text{laser}} + T_{\text{time}} + T_{\text{cable}}.$$

Charge Dependence of the Timing

The rise time of a pulse depends on the charge. The dependence differs PMT by PMT because each PMT has a different gain. Thus the laser calibrations were conducted several times (see Table 4.1) with various light intensities and tables, $T_{\text{laser}} = T_{\text{laser}}(Q)$, were created for each PMT. We call them *TQ-map*'s. Figure 4.4 shows the example of the TQ-relation of a PMT.

Correction for the Time Variation

The timing information changes as time goes by due to the LS quality change (by the purification campaign), KamFEE board replacements, and HV reductions of PMTs.

As shown in Table 4.1, there was no laser calibration in *SolarPhase*, *Zen400*, and *Zen800* periods. In *SolarPhase*, calibrations with ^{60}Co source at the center of the detector are used for the correction of the time variation of the timing [66]. In *Zen400* and *Zen800*, radioactivities from the supporting structures of the inner balloons are used [81].

Summary of the Timing Correction

The summary of the timing correction for the periods used in the solar neutrino analysis of this thesis is as follows:

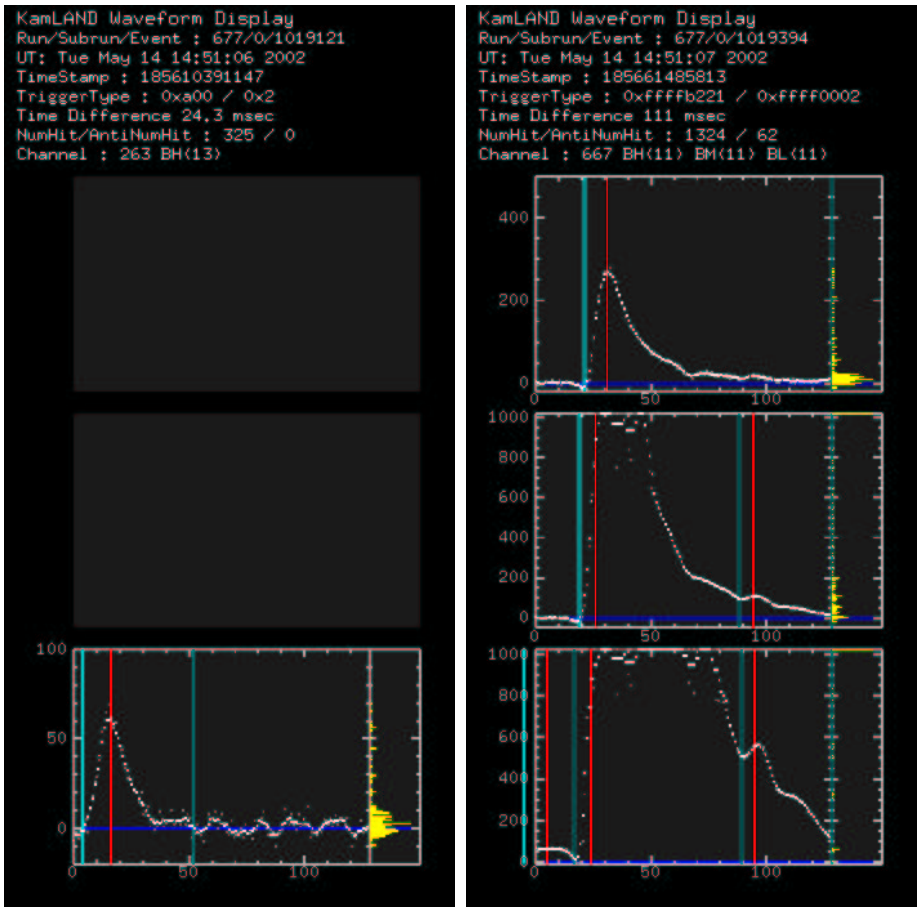

Figure 4.2: Examples of waveforms of KamFEE after pedestal subtraction. (Left) A low energy event with only high gain. (Right) A high energy event with low (top), middle (middle), and high (bottom) gains. The middle and high gains are saturated. Horizontal axises show the timing information (1 unit = 1.5 ns). Vertical axises show the charge information (1 unit = 0.00405 pC). Figure from [56].

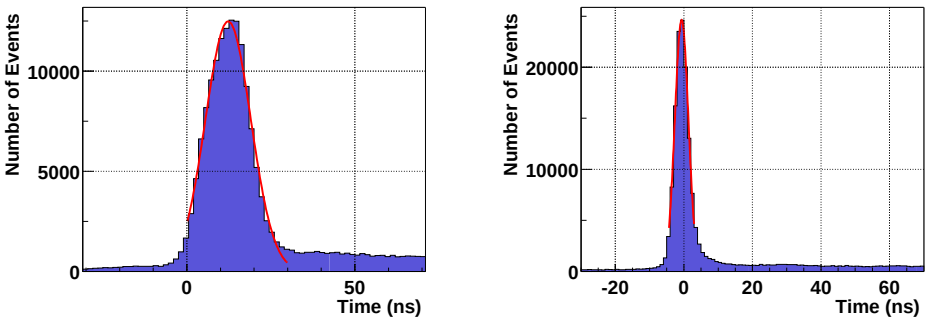

Figure 4.3: Hit timings of 1 p.e. signals of all 17" PMTs. (Left) Before the timing correction. (Right) After the timing correction. Figure from [56].

Table 4.1: History of laser calibrations

Period	Year Month
BeforePurif	2002 Jun., Jul., Nov., Dec.
	2003 Mar., Nov.
	2004 Jan., Mar., May
	2005 Dec.
	2006 Dec.
SolarPhase	-
Zen400	-
AfterZen	2017 Jun.
Zen800	-

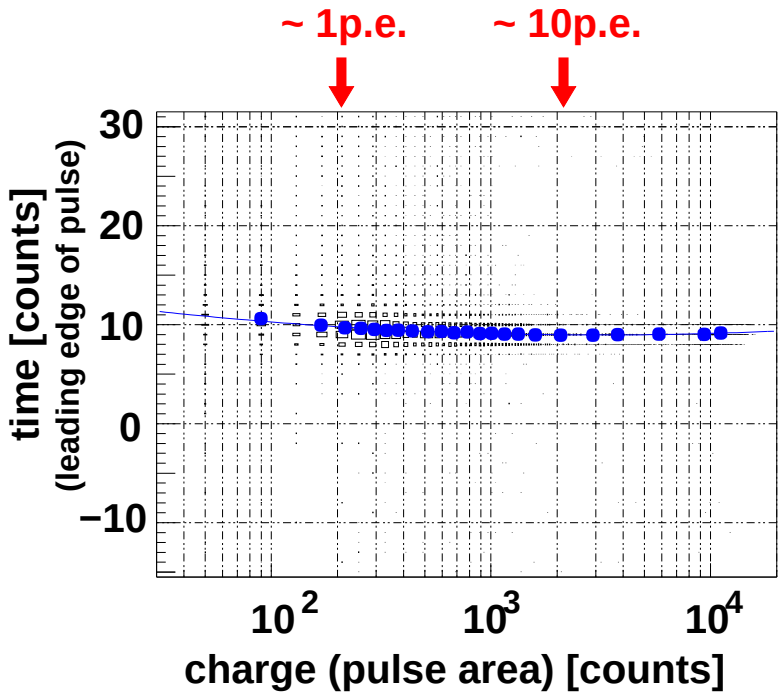

Figure 4.4: TQ-relation of a 17" PMT. The blue line indicates the best-fit result with a function, $p_0 + p_1(\log_{10} Q) + p_2(\log_{10} Q)^2$. Figure from [58].

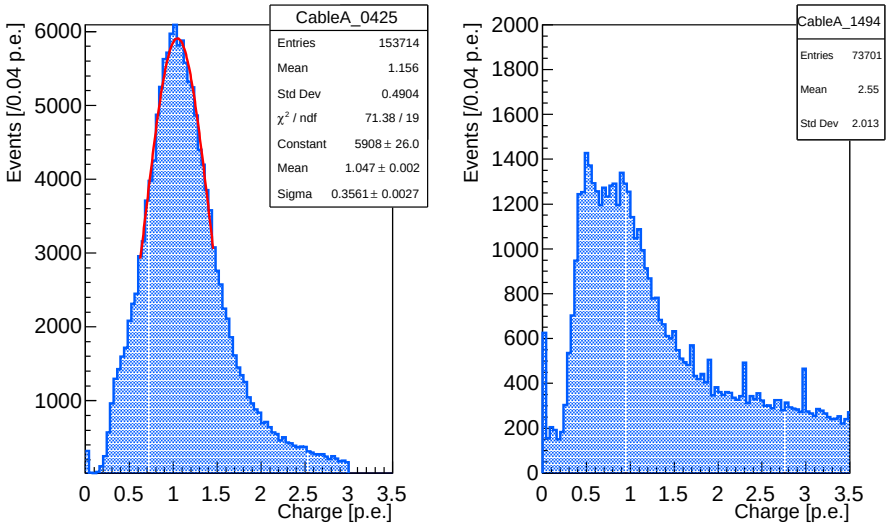

Figure 4.5: 1 p.e. charge distribution. (Left) 17" PMT. (Right) 20" PMT. Figure from [82].

- *BeforePurif*: T_{laser}
- *SolarPhase*: $T_{\text{laser-BeforePurif}} + T_{\text{time-Co}} + T_{\text{cable}}$
- *AfterZen*: T_{laser}.

4.2.2 Gain Correction

We define an area of a 1 p.e. signal waveform as the 1 p.e. charge. The area keeps changing gradually since the start of KamLAND. Therefore it needs run by run correction.

The 1 p.e. charge of a PMT is monitored using low energy events ($N_{\text{PMT-Hits}} \sim 100$–200), and the distances between the PMT and the events are chosen to be farther than 5.6 m. Figure 4.5 Left shows an example of the 1 p.e. distribution. A 20" PMT doesn't have a clear peak in the distribution, see Figure 4.5 Right.

Figure 4.6 Left (Right) shows the time variation of the average 1 p.e. charge of a 17" (20") PMTs.

4.2.3 Bad Channel Selection

Strange behavior PMTs (low responsive etc.) are marked as bad channels and omitted in the final event reconstruction process. Selection criterions for the bad channel are described in [82, Section 3.4].

Figure 4.7 shows the time variation of the number of bad channels. The number of bad 17" PMTs has been increasing since around run010000. The cause is unknown, and it is still being investigated.

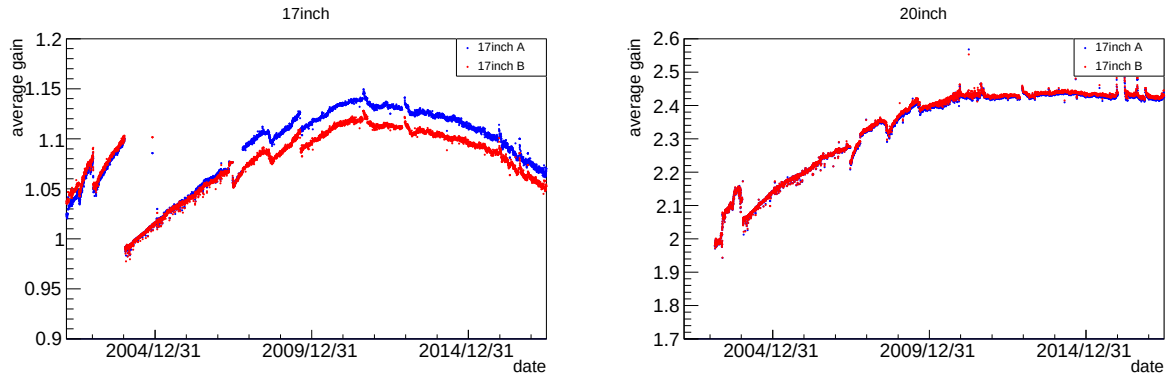

Figure 4.6: Time variation of the average 1 p.e. charge distribution. (Left) 17" PMT. (Right) 20" PMT. Figure from [82].

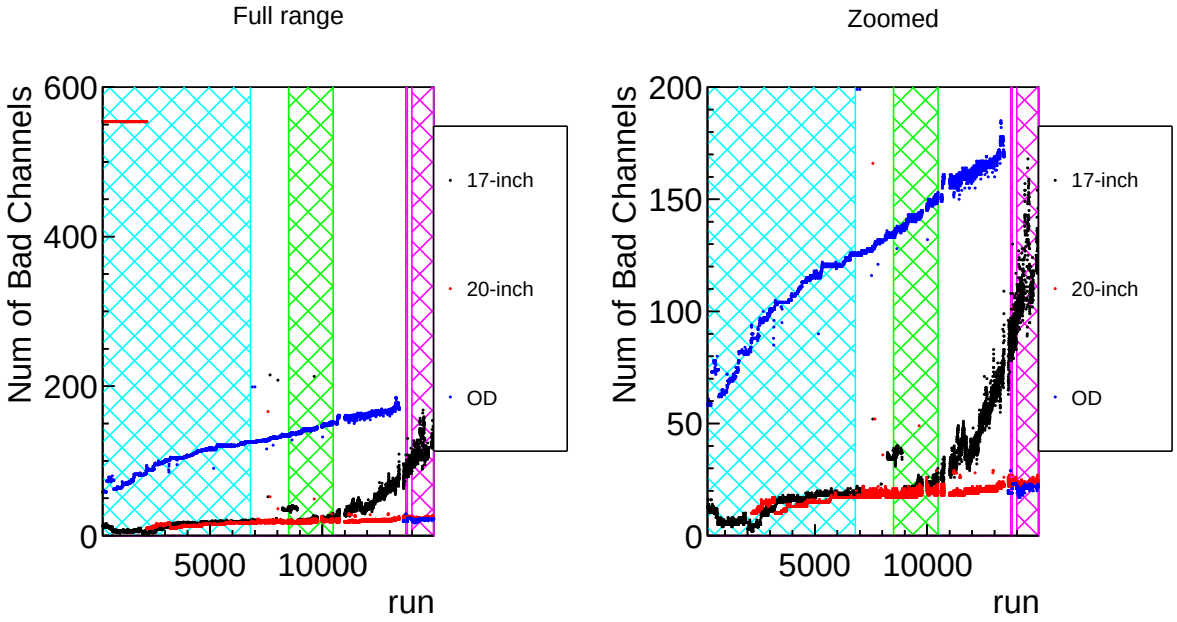

Figure 4.7: Time variation of the number of bad channels. Left: Full range view. Right: Zoomed view. Colored hatched regions correspond to *BeforePurif* (cyan), *SolarPhase* (green), and *AfterZen* (magenta). 20" PMTs have been used in analyses since run002194. There was the OD refurbishment campaign after run013430.

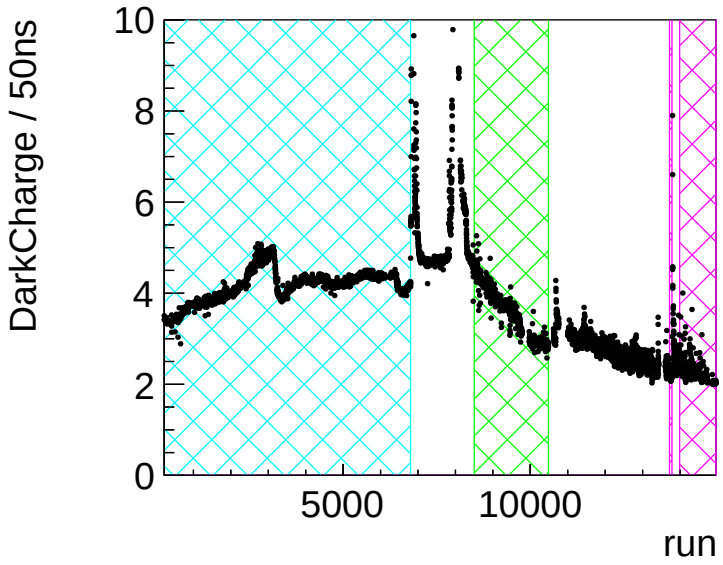

Figure 4.8: Time variation of the dark charge. Colored hatched regions correspond to *BeforePurif* (cyan), *SolarPhase* (green), and *AfterZen* (magenta).

4.2.4 Dark Charge Estimation

The dark charge of the PMTs is affected by the electronics conditions and the temperature of the LS. It is estimated from the charge in the off-time window, which is defined as $[-100\ \text{ns}, -50\ \text{ns}]$ from the rise time of the time-of-flight subtracted hit timing distribution. Figure 4.8 shows the history of the dark charge summed over all PMTs.

4.3 Reconstruction of Point Like Events

A pair of vertex and energy is reconstructed for a point like event.

4.3.1 Vertex

The vertex fitter of KamLAND [83, Appendix A] uses a time-based maximum likelihood method. Charge information isn't used. Given an event, when PMT hit-timings are correctly ordered considering time-of-flight (TOF) from an event vertex (x, y, z), the timing of a hit-PMT can be expressed as

$$\tau_i = t_i - t - \text{TOF}_i(x, y, z),$$

where t_i is the original hit-timing and t the timing of the event occurrence. Typical *pulse-shape* of an event, $\varphi(\tau_i)$, is derived from source calibrations.

The likelihood is defined as follows:

$$L = \prod_{i=\text{hit}} \varphi\left(\tau_i(x, y, z, t)\right). \tag{4.44}$$

Its maximum can be achieved when the following conditions are satisfied:

$$\left.\frac{\partial \log(L)}{\partial x_\alpha}\right|_{x_\alpha=x,y,z,t} = 0. \tag{4.45}$$

In more explicit forms, they are

$$\left.\sum_{i=\text{hit}} \frac{1}{\varphi(\tau_i)} \frac{d\varphi(\tau_i)}{d\tau_i} \frac{\partial \tau_i}{\partial x_\alpha}\right|_{x_\alpha=x,y,z,t} = 0. \tag{4.46}$$

4.3.2 Vertex Reconstruction Quality

Vertex Resolution

Vertex resolutions of *BeforePurif* and *SolarPhase* were estimated using source calibrations as follows [66]:

- *BeforePurif*: 11.7 ± 2.2 cm $/\sqrt{E[\text{MeV}]}$
- *SolarPhase*: 13.8 ± 2.3 cm $/\sqrt{E[\text{MeV}]}$

There is no direct estimation for *AferZen*, however one for *Zen800* was estimated as 13.7 cm$/\sqrt{E[\text{MeV}]}$ [7].

Miss Reconstruction Probability

Vertex miss reconstruction probability was estimated from the fraction of ^{60}Co source calibration events reconstructed farther than 3 m from the source position [66]. It was within $\pm 0.2\%$ range in *BeforePurif* and *SolarPhase*. I assume the situation doesn't change much in *AfterZen*.

4.3.3 Vertex Bias and Fiducial Volume Uncertainty

Vertex bias was estimated from results of off-axis ($20^\circ < \theta < 180^\circ$) calibrations which were performed in 2006 (*BeforePurif*) [84, Sec. 3.9.2] and 2011 (*SolarPhase*) [85]. Figure 4.9 shows the result for *BeforePurif* and Figure 4.10 shows the result for *SolarPhase*. The estimated biases are as follows:

- *BeforePurif*: < 3 cm
- *SolarPhase* ($r < 4.9$ m): < 5 cm

AfterZen

There weren't any off-axis calibration campaigns in *AfterZen*. Therefore I estimate the bias by combining one of *SolarPhase* and the difference between *SolarPhase* and *AfterZen*. Fiducial volume difference with an $r < 6$ m selection between *SolarPhase* and after-*SolarPhase* (2011 Aug.–2020 Dec.) was estimated as 2.3% using ^{12}B events [86, Sec. 4.8.2]. This corresponds to a vertex bias of 4.57 cm. Thus the total vertex bias of *AfterZen* is estimated as follows:

- *AfterZen* ($r < 4.9$ m): $< \sqrt{5^2 + 4.57^2} = 6.77$ cm

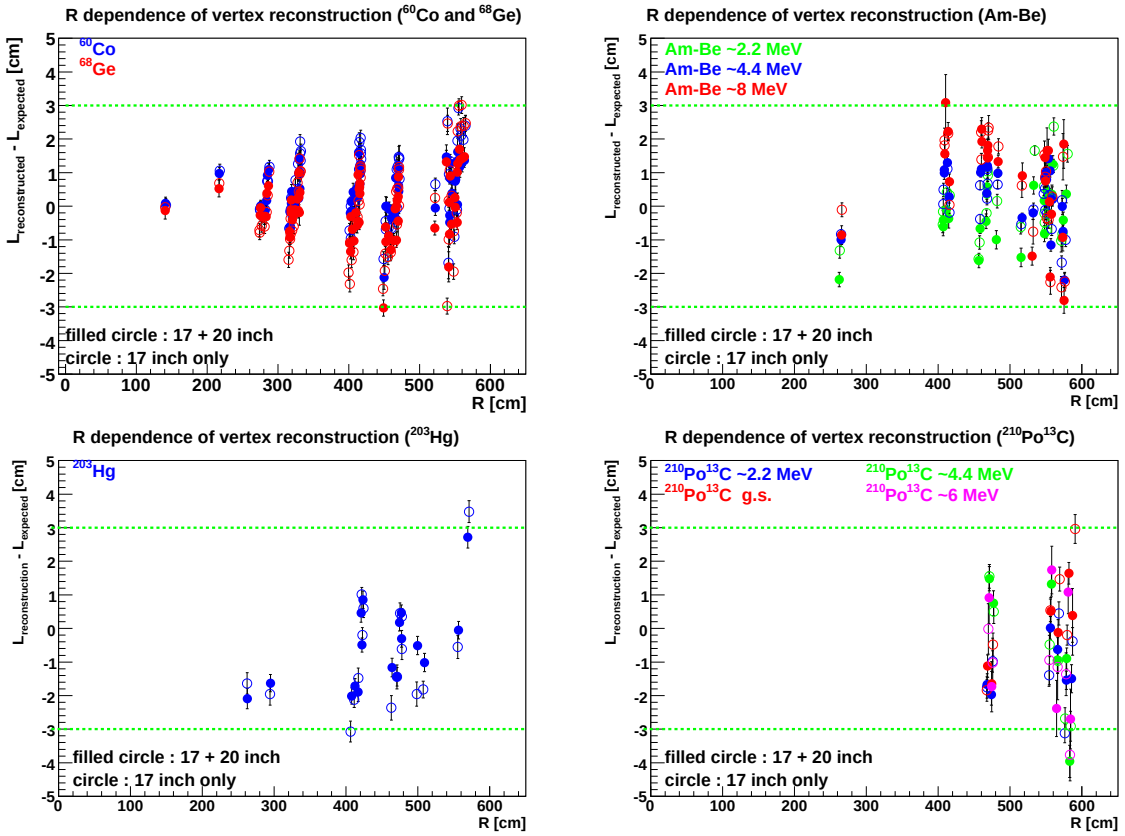

Figure 4.9: Radial position dependence of the vertex bias of *BeforePurif*. Figure from [84].

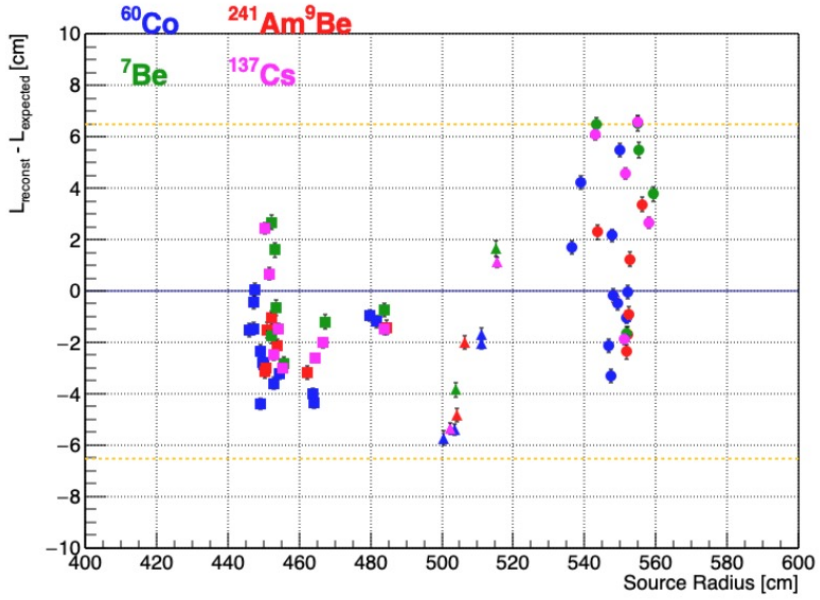

Figure 4.10: Radial position dependence of the vertex bias of *SolarPhase*. Figure from [85].

Table 4.2: Summary of fiducial volume uncertainties

	$r < 2.0$ m	$r < 3.0$ m	$r < 3.5$ m
BeforePurif	-	3.0%	-
SolarPhase	7.7%	5.1%	4.3%
AfterZen	10.5%	6.9%	5.9%

Fiducial Volume Uncertainty

Fiducial volume uncertainty is calculated from the vertex bias. In the solar neutrino analysis of this thesis, there are three volume selections ($r < 2.0$, 3.0, 3.5 m). Table 4.2 shows the summary of fiducial volume uncertainties.

4.3.4 Energy

Principle of the Energy Reconstruction

The visible energy in KamLAND, $E_{\rm vis}$, is basically expressed in proportion to the light output of a neutron-capture-on-proton event, a 2.22 MeV gamma-ray.

A charge-based energy fitter (KatEnergyFitter) is operational since the beginning of KamLAND [58, 56]. Later, a hit-time-charge-based energy fitter (A2EnergyFitter) is developed for low energy ($E < 1$ MeV) solar neutrino analysis [87, 88, 64]. A2EnergyFitter has better resolution than KatEnergyFitter in low energy region, however it can only work in $E < 50$ MeV. In the solar neutrino analysis of this thesis, A2EnergyFitter is used.

The likelihood of A2EnergyFitter is defined as follows:

$$L = \prod_{i=\text{no-hit}} \kappa_{i,0}\left(\overrightarrow{R}_{\text{PMT}_i}, \overrightarrow{R}_{\text{event}}, E_{\text{vis}}\right) \prod_{i=\text{hit}} \left[\sum_{j=1}^{\infty} \kappa_{i,j}\left(\overrightarrow{R}_{\text{PMT}_i}, \overrightarrow{R}_{\text{event}}, E_{\text{vis}}\right) f_{i,j}(q_i)\right] \eta_i(t_i|\mu_i), \tag{4.47}$$

where

- $\overrightarrow{R}_{\text{PMT}_i}$: position of i-th PMT
- $\overrightarrow{R}_{\text{src}}$: position of the event
- $\kappa_{i,j}$: probability for i-th PMT to be hit by j photons
- $f_{i,j}(q_i)$: charge probability function for i-th PMT, gvien j actual photon hits
- $\mu_i = \mu\left(\overrightarrow{R}_{\text{PMT}_i}, \overrightarrow{R}_{\text{event}}, E_{\text{vis}}\right)$: expected number of photons hitting i-th PMT
- $\eta_i(t_i|\mu_i)$: hit-time probability density function for i-th PMT, given the expected number of incident photons μ_i, also called *pulse shape*.

μ_i can be more explicitly written as

$$\mu_i = c\Omega_{\text{eff}i}\left(\overrightarrow{R}_{\text{PMT}_i}, \overrightarrow{R}_{\text{event}}\right) E_{\text{vis}} + d_i \tag{4.48}$$

$$\equiv b_i\left(\overrightarrow{R}_{\text{PMT}_i}, \overrightarrow{R}_{\text{event}}\right) E_{\text{vis}} + d_i, \tag{4.49}$$

where

- c: scaling factor
- Ω_{eff}: effective solid angle including Ω_{real}, Q.E. of PMT, attenuation and shadowing effects
- d_i: dark hit.

See Ref. [64, Section 5.6] for detailed calculation of μ_i. $\kappa_{i,j}$ is basically a Poisson distribution, however the detection efficiency of 1 p.e. signal, ϵ, should be considered for the no-hit case:

$$\kappa_{i,j>0} = \frac{e^{-\mu_i}}{j!}{\mu_i}^j \tag{4.50}$$

$$\kappa_{i,0} = [1 + (1-\epsilon)\mu_i]e^{-\mu_i} \equiv \nu_i e^{-\mu_i} \tag{4.51}$$

$$\sum_{j=1}^{\infty} \kappa_{i,j} = 1 - \kappa_{i,0} = 1 - \nu_i e^{-\mu_i}. \tag{4.52}$$

ϵ is determined from 1 p.e. distribution as 0.964. $f_{i,j}$ is modeled by a Gaussian distribution:

$$f_{i,j} = \frac{1}{\sqrt{2\pi j\sigma^2}} \exp\left(-\frac{(q_i - j)^2}{2j\sigma^2}\right). \tag{4.53}$$

Thus, (4.47) becomes as follows:

$$L = \prod_{i=\text{no-hit}} \nu_i e^{-\mu_i} \prod_{i=\text{hit}} \left[(1-\nu_i e^{-\mu_i}) \sum_{j=1}^{\infty} \frac{1}{1-\nu_i e^{-\mu_i}} \frac{e^{-\mu_i}}{j!}{\mu_i}^j \frac{1}{\sqrt{2\pi j\sigma^2}} \exp\left(-\frac{(q_i - j)^2}{2j\sigma^2}\right)\right] \eta(t_i|\mu_i). \tag{4.54}$$

See Ref. [64, Section 5.6] for how to get a solution which maximizes this likelihood.

Combination of 20-inch PMTs

A 20" PMT doesn't have clear 1 p.e. peak and the charge dependence is different from that of a 17" PMT. Thus the energy reconstructed from 20" PMTs is tuned with the 17" PMT energy. The (17" PMTs + 20" PMTs) combined energy is defined as follows:

$$E_{\text{vis}} = (1-\alpha)E_{17"} + \alpha E_{20"}, \tag{4.55}$$

where $\alpha = 0.3$ is the combination factor, which was determined to achieve the best energy resolution [89].

4.3.5 Energy Correction

Time and position dependence of the deviation of reconstructed energy is corrected using some known events [90, Section 4.7.4].

BeforePurif

Only time variation is corrected with ^{40}K events ($\sim$ 1.3 MeV peak in KamLAND single events spectrum).

SolarPhase

- Z-axis: ^{60}Co source calibration
- Off-axis: neutron capture on proton
- Time: neutron capture on proton run by run

The neutron capture event selections are as follows:

- time difference from muons dT: 200–600 μs
- remove missing-waveform-events: Nhit17 $\geqq$ NsumMax.

AfterZen

I added +1.33% overall correction[1] after applied the same correction as *SolarPhase*. The factor was derived from the comparison of neutron capture (2.22 MeV) events from AmBe source calibrations between *SolarPhase* and *AfterZen*. The calibration runs and dates are as follows:

- *SolarPhase*
  - run008734: 2009/07/16
  - run009602: 2010/07/14
  - run010139: 2011/02/24
- *AfterZen*
  - run014799: 2018/01/19.

Study of Neutron Events Selection

The reason why the 1.33% difference is produced despite the application of the time dependence correction is that the neutron event selection is too aggressive.

Figure 4.11 shows the distribution of energy of neutron candidates versus the time difference from muons (dT). The events around 2.2 MeV are properly reconstructed, however there are many events below 2 MeV and $0 < dT < 400$ μs region. They indicates the detector isn't fully recovered from the shocks of incident muons. In such condition, so called *missing-waveform* occurs. The waveform-analyzed PMT hits (Nhit17) becomes lower than the trigger-decision hits (NsumMax). Figure 4.12 shows the distribution of Nhit17/NsumMax versus dT. The *missing-waveform* events occur in $dT < 1200$ μs in

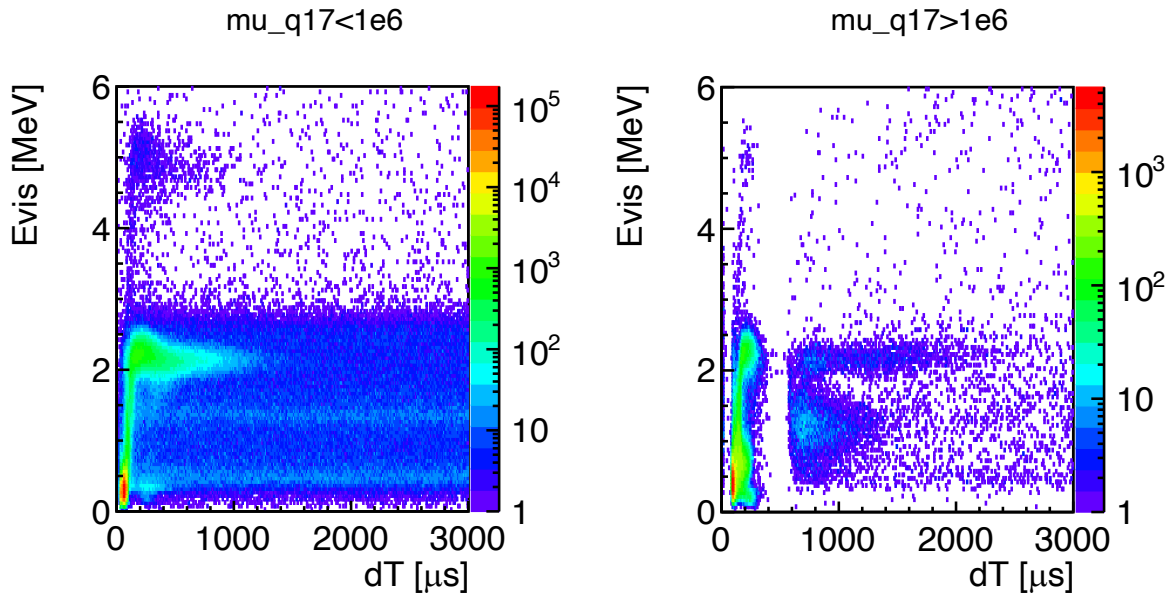

Figure 4.11: Energy vs dT distribution of neutron candidates in *AfterZen*. (Left): Muon charge $< 10^6$ p.e. case. (Right): Muon charge $> 10^6$ p.e. case. $R < 6$ m selection is applied in both cases.

high charge muon case, however they converge faster, $dT < 900$ μs, in low charge muon case.

The neutron selection for the time dependent correction is as follows:

- $R < 6$ m
- Ontime: $200 < dT < 600$ μs (Offtime: $2800 < dT < 4000$ μs)
- Nhit17 >= NsumMax.

Here, I call this *aggressive* selection. I set another *conservative* selection as follows:

- Muon charge $< 10^6$ p.e.
- $R < 6$ m
- Ontime: $900 < dT < 1400$ μs (Offtime: $1500 < dT < 2000$ μs).

The neutron energy peak is evaluated from the ontime minus offtime energy spectrum.

Figure 4.13 (Left) shows the time variation of the energy deviation of the evaluated peak. Note that the time dependence correction isn't applied in it; hence the result (of the *aggressive* selection) itself is to be used for the correction.

[1]This correction is only applied to the analysis of this thesis, which uses vector-file version *v2-v1.04-151106*. Usual collaboration-shared-tool-set doesn't include the correction. The newer versions (*v2-v1.04-220408* or later) have different energy corrections (using ^{8}He/^{9}Li neutrons etc.) to mitigate the time variation.

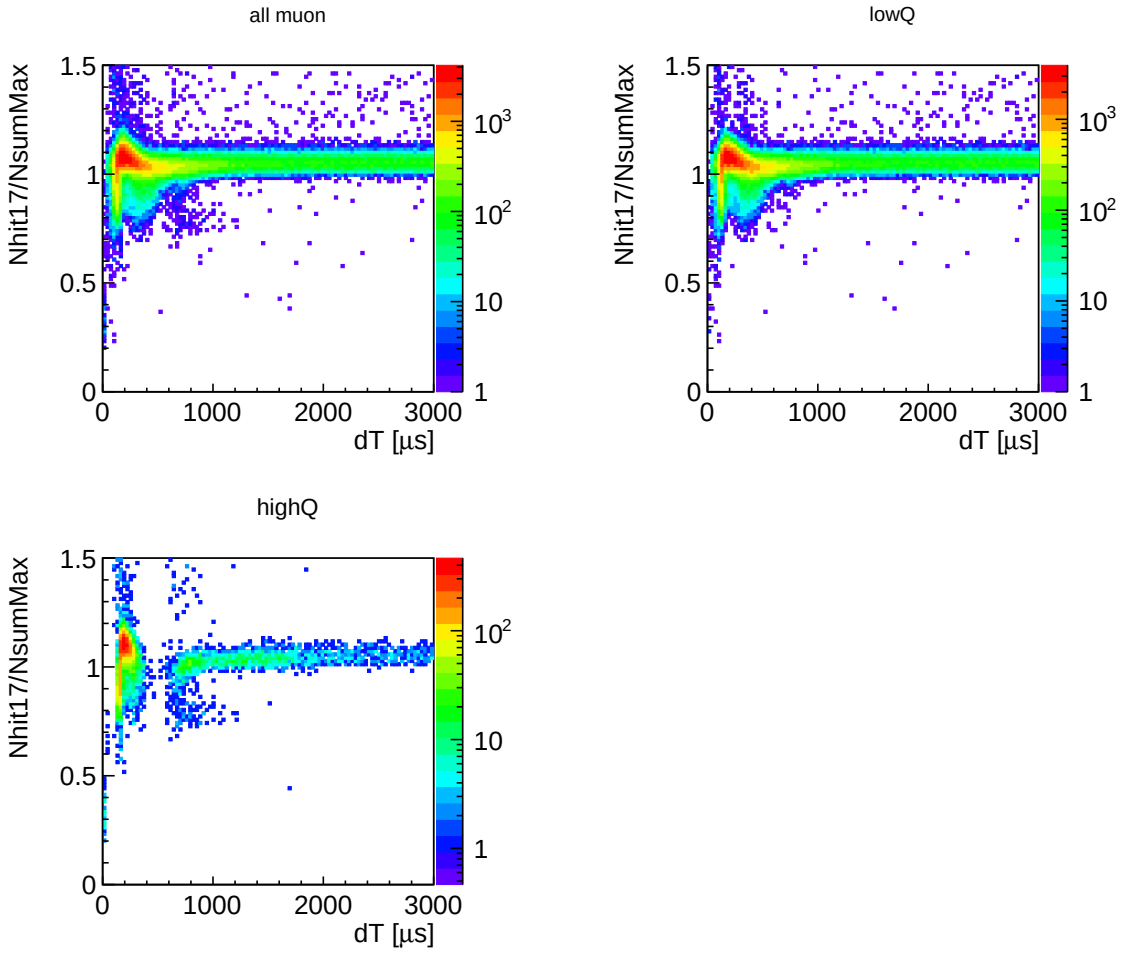

Figure 4.12: Nhit17/NsumMax vs dT distribution of neutron candidates in *AfterZen*. (Left upper): All muons. (Right upper): Muon charge $< 10^6$ p.e. case. (Left bottom): Muon charge $> 10^6$ p.e. case.

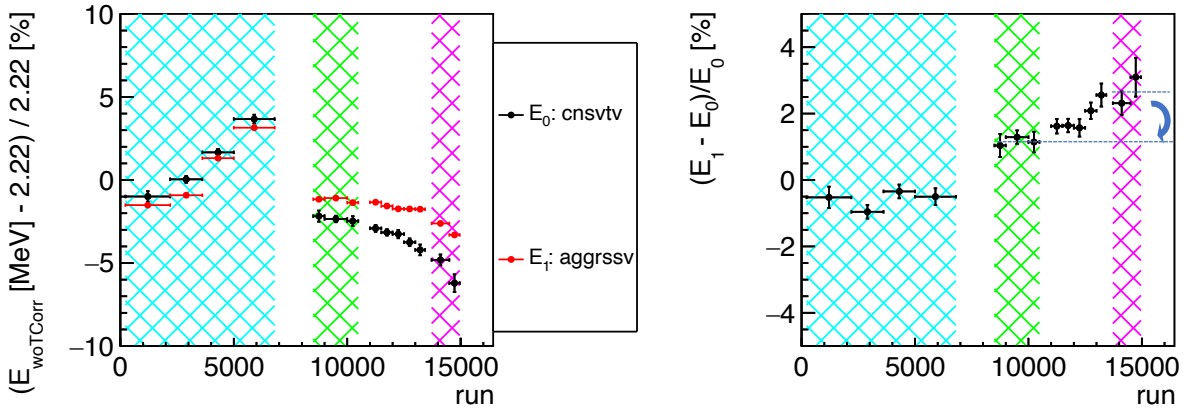

Figure 4.13: Reconstructed energy of neutron events without the time dependence correction. (Left): Deviation from the gamma-ray energy (2.223 MeV). Black points correspond to the conservative selection. Red points correspond to the aggressive selection used in the time dependence correction. (Right): Difference between the conservative selection and the aggressive selection.

The energy of the *aggressive* selection (E_1) well traces the energy of the *conservative* selection (E_0) in *BeforePurif*. It, however, isn't the case for *SolarPhase* and *AfterZen*. In *SolarPhase*, it actually doesn't matter since the visible-real energy conversion table *absorbs* the deviation. The $E_1 - E_0$ deviation is almost stable in *SolarPhase*, however it becomes larger in *AfterZen*. The 1.33% correction in *AfterZen* pushes the deviation back to the same level as *SolarPhase* so that the same energy conversion table can be used, see Figure 4.13 (Right).

Figure 4.14 (Left) shows the time variation of the energy deviation from the expected value of the KamLAND energy model (see Section 4.3.8) of the neutron events after being applied all the corrections.

4.3.6 Energy Resolution

Evaluation with the Conservatively Selected Neutron Events

The energy resolution of each period is evaluated using the *conservative*-ly selected neutrons as follows:

- *BeforePurif*: $(6.34 \pm 0.14_{\text{stat.}})\%/\sqrt{E_{\text{vis}}\ [\text{MeV}]}$
- *SolarPhase*: $(6.77 \pm 0.21_{\text{stat.}})\%/\sqrt{E_{\text{vis}}\ [\text{MeV}]}$
- *AfterZen*: $(7.44 \pm 0.30_{\text{stat.}})\%/\sqrt{E_{\text{vis}}\ [\text{MeV}]}$

Time and spatial variations are both ±0.5% (see Figure 4.14 [Right], 4.15).

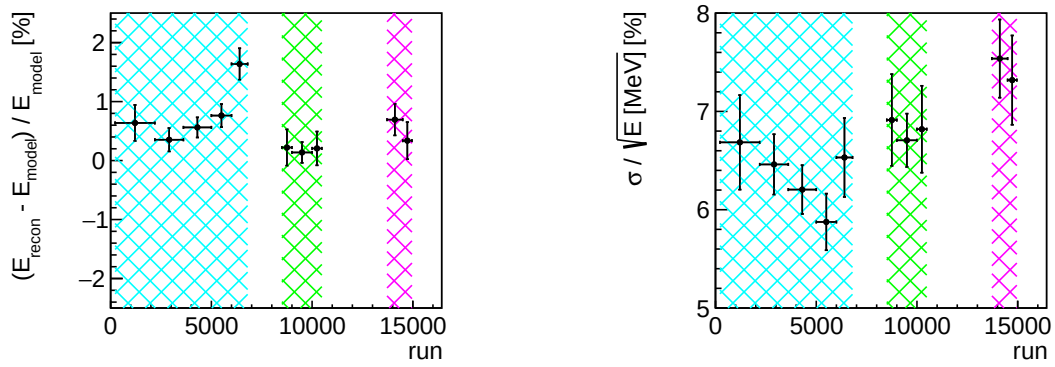

Figure 4.14: Time variation of the energy reconstruction quality checked with spallation neutron events after being applied all the corrections. (Left): Deviation from the model. E_{model}'s are 2.209 MeV, 2.165 MeV and 2.165 MeV for *Before-Purif*, *SolarPhase* and *AfterZen*, respectively. (Right): Energy resolution.

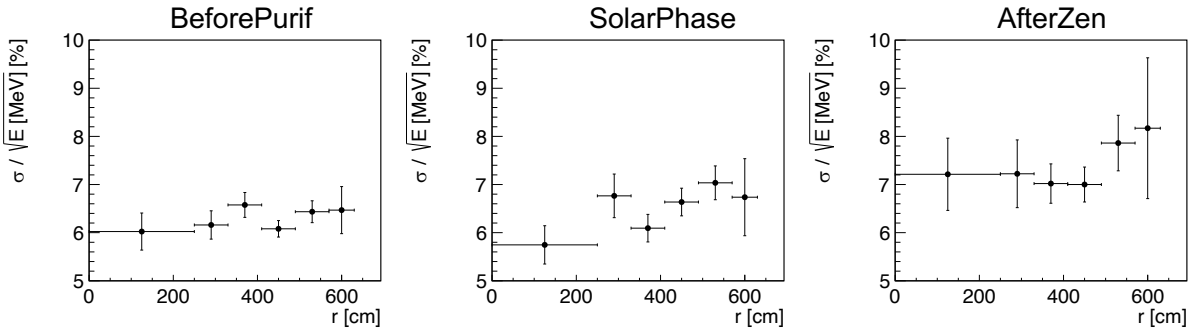

Figure 4.15: Radial position dependence of the energy resolution evaluated with spallation neutron events.

Evaluation with Source Calibrations

Evaluation with calibration sources (^{203}Hg, ^{137}Cs, ^{68}Ge, ^{60}Co) was performed except for *AfterZen* in Ref. [66] as follows:

- *BeforePurif*: $(6.1 \pm 0.1)\%/\sqrt{E_{\text{vis}}\ [\text{MeV}]}$
- *SolarPhase*: $(7.0 \pm 0.1)\%/\sqrt{E_{\text{vis}}\ [\text{MeV}]}$

Spatial variation is $\pm 0.2\%$ in both periods.

I evaluated the resolution of *AfterZen* using neutron events from an Am/Be source calibration at the detector center which was performed on Jan. 19th, 2018 (3 months before the end of the period). The result is as follows:

- *AfterZen*: $(7.97 \pm 0.09_{\text{stat.}})\%/\sqrt{E_{\text{vis}}\ [\text{MeV}]}$

Summary

The following values are used in the solar neutrino analysis of this thesis:

- *BeforePurif*: $6.5\%/\sqrt{E_{\text{vis}}\ [\text{MeV}]}$
- *SolarPhase*: $6.9\%/\sqrt{E_{\text{vis}}\ [\text{MeV}]}$
- *AfterZen*: $6.9\%/\sqrt{E_{\text{vis}}\ [\text{MeV}]}$

Those of *BeforePurif* and *AfterZen* are slightly different from the ones from the evaluations by 0.5–1.0% (absolute). However they are negligibly small as compared to the energy bias/scale uncertainties ($> 3\%$).

4.3.7 Time and Spatial Variation of the Reconstructed Energy

In the solar neutrino analysis of this thesis, candidates with following properties are used:

- Electron-kinetic-energy-scale energy (E_{kin}) $\sim E_{\text{vis}}$: [2, 20] MeV
- Radial position from the detector center (r) < 3.5 m

In this section, the energy reconstruction quality for the events with the above conditions is described.

Evaluation wtih Source Calibrations

Evaluation with source calibrations ($2 < E_{\text{vis}} < 8$ MeV) was performed in Ref. [66, Section 3.4.3] for *BeforePurif* and *SolarPhase*. The results are summarized as follows:

- Time variation $< 1\%$ (see ^{60}Co and Am/Be of Figure 4.16)
- Spatial variation $< 2\%$ (see $|z| < 400$ cm [17"+20"] of Figure 4.17, 4.18)

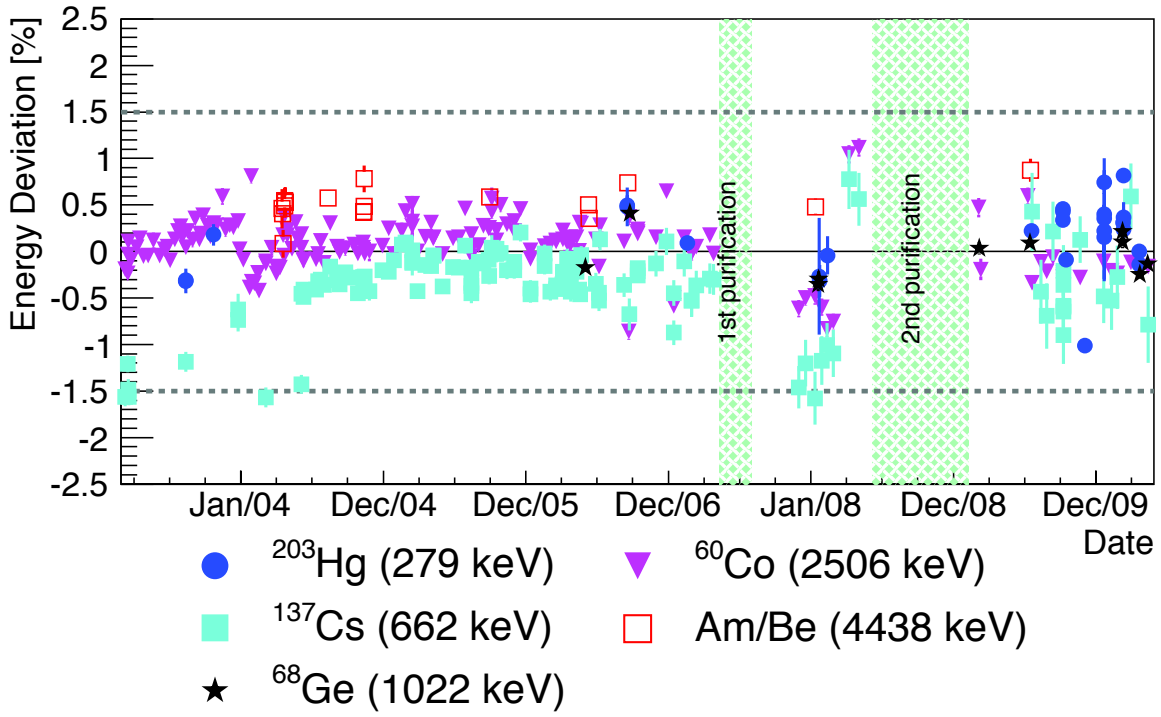

Figure 4.16: Time variation of the energy reconstruction quality of source calibration events. See before the 1st purification for *BeforePurif* and after the 2nd purification for *SolarPhase*. Figure from [66].

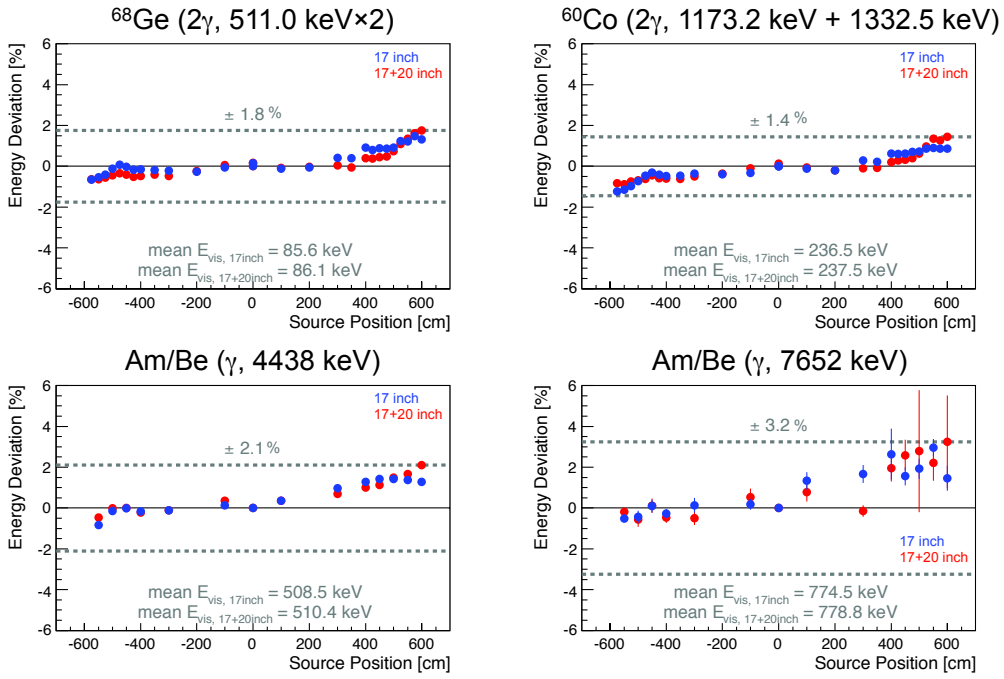

Figure 4.17: z-position variation of the energy reconstruction quality of source calibration events (*BeforePurif*). Figure from [66].

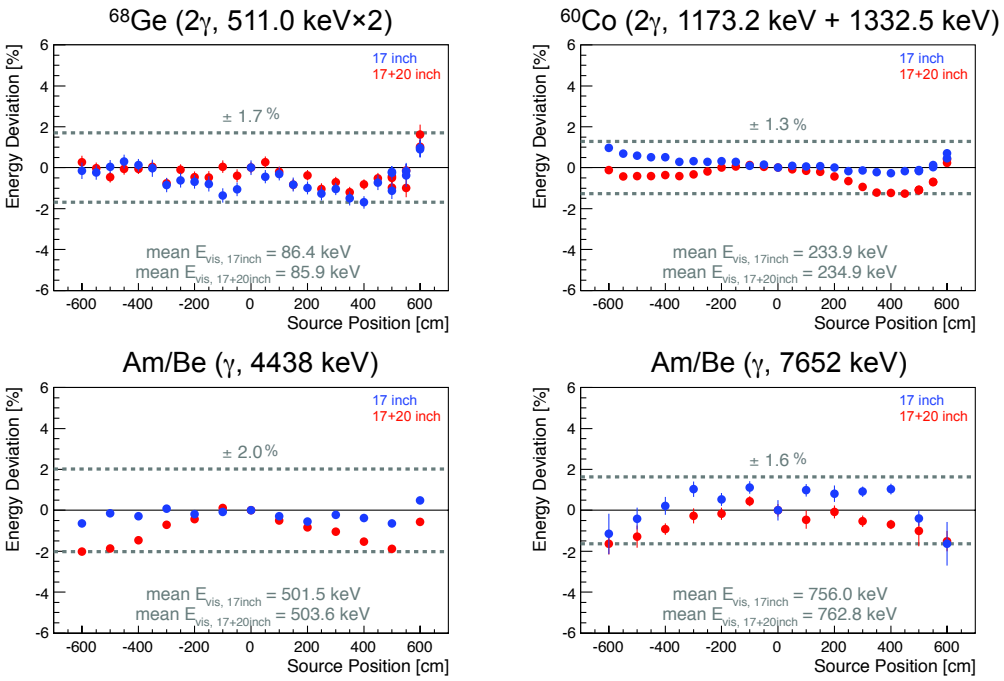

Figure 4.18: z-position variation of the energy reconstruction quality of source calibration events (*SolarPhase*). Figure from [66].

Evaluation wtih the Conservatively Selected Neutron Events

The quality evaluated with neutron events ($E_{\text{gamma}} = 2.2$ MeV) with the *conservative* selection (see Section 4.3.5) is summarized as follows:

- Time variation $< 1\%$ in each period (see Figure 4.14)
- Spatial variation (see Figure 4.19, 4.20)
  - *BeforePurif*: $< 1\%$
  - *SolarPhase*: $< 1\%$
  - *AfterZen*: $< 2\%$

Evaluation wtih Higher Energy Spallation Products

^{12}B ($\tau = 29.1$ ms, $Q_\beta = 13.4$ MeV) can be easily tagged by applying a timing selection after muon events as follows:

- Time difference from a muon (dT): [5, 100] ms (Offtime: [300, 1000] s)

Under this condition, ^{12}B purity is $\sim$90% in an energy region of [6, 12] MeV and ^{12}N ($\tau = 15.9$ ms, $Q_{\beta^+} = 17.3$ MeV) dominates above 15 MeV (see Figure 4.21).

I compared energy spectra of data with expectations from the model (see Section 4.3.8) with an energy selection of [6, 18] MeV. The results are as follows:

- Time variation $< 1.5\%$ in each period (see Figure 4.22)
- Spatial variation $< 2\%$ in each period (see Figure 4.23, 4.24)

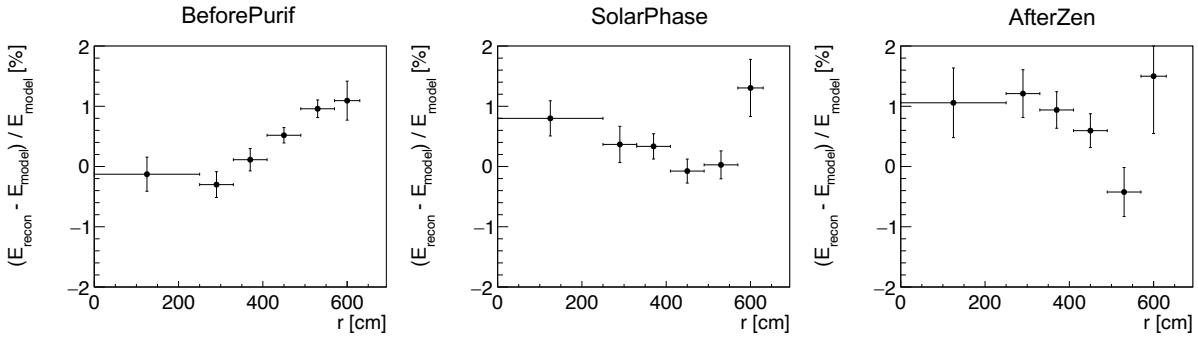

Figure 4.19: Radial-position dependence of the deviation of the energy of neutron events.

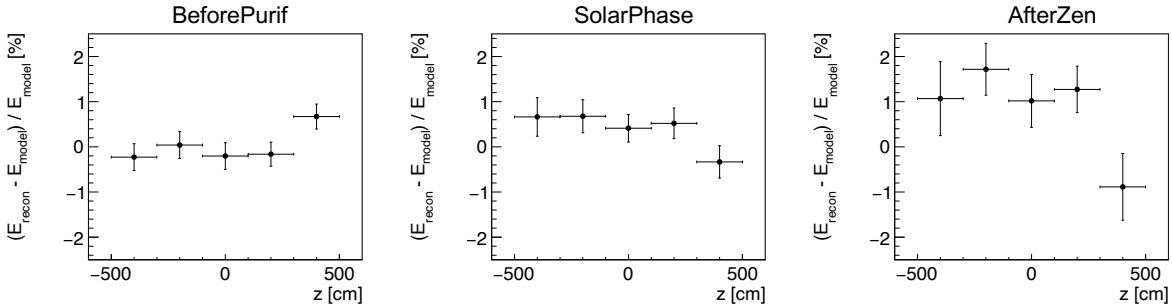

Figure 4.20: z-position dependence of the deviation of the energy of neutron events. A selection of $\sqrt{x^2+y^2} < 3$ m is applied.

Summary

Energy region of the ^{8}B solar neutrinos is close to the one of ^{12}B. Thus prioritizing the results of ^{12}B, I consider 1.5% and 2% as time and spatial uncertainties of the energy, respectively, in each period.

4.3.8 Modeling of the Visible Energy

The visible energy of KamLAND is not completely proportional to the incident energy deposition by particles. The following causes affect the non-linearity:

- Quenching effect in the scintillator

  The efficiency of energy transfer to scintillation light emission depends on the ionization density. The quenching effect gets higher for lower energy and heavier particles. It can be approximated with the Birks' law

  $$\frac{dL}{dX} \propto \frac{dE/dX}{1 + k_B(dE/dX)}, \tag{4.56}$$

  where dL/dX is the light emission per unit length, dE/dX the energy deposition per unit length, and k_B the Birks' constant.

- Contribution of Cherenkov light

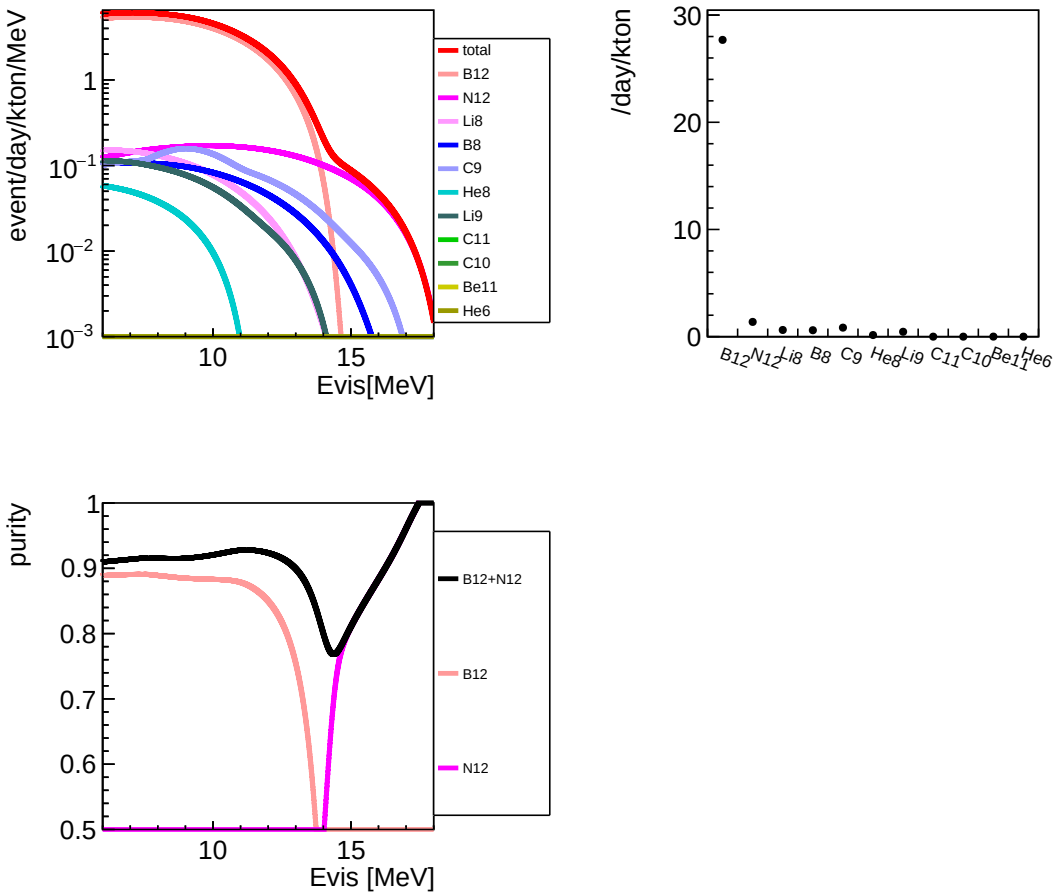

Figure 4.21: (Left top): Energy spectra of spallation products in KamLAND selected with the ^{12}B window ($5 < dT < 100$ ms). (Right top): Event rate of spallation products with the selection of $5 < dT < 100$ ms and $6 < E_{\rm vis} < 18$ MeV. (Left bottom): Energy dependence of ^{12}B and ^{12}N purities. Visible energy of *BeforePurif* is used. Production rates of spallation isotopes are taken from Ref. [55].

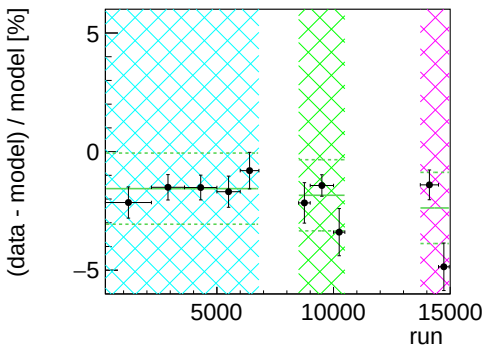

Figure 4.22: Time variation of the energy reconstruction quality of ^{12}B events. A selection of $r < 5.5$ m is applied.

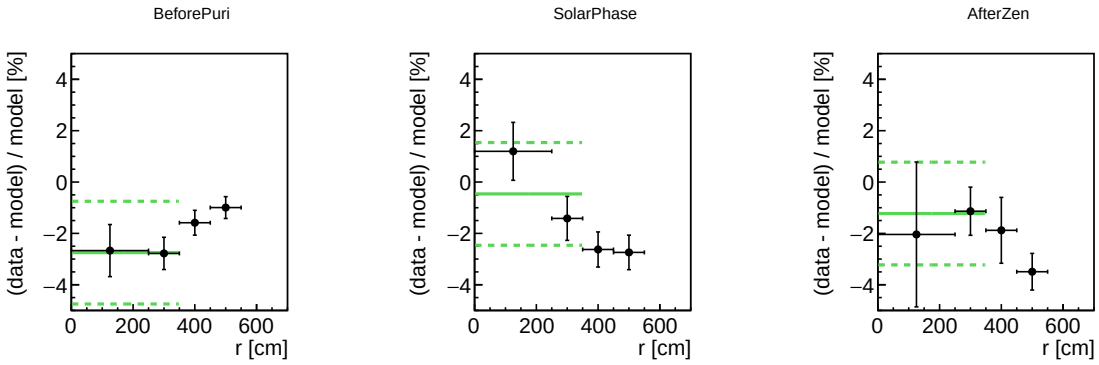

Figure 4.23: Radial-position dependence of the deviation of the energy of ^{12}B events.

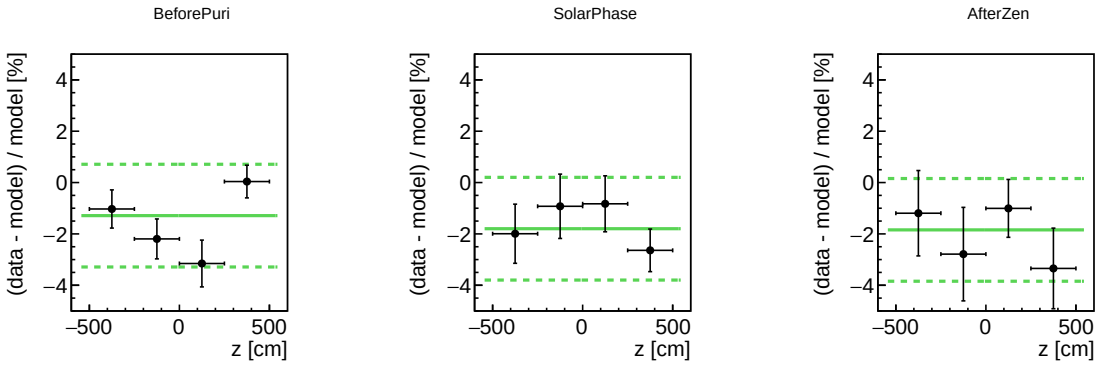

Figure 4.24: z-position dependence of the deviation of the energy of ^{12}B events. The following selections are applied: (i) $\sqrt{x^2 + y^2} < 3$ m (ii) $r < 5.5$ m.

A charged particle has to satisfy the following condition to produce Cherenkov light:

$$\beta > \frac{1}{n}, \tag{4.57}$$

where β is the relative velocity of the particle normalized by the speed of light and n the refractive index of the scintillator. In the KamLAND LS (n=1.46), the condition corresponds to the kinetic energy threshold of ∼0.1 MeV for an electron.

- Contribution of dark charge

Considering them, the following model was constructed [91, 92][90, Sec. 4.7.6]:

$$E_{\rm vis} = C_{\rm sci}E_{\rm sci}(k_B) + C_{\rm che}E_{\rm che} + E_{\rm dark}/n_\gamma, \tag{4.58}$$

where $C_{\rm sci}$ is the scintillation intensity, $C_{\rm che}$ the Cherenkov light intensity, and n_γ the number of γs (2 for ^{60}Co and ^{68}Ge and 1 for other calibration sources). The best-fit parameter sets ($C_{\rm sci}, C_{\rm che}, k_B, E_{\rm dark}$) were derived for *BeforePurif* and *SolarPhase* to explain the following 9 calibration points:

- e^-: ^{12}B
- γ: ^{203}Hg, ^{68}Ge, ^{137}Cs, ^{60}Co, n-capture on p, n-capture on ^{12}C
- e^+: (^{68}Ge), ^{11}C, ^{10}C

Figure 4.25 shows the best-fit visible-real conversion model and calibration points (the 1st iteration for the A2-fitter energy in 2009). Figure 4.26 shows the latest model (small updated from Figure 4.25).

Uncertainty of the Energy Model

I evaluated the uncertainty of the latest model for each phase using events selected with the following conditions:

- Spallation neutron γ (2.22 MeV)
  - $r < 6$ m
  - Ontime: $900 < dT_{\rm fromMuon} < 1400$ μs
  - Offtime: $1500 < dT_{\rm fromMuon} < 2000$ μs
  - Muon charge $< 10^6$ p.e.
- ^{10}C ($\beta^+\gamma$)
  - $r < 4$ m
  - $2.2 < E_{\rm vis} < 4.0$ MeV
  - Ontime: $10 < dT_{\rm fromMuon} < 90$ s
  - Offtime: $300 < dT_{\rm fromMuon} < 1000$ s
  - Delayed coincidence veto (events interval > 3 ms)

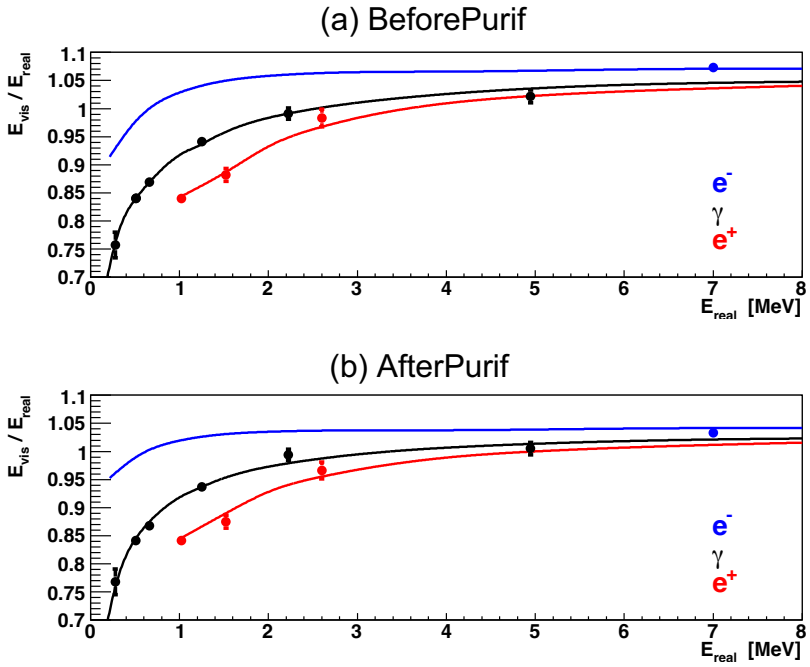

Figure 4.25: Energy-scale model (2009) and calibration points. (a): BeforePurification. (b): AfterPurification. Figure from [90, Section 4.7.6].

  - Distance from the nearest neutron < 1 m
  - $\log_{10}$(SpallationLikelihood) > 6.5 [2]
  - Fit parameters: ^{10}C, ^{11}Be

- ^{12}B (β^-) (lower energy)
  - $r < 5.5$ m
  - $6 < E_{\text{vis}} < 12$ MeV
  - Ontime: $5 < dT_{\text{fromMuon}} < 105$ ms
  - Offtime: $300 < dT_{\text{fromMuon}} < 1000$ s
  - Fit parameters: ^{12}N, ^{12}B, ^{9}C, ^{9}Li, ^{8}Li, ^{8}B

- ^{12}B (β^-) / ^{12}N (β^+)
  - $r < 5.5$ m
  - $12 < E_{\text{vis}} < 20$ MeV
  - Ontime: $5 < dT_{\text{fromMuon}} < 55$ ms
  - Offtime: $300 < dT_{\text{fromMuon}} < 1000$ s
  - Fit parameters: ^{12}N, ^{12}B, ^{9}C, ^{9}Li, ^{8}Li, ^{8}B

- ^{11}Be ($\beta^-\gamma$)

[2] SpallationLikelihood is calculated from distanceToMuonTrack and localMuonChargeAroundSingleEventPosition.

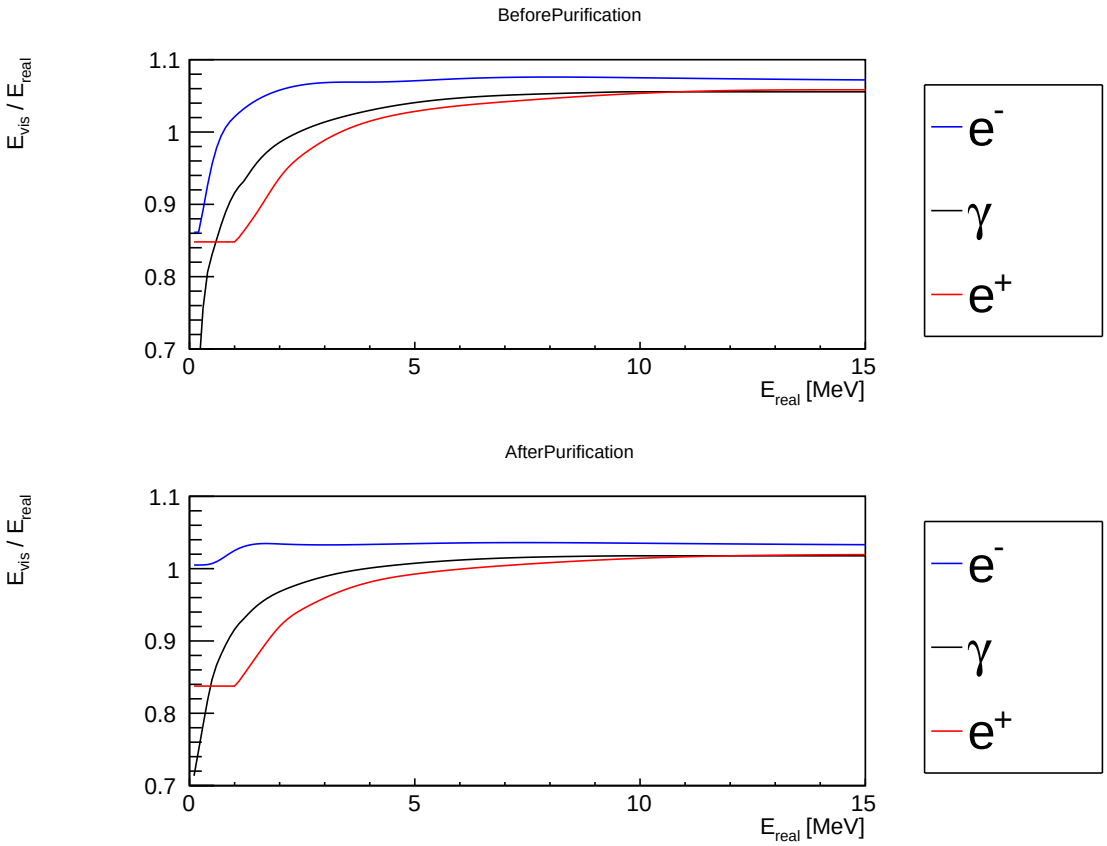

Figure 4.26: Energy-scale model (latest). (Top): BeforePurification. (Bottom): AfterPurification.

- $r < 5.5$ m
- $4 < E_{\mathrm{vis}} < 15$ MeV
- Ontime: $10 < dT_{\mathrm{fromMuon}} < 50$ s
- Offtime: $300 < dT_{\mathrm{fromMuon}} < 1000$ s
- Delayed coincidence veto (events interval > 3 ms)
- Distance from the nearest neutron < 1 m
- $\log_{10}(\mathrm{SpallationLikelihood}) > 6.5$
- Fit parameters: ^{11}Be only

Figure 4.27 shows the results. Since solar neutrino signals of interest in this thesis are mostly recoil electrons, I prioritize the result of ^{12}B ($> 98\%$ pure β^-) and consider 3.5% as the uncertainty of the model in each period.

4.3.9 Summary of the Energy-related Uncertainty

The energy-related uncertainties discussed in the previous sections can be summarized as follows:

- Time variation: 1.5%
- Spatial variation: 2.0%
- Model: 3.5%

In total, 4.3% is the uncertainty.

4.4 Reconstruction of Muon Track Events

4.4.1 Muon Selection

In KamLAND, high energy events or OD-triggering events are considered as muons. The following are the selections:

- $Q_{17} \geqq 10^4$ p.e.
- $Q_{17} \geqq 500$ p.e. and $N_{\mathrm{hit}}^{\mathrm{OD}} \geqq \begin{cases} 5 \text{ (before the OD refurbishment)} \\ 9 \text{ (after the OD refurbishment)} \end{cases}$

The rate of the muons that fall under these conditions is estimated to be 0.32 Hz and stable within ± 0.02 Hz through 2002–2020 [86, Sec. 4.6].

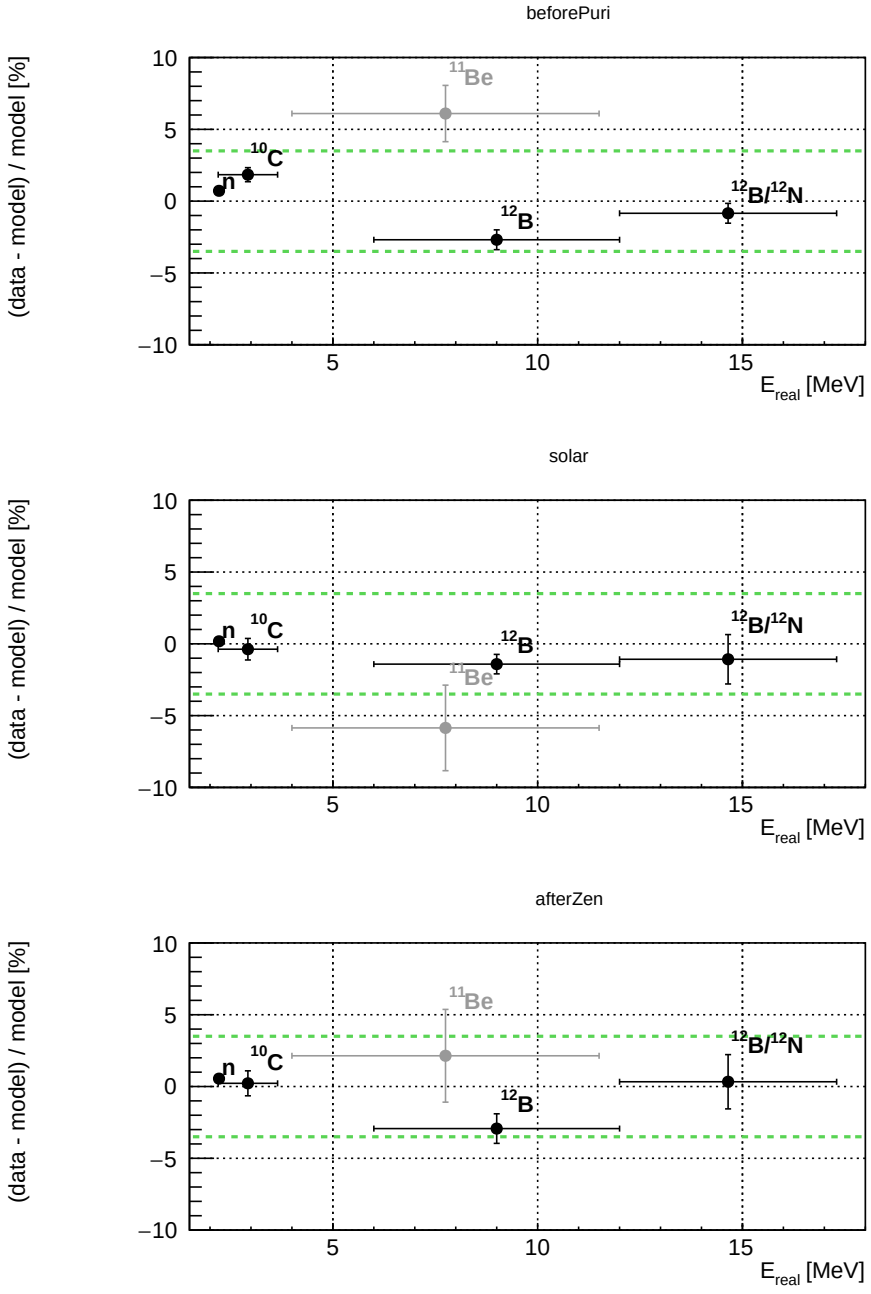

Figure 4.27: Energy-scale uncertainty evaluated with higher energy sources.

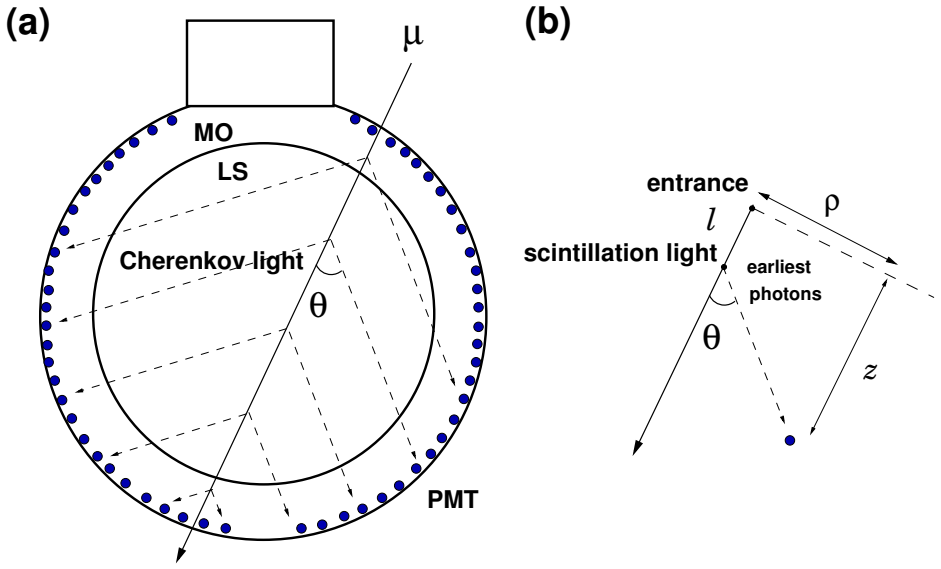

Figure 4.28: (a): Schematic view of a muon passing through KamLAND and Cherenkov lights emitted from the muon track. (b): Angle θ of the earliest photon from a point on the muon track is equal to the Cherenkov angle. Figure from [89, Sec. 3.7].

4.4.2 Algorithm of the Track Reconstruction

Tracks of muons are reconstructed using PMT hit-timings. A muon generates Cherenkov photons to a direction θ, Cherenkov angle, and scintillation photons isotropically, see Figure 4.28 (a). Assuming a muon flies with almost the speed of light, c, the detection timing of a photon from a point on a muon track is expressed as follows [93]

$$t = t_0 + l/c + \frac{z - l}{\cos\theta}\frac{1}{c/n}, \tag{4.59}$$

where t_0 is the time when a muon enters to the detector, n is the refractive index of the liquids, and other parameters are explained in Figure 4.28 (b). The earliest photon from a given on-track point l satisfies $dt/dl = 0$. From the condition, the following formula is obtained:

$$\cos\theta = 1/n. \tag{4.60}$$

That is, the angle of the earliest photon is Cherenkov angle. Based on this principle, a muon track is reconstructed using the earliest hits of PMTs. There are two types of liquids in the detector, therefore n is tuned as an effective value.

4.4.3 Performance of the Track Reconstruction

Figure 4.29 shows the correlation between the charge and the distance from the center of the detector (impact parameter) of muons. The gap around 650 cm corresponds to the radius of LS volume. Muons going through the LS volume of the detector give $\gtrsim 10^{5.8}$ p.e. and ones going through only the buffer-oil volume give $\gtrsim 10^{4.4}$ p.e.

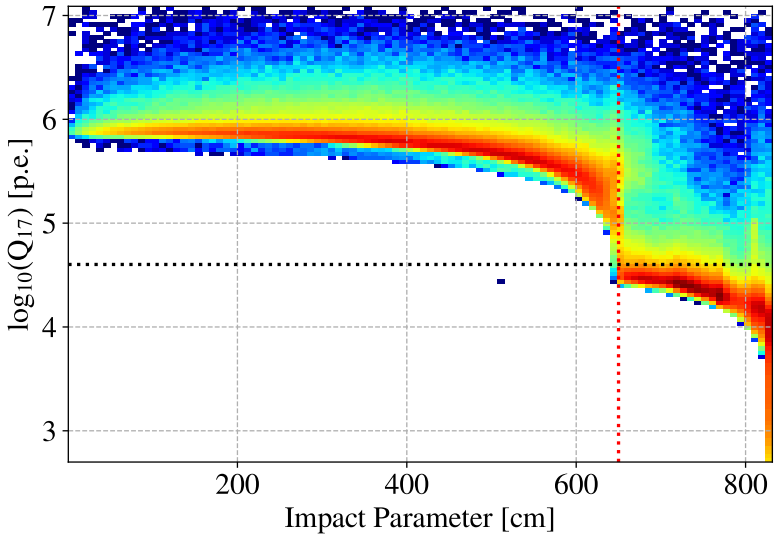

Figure 4.29: Correlation between the charge and impact parameter of muons. Figure from [86, Sec. 4.6].

Cherenkov light emission per muon track length can be calculated using buffer-oil muons as

$$\frac{dQ}{dx}_{\text{che}} = \frac{Q_{17}^{\text{BO-Muon}}}{L_{\text{BO}}}, \tag{4.61}$$

where L_{BO} is the muon track length in the buffer-oil. It was estimated using data from the beginning of KamLAND as [89, Sec. 3.7]

$$\frac{dQ}{dx}^{\text{base}}_{\text{che}} = 31.45 \text{ p.e./cm} . \tag{4.62}$$

The muon charge is calibrated to keep this value stable.

Scintillation light emission per muon track length can be obtained using $(dQ/dx)_{\text{che}}$ as

$$\frac{dQ}{dx}_{\text{sci}} = \frac{Q_{17} - L_{\text{BO}} \frac{dQ}{dx}_{\text{che}}}{L_{\text{LS}} + L_{\text{BO}}}, \tag{4.63}$$

where L_{LS} is the muon track length in the LS region. This value started from ~ 600 p.e./cm at the beginning of KamLAND and decreased to ~ 400 p.e./cm after the purification campaign.

So-called residual charge, whose intensity implies the occurrence of energetic interactions in the detector, is defined as follows:

$$\Delta Q = Q_{17} - L_{\text{ID}} \frac{dQ}{dx}_{\text{che}} - L_{\text{LS}} \frac{dQ}{dx}_{\text{sci}}, \tag{4.64}$$

where L_{ID} is the muon track length in the ID and L_{LS} is the muon track length in the LS region. This value has been widely used in the KamLAND analysis to veto spallation-produced isotopes. In this thesis, however, it isn't used. Instead, *local* residual charge is used to achieve more efficient veto.

5 Muon Spallation Background Reduction

This chapter describes improvements of the muon spallation backgrounds reduction method. The three main improvements are as follows:

- Utilization of FBE neutrons
- Improvement of muon-based rejection method
- Simultaneous application of muon-based and neutron-based removal methods

5.1 Review

Cosmic-ray muons produce radioactive isotopes through spallation interactions. Decays of the isotopes are a background for rare-event search experiments. Spallation products in KamLAND were comprehensively studied in Ref. [55]. This thesis mainly focuses on events with energy above 2 MeV. Table 5.1 shows such isotopes.

5.1.1 Traditional Cuts

The following measures have been taken in the KamLAND analysis to veto spallation backgrounds:

- Muon-based method
  - Full-volume veto after high Residual charge (ΔQ, see Section 4.4.3) muons (*showering* muons)
  - 3-m-radius-cylinder-along-track veto after low ΔQ muons (*non-showering* muons)
- Neutron-based method (*n-tag*)
  - 1.6-m-radius spherical-volume veto around neutrons produced by muons

These have been adopted separately. The muon-based method was used only in the anti-neutrino analysis [50] and previous ^{8}B solar neutrino analysis [48], and *n-tag* was used only in the double-beta decay analysis [6].

The pros and cons of each method are as follows:

- Muon-based method
  - Pros: high tagging efficiency
  - Cons: cannot be used for a long time (more than 5 s) veto because the rate of muons coming to KamLAND is 0.3 Hz

Table 5.1: Spallation products in KamLAND ($E_{\mathrm{vis}} > 2$ MeV) [55]

Isotope	Lifetime	Radiation energy (MeV)	Production rate (/day/kton$_{\mathrm{LS}}$)	n emission
^{12}B	29.1 ms	13.4 (β^-)	54.8 ± 1.5	-
^{12}N	15.9 ms	17.3 (β^+)	2.2 ± 0.5	-
^{8}Li	1.21 s	16.0 ($\beta^-\alpha$)	15.6 ± 3.2	-
^{8}B	1.11 s	18.0 ($\beta^+\alpha$)	10.7 ± 2.9	-
^{9}C	182.5 ms	16.5 (β^+)	3.8 ± 1.5	-
^{8}He	171.1 ms	10.7 ($\beta^-\gamma n$)	1.0 ± 0.5	16% [94]
^{9}Li	257.2 ms	13.6 ($\beta^-\gamma n$)	2.8 ± 0.2	51% [95]
^{10}C	27.8 s	3.65 ($\beta^+\gamma$)	21.1 ± 1.8	-
^{11}Be	19.9 s	11.5 ($\beta^-\gamma$)	1.4 ± 0.3	-
^{6}He	1.16 s	3.51 (β^-)	Not measured	-

- Neutron-based method
  - Pros: less deadtime/volume
  - Cons: neutron detection efficiency is not perfect, some isotopes do not correlate with neutrons.

5.1.2 Recent Study and Room of Improvement

A study to improve the muon-based method was done in Ref. [96] (inspired by Ref. [97]). The basic concept is to reconstruct the muon-generated photons on its track and estimate where large energy deposits have occurred (*shower-tag*). By narrowing down the volume to be vetoed, it is possible to veto for longer periods of time. Figure 5.1 shows an example of the reconstructed local energy deposit ($\propto$charge) (dE/dx) for a muon. The muon-induced neutron positions are also shown. They are close to high dE/dx points in L_{long} axis. The remaining tasks for the implementation of *shower-tag* to a physics search are as follows:

- Optimizing the use of energy deposit information
- Realistic modeling of the correlation between energy deposits and dL (distance from an isotope vertex to a muon track)
- Accurate estimation of tagging efficiency
- Support for all spallation isotopes (Ref. [96] focused only on ^{10}C)

n-tag has so far been applied only during periods when MoGURA (see 3.6.3) is in operation. It has not been implemented so far with FBE neutrons.

5.1.3 Toward Better Rejection Efficiency

Given the above-mentioned situation, the following should be addressed:

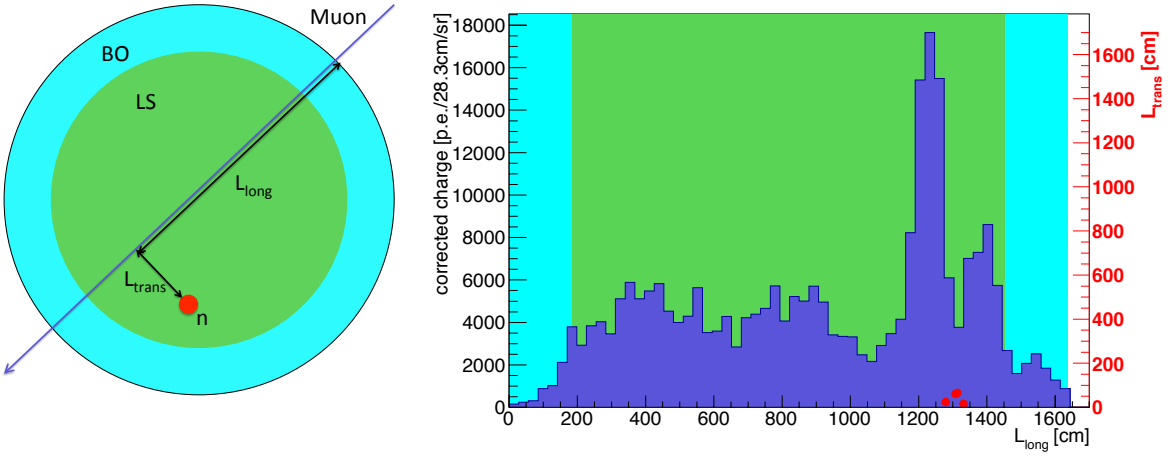

Figure 5.1: Left: Schematic drawing of a muon going through KamLAND. L_{long} is the position on a muon track and $L_{\text{trans}}(= dL)$ is the distance from a muon. Right: Reconstructed local energy deposit of a muon on its track (left vertical axis) and L_{trans} of the muon-induced neutrons (right vertical axis). Figure from [96].

- Complete implementation of *shower-tag*
- *n-tag* with FBE neutrons (for MoGURA unavailable periods)
- *Shower-tag* + *n-tag*

A challenge of the simultaneous application of *shower-tag* and *n-tag* is in the estimation of the tagging efficiency. The cuts are correlated since showering muons produce more neutrons.

5.2 Shower-tag

5.2.1 Karino's Likelihood

In Ref. [96], the author constructed a ^{10}C discriminator, *Karino's likelihood*, using dE/dx of muons

$$\mathcal{L}^{\text{withDt}}_{\text{Karino}}\left(\frac{dE}{dx}, dL, dT\right) = \mathcal{L}^{\text{woDt}}_{\text{Karino}}\left(\frac{dE}{dx}, dL\right)\mathcal{L}_{\text{Karino}}(dT) \tag{5.65}$$

$$= \mathcal{L}_{\text{Karino}}\left(\frac{dE}{dx}\right)\mathcal{L}_{\text{Karino}}(dL)\mathcal{L}_{\text{Karino}}(dT) \tag{5.66}$$

$$= \frac{dE}{dx}\cdot\exp(-dL/100\text{ cm})\cdot\exp(-dT/\tau_{\text{C-10}}). \tag{5.67}$$

Karino's likelihood has the following issues:

- Raw dE/dx is used with linear weighting.

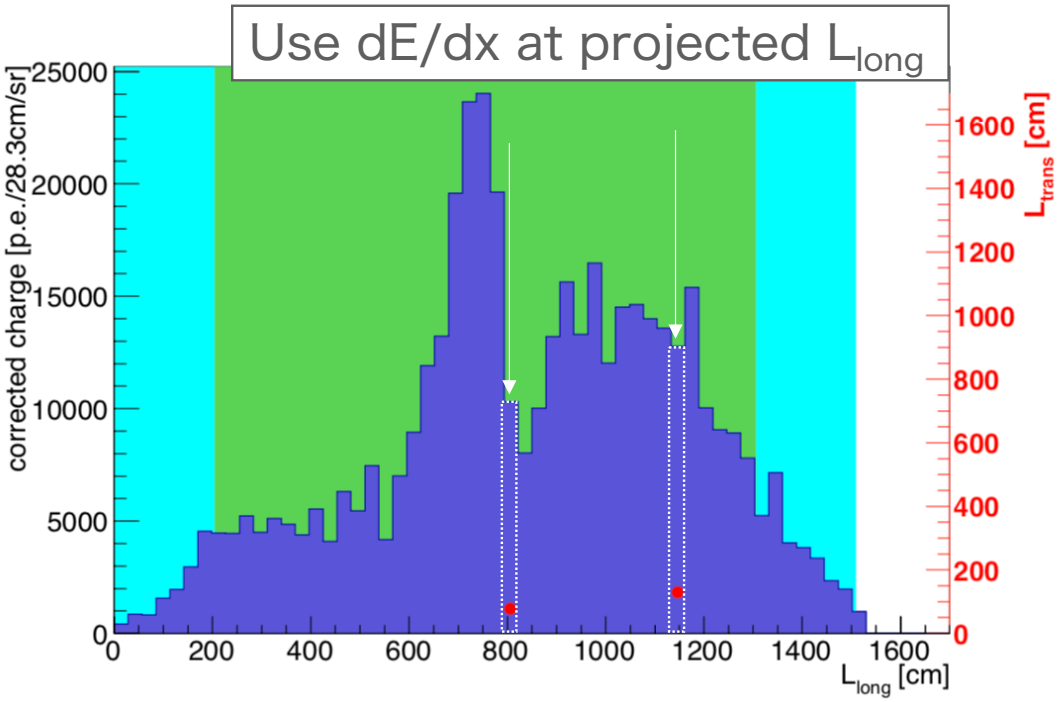

Figure 5.2: Illustration of the use of dE/dx information in *Karino's likelihood*. Red points are positions of ^{12}B candidates. Figure from [96].

- Correlation between dE/dx and dL is not considered.
- dE/dx at the projected point of a spallation isotope event does not match the maximum of dE/dx (see Figure 5.2).
- the width of a shower on a track is wider than the binning used in the tool of Ref. [96] (28.3 cm/sr).

5.2.2 Bias of Shower Position

I evaluated the bias of the shower position, the maximum of dE/dx of a muon, using ^{12}B events of *AfterZen*

$$\Delta L_{\text{long}} = L_{\text{long}}^{\text{B-12}} - L_{\text{long}}^{\text{Max}(dE/dx)}. \tag{5.68}$$

Figure 5.3 and 5.4 show the ΔL_{long} distribution of the cases for *n-tagged* and *n-untagged* ^{12}B, respectively. Here *n-tagged* means $dR_{\text{nearest}}^{\text{neutronToB-12}} < 1.6$ m and the neutrons are MoGURA-reconstructed ones.

The best-fit results of a fit to the peak with a Gaussian are as follows:

- *n-tagged* case
  - Mean: 64.6 ± 7.3 cm
  - Sigma: 91.1 ± 8.7 cm

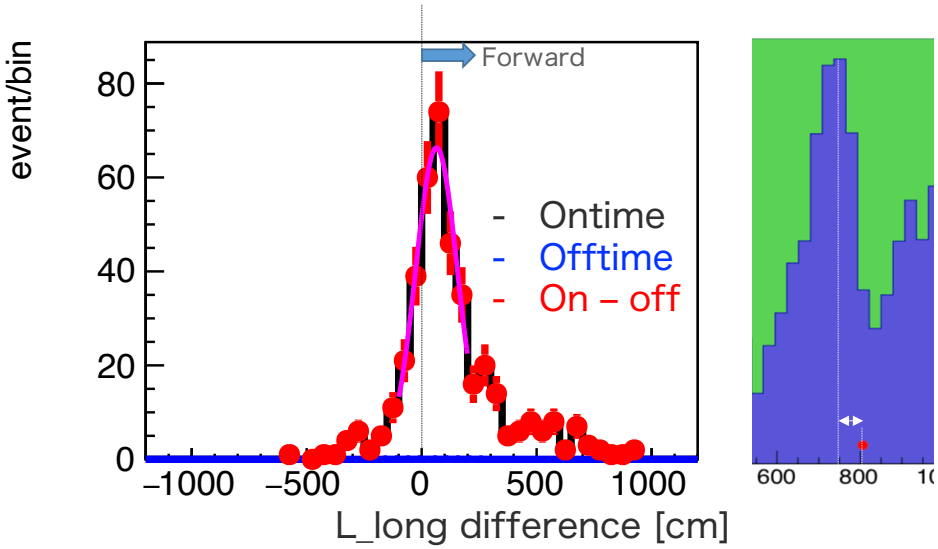

Figure 5.3: Shower position bias (*n-tagged* ^{12}B case). Selection: $4 < E_{\text{vis}}^{\text{B-12}} < 15$ MeV, $0.002 < dT_{\text{ontime}} < 0.2$ s, $180 < dT_{\text{offtime}} < 1000$ s.

- *n-untagged* case
  - Mean: 129 ± 24 cm
  - Sigma: 179 ± 37 cm
  - (Offtime sigma: ~ 290 cm)

5.2.3 Width of Shower

I evaluated the shower width using the left-side-HWHM of L_{long} peaks of showering muons ($\Delta Q > 10^6$ p.e.). Figure 5.5 shows the distribution. ~ 85 cm, which corresponds to three hard-coded bins in the tool (28.3 cm $\times$ 3), is the most frequent value.

5.2.4 New Algorithm for dE/dx Extraction

Based on the study of the bias and width of a shower, I constructed the following algorithm for dE/dx extraction:

1. Bias correction: $\text{bin}_0 = \text{bin}(L_{\text{long}}^{\text{single}} - 64.6 \text{ cm})$
2. Search bin_{max} in a range $[\text{bin}_0 - 6, \text{bin}_0 + 6]$ (± 170 cm)
3. Integral dE/dx in a range $[\text{bin}_{\text{max}} - 3, \text{bin}_{\text{max}} + 3]$ (± 85 cm)

Figure 5.6 shows the schematic view of the algorithm.

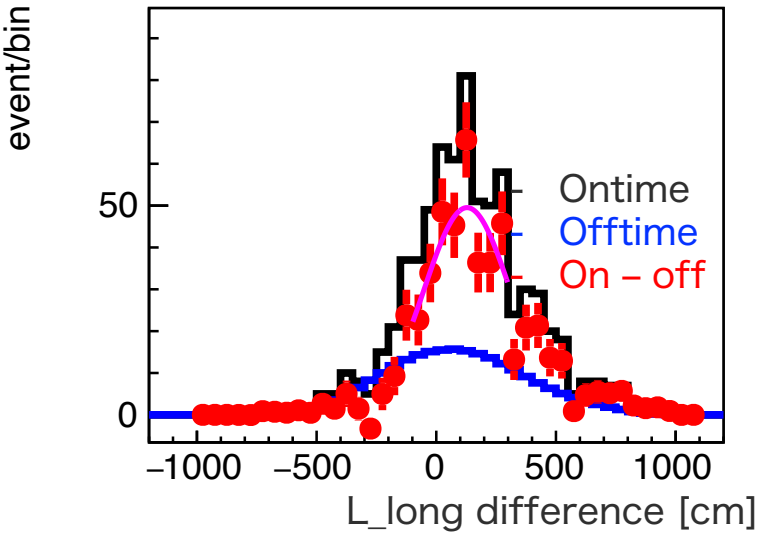

Figure 5.4: Shower position bias (*n-untagged* ^{12}B case)

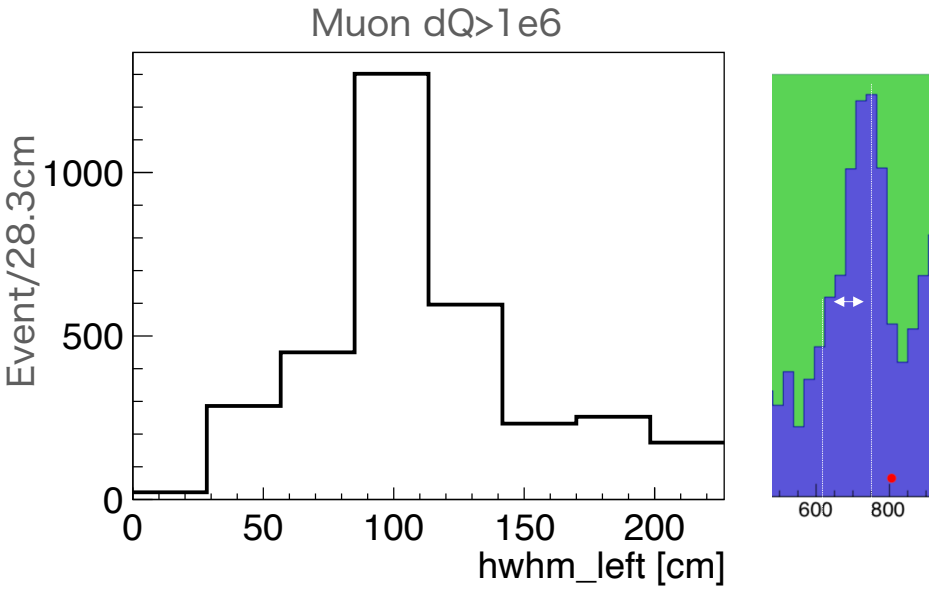

Figure 5.5: HWHM of L_{long} of showering muons.

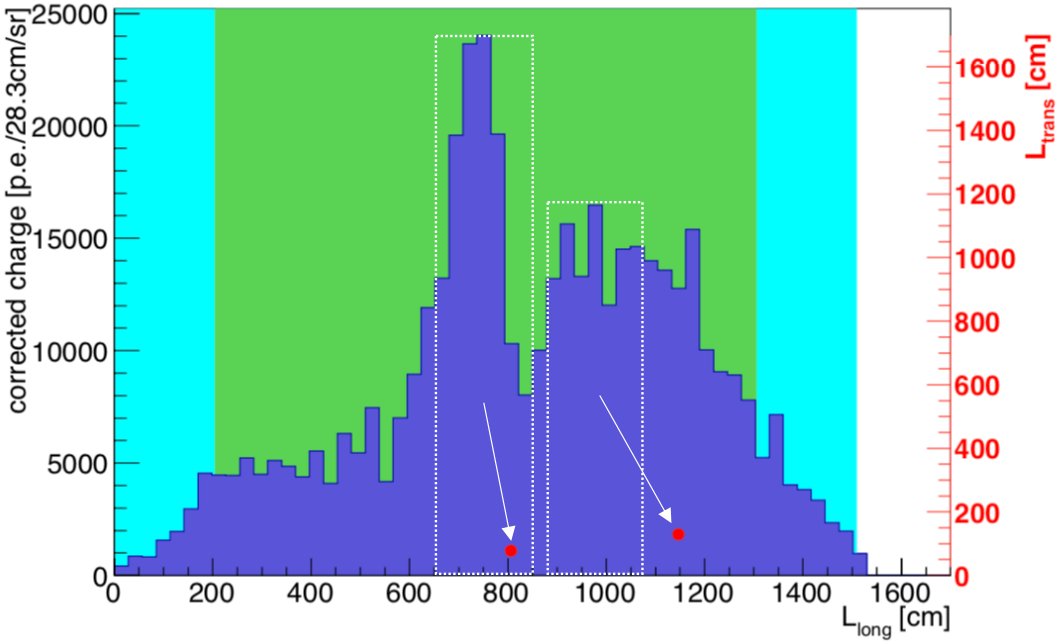

Figure 5.6: New method of the dE/dx extraction. Integral of an area boxed by white dotted lines is assigned.

5.2.5 $(dE/dx, dL)$ 2D PDF

It is expected that in an energetic muon event, spallation products may locate farther from the muon track. To take into account of the correlation between dE/dx and dL, I created their 2D PDF (likelihood) using ^{12}B events of *Zen400 2nd phase* ($r < 400$ cm), see Figure 5.7. In the spallation PDF, dL reaches ~ 300 cm when dE/dx is high ($\sim 10^{5.5}$ p.e.), while it reaches only ~ 100 cm when dE/dx is low ($\sim 10^{4.5}$ p.e.).

5.2.6 dT Likelihood

I construct the dT likelihood to include all spallation isotopes in the LS as

$$\mathcal{L}_{\rm spa}(dT) = \frac{1}{\sum_i A_i} \sum_i \frac{A_i}{\tau_i} \exp(-dT/\tau_i), \tag{5.69}$$

$$\mathcal{L}_{\rm acc}(dT) = \frac{1}{180}, \tag{5.70}$$

$$\mathcal{L}_{\rm ratio}(dT) = \mathcal{L}_{\rm spa}/\mathcal{L}_{\rm acc}, \tag{5.71}$$

where $A_i = R_i \epsilon_i^E \epsilon_i^{dT}$ is the amplitude for an isotope which depends on the energy selection and dT selection. R_i is the production rate estimated in [55]. $R_{\text{He-6}}$ wasn't estimated in [55], therefore I temporarily set 12.8 /day/kton (10×10^{-7} cm$^2/\mu$/g). Due to the *n-tag* efficiency differences among isotopes, the relation of R_i's among isotopes may not be the same. However, for the simplicity, I assume the same R_i's for *n-untagged* case in the dT likelihood construction.

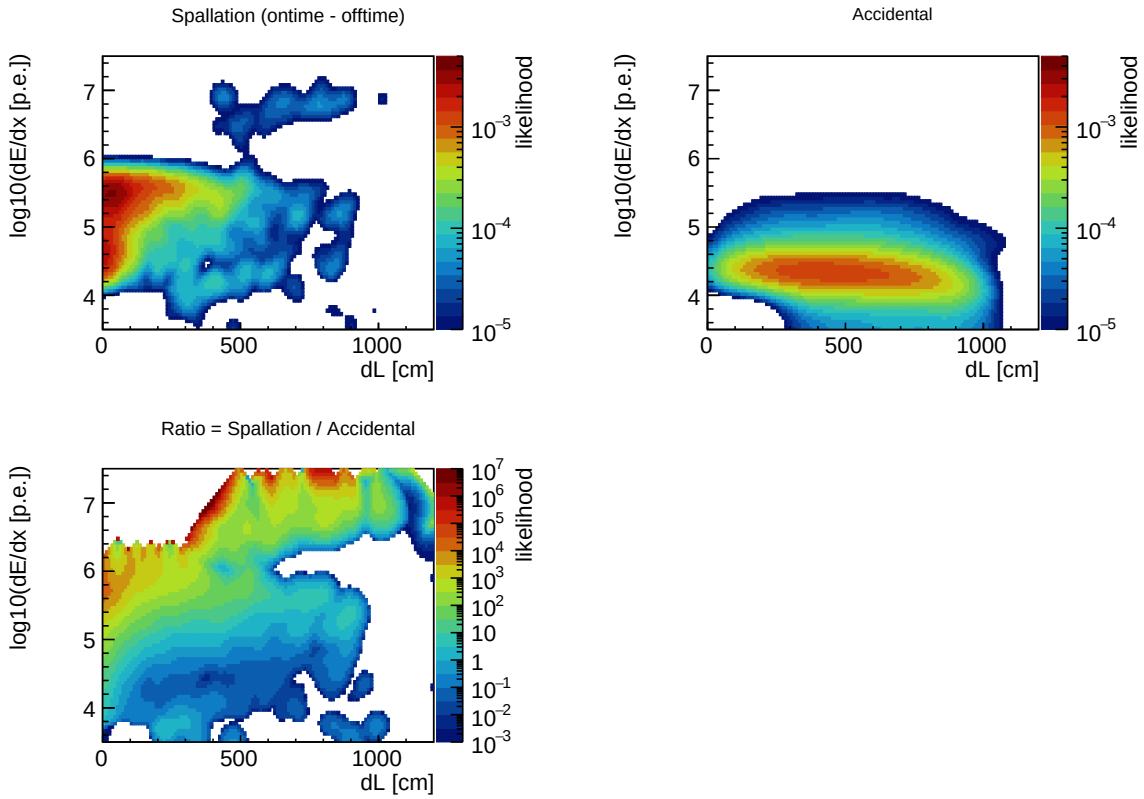

Figure 5.7: $(dE/dx, dL)$ 2D PDF (*n-tag* related selection not applied). (Top left): PDF for spallation isotopes. (Top right): PDF for accidental events. (Bottom left): LikelihoodRatio = SpallationPDF / AccidentalPDF. dE/dx (vertical axis) is derived with the new algorithm. Smoothing is applied several times.

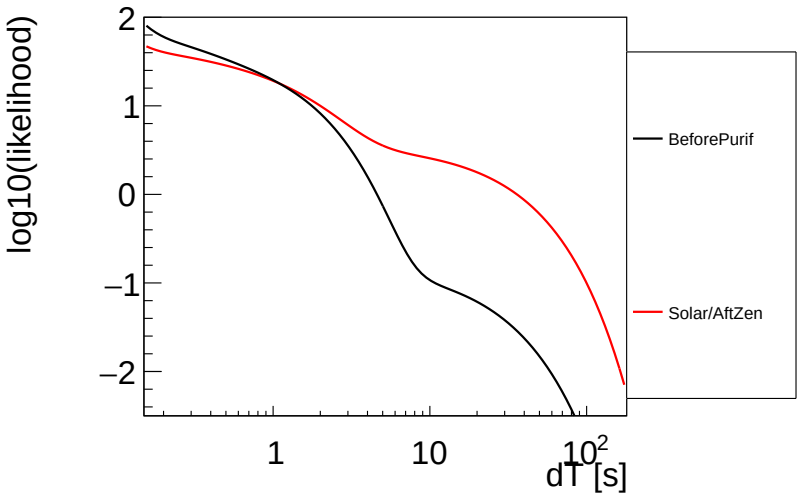

Figure 5.8: dT likelihood

The most produced isotope ($E_{\text{vis}} > 2$ MeV), ^{12}B, can be efficiently cut with a simple dT box cut (150 ms veto for the whole volume of the detector after a muon event). Therefore I optimize $\mathcal{L}(dT)$ for $0.15 < dT < 180$ s. The upper limit is $\sim 5 \times \tau_{\text{C-10}}$.

For the ϵ_i^E calculation, two energy selections were considered as follows:

- $3.5 < E < 20$ MeV (for *BeforePurif*)
  - No ^{10}C and ^{6}He
  - ^{8}Li and ^{8}B dominant ($\tau \sim 1$ s)
  - ^{11}Be has the longest lifetime ($\tau = 20$ s)
- $2 < E < 3.5$ MeV (for *SolarPhase* and *AfterZen*)
  - ^{10}C ($\tau \sim 30$ s) and ^{6}He ($\tau \sim 1$ s) dominant
  - ^{10}C has the longest lifetime

Figure 5.8 shows the dT likelihoods for *BeforePurif* and *SolarPhase*/*AfterZen*.

5.2.7 Demonstration of the Likelihood Cut

I use the following events to demonstrate the performance of the improved *shower-tag*:

- Single events: MC-generated space-time uniform events
- *n-tagged* spallation events of *AfterZen* data (^{10}C and ^{6}He dominant)
  - $2 < E_{\text{vis}} < 3.5$ MeV
  - $r < 3.5$ m
  - $0.15 < dT_{\text{fromMuon}} < 180$ s (ontime), $180 < dT_{\text{fromMuon}} < 1000$ s (offtime)
  - $dR^{\text{nearest}}_{\text{fromNeutron}} < 160$ cm,

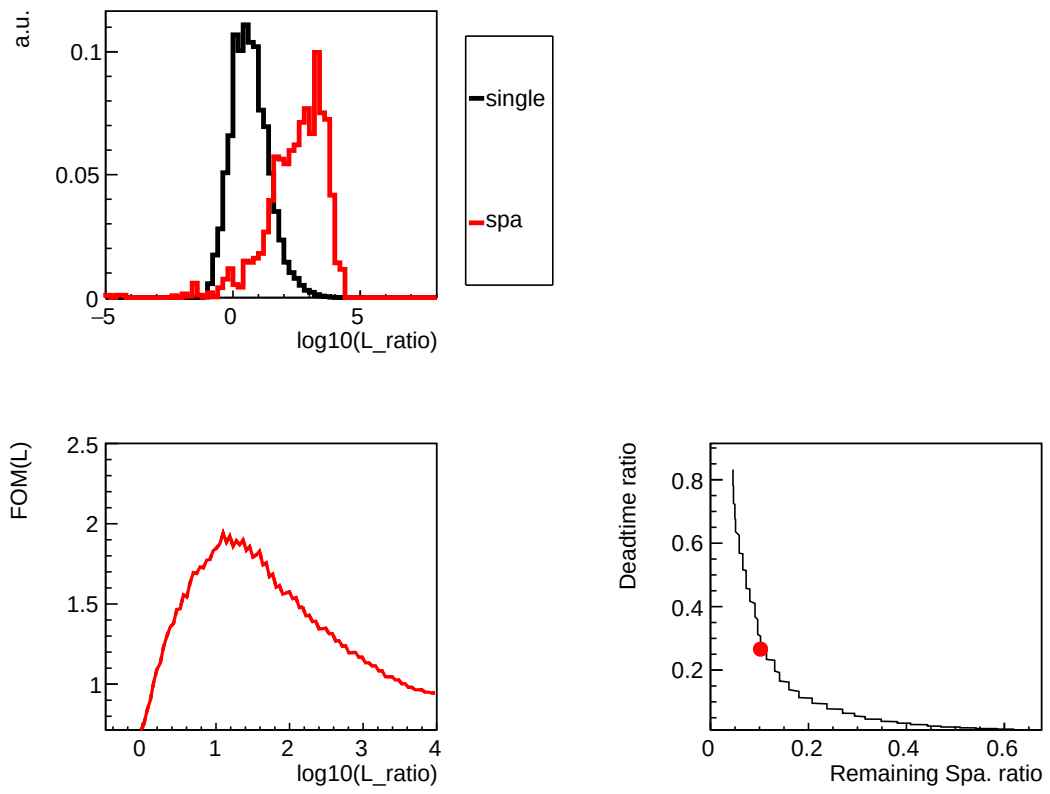

Figure 5.9: Example of the likelihood cut optimization

In the likelihood calculation of a single event, a pair of the event and a muon ($0.15 < dT_{\rm fromSingle} < 180$ s) which gives the highest $\mathcal{L}^{\rm woDt}(dE/dx, dL)$ was selected. In the spallation event case, all pairs of a spallation isotope and a muon were considered and $\mathcal{L}^{\rm woDt}_{\rm spa}(dE/dx, dL)$ was derived by subtracting an offtime distribution from an ontime distribution.

Figure 5.9 (Top left) shows the likelihood distribution of the single events and the spallation events. To determine the optimal likelihood threshold, the following figure of merit was considered

$$\mathrm{FOM}(\mathcal{L}) = \sqrt{A}\frac{N_{\rm signal}\epsilon_{\rm signal}(\mathcal{L})}{\sqrt{N_{\rm signal}\epsilon_{\rm signal}(\mathcal{L}) + N_{\rm bg}\epsilon_{\rm bg}(\mathcal{L})}}, \tag{5.72}$$

where $\epsilon(\mathcal{L})$ is the acquisition efficiency, $N_{\rm signal}$ was set to 0.785 /day/kton, the solar neutrino event rate at $2 < E_{\rm vis} < 3$ MeV, $N_{\rm bg}$ was set to 19.4 /day/kton, a sum of the event rate of spallation isotopes ($2 < E_{\rm vis} < 3$ MeV, $0.15 < dT_{\rm fromMu} < 180$ s), and A, the exposure, was set to 29 kton-day. Figure 5.9 (Bottom left) shows the FOM. Figure 5.9 (Bottom right) shows the relation between the deadtime ratio ($1 - \epsilon_{\rm signal}$) and the remaining spallation BG ratio ($\epsilon_{\rm bg}$) which depends on the likelihood threshold. In this example, $\log_{10}(\mathcal{L}) \sim 1.2$ is the optimal likelihood cut threshold.

In the same way with the above example, the relations between the deadtime ratio and the remaining spallation ratio were checked for the following cuts:

- (dQ, dL) likelihood without dT

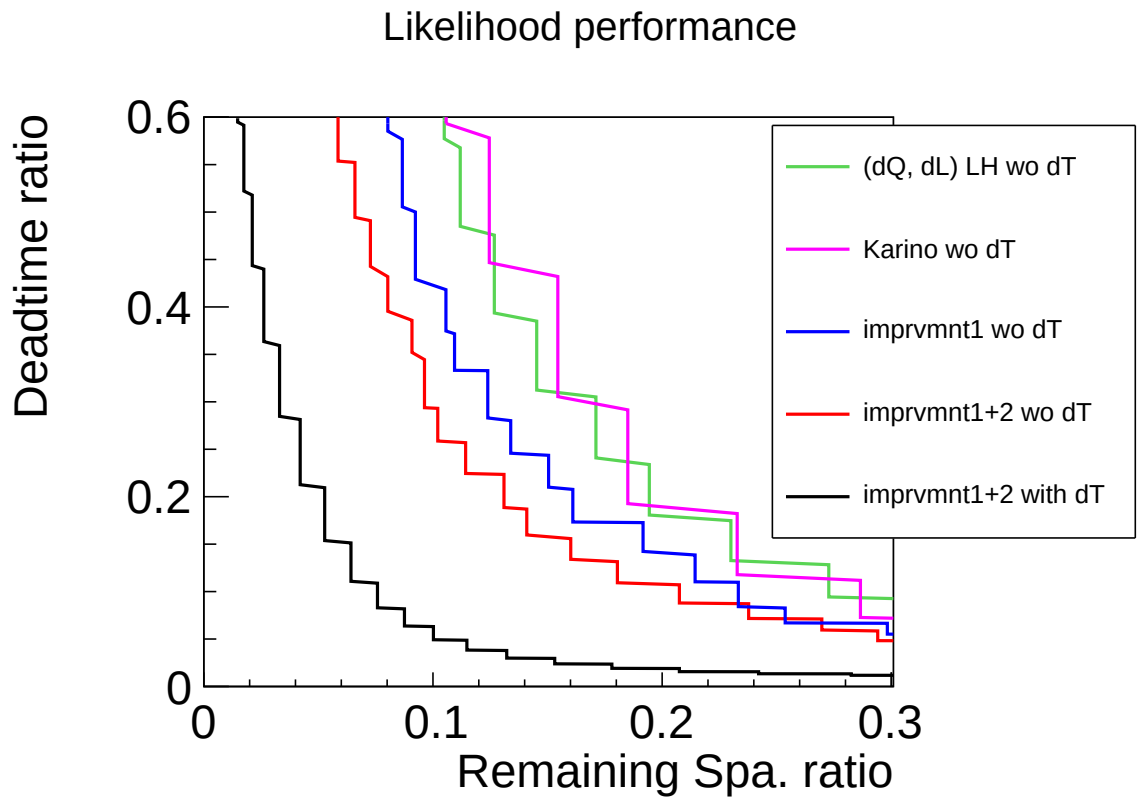

Figure 5.10: Comparison of the muon-based cuts

  - Total residual charge (dQ) was used instead of dE/dx (local charge).
  - 1D x 1D treatment ($\mathcal{L}(dQ) \cdot \mathcal{L}(dL)$)
  - Weighing of $\mathcal{L}(dQ)$ and $\mathcal{L}(dL)$ are data driven.
  - Used in [98].
- *Karino's likelihood* without dT
- *Improvement1* without dT
  - dE/dx extraction is the same as *Karino's likelihood*
  - 2D likelihood $\mathcal{L}(dE/dx, dL)$
  - Accidental likelihood is taken into account (likelihood ratio)
- *Improvement1+2* without dT
  - dE/dx extraction with the new algorithm.
- *Improvement1+2* with dT

Figure 5.10 shows the results. The performance of *Karino's likelihood* is almost same as the one of the (dQ, dL) likelihood which doesn't use the dE/dx (local charge) information. *Shower-tag* with the dE/dx is finally worth implementing after applying the improvements described in this section.

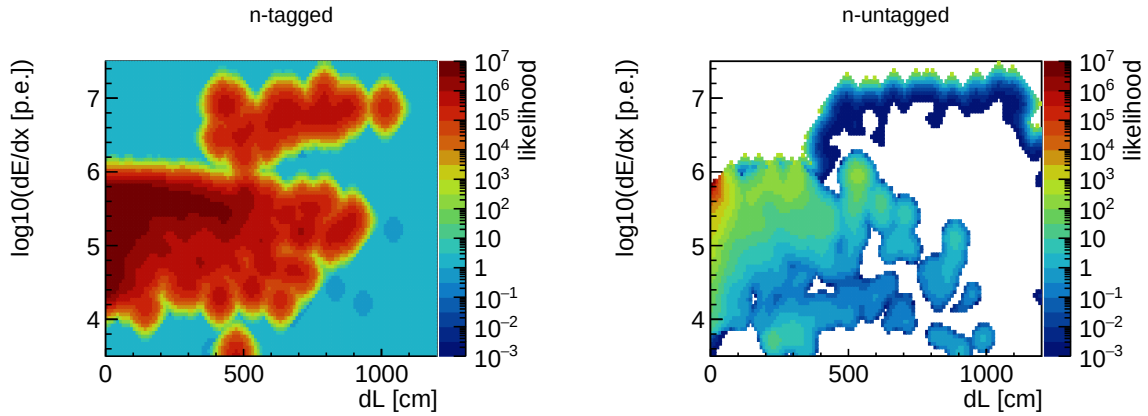

Figure 5.11: $(dE/dx, dL)$ likelihood ratio. (Left): *n-tagged* case. (Right): *n-untagged* case. In *shower-tag*, white regions which don't have data are vetoed if $\log_{10} dE/dx > 5.5$ and not vetoed if $\log_{10} dE/dx \leqq 5.5$.

n-untagged Case

Figure 5.10 shows that the new *shower-tag* can achieve very high performance when dT-likelihood is Combined (black line). This is, however, the case for *n-tagged* events. It is expected that energetic muons (high dE/dx) produce more neutrons (high *n-tagged* probability). Figure 5.11 shows the difference of the contrasts of the likelihood between *n-tagged* and *n-untagged*. I will address this correlation between *n-tag* and *shower-tag* later.

5.3 n-tag

When a radioactive isotope is produced by a muon spallation, neutrons are often produced near it. Figure 5.12 shows the simulated result of the number of neutrons near ^{10}C produced in KamLAND. Taking advantage of this property, a three-fold coincidence of

- incident muon
- neutron(s) capture gamma-ray(s)
- decay of a spallation product

can used to tag the decay of an isotope produced by a spallation. I call it *n-tag*. *n-tag* have been implemented in the double-beta decay analysis [81, 6, 7] using neutrons of MoGURA data.

5.3.1 n-tag using MoGURA Neutrons

MoGURA is better than FBE in detecting neutrons after muons, see Section 3.6.3. It has been analysis-ready since *Zen400 2nd phase*.

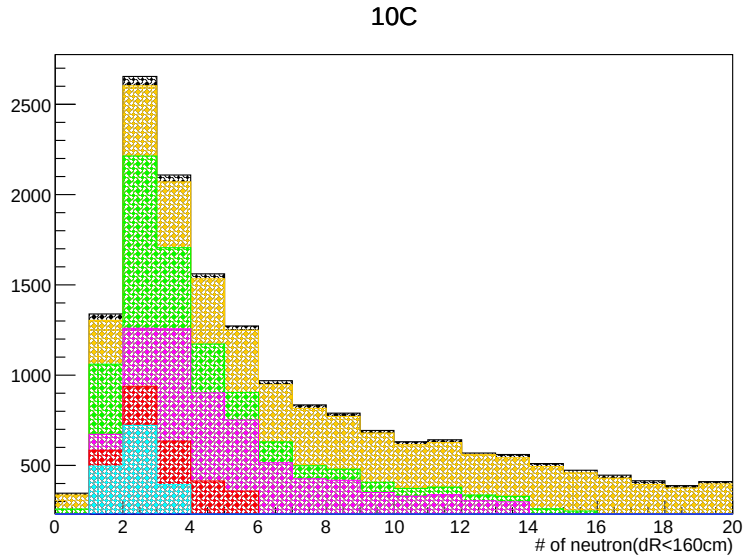

Figure 5.12: (MC) Number of neutrons near the ^{10}C in KamLAND. Colors indicate different production processes/parents: γ (yellow), π (green), n (magenta), p (red), μ (sky blue). Figure from [99].

Reconstruction of Neutrons with MoGURA

An event just after a muon is affected by electronics noises, shift of the baseline, and after-pulses of PMTs. Therefore a subtracted-number-of-hits N_s is used as "energy" of a neutron

$$N_s = N_{\text{in}} - N_{\text{out}} \frac{30\ [\text{ns}]}{170\ [\text{ns}]}, \tag{5.73}$$

where N_{in} is the number of hits around a peak ($\pm$15 ns window) and N_{out} is the number of hits of the event (200 ns window) except the N_{in} window, see Figure 5.13. For the vertex reconstruction, a legacy fitter, KAT-LT-Vertex, described in [58, Sec. 3.6] is used.

Pairing of MoGURA Neutrons and a FBE Muon

MoGURA neutrons are paired with a FBE muon based on their unixtime. The FBE muon selection is as follows:

- ($Q_{17} > 10^4$ p.e.) or ($Q_{17} > 500$ p.e. and $N_{\text{OD}} \geq 9$)[1]
- Fake muon cut: $dT_{\text{fromPrevMuon}} > 10$ μs

Figure 5.14 shows the N_s versus $dT_{\text{muonToNeutron}}$ distribution of the paired neutrons and muons.

Using the $dT_{\text{muonToNeutron}}$ the following selections are applied to the MoGURA neutrons:

- $10 \leq dT_{\text{fromMu}} < 1200$ μs

[1] $N_{\text{OD}} \geq 5$ for *BeforePurif* and *SolarPhase*

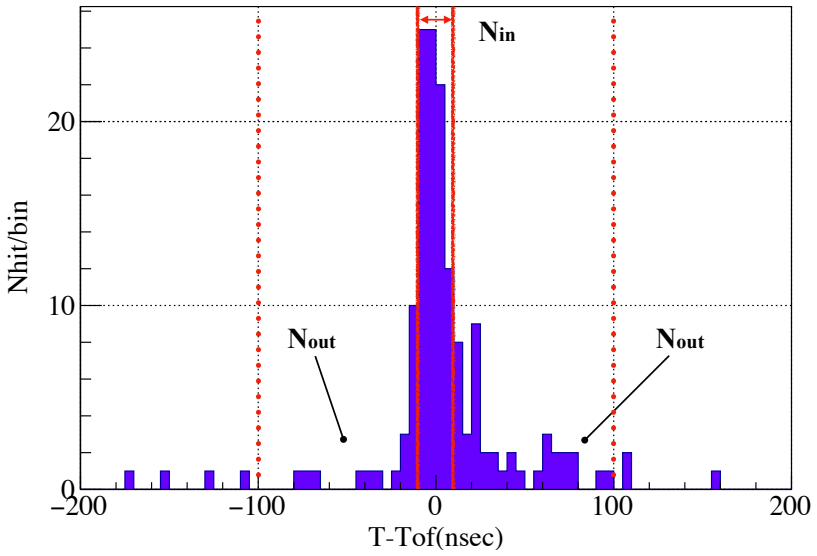

Figure 5.13: N_{in} and N_{out}. Figure from [100]

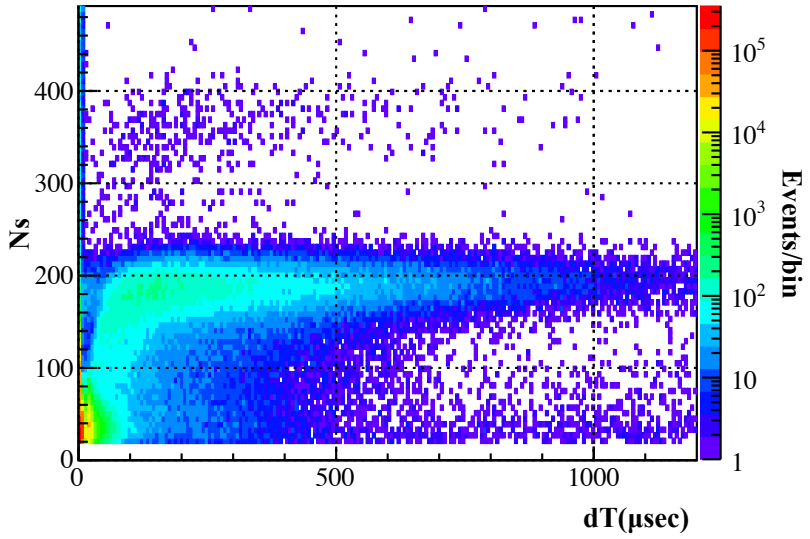

Figure 5.14: N_s vs dT of MoGURA neutrons and FBE muons (in *Zen800* period). $N_s \sim 200$ corresponds to the energy of the neutron capture gamma-ray (2.2 MeV). Figure from [100].

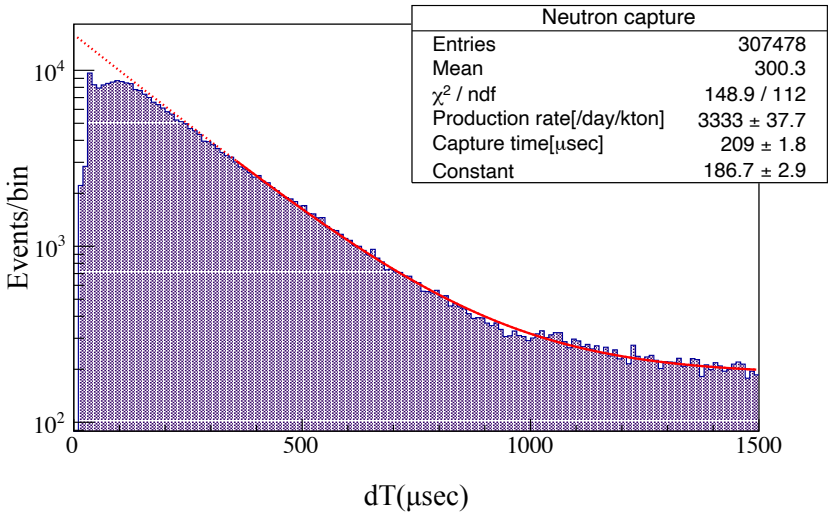

Figure 5.15: Time difference from a MoGURA neutron to a FBE muon (in *Zen800* period). Figure from [100]

- $(10 \leq dT_{\mathrm{fromMu}} < 30\ \mu\mathrm{s}$ and $N_s \geq 80)$ or $(dT_{\mathrm{fromMu}} > 30\ \mu\mathrm{s}$ and $N_s \geq 50)$
- $N_{\mathrm{in}} + N_{\mathrm{out}} \geq 150$

Figure 5.15 shows the dT distribution of the selected neutrons. Comparing the number of selected neutron events after the accidental events subtraction to the expectation, which was estimated from the decay curve ($dT > 350\ \mu$s), the neutron detection efficiency is estimated to be $\sim 80\%$ [100].

dR Cut

The above selected neutrons are paired with spallation isotope candidates. Here I show examples of ^{10}C and ^{12}B. Their selections are as follows:

- *AfterZen* data
- $r < 4$ m
- ^{10}C
  - $2.2 < E_{\mathrm{vis}} < 4.0$ MeV
  - $10 < dT_{\mathrm{fromNeutron}} < 90$ s (ontime), $300 < dT_{\mathrm{fromNeutron}} < 1000$ s (offtime)
- ^{12}B
  - $4 < E_{\mathrm{vis}} < 12$ MeV
  - $30 < dT_{\mathrm{fromNeutron}} < 60$ ms (ontime), $300 < dT_{\mathrm{fromNeutron}} < 1000$ s (offtime)

Figure 5.16 (5.17) show the distribution of the distance between the ^{10}C (^{12}B) candidate and the nearest neutron (dR). The event excess at $dR > 200$ cm region of Figure 5.17 indicates that some of ^{12}B are produced through neutron-non-related processes such as μ^- capture on ^{12}C. Based on the ^{10}C case, the *n-tag* condition is set to $dR < 1.6$ m ($dT < 180$ s) for *AfterZen*.

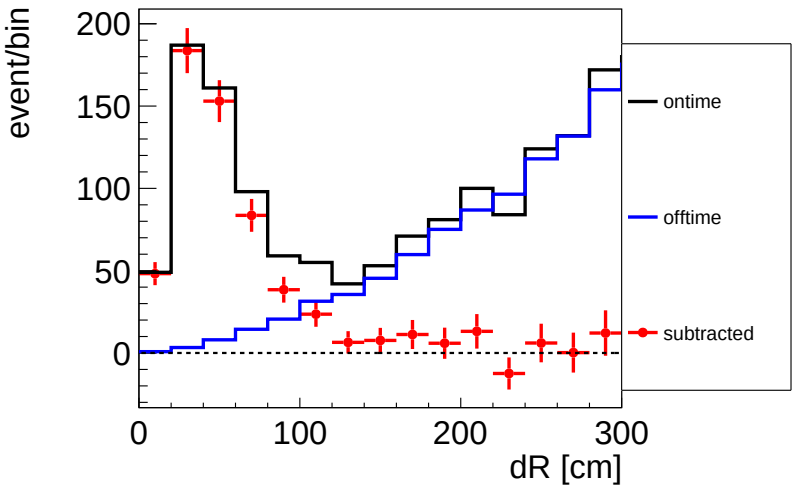

Figure 5.16: Distance between a ^{10}C candidate to the nearest MoGURA-neutron (*AfterZen*).

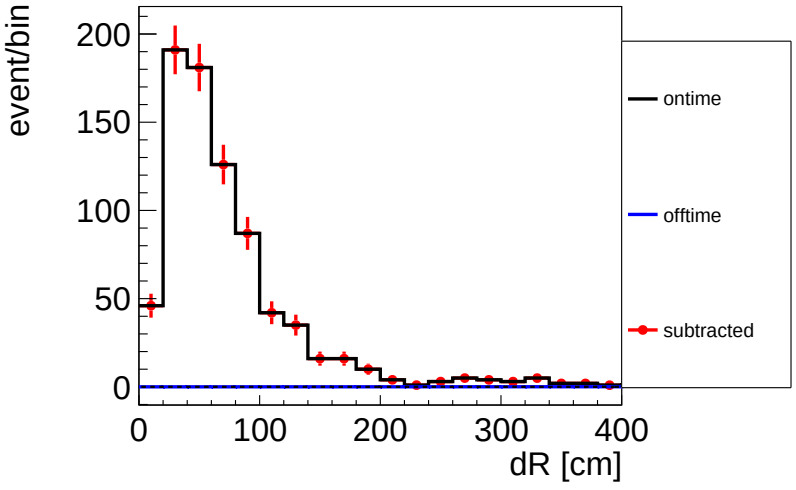

Figure 5.17: Distance between a ^{12}B candidate to the nearest MoGURA-neutron (*AfterZen*).

5.3.2 FBE Neutron

To deploy the *n-tag* to MoGURA-unavailable periods (*BeforePurif* and *SolarPhase*), I studied FBE neutron events after muons.

Reconstruction of Neutron Events

I used a legacy charge-only based energy fitter, KAT-Energy [58, Sec. 3.7], to reconstruct the energy of the neutrons. KAT-LT-Vertex was used for the vertex reconstruction as in the MoGURA case.

Figure 5.18 (5.19) show the dT and E_{vis} property of the neutron candidates ($r < 6$ m) of *BeforePurif* (*SolarPhase*). The band around 2.2 MeV is significant. The visual differences between *BeforePurif* and *SolarPhase* come from the difference of their trigger conditions. The dT range of the low energy ($\sim$ 0.5 MeV) band corresponds to the delayed trigger window.

By checking the dR correlation between the neutrons and ^{12}B events, I decided the following neutron selection criteria:

- $10 < dT < 1200$ μs
- *BeforePurif*
  - $Q_\mu < 10^6$ p.e.: $E_{\mathrm{vis}}^{\mathrm{Kat}} > 1.2$ MeV
  - $Q_\mu \geq 10^6$ p.e.: $E_{\mathrm{vis}}^{\mathrm{Kat}} > 0.7$ MeV
- *SolarPhase*
  - $Q_\mu < 10^6$ p.e.: ($E_{\mathrm{vis}}^{\mathrm{Kat}} > 0.6$ MeV and $dT < 100$ μs) or ($E_{\mathrm{vis}}^{\mathrm{Kat}} > 1.6$ MeV)
  - $Q_\mu \geq 10^6$ p.e.: ($E_{\mathrm{vis}}^{\mathrm{Kat}} > 0.05$ MeV and $90 < dT < 200$ μs) or ($E_{\mathrm{vis}}^{\mathrm{Kat}} > 0.6$ MeV)

Under the above condition, the neutron detection efficiencies are estimated as follows:

- *BeforePurif*
  - $Q_\mu < 10^6$ p.e.: $\sim 85\%$
  - $Q_\mu \geq 10^6$ p.e.: $\sim 40\%$
- *SolarPhase*
  - $Q_\mu < 10^6$ p.e.: $\sim 80\%$
  - $Q_\mu \geq 10^6$ p.e.: $\sim 33\%$

dR Cut

The dR distributions for ^{10}C and ^{12}B are derived for *SolarPhase*, see Figure 5.20 and 5.21, respectively. The resolution of dR in this case is larger than that in the MoGURA case. Agasin, based on the ^{10}C case, the *n-tag* condition for *BeforePurif* and *SolarPhase* is set to $dR < 2$ m ($dT < 180$ s).

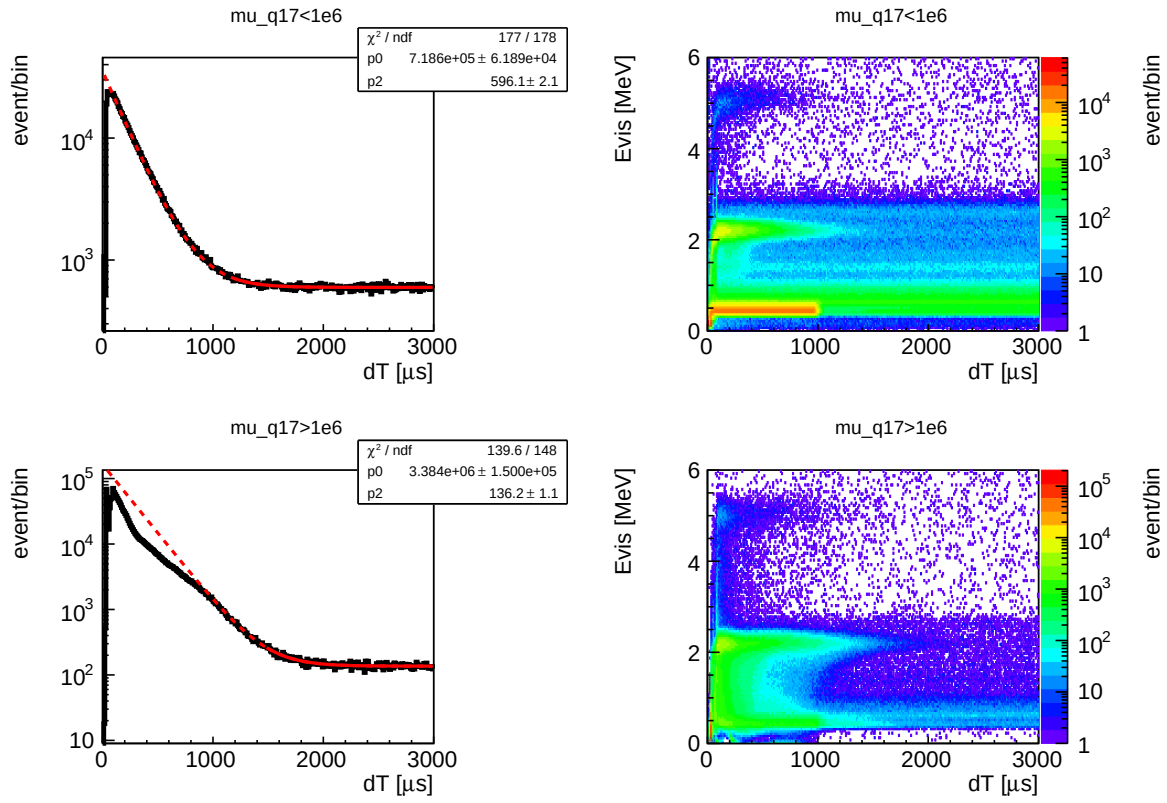

Figure 5.18: FBE neutrons (*BeforePurif*). Selection for dT projection: $E_{\mathrm{vis}}^{\mathrm{Kat}} > 1.2$ MeV ($Q_\mu < 10^6$ p.e.), $E_{\mathrm{vis}}^{\mathrm{Kat}} > 0.7$ MeV ($Q_\mu \geq 10^6$ p.e.).

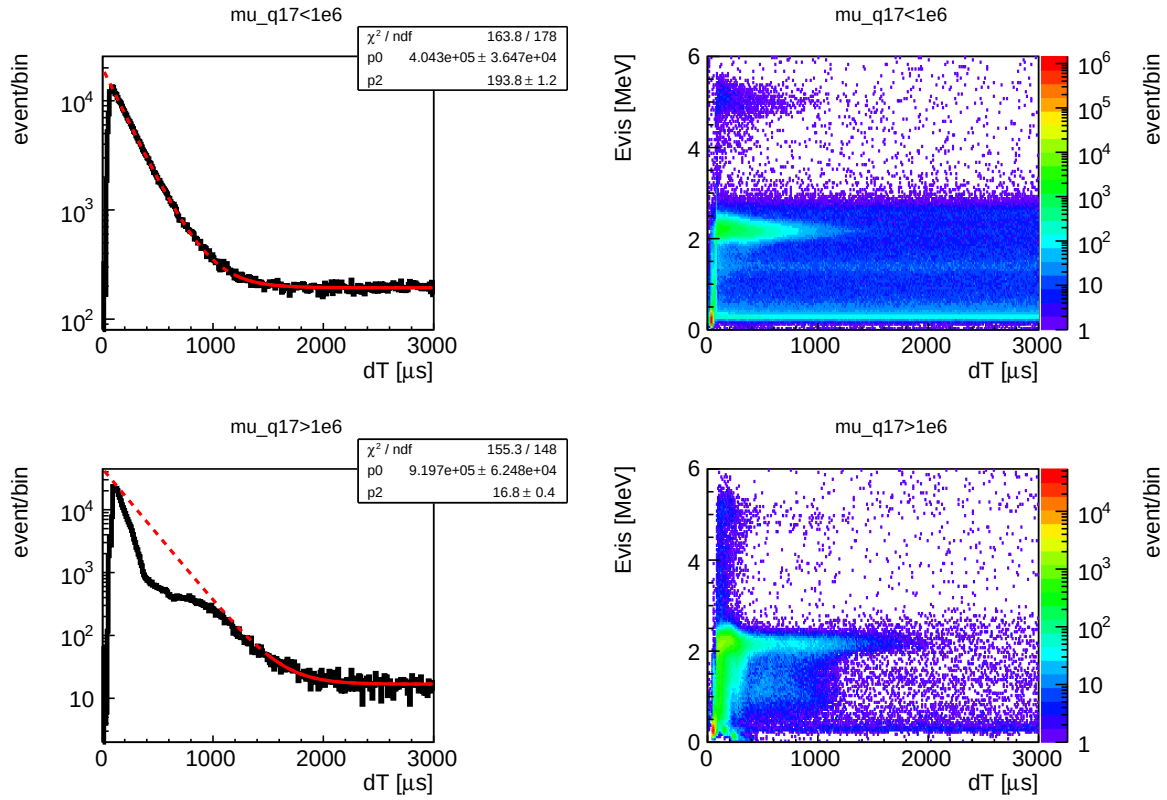

Figure 5.19: FBE neutrons (*SolarPhase*). Selection for dT projection: $\{$ ($E_{\text{vis}}^{\text{Kat}} > 0.6$ MeV and $dT < 100$ μs) or ($E_{\text{vis}}^{\text{Kat}} > 1.6$ MeV) $\}$ ($Q_\mu < 10^6$ p.e.), $\{$ ($E_{\text{vis}}^{\text{Kat}} > 0.05$ MeV and $90 < dT < 200$ μs) or ($E_{\text{vis}}^{\text{Kat}} > 0.6$ MeV) $\}$ ($Q_\mu \geq 10^6$ p.e.).

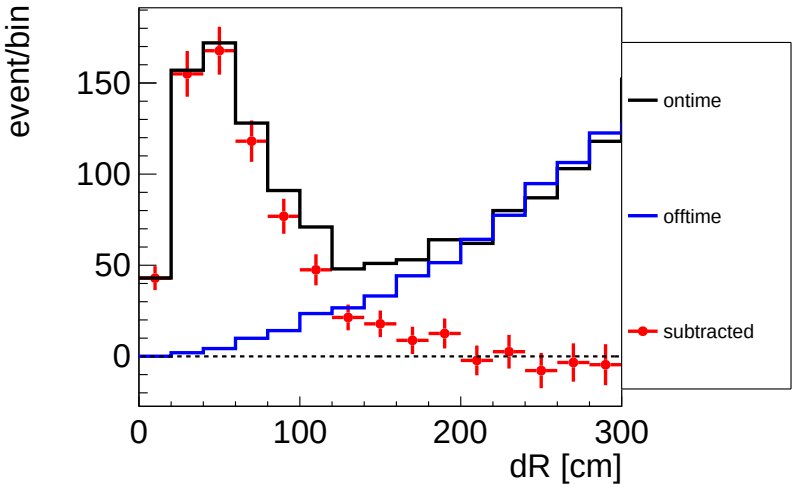

Figure 5.20: Distance between a ^{10}C candidate to the nearest FBE-neutron (*SolarPhase*).

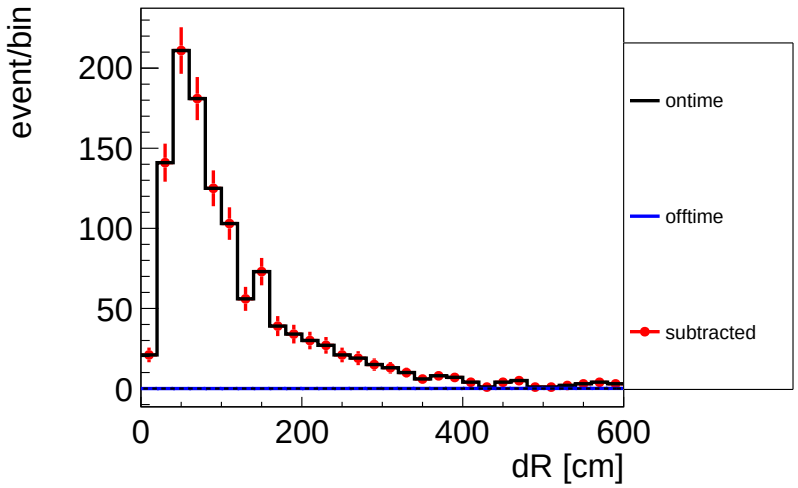

Figure 5.21: Distance between a ^{12}B candidate to the nearest FBE-neutron (*SolarPhase*).

5.4 Strategy for the Combination of Shower-tag and n-tag

Hence *shower-tag* and *n-tag* are correlated, it is ideal to construct a spallation likelihood as

$$\mathcal{L}_{\mathrm{spa}} = \mathcal{L}_{\mathrm{woDt}}\left(\frac{dE}{dx}, dL_{\mathrm{toMu}}, dR_{\mathrm{toNeutron}}\right)\mathcal{L}(dT). \tag{5.74}$$

However, creation of the $\mathcal{L}_{\mathrm{woDt}}$ requires further detailed study because both the neutron detection efficiency and the track reconstruction are not perfect. Therefore, for simplicity, I consider a staged cut as follows:

1. Apply an all volume veto ($dT_{\mathrm{fromMu}} < 150$ ms)
2. Apply *n-tag*
3. Apply *shower-tag*

The *shower-tag* is applied on *n-untagged* events. Thus it is important to estimate the following values for the remaining background estimation after the cut:

- *n-untagged* rate of the isotopes
- *shower-tag* efficiency on *n-untagged* events

5.5 n-tag Efficiency and n-untagged rate

n-tagging is a binary cut; $dR < 1.6(2.0)$ m or not. Thus a total production rate of an isotope is given by

$$R_i^{\mathrm{total}} = R_i^{\text{n-tagged}} + R_i^{\text{n-untagged}}. \tag{5.75}$$

Hence R_i^{total} is already estimated in Ref. [55], it is possible to obtain $R_i^{\text{n-untagged}}$ by a subtraction, $R_i^{\text{total}} - R_i^{\text{n-tagged}}$. However, as can be seen later, the *n-tag* efficiency is relatively high ($\gtrsim$ 70%). The subtraction tends to be a large number minus another large number. The resulting $R_i^{\text{n-untagged}}$ would have a huge relative uncertainty. Therefore $R_i^{\text{n-untagged}}$ needs to be obtained independently from R_i^{total}.

5.5.1 Estimation of the Production Rates

I estimated the production rates by fitting 2D ($E_{\text{vis}}, dT_{\text{fromMu}}$) distributions.

n-tagged

The estimation of *n-tagged* rates were performed with the following classes:

- ^{9}Li, ^{8}He
  - $r < 5.5$ m
  - Neutron emitters.
  - Tagged with additional delayed-coincidence (3 ms window) tag.
- ^{12}B, ^{12}N, ^{9}C, ^{8}Li, ^{8}B, ^{11}Be
  - $r < 5.5$ m
  - $0.005 < dT < 1000$ s
  - $6 < E_{\text{vis}} < 18$ MeV
- ^{10}C, ^{6}He
  - $r < 4.0$ m (avoid external gamma-ray backgrounds)
  - $0.15 < dT < 1000$ s
  - $2.2 < E_{\text{vis}} < 6$ MeV

n-untagged Rate

The rate estimations of *n-untagged* cases suffer from accidental backgrounds compared to *n-tagged* cases. Thus more classes are needed as follows:

- ^{9}Li, ^{8}He
  - $r < 5.5$ m
  - Tagged with additional delayed-coincidence (3 ms window) tag.
- ^{12}B, ^{12}N
  - $r < 5.5$ m
  - $0.005 < dT < 1000$ s
  - $6 < E_{\text{vis}} < 18$ MeV
- ^{9}C, ^{8}Li, ^{8}B

  - $r < 4.5$ m
  - $0.15 < dT < 1000$ s
  - $6 < E_{\mathrm{vis}} < 18$ MeV
- ^{11}Be
  - $r < 4.5$ m
  - $0.15 < dT < 1000$ s
  - $6 < E_{\mathrm{vis}} < 18$ MeV
  - Enriched by $\mathcal{L}_{\mathrm{woDt}}\left(\frac{dE}{dx}, dL\right)$ selection
- ^{10}C, ^{6}He
  - $r < 3.0$ m
  - $0.15 < dT < 1000$ s
  - $2.2 < E_{\mathrm{vis}} < 6$ MeV
  - Enriched by $\mathcal{L}_{\mathrm{woDt}}\left(\frac{dE}{dx}, dL\right)$ selection

The efficiency of the $\mathcal{L}_{\mathrm{woDt}}\left(\frac{dE}{dx}, dL\right)$ selection used for ^{11}Be, ^{10}C and ^{6}He were estimated based on *n-untagged* ^{8}Li events ($0.15 < dT < 2$ s, $6 < E_{\mathrm{vis}} < 20$ MeV). The uncertainty coming from the isotope difference was estimated from MC (FLUKA).

Results

The results are shown in Figure 5.22 (*n-tagged*) and 5.23 (*n-untagged*). Figure 5.24 shows the results of total rates (= *n-tagged* + *n-untagged*), see Table 5.2 for exact values. Total rates of all three phases are in good agreements and they also agree with the estimation of Ref. [55]. A slight tension in ^{8}B and ^{8}Li may be related to the difference of energy reconstruction tools. They are correlated isotopes in the estimation because they have similar energy and lifetimes (~ 1 s). Sums of their rates (~ 25 /day/kton) are almost same in this work and Ref. [55].

The production rate of ^{6}He, which wasn't measured in Ref. [55], was estimated from *BeforePurif* data as

$$R_{\text{He-6}} = 11.9 \pm 1.2 \text{ /day/kton}$$

or $(9.33 \pm 0.95) \times 10^{-7}$ $\mu^{-1}\mathrm{g}^{-1}\mathrm{cm}^{2}$ in yield.

5.5.2 Efficiency

n-tag Efficiency

The *n-tag* efficiency for an isotope is estimated as

$$\epsilon_i^{\text{n-tag}} = \frac{R_i^{\text{n-tagged}}}{R_i^{\text{n-tagged}} + R_i^{\text{n-untagged}}}. \tag{5.76}$$

Figure 5.25 shows the efficiencies for all periods and isotopes. *AfterZen* has the best performance ($\sim 90\%$ efficiencies) thanks to MoGURA. The differences between *BeforePurif* and *SolarPhase* may be due to the difference in the trigger thresholds. With a lower threshold (*SolarPhase*), buffers of the electronics tend to be full after muons.

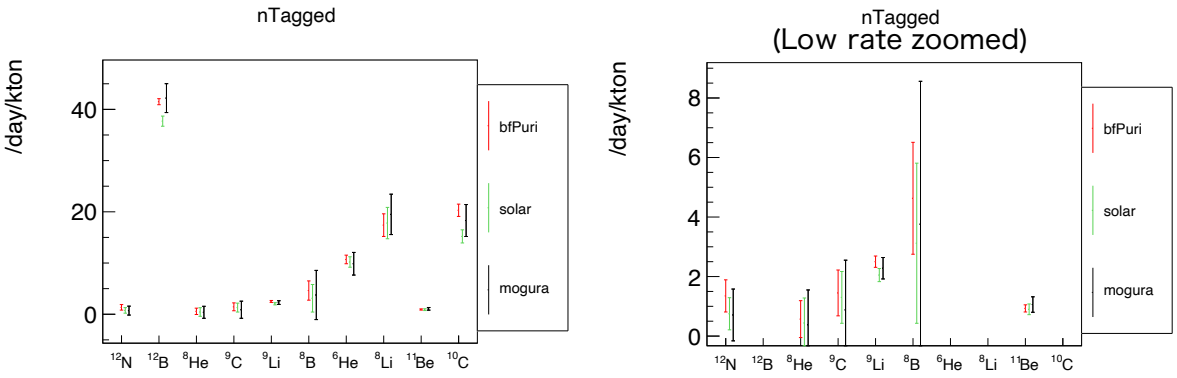

Figure 5.22: *n-tagged* rates. *mogura* means *AfterZen*.

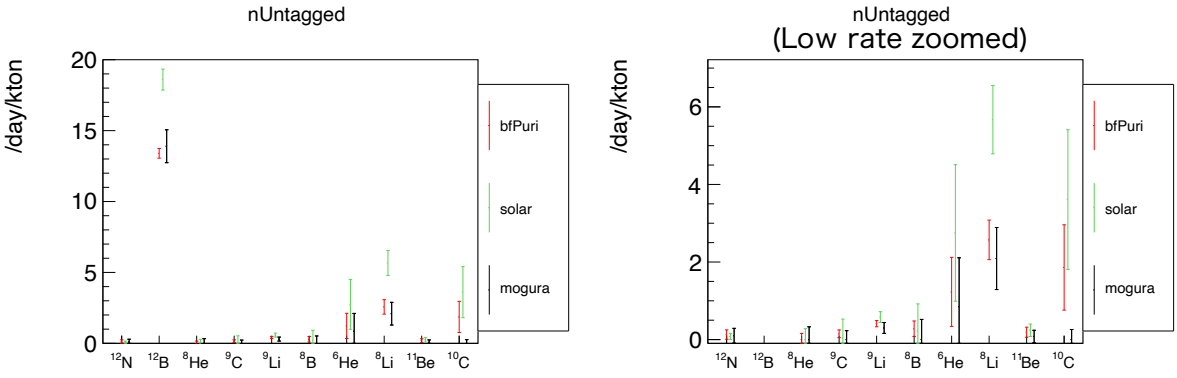

Figure 5.23: *n-untagged* rates. *mogura* means *AfterZen*.

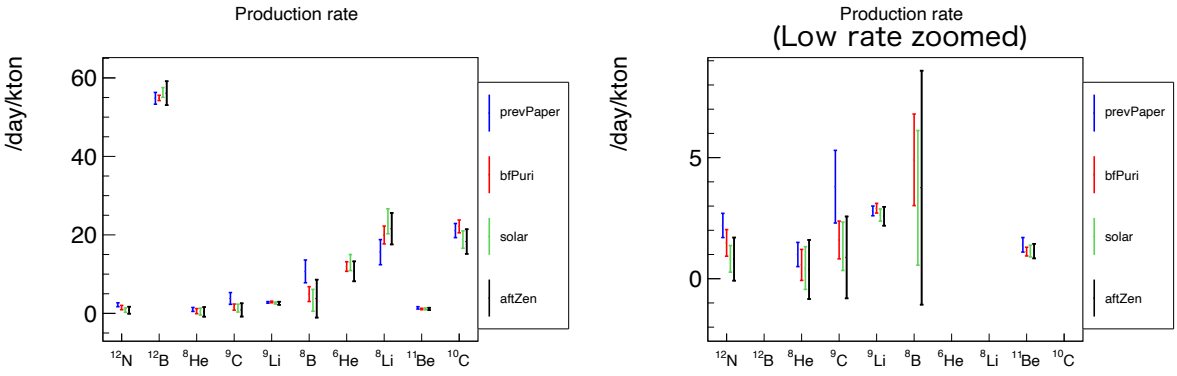

Figure 5.24: Total production rates (= *n-tagged* + *n-untagged*). *prevPaper* means Ref. [55].

Table 5.2: Total production rates

Isotopes	Rate [/d/kt]		
	BeforePurif	*SolarPhase*	*AfterZen*
^{12}N	1.48 ± 0.55	0.82 ± 0.55	0.81 ± 0.89
^{12}B	54.90 ± 0.68	56.30 ± 1.24	56.10 ± 3.05
^{8}He	0.57 ± 0.64	0.44 ± 0.88	0.38 ± 1.22
^{9}C	1.60 ± 0.78	1.34 ± 1.00	0.88 ± 1.69
^{9}Li	2.91 ± 0.20	2.63 ± 0.25	2.58 ± 0.39
^{8}B	4.91 ± 1.89	3.34 ± 2.78	3.76 ± 4.83
^{6}He	11.93 ± 1.22	12.95 ± 2.04	10.71 ± 2.54
^{8}Li	19.97 ± 2.27	23.47 ± 3.18	21.59 ± 4.02
^{11}Be	1.12 ± 0.18	1.14 ± 0.24	1.14 ± 0.30
^{10}C	22.16 ± 1.63	18.81 ± 2.21	18.30 ± 3.13

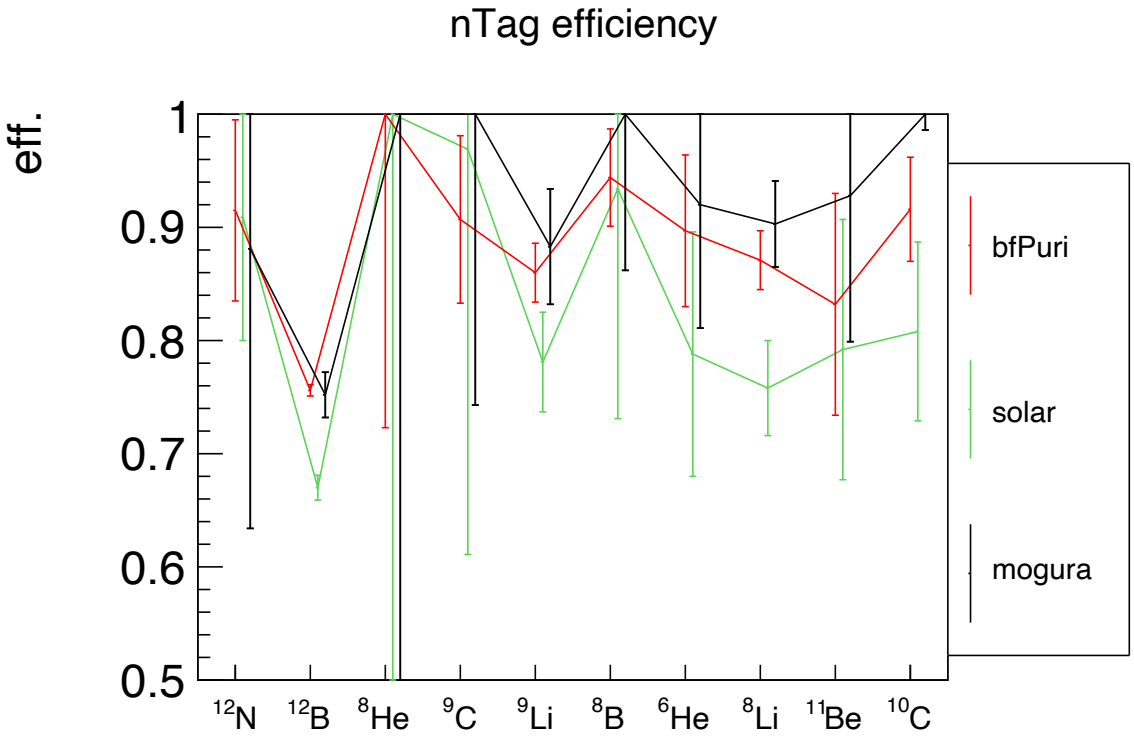

Figure 5.25: *n-tag* efficiency. *mogura* means *AfterZen*.

Deadtime Ratio

The deadtime ratio (the efficiency of accidentally tagging non-spallation events) is calculated using space-time-uniform MC events ($r < 3$ m). Actual muons and neutrons are paired in each phase. The results are as follows:

- *BeforePurif*: 6.24%
- *SolarPhase*: 5.32%
- *AfterZen*: 4.79%

In *AfterZen*, periods in which MoGURA was not running due to some troubles were also treated as the deadtime.

5.6 Combination of Shower-tag and n-tag

The strategy for the combination of *shower-tag* and *n-tag* is described in 5.4. The *shower-tag* efficiency on *n-untagged* events needs to be estimated.

5.6.1 PDF

The *shower-tag* likelihood is constructed as

$$\mathcal{L}_{\mathrm{wDt}}(dE/dx, dL, dT) = \mathcal{L}_{\mathrm{woDt}}(dE/dx, dL)\mathcal{L}(dT). \tag{5.77}$$

As for $\mathcal{L}_{\mathrm{woDt}}(dE/dx, dL)$, a PDF created from *n-untagged* events is used, see Figure 5.11 (right).

5.6.2 Determination of Likelihood Cut Conditions

The likelihood cut conditions were optimized in a similar way described in Section 5.2.7. This time, however, *n-untagged* ^{8}Li was used as a referential spallation isotope, see the red solid line in Figure 5.26 (top left). I substituted *n-untagged* amounts for N_{bg} in the formula 5.72. The $\mathcal{L}_{\mathrm{wDt}}$ was created from a random combination of $\mathcal{L}_{\mathrm{woDt}}$ and $\mathcal{L}(dT)$ and the statistical error which comes from the ontime-minus-offtime subtraction was ignored.

The following are derived likelihood cut conditions:

- *BeforePurif*: $\log_{10}(\mathcal{L}_{\mathrm{wDt}}) \geq 1.2$
- *SolarPhase*: $\log_{10}(\mathcal{L}_{\mathrm{wDt}}) \geq 1.6$
- *AfterZen*: $\log_{10}(\mathcal{L}_{\mathrm{wDt}}) \geq 1.6$

5.6.3 Estimation of Efficiencies

The $\mathcal{L}_{\mathrm{wDt}}$ cut efficiencies against *n-untagged* events were estimated based on *n-untagged* ^{8}Li events. Again, the uncertainty coming from the isotope difference was estimated from MC (FLUKA). In order to treat the statistical uncertainty comes from the ontime-minus-offtime subtraction process, a conversion of dT is considered.

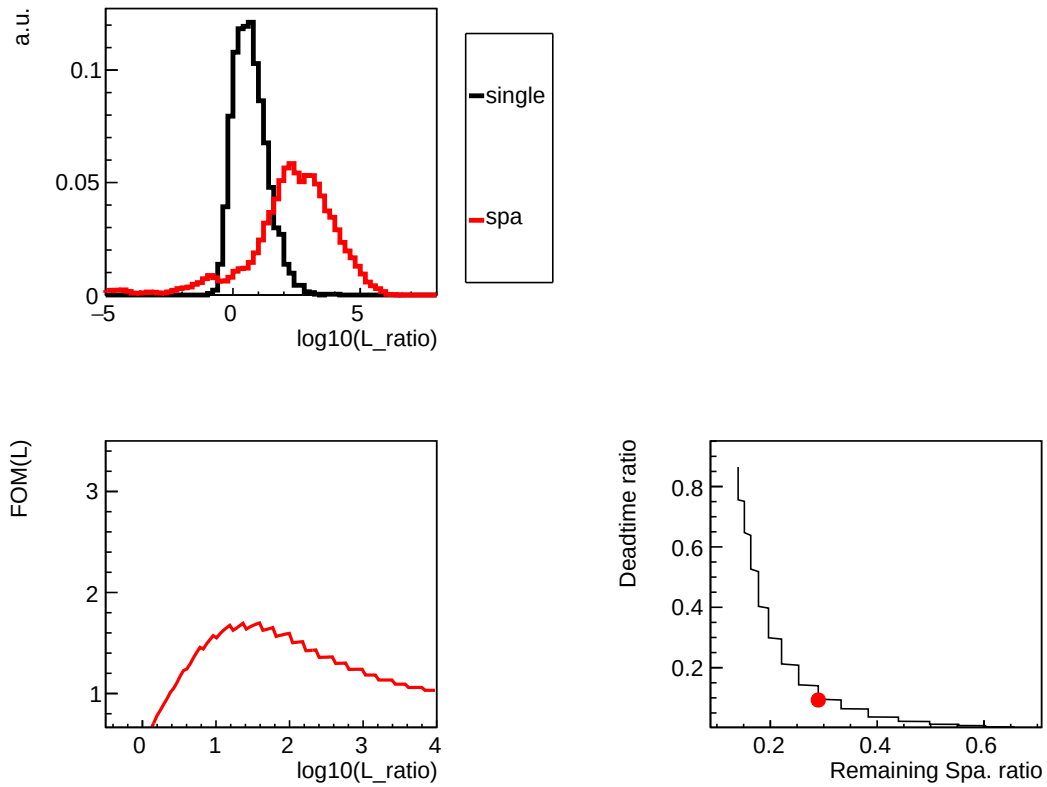

Figure 5.26: Example of the likelihood cut condition determination (*SolarPhase*).

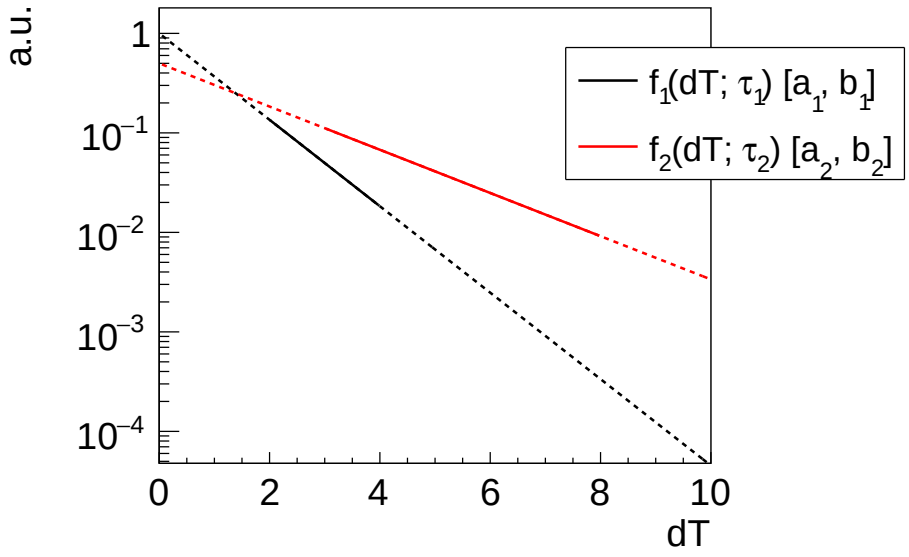

Figure 5.27: Schematic of the dT conversion.

dT Conversion

^{8}Li events are selected with ontime and offtime dT ranges:

- ontime: $0.15 < dT < 2$ s
- offtime: $180 < dT < 1000$ s

And, of course, dT's of the ^{8}Li candidates follow the lifetime $\tau_{\text{Li-8}}$.

In order to consider likelihood distributions for each isotope, the paired property of a ^{8}Li candidate needs a conversion

$$\left(\frac{dE}{dx}, dL, dT_{\text{rawLi-8}}\Big|_{dT_1}^{dT_2}\right) \rightarrow \left(\frac{dE}{dx}, dL, dT^{\text{converted}}_{\text{C-10,He-6,etc.}}\Big|_{150\text{ ms}}^{180\text{ s}}\right). \tag{5.78}$$

Thus I have to consider 1-to-1 mapping from a ranged-exponential distribution, $f_1(dT;\tau_1)$ $[a_1, b_1]$, to another one, $f_2(dT;\tau_2)$ $[a_2, b_2]$, see Figure 5.27. This is achieved by considering their integrals as

$$\frac{I(\tau_2, a_2, dT_2)}{I(\tau_2, a_2, b_2)} = \frac{I(\tau_1, a_1, dT_1)}{I(\tau_1, a_1, b_1)}, \tag{5.79}$$

where

$$I(\tau, a, b) = e^{-\frac{b}{\tau}} - e^{-\frac{a}{\tau}}. \tag{5.80}$$

Generally, the origin can be a multi-component function as follows

$$\frac{I(\tau_2, a_2, dT_2)}{I(\tau_2, a_2, b_2)} = \frac{\sum_i A_i I(\tau_i, a_1, dT_1)}{\sum_i A_i I(\tau_i, a_1, b_1)}. \tag{5.81}$$

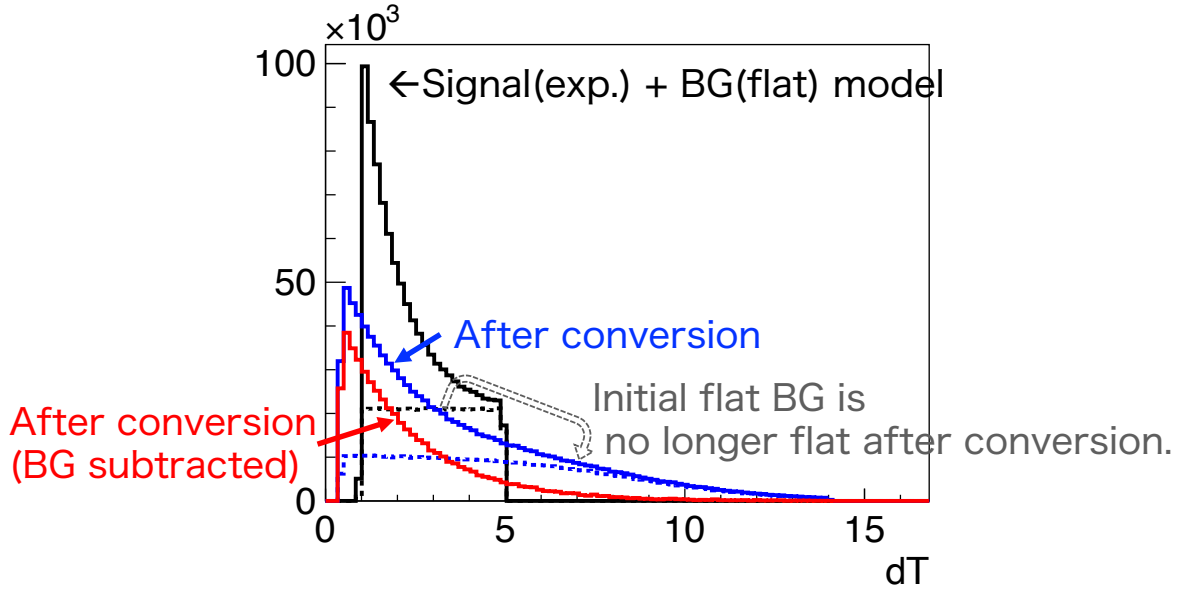

Figure 5.28: Example of dT conversion.

Solving this for dT_2, I get

$$dT_2 = -\tau_2 \ln\left(e^{-\frac{a_2}{\tau_2}} + I(\tau_2, a_2, b_2)\frac{\sum_i A_i I(\tau_i, a_1, dT_1)}{\sum_i A_i I(\tau_i, a_1, b_1)}\right). \tag{5.82}$$

Figure 5.28 shows an example of the dT conversion from an exponential + flat model. The flat background in the original model is converted to a non-flat distribution.

Results

Table 5.3 shows the summary of *shower-tag* efficiencies against *n-untagged* events. The relatively lower efficiency for ^{11}Be and ^{10}C is due to the difference of the optimized energy region in $\mathcal{L}(dT)$ construction. The *n-tag* efficiency of *SolarPhase* is not as good as *AfterZen*. Instead, its *shower-tag* efficiency is higher.

The total rejection efficiency, including 150 ms all volume veto, is summarized in Table 5.4. The remaining event rate, corresponds to the total rejection efficiency, is shown in Table 5.5.

More than 90% rejection efficiencies were achieved for all isotopes and phases. The event rates were lowered to the ^{8}B solar neutrino level, $\mathcal{O}(1)$ /day/kton.

Deadtime Ratio

The deadtime ratio was estimated in the same way with that for *n-tag* case (See Section 5.5.2). Table 5.6 shows the summary.

Table 5.3: *Shower-tag* efficiency against *n-untagged* events

Isotopes	Efficiency		
	BeforePurif	*SolarPhase*	*AfterZen*
^{12}N	$100 \pm 11\%$	$96 \pm 8\%$	$100 \pm 39\%$
^{12}B	$100 \pm 13\%$	$94 \pm 8\%$	$90 \pm 18\%$
^{8}He	$100 \pm 8\%$	$95 \pm 8\%$	$88 \pm 18\%$
^{9}C	$99 \pm 8\%$	$95 \pm 8\%$	$89 \pm 19\%$
^{9}Li	$100 \pm 8\%$	$95 \pm 8\%$	$91 \pm 19\%$
^{8}B	$99 \pm 8\%$	$94 \pm 7\%$	$81 \pm 16\%$
^{6}He	$99 \pm 8\%$	$93 \pm 7\%$	$82 \pm 17\%$
^{8}Li	$100 \pm 8\%$	$93 \pm 7\%$	$81 \pm 17\%$
^{11}Be	$52 \pm 14\%$	$79 \pm 21\%$	$69 \pm 23\%$
^{10}C	$45 \pm 12\%$	$74 \pm 19\%$	$62 \pm 21\%$

Table 5.4: Total (150 ms veto + *shower-tag* + *n-tag*) rejection efficiency

Isotopes	Efficiency		
	BeforePurif	*SolarPhase*	*AfterZen*
^{12}N	$100 \pm 0.00008\%$	$100 \pm 0.00007\%$	$100 \pm 0.00037\%$
^{12}B	$100 \pm 0.019\%$	$99.989 \pm 0.014\%$	$99.99 \pm 0.03\%$
^{8}He	$100 \pm 0.3\%$	$100 \pm 1.2\%$	$100 \pm 4.29\%$
^{9}C	$99 \pm 0.3\%$	$99.9 \pm 0.8\%$	$100 \pm 1.27\%$
^{9}Li	$100 \pm 0.6\%$	$99.4 \pm 1.0\%$	$99.4 \pm 1.25\%$
^{8}B	$99 \pm 0.4\%$	$99.6 \pm 1.3\%$	$100. \pm 2.29\%$
^{6}He	$99.9 \pm 0.7\%$	$98.7 \pm 1.6\%$	$98.76 \pm 2.21\%$
^{8}Li	$100 \pm 1.0\%$	$98.5 \pm 1.6\%$	$98.39 \pm 1.61\%$
^{11}Be	$92.0 \pm 6.1\%$	$95.7 \pm 5.2\%$	$97.79 \pm 4.56\%$
^{10}C	$95.4 \pm 2.9\%$	$95.0 \pm 4.5\%$	$100 \pm 0.54\%$

Table 5.5: Remaining event rate

Isotopes	Rate [/day/kton$_{\mathrm{LS}}$]		
	BeforePurif	*SolarPhase*	*AfterZen*
^{12}N	$< 10^{-6}$	$< 10^{-6}$	$< 10^{-5}$
^{12}B	0 ± 0.01	0.006 ± 0.008	0.008 ± 0.014
^{8}He	0 ± 0.005	0 ± 0.005	0 ± 0.016
^{9}C	0.001 ± 0.005	0.001 ± 0.010	0 ± 0.011
^{9}Li	0.001 ± 0.018	0.017 ± 0.025	0.02 ± 0.032
^{8}B	0.002 ± 0.020	0.013 ± 0.042	0 ± 0.086
^{6}He	0.02 ± 0.086	0.16 ± 0.21	0.13 ± 0.23
^{8}Li	0 ± 0.19	0.36 ± 0.37	0.35 ± 0.34
^{11}Be	0.09 ± 0.07	0.05 ± 0.059	0.03 ± 0.052
^{10}C	1.01 ± 0.64	0.93 ± 0.84	0 ± 0.099

Table 5.6: Summary of the spallation cut related deadtime

Period	Deadtime ratio [%]				
	150 ms veto only	*n-tag* only	*shower-tag* only	*n-tag* + *shower-tag*	*n-tag* + *shower-tag* + 150 ms veto
BeforePurif	4.98	6.24	7.28	12.9	17.2
SolarPhase	4.88	5.32	8.72	13.1	17.3
AfterZen	4.66	4.79	8.81	12.6	16.7

5.6.4 Comparison with the Previous Study

In the previous study of ^{8}B solar neutrino measurement using KamLAND [48], the remaining event rates and deadtime ratio were estimated as follows:

- ^{8}Li: 0.29 ± 0.057 /day/kton
- ^{11}Be: 1.17 ± 0.25 /day/kton
- Deadtime ratio: 37.6%

BeforePurif corresponds to the period used in Ref. [48]. The improvements with the new rejection method are as follows:

- ^{11}Be reduction ($\sim 90\%$)
- The scale of the uncertainty (~ 0.2 /day/kton) kept same
- 20% less deadtime ratio

6 Thorium Series Background Reduction

Descendants of ^{232}Th, mainly ^{208}Tl and ^{212}Bi(–^{212}Po), are backgrounds for underground low-background experiments. Figure 6.1 shows the decay chain of ^{232}Th series.

Commonly used delayed coincidence methods and their problems are as follows:

- ^{212}Bi ($Q_\alpha = 6.21$ MeV)–^{208}Tl ($Q_\beta = 5.00$ MeV, $\tau = 4.40$ min)
  - Problem: Long coincidence window (~ 20 min) and low prompt energy ($E_{\rm vis} \sim 0.35$ MeV) make efficient veto difficult.
- ^{212}Bi ($Q_\beta = 2.25$ MeV)–^{212}Po ($Q_\alpha = 8.95$ MeV, $\tau = 431$ ns)
  - Problem: They become a pile-up event when ^{212}Po decays earlier than the timing resolution of the detector (~ 20 ns).

In this chapter, I introduce a new delayed coincidence method which uses ^{220}Rn–^{216}Po events. I call it *Day-scale* tag. I consider a combination of *Day-scale* tag and Bi–Tl tag to reduce the ^{208}Tl backgrounds in the solar neutrino analysis of this thesis.

6.1 Event Rate in KamLAND

The event rate of ^{232}Th series isotopes can be easily estimated using the ^{212}Bi–^{212}Po coincidence. The selection is as follows:

- $r_{\rm prompt} < 3.5$ m
- Prompt energy $E_p (= E_{\rm Bi})$: $1.0 < E_p < 2.5$ MeV

  Selection efficiency: 45% (29% when the 64% branching ratio included)
- Delayed energy $E_d (= E_{\rm Po})$: $0.5 < E_d < 1.0$ MeV

  Selection efficiency: 100%
- Time difference from the prompt to the delayed dT: $0.4 < dT < 2.5$ μs (fit range)
- Spatial difference from the prompt to the delayed dR: $dR < 2$ m

  Selection efficiency: 100%

Figure 6.2 shows the distribution of the coincidence-related parameters of *SolarPhase*. The accidental events in longer dT are due to ^{214}Bi–^{214}Po ($\tau = 237$ μs) coincidence. From the dT fitting (fit range $0.5 < dT < 10$ μs), the rate can be estimated. The results for *SolarPhase* and *AfterZen* are summarized in Table 6.1.

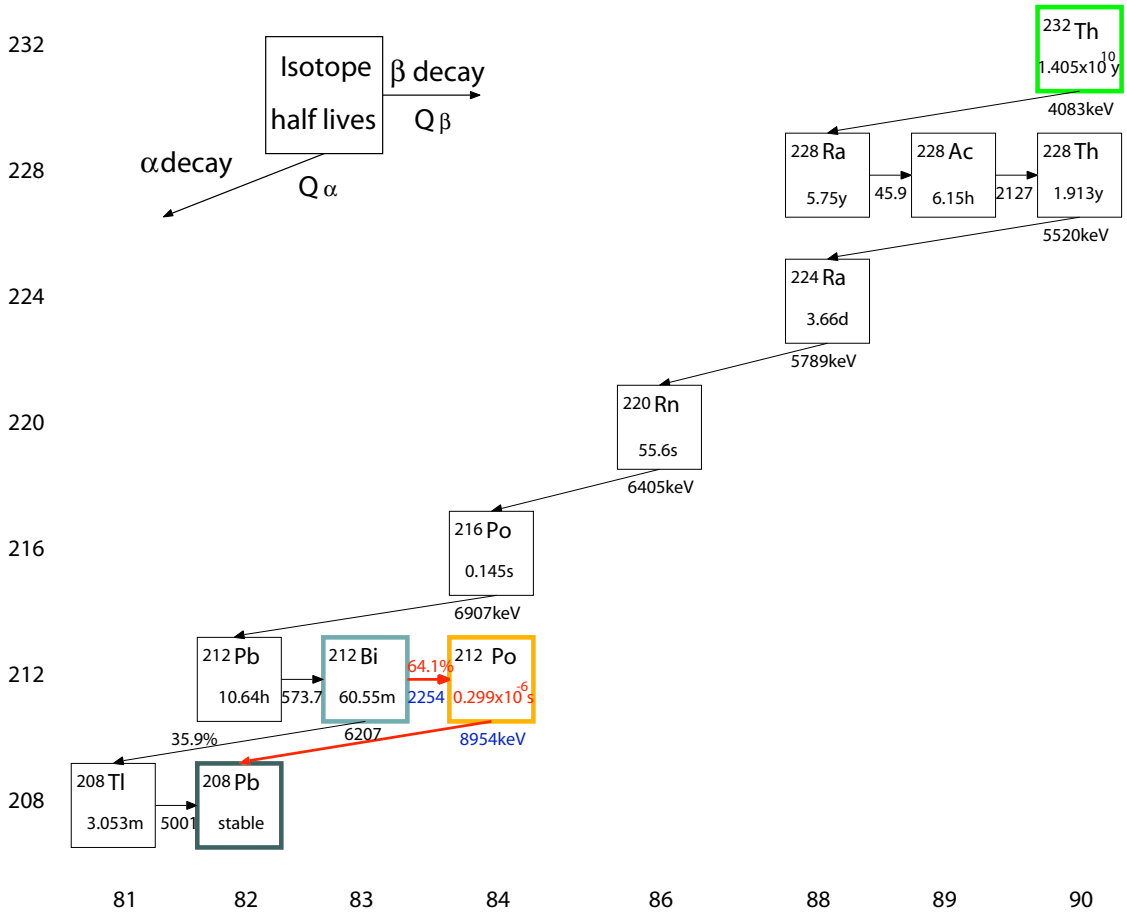

Figure 6.1: Decay chain of ^{232}Th series. Figure from [64].

Table 6.1: Th series rate in KamLAND. Only ^{212}Bi–^{212}Po rate is actually measured. Others are estimated based on the branching ratio and assuming radioactive equilibrium.

Period	^{212}Bi–^{212}Po rate [/day/kton$_{\mathrm{LS}}$]	^{212}Bi–^{208}Tl rate [/day/kton$_{\mathrm{LS}}$]	Total rate [/day/kton$_{\mathrm{LS}}$]	^{232}Th concentration [$\times 10^{-17}$ g/g$_{\mathrm{LS}}$]
SolarPhase	3.54 ± 0.57	(1.98 ± 0.32)	(5.52 ± 0.88)	(1.56 ± 0.25)
AfterZen	3.72 ± 0.65	(2.08 ± 0.37)	(5.80 ± 1.02)	(1.64 ± 0.29)

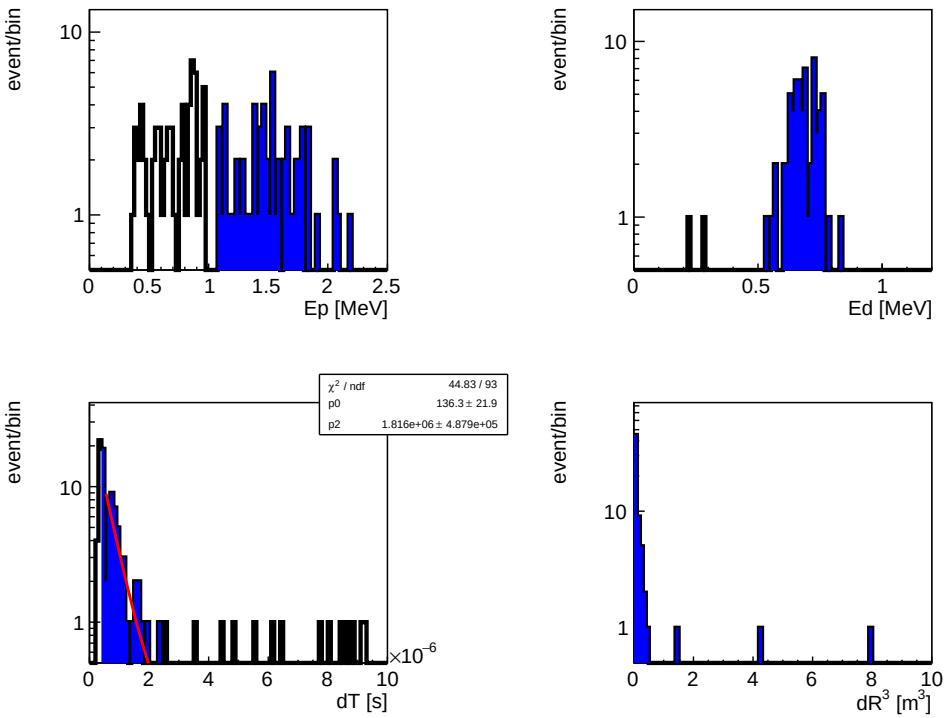

Figure 6.2: ^{212}Bi–^{212}Po coincidence parameters (*SolarPhase*). Black lines show the events with the selections to other parameters applied. Blue filled regions show the selections for the parameter.

6.1.1 Comparison With the Solar Neutrino Rate

The expected ^{8}B solar neutrino event rate around $E_{\rm vis} = 3$ MeV is ~ 0.5 /day/kton/MeV.

^{212}Bi–^{212}Po

The rejection efficiency of ^{212}Bi–^{212}Po is 95% with a dT resolution limit of 20 ns. With an energy selection ($E_{\rm vis} > 2$ MeV), the remaining rate of the BiPo pile-up event ($dT < 20$ ns) would be ~ 0.1 /day/kton. This is not so problematic.

^{208}Tl

Rejection of the ^{208}Tl is not easy and it is the theme of this chapter. The raw rate (~ 2 /day/kton) is a factor of 2–3 higher than the solar neutrino rate. This needs to be removed.

6.2 Day-scale Tag

Brief summary of the *Day-scale* tag is as follows:

1. Search for a pair of ^{220}Rn ($Q_\alpha = 6.41$ MeV)–^{216}Po ($Q_\alpha = 6.91$ MeV, $\tau = 0.21$ s) (*PromptCoincidence* [*PC*] with a time window of ~ 1 s)
2. Open a time window of ~ 2 days

   It is difficult to tag ^{212}Pb ($Q_\beta = 0.57$ MeV, 15.4 h). ^{212}Pb is just ignored.
3. Search for ^{208}Tl or ^{212}Bi near the *PromptCoincidence* vertex

Compared to the common methods, *Day-scale* tag has the following strengths:

- to ^{212}Bi–^{208}Tl

  Alpha particles from ^{220}Rn and ^{216}Po have higher energy than one from ^{212}Bi. *PC* can reduce accidental backgrounds.
- to ^{212}Bi–^{212}Po

  The timing resolution of the detector doesn't matter.

6.2.1 Prompt Coincidence (^{220}Rn–^{216}Po)

The *PC* can be purely selected with the following condition (see blue-filled histograms of Figure 6.3):

- *SolarPhase* data

  ($dT_{\rm fromMuon} > 2$ ms, Short [<3 ms] delayed coincidence vetoed)
- $r_{p,d} < 5$ m
- $0.38 < E_p (= E_{\rm vis}^{\rm Rn}) < 0.5$ MeV

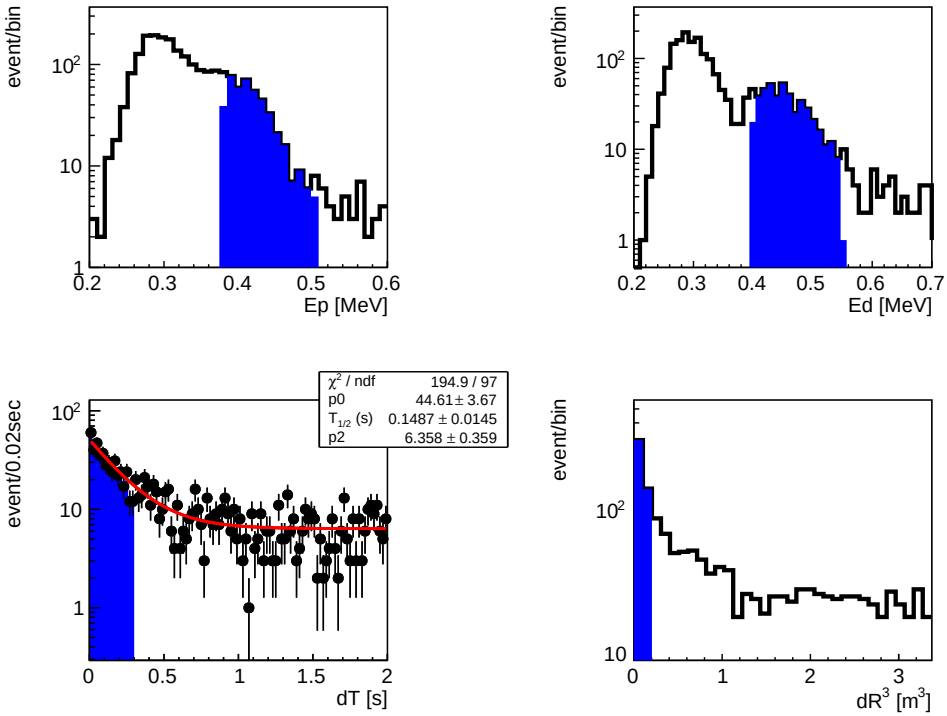

Figure 6.3: N - 1 plot of *PC*. Black lines (points) show the events with the selections to other parameters applied.

- $0.4 < E_d (= E_{\text{vis}}^{\text{Po}}) < 0.55$ MeV
- $dR^3_{\text{Rn-Po}} < 0.2$ m^3
- ontime: $0 < dT_{\text{Rn-Po}} < 0.3$ s (offtime: $1 < dT_{\text{Rn-Po}} < 2$ s)

The dT distribution in Figure 6.3 (bottom left) agrees with the decay curve with the half-life of ^{216}Po.

Figure 6.4 shows ontime, offtime, and subtracted (ontime - offtime) spectra of E_p, E_d, and dR. The visible energies were evaluated by gaussian-fittings. The lower limit of the fit range was set to 0.35 MeV to avoid the threshold effect. The best-fit mean values are as follows:

- ^{220}Rn: 0.384 ± 0.004 MeV
- ^{216}Po: 0.439 ± 0.003 MeV

The dR distribution was fitted with a exponentially-modified-gaussian (EMG),

$$f(dR;\mu,\tau,\sigma) = \frac{1}{2\tau}\exp\left(\frac{1}{2}\left(\frac{\sigma}{\tau}\right)^2 - \frac{dR-\mu}{\tau}\right)\text{Erfc}\left(\frac{\mu+\frac{\sigma^2}{\tau}-dR}{\sqrt{2}\sigma}\right). \tag{6.83}$$

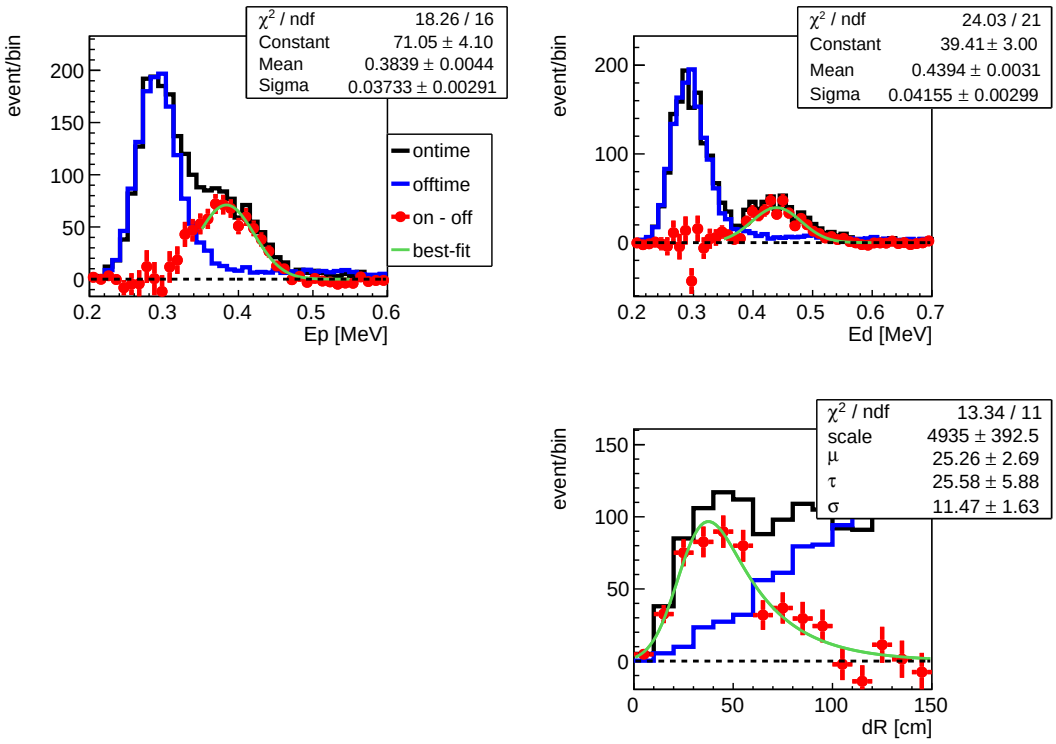

Figure 6.4: Ontime, offtime, and subtracted spectra of E_p, E_d, and dR of PC.

6.2.2 Proof of Concept Using ^{212}Bi–^{212}Po

^{212}Bi–^{212}Po events can be purely tagged thanks to the short life time of ^{212}Po. Therefore it is suitable for studying the *Day-scale* tag. Figure 6.5 shows the *Day-scale* coincidence candidates. For the calculation of the distance between PC and BiPo, energy-weighted vertices were used as follows:

$$\boldsymbol{x}_{\text{PC}} = \frac{E_{\text{Rn-220}}\boldsymbol{x}_{\text{Rn-220}} + E_{\text{Po-216}}\boldsymbol{x}_{\text{Po-216}}}{E_{\text{Rn-220}} + E_{\text{Po-216}}} \tag{6.84}$$

$$\boldsymbol{x}_{\text{Bi-212Po-212}} = \frac{E_{\text{Bi-212}}\boldsymbol{x}_{\text{Bi-212}} + E_{\text{Po-212}}\boldsymbol{x}_{\text{Po-212}}}{E_{\text{Bi-212}} + E_{\text{Po-212}}} \tag{6.85}$$

$$dR_{\text{PC-BiPo}} = |\boldsymbol{x}_{\text{PC}} - \boldsymbol{x}_{\text{Bi-212Po-212}}| \tag{6.86}$$

The events are clearly clustering at shorter dT and dR region. The dT distribution was fitted with a sequential-decay model,

$$f(dT) = N_0 \frac{1/\tau_{\text{Pb-212}}}{1/\tau_{\text{Bi-212}} - 1/\tau_{\text{Pb-212}}} \left(\exp\left(-\frac{dT}{\tau_{\text{Pb-212}}}\right) - \exp\left(-\frac{dT}{\tau_{\text{Bi-212}}}\right) \right) + \text{const}, \tag{6.87}$$

and the best-fit half-lives ($T_{1/2}^{\text{Pb-212}} = 11.9 \pm 2.7$ h, $T_{1/2}^{\text{Bi-212}} = 0.76 \pm 0.71$ h) agree with known values.

6.2.3 Convection

Sometimes convection happens in KamLAND due to changes in OD water-flow condition. The dR correlation may get worse when the convection happens. The missing-coincidence

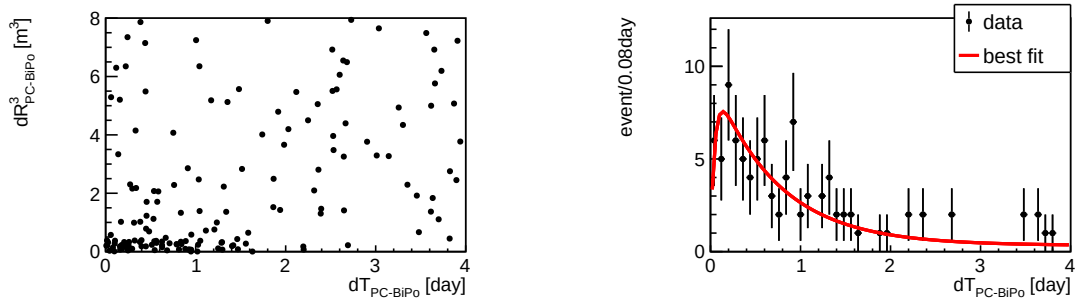

Figure 6.5: Candidates of PC–^{212}Bi^{212}Po. (Left): Space-time correlation. (Right): dT distribution ($dR^3 < 2$ m^3). Selections: $0.37 < E_{\text{Rn-220}} < 0.6$ MeV, $0.4 < E_{\text{Po-216}} < 0.6$ MeV, $dR^3_{\text{Rn-220ToPo-216}} < 0.2$ m^3, $dT_{\text{Rn-220ToPo-216}} < 1.0$ s, $0.45 < E_{\text{Bi-212}} < 2.5$ MeV, $0.7 < E_{\text{Po-212}} < 1.0$ MeV, $dR_{\text{Bi-212ToPo-212}} < 2$ m, $0.4 < dT_{\text{Bi-212ToPo-212}} < 2.5$ μs.

ratio was evaluated using *SolarPhase* data ($r < 5$ m) in the following method [68]:

1. Count PC events
2. Count PC–BiPo and PC–Tl events ($dR_{\text{PC-BiPo(Tl)}} < 1.26$ m)
3. Compare (1) vs (2)

The estimated missing-coincidence ratio were as follows:

- PC–BiPo: $(6 \pm 14)\%$
- PC–Tl: $(12 \pm 15)\%$

From these results, the combined upper limit was obtained as $< 22\%$ (90%C.L.).

6.2.4 dR Distribution

The dR distribution of PC–^{208}Tl was derived by an ontime-minus-offtime subtraction and evaluated with an EMG model, see Figure 6.6. The result will be used in the construction of a likelihood model later.

6.3 ^{212}Bi–^{208}Tl Coincidence

Utilization of the ^{212}Bi(α)–^{208}Tl coincidence for a solar neutrino analysis in KamLAND was first tried in Ref. [101]. However, due to the low statistics available at that time (only first 130 days of *SolarPhase*), the coincidence itself wasn't clearly observed.

Here I present the clear signals using entire *SolarPhase* data. The selection is as follows (see Figure 6.7):

- *SolarPhase* data

  ($dT_{\text{fromMuon}} > 2$ ms, Short [<3 ms] delayed coincidence vetoed)

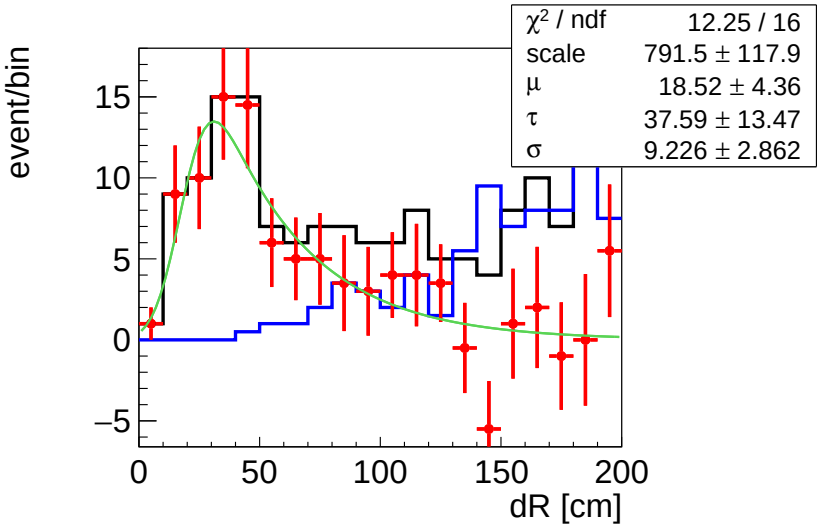

Figure 6.6: Distance from PC to Tl. The black line is ontime ($0 < dT < 2.5$ d), the blue line is offtime ($2.5 < dT < 7.5$ d) and the red point is the subtracted.

- $r_{p,d} < 5$ m
- $0.37 < E_p (= E_{\text{vis}}^{\text{Bi}}) < 0.45$ MeV
- $3.5 < E_d (= E_{\text{vis}}^{\text{Tl}}) < 4.5$ MeV
- $dR^3_{\text{Bi-Tl}} < 0.1$ m^3
- Ontime: $0 < dT_{\text{Bi-Tl}} < 300$ s (Offtime: $1500 < dT_{\text{Bi-Tl}} < 6000$ s)

The half-life estimated from the dT decay curve agrees with the known one of ^{208}Tl.

The on-minus-off subtraction histograms for E_p, E_d, dR are shown in Figure 6.8. Peaks in the E_p (E_{Bi}) and E_d (E_{Tl}) are significant in the subtracted histograms. A gaussian fit to the E_p yielded the following results:

- Mean: 0.393 ± 0.006 MeV
- Sigma: 0.033 ± 0.005 MeV

The dR distribution was fitted with an EMG in the same way with the PC's case.

6.4 ^{210}Po Accidental Background

Visible energies of alpha particles from ^{220}Rn, ^{216}Po, and ^{212}Bi are 0.3–0.4 MeV. The energy resolution around this energy region is ~ 0.04 MeV. Thus decays of ^{210}Po ($Q_\alpha = 5.41$ MeV, $E_{\text{vis}} \sim 0.3$ MeV) in the LS become accidental backgrounds for them, see the peaks in offtime spectra of E_p and E_d of Figure 6.4.

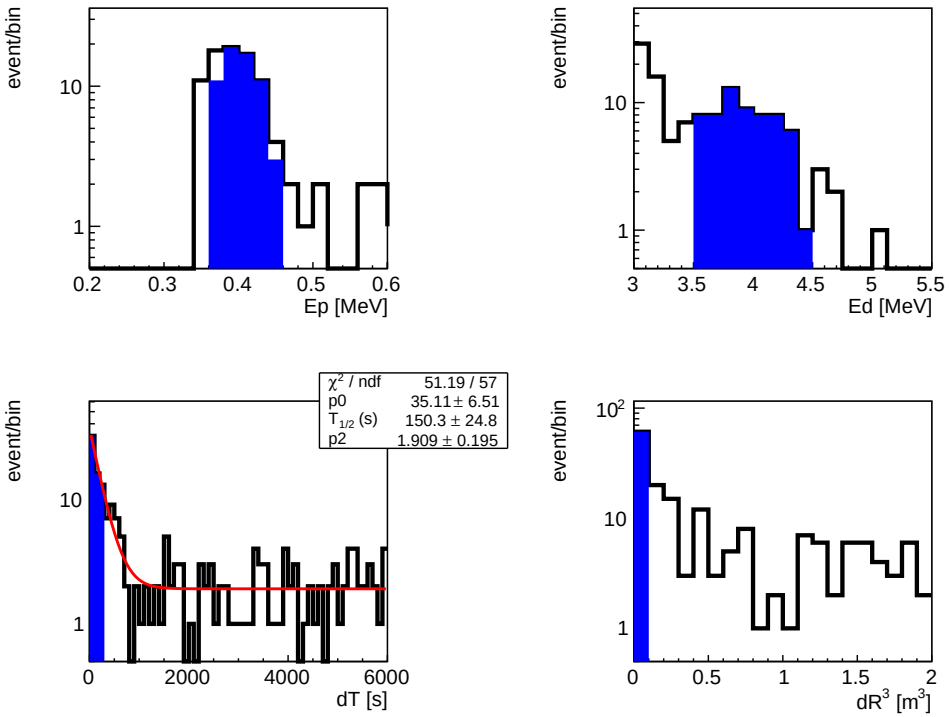

Figure 6.7: Selection of ^{212}Bi–^{208}Tl coincidence candidates

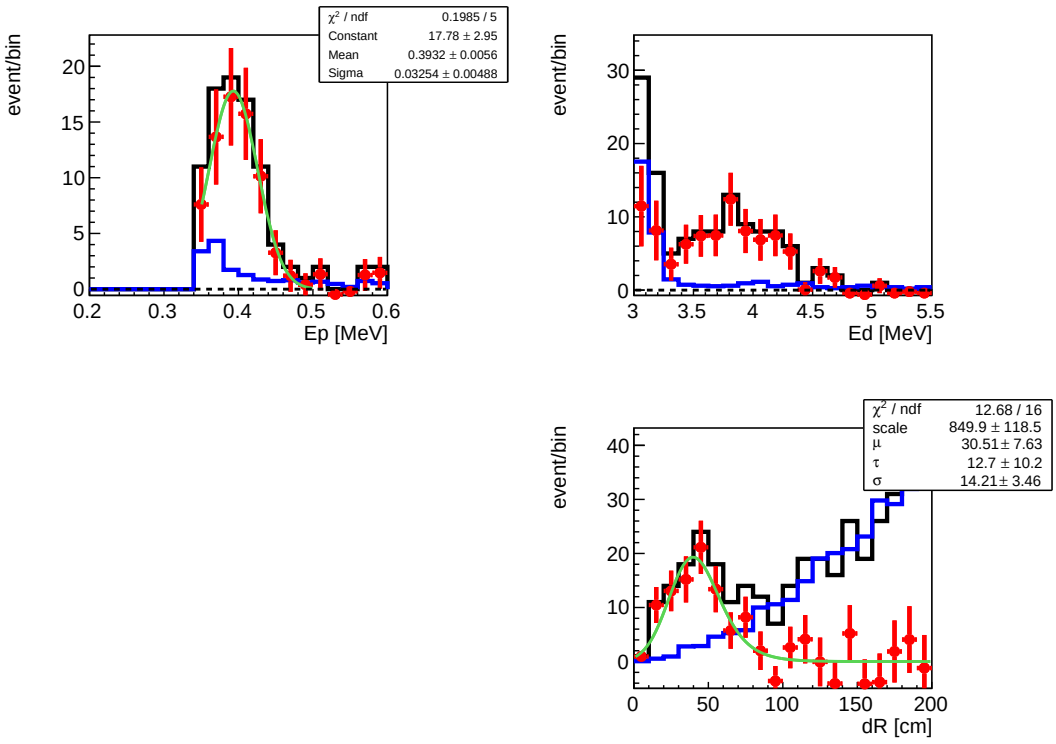

Figure 6.8: Ontime-minus-offtime subtracted distributions of Bi–Tl candidates. The black lines are ontime, blue lines are offtime and red points are the subtracted events.

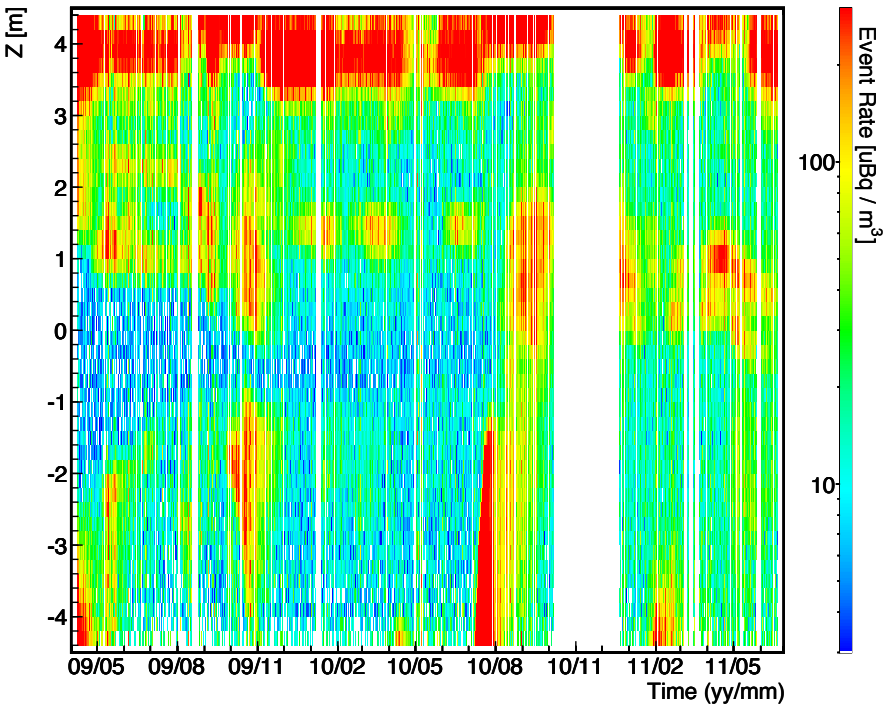

Figure 6.9: Position and time dependence of the rate of events with energy of 0.5–0.8 MeV (mainly ^{210}Bi, a parent of ^{210}Po). Radius selection is $r < 4.5$ m. Figure from [57].

The rate of ^{210}Po in KamLAND was decreased by a factor of >10 by the purification campaign (see Section 3.5.3). In *SolarPhase*, it ranged from 10 to 1000 μBq/m^3 depending on the time and position (see Figure 6.9). Convection in the KamLAND brings contamination from the outer-balloon surface to the inside of the detector.

As can be seen from the following comparison, *Day-scale* tag is $\mathcal{O}$(10–1000) times more resilient to the ^{210}Po accidental background than Bi–Tl tag.

Impact on ^{212}Bi–^{208}Tl

Given the ^{210}Po rate and assuming ^{210}Po is rejected by $\sim 50\%$ by an energy selection, the probability of observing one event within a time difference (dT) of 20 min and a spatial difference (dR) of 2 m from another event ranges from 20 to 2000%.

Impact on PC–^{208}Tl/^{212}Bi

In a similar way, the probability for the *PC* ($dT < 1$ s and $dR < 1$ m) is calculated as 0.00042–0.042%, where ^{210}Po rejection efficiencies were assumed as $\sim 50\%$ and $\sim 80\%$ for ^{220}Rn and ^{216}Po energy selections, respectively. Thus the accidental *PC* rate is 0.000042–0.42 μBq/m^3. Therefore the probability of finding an accidental *PC* with a selection ($dT_{\mathrm{fromPC}} < 2$ days and $dR_{\mathrm{fromPC}} < 2$ m) is 0.024–240%.

6.5 Background Reduction Strategy

I described *Day-scale* tag and BiTl tag in previous sections. From here, I consider a combination of the two methods. Ideally, for ^{208}Tl reduction, a 9-parameters likelihood can be prepared as

$$\mathcal{L}_{\mathrm{Tl}} = \mathcal{L}_{\mathrm{Day}}\mathcal{L}_{\mathrm{BiTl}},$$

where

$$\mathcal{L}_{\mathrm{Day}} = \mathcal{L}(E_{\text{Rn-220}})\mathcal{L}(E_{\text{Po-216}})\mathcal{L}(dT_{\mathrm{RnPo}})\mathcal{L}(dR_{\mathrm{RnPo}})\mathcal{L}(dT_{\text{PC-Tl(Bi)}})\mathcal{L}(dR_{\text{PC-Tl(Bi)}})$$

and

$$\mathcal{L}_{\mathrm{BiTl}} = \mathcal{L}(E_{\text{Bi-212}})\mathcal{L}(dT_{\mathrm{BiTl}})\mathcal{L}(dR_{\mathrm{BiTl}}).$$

However, the alpha ray signals (^{220}Rn, ^{216}Po, ^{212}Bi) are close to the trigger threshold. There is a possibility of the correlated loss of the events depending on the time and position dependence of the light yield. Therefore I will construct the new background reduction strategy in the following steps:

1. Optimize *Day-scale* tag
2. Optimize BiTl tag based on remaining events after *Day-scale* tag

6.5.1 Likelihoods

The PDFs of the energies, dT's and dR's of *Day-scale* tag and BiTl tag were already modeled in previous sections. The accidental PDF for the energies, which is mainly consists of ^{210}Po ($E_{\mathrm{vis}} \sim 0.3$ MeV peak) and ^{210}Bi (continuum up to $E_{\mathrm{vis}} \sim 1.1$ MeV), was

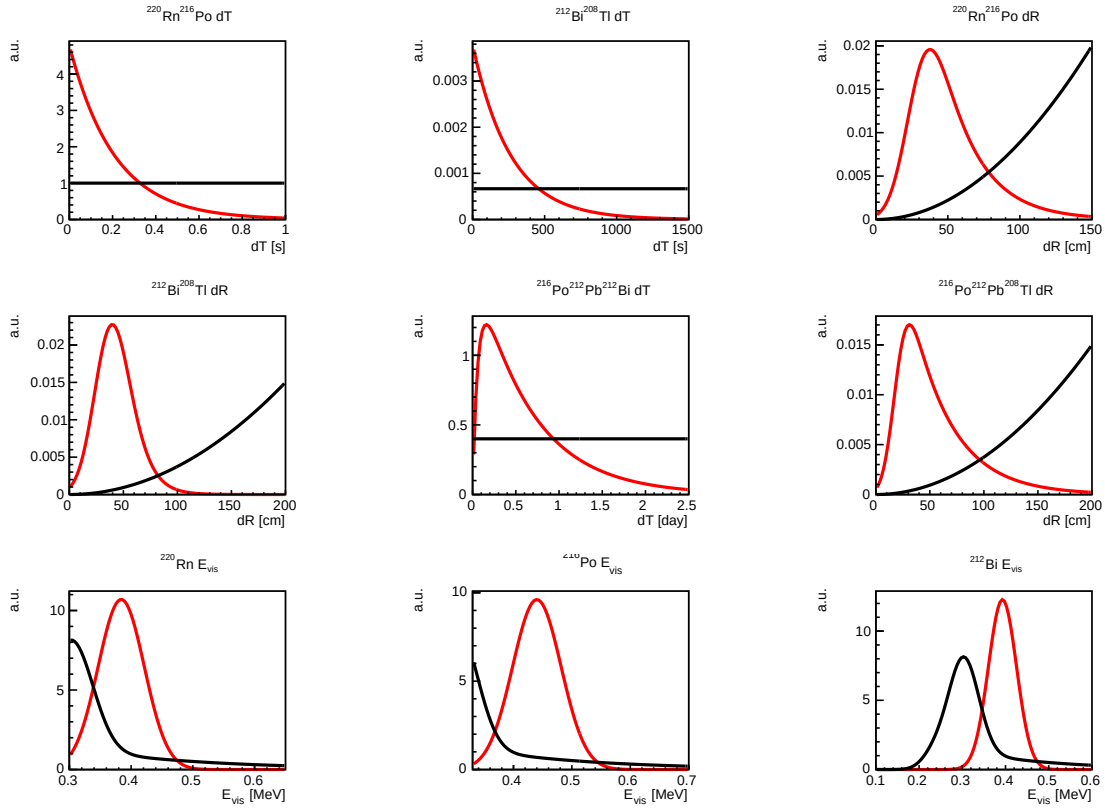

Figure 6.10: *Day-scale* tag and BiTl tag related PDFs. Red lines are for ^{232}Th series isotopes. Black lines are for accidental events.

Table 6.2: Maximum tagging efficiency

Period	Efficiency [%]	
	Day-scale tag	BiTl tag
SolarPhase	76 ± 15	84 ± 12
AfterZen	64 ± 14	43 ± 11

modeled with an EMG. The PDFs are summarized in Figure 6.10. For each parameter, the ratio of the likelihood

$$\mathcal{L}_{\text{ratio}} = \frac{\mathcal{L}_{\text{Th-series}}}{\mathcal{L}_{\text{accidental}}}$$

is used. $\mathcal{L}(dR_{\text{PC-BiPo}})$ and $\mathcal{L}(dR_{\text{PC-Tl}})$ are not the same in reality, however $\mathcal{L}(dR_{\text{PC-Tl}})$, which was estimated in Section 6.2.4, is used also as $\mathcal{L}(dR_{\text{PC-BiPo}})$ for simplicity.

Maximum Tagging Efficiency

Due to the trigger efficiency for low energy alpha ray events, > 1 hour detector deadtimes and the convection, *Day-scale* tag and BiTl tag can not reach 100% efficiency. The maximum efficiency for each tag was estimated by comparing the expected total number of events (from ^{212}Bi–^{212}Po) with the number of likelihood-tagged ^{208}Tl events. The results are summarized in Table 6.2.

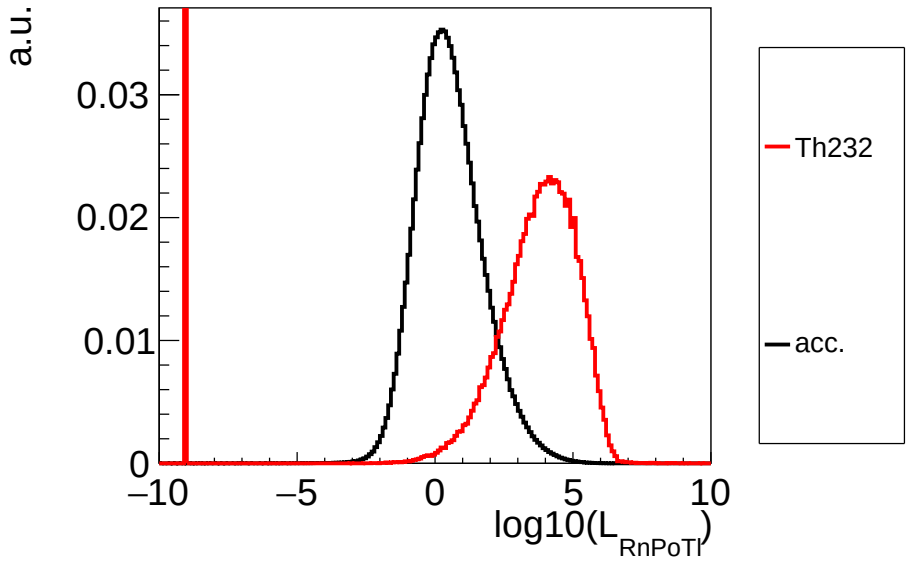

Figure 6.11: *PC*–Tl(Bi) likelihood ratio (*SolarPhase*). Red line is for ^{208}Tl and ^{212}Bi. Black line is for accidental events.

6.6 Determination of Likelihood Cut Thresholds

I determined likelihood cut thresholds in a similar way with the spallation likelihood case (see Section 5.2.7 and 5.6.2). As a signal, the solar neutrino rate at 2–5 MeV (2 /day/kton) was assumed. The irreducible component (= 1− MaximumTaggingEfficiency) was considered as very low likelihood events and the ^{232}Th likelihood was re-normalized. Figure 6.11 shows the likelihood distributions of ^{232}Th and accidental events.

The *Day-scale* tag optimization yielded the following results:

- *SolarPhase*
  - Cut condition: $\log_{10}(\mathcal{L}_{\mathrm{Day}}) > 2.4$
  - Tl (or Bi) tagging efficiency: 63%
    (83% of the maximum tagging efficiency)
  - Accidental tagging efficiency: 6.3%
- *AfterZen*
  - Cut condition: $\log_{10}(\mathcal{L}_{\mathrm{Day}}) > 2.7$
  - Tl (or Bi) tagging efficiency: 54%
    (84% of the maximum tagging efficiency)
  - Accidental tagging efficiency: 2.9%

Note that these efficiencies are derived just for optimization assuming the likelihood PDFs are perfect and using one arbitrary run for the accidental likelihood calculation. Precise estimations using the determined cut conditions will be shown later.

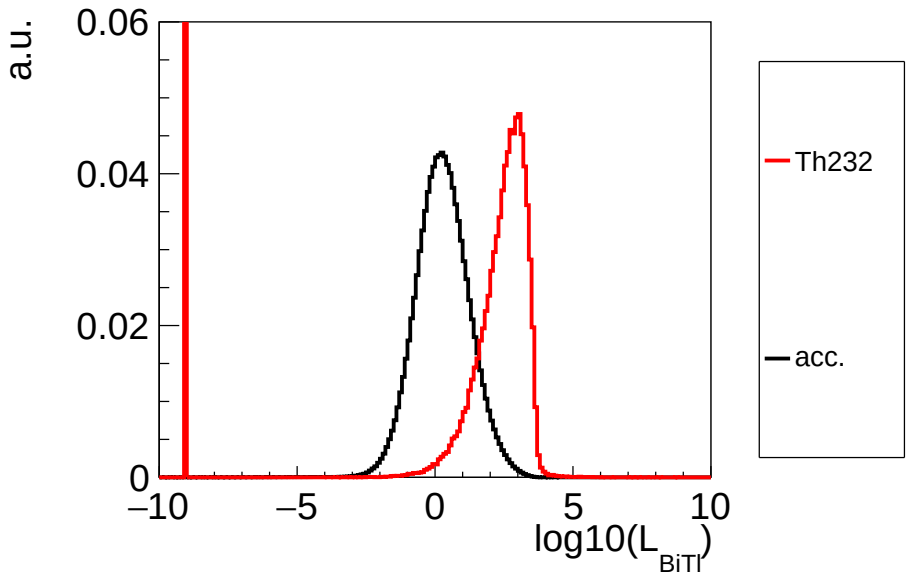

Figure 6.12: Bi–Tl likelihood ratio (*SolarPhase*). Red line is for ^{208}Tl. Black line is for accidental events.

In the BiTl tag optimization, the N_{bg} calculation was started from the value after *Day-scale* tag application. Figure 6.12 shows the likelihood ratio distributions for ^{208}Tl and accidental events.

The optimization results were as follows:

- *SolarPhase*
  - Cut condition: $\log_{10}(\mathcal{L}_{\mathrm{BiTl}}) > 1.92$
  - Tl tagging efficiency: 62%
    (75% of the maximum tagging efficiency)
  - Accidental tagging efficiency: 3.9%
- *AfterZen*
  - Cut condition: $\log_{10}(\mathcal{L}_{\mathrm{BiTl}}) > 2.3$
  - Tl tagging efficiency: 26%
    (60% of the maximum tagging efficiency)
  - Accidental tagging efficiency: 2.1%

6.7 Evaluation of the Cut Performance

6.7.1 Deadtime

The deadtime ratio for each cut was estimated using space-time uniform MC events and real ^{220}Rn, ^{216}Po, ^{212}Bi (α) candidates. The results are summarized in Table 6.3.

Table 6.3: Deadtime ratio of the thorium series tag. ($r < 3.5$ m).

Period	Deadtime ratio [%]		
	Day-scale tag	BiTl tag	*Day-scale* tag + BiTl tag
SolarPhase	4.7	7.2	11.5
AfterZen	2.7	3.4	5.9

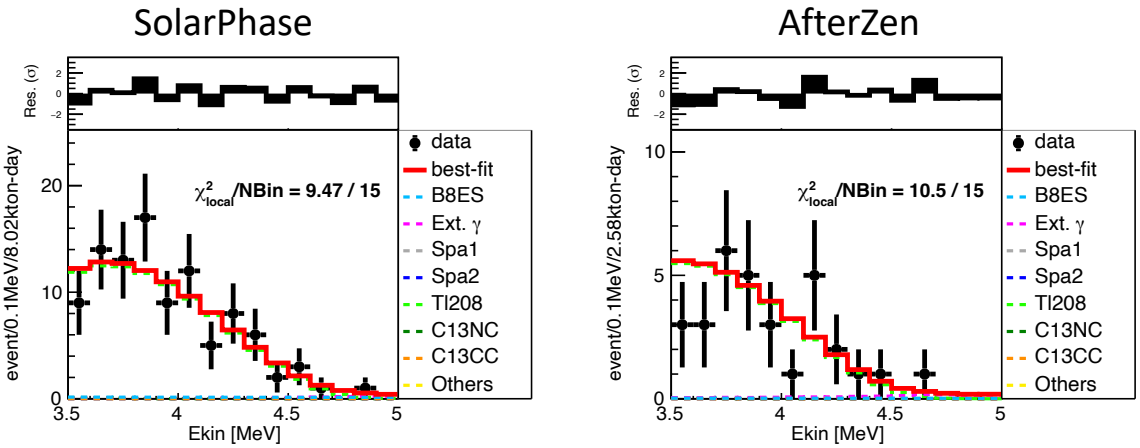

Figure 6.13: Energy spectrum of the final solar neutrino candidates but tagged with the thorium series likelihoods. Exposures are for the solar neutrino rate. Those for the Tl rate are 69.5 kton-day (*SolarPhase*) and 43.3 kton-day (*AfterZen*).

6.7.2 Tagging Efficiency

The tagged amounts were estimated by fitting the energy spectrum of the final solar neutrino candidates but flagged as Tl events. Figure 6.13 shows the example of events tagged with *Day-scale* tag or BiTl tag.

I evaluated the tagging efficiencies by comparing the tagged amounts with the evaluated rates before tagged. Table 6.4 shows the summary of the results. The mean values for *SolarPhase* are better than the ones assumed at the cut optimization. Those for *AfterZen* are almost same as the assumptions.

Table 6.4: Tagging efficiency of the thorium series tags ($r < 3.5$ m).

Period	Tagging efficiency [%]		
	Day-scale tag	BiTl tag	*Day-scale* tag + BiTl tag
SolarPhase	81 ± 17	67 ± 13	98 ± 19
AfterZen	49 ± 13	37 ± 10	63 ± 16

6.8 Remaining ^{212}Bi–^{212}Po Pileup

Day-scale tag efficiency should be higher for a ^{212}Bi–^{212}Po pileup because its reconstructed vertex isn't as widespread as ^{208}Tl due to lower energy of γ's. Thus assuming the same *Day-scale* tagging efficiencies as ^{208}Tl as the baseline and a micro-sec scale delayed coincidence tagging efficiency ($\Delta T > 20$ ns) of 95.5%, the remaining pileup event rates are:

- *SolarPhase*: 0.0303 ± 0.0275 /d/kt
- *AfterZen*: 0.0854 ± 0.0264 /d/kt

Considering the energy efficiency ($E_{\mathrm{Bi}} > 1.25$ MeV[1]) of 30%, these are negligible for the 2–3 MeV analysis of this work.

[1] To reach 2 MeV with a pileup event assuming $E_{\mathrm{vis}}^{\mathrm{Po}} \sim 0.75$ MeV

7 Selection of Single Events

7.1 Energy and Volume Selection

Considering impacts of external backgrounds, see 8.3, the following energy-dependent volume selections are applied:

- $2.0 < E_{\mathrm{kin}} < 3.5$ MeV: $r < 2.0$ m
- $3.5 < E_{\mathrm{kin}} < 5.0$ MeV: $r < 3.5$ m
- $5.0 < E_{\mathrm{kin}} < 20$ MeV: $r < 3.0$ m

7.2 Cuts

- Flasher event cut
  - Light emission from a PMT is called flasher. Such PMT (event) can be identified by monitoring its neighboring PMTs. See [100, Sec. 6.3.2] for the detailed cut condition.
- 100 μs veto after 1 pps trigger
  - Noises after 1-pps trigger is cut.
- 150 ms veto after a muon
  - Short-lived spallation products ($np\gamma$, ^{12}B, ^{12}N) are cut.
- Delayed coincidence veto
  - $\bar{\nu_e}$ (inverse β decay): $dT < 1$ ms, $dR < 2$ m
  - ^{214,212}Bi–^{214,212}Po: $dT < 1.9$ ms, $dR < 1.7$ m
- Pileup veto (Event separation limit $\Delta T > 20$ ns)
  - $^{214(212)}$Bi–$^{214(212)}$Po pileup events (in one event window) are cut. See [81, Sec. 7.3.2] for the detail.
- 150 ms veto after a trigger disable period
  - This is care for possible muons coming during trigger disable periods.
- 25 min veto after a long (> 1 s) deadtime
  - This ensures efficiencies of BiTl tag (25 min window) and *n-tag* (3 min window).
- Spallation products veto (*n-tag* and *shower-tag*)

- Th series veto (*Day-scale* tag and BiTl tag)
- Bad event cut
  - Based on the reference hit-and-charge pattern, *Badness(Goodness)* of an event is evaluated. *Bad* events are cut. Conditions are different among phases.
    - *BeforePurif*: Events with $\chi^2_{TQ} > 2$ are cut [101, Sec. 7.1]. Bad events in this period seem to be thermometer-related events.
    - *SolarPhase/AfterZen*: Events with

$$B > \begin{cases} 41.1\exp(-7.1E_{\mathrm{vis}}/\mathrm{MeV}) + 2.7 & (E_{\mathrm{vis}} < 5\mathrm{MeV}) \\ [3(\log_{10}(E_{\mathrm{vis}}/\mathrm{MeV}) - 0.6)]^2 + 2 & (E_{\mathrm{vis}} \geqq 5\mathrm{MeV}) \end{cases}$$

      are cut. Here B is *Badness* defined in [64, Sec. 6.2]. Accidental pileups of uncorrelated events are the cause of bad events [57, Sec. 6.4].

Signal inefficiencies from event-quality cuts (Pileup veto and Bad event cut) are $\mathcal{O}(0.1)\%$ and negligibly small as compared to fiducial volume uncertainties. Inefficiencies from other cuts are reflected to the livetime which is calculated by applying all other cuts to space-time uniform MC events. See 9.2 for the results.

8 Background Model and Estimation

Figure 8.1 shows the summary of backgrounds for ^{8}B solar ν ES signals in KamLAND. The 5 MeV analysis threshold for *BeforePurif* is due to ^{208}Tl and the 2 MeV threshold for *SolarPhase* and *AfterZen* is due to ^{11}C.

See Table 9.2, 9.3, 9.4 for the exact event rates after the all event selections.

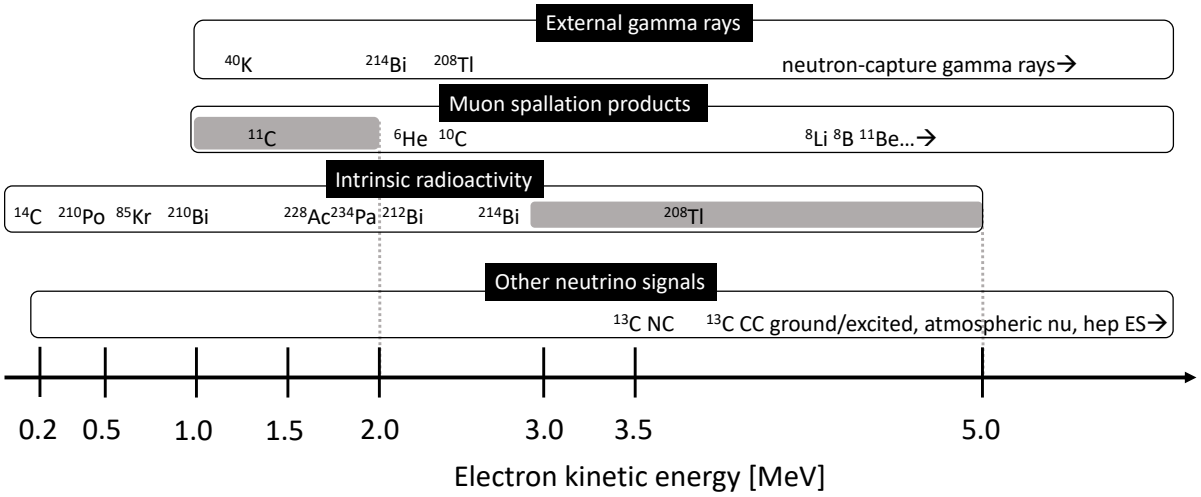

Figure 8.1: Summary of backgrounds for ^{8}B solar ν ES signals

8.1 Muon Spallation Products

Capture events of neutrons produced by muons (2.2 MeV γ) can be backgrounds in a single event analysis. However they can be easily removed by a 2-ms whole detector veto. Veto strategies for other short-lived ($\tau < 30$ s) spallation isotopes are discussed in Section 5. Figure 8.2 shows energy spectra of main spallation backgrounds before the application of reduction techniques.

8.1.1 ^{11}C

^{11}C ($Q_{\beta+} = 1.98$ MeV) has a long lifetime of $\tau = 29.4$ min. Its production rate in KamLAND was measured as (973 ± 10) /d/kt[51]. The spallation cuts (see Section 5) cover up to $\Delta T_{\mathrm{fromMuon}} = 180$ s. Therefore at most 10% of ^{11}C events may be rejected. Thus I estimated the remaining ^{11}C event rate from the side band (1.5–2 MeV) of energy spectrum.

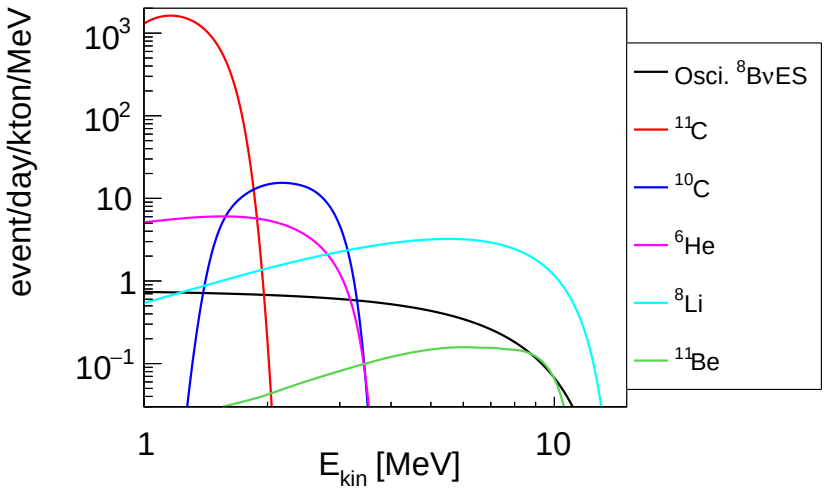

Figure 8.2: Energy spectra of main spallation backgrounds before the application of reduction techniques.

8.2 LS Intrinsic Radioactivity

8.2.1 ^{232}Th Series

^{212}Bi(^{212}Po) and ^{208}Tl

The event rate of ^{208}Tl in *BeforePuri* was estimated from the side band of the energy spectrum (3.5–5 MeV). See Section 6 for the estimation in *SolarPhase* and *AfterZen*. Figure 8.3 shows energy spectra of ^{208}Tl and ^{212}Bi–Po backgrounds (*SolarPhase*) before the application of reduction techniques.

^{228}Ac

We cannot expect secular equilibrium between ^{212}Bi and ^{228}Ac due to the relatively long lifetime of ^{228}Th. Therefore ^{228}Pa is just constrained from the single event energy spectrum below 2 MeV.

8.2.2 ^{238}U Series

^{214}Bi

The U concentration in the LS after the purification campaign estimated from ^{214}Bi is 5×10^{-18} g/g. This corresponds to a raw ^{214}Bi event rate of 5 /d/kt. The efficiency of ^{214}Bi–^{214}Po ($T_{1/2}$ = 164 ms) delayed-coincidence tagging is estimated to be more than 99.99% assuming the event separation time limit (ΔT = 20 ns). Therefore the rejection limit of ^{214}Bi is determined by the branching ratio to the ^{214}Po mode, 99.98%. The remaining ^{214}Bi (and ^{210}Tl [Q_β = 5.48 MeV]) rate 0.001 /d/kt is negligible for this solar neutrino analysis.

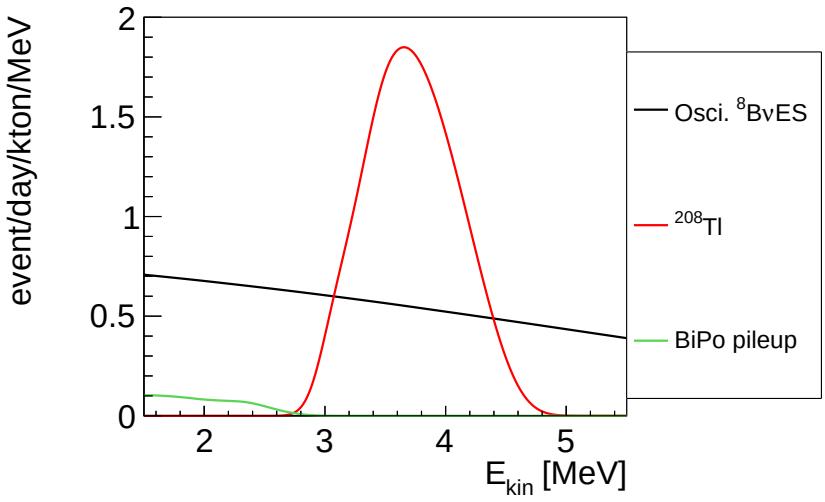

Figure 8.3: ^{208}Tl and ^{212}Bi–Po backgrounds (*SolarPhase*) before the application of reduction techniques.

^{234}Pa

We cannot expect secular equilibrium between ^{214}Bi and ^{234}Pa due to the long lifetime of ^{234}U, ^{230}Th, and ^{226}Ra. Therefore ^{234}Pa is just constrained from the single event energy spectrum below 2 MeV.

Figure 8.4 shows example energy spectra of ^{234}Pa and ^{228}Ac whose rates are set to 10 /d/kt.

8.3 External Backgrounds

8.3.1 Neutron Capture Gamma-rays

External backgrounds above 3 MeV are neutron capture γ's from the rock-wall and stainless steel supportings (vessel, deck, etc.). Their energy and vertex distribution were estimated by an MC simulation [101]. The uncertainty of the MC estimation was determined from the difference between the exponential curves of radial position distributions of the data and the MC at the outer-region ($r \sim 6$ m). I selected the analysis volumes to suppress the impact of the uncertainty to less than the statistical one as follows:

- 3.5–5 MeV: $r < 3.5$ m
- 5–20 MeV: $r < 3$ m

Expected event rates in the selected regions are ~ 0.03 /d/kt (3.5–5 MeV and $r < 3.5$ m) and ~ 0.15 /d/kt (5–20 MeV and $r < 3$ m).

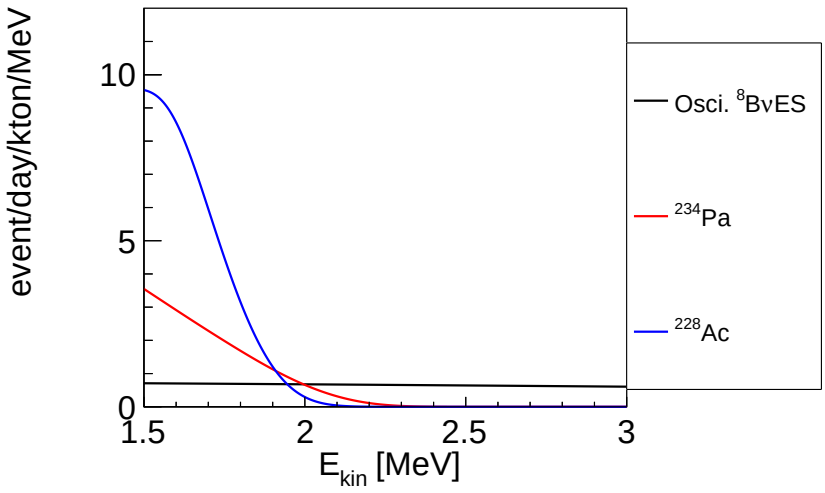

Figure 8.4: Energy spectra of ^{234}Pa and ^{228}Ac. Both event rates are set to 10 /d/kt just for a reference.

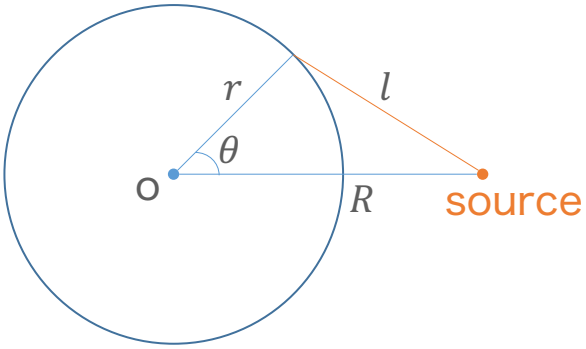

Figure 8.5: Parameters for the modeling of external γ's

8.3.2 Gamma-rays from U/Th Series

γ's from U/Th series isotopes (^{208}Tl and ^{214}Bi) from PMTs are dominant below 3 MeV region. The r-distribution was modeled with a single-scatter-and-disappear model as

$$\frac{dN}{dr} \propto 4\pi r^2 \int_0^\pi d\theta \frac{e^{-l/\lambda}}{4\pi l^2}, \tag{8.88}$$

$$l = \sqrt{R^2 + r^2 - 2Rr\cos\theta}, \tag{8.89}$$

where R is the position of PMTs (8.25 m), and λ is the attenuation length, see also Figure 8.5 for the notations.

The r-distribution of data ($0 < r < 5$ m) was fitted with the model (plus uniform component $\propto r^2$) energy by energy (0.1 MeV bin from 1.5 MeV to 3.5 MeV). Figure 8.6 shows the radial distribution of *SolarPhase* data. Attenuation length λ obtained from the fit almost agreed with the expectation of a mono-energetic γ-ray in a referential plastic scintillator at below 2.6 MeV, see Figure 8.7. At above 2.6 MeV, shorter λ was obtained because there are multiple γ's from ^{208}Tl (2.6 MeV + 0.51, 0.58, or 0.86 MeV).

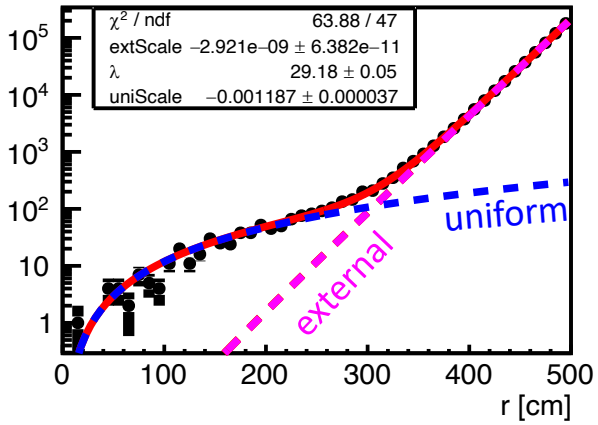

Figure 8.6: Radial distribution of events with energy of 2–3 MeV (*SolarPhase*).

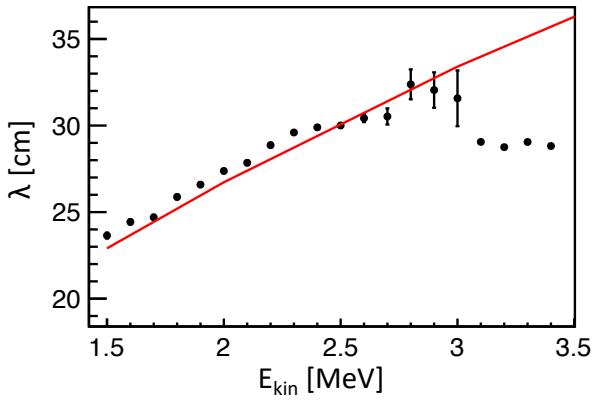

Figure 8.7: Fit results of the attenuation length λ in the model (8.88). Red line is a referential attenuation length of a γ-ray in a plastic scintillator (vinyltoluene-based) [102] with the same density as Outer-LS .

Under a fiducial volume selection of $r < 2$ m, the 1.5–3.5 MeV integrated event rate was ~ 0.4 /d/kton. The uncertainty of this estimation method was derived by comparing this model with a simple exponential model. When both models are normalized at $r = 5$ m region, the difference between them at $r = 2$ m becomes 20%, see Figure 8.8.

Figure 8.9 shows the estimated external background energy spectrum in each energy region.

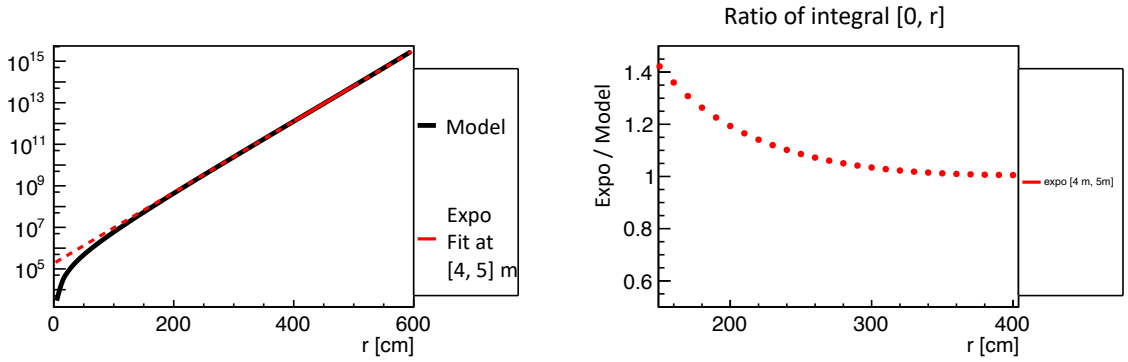

Figure 8.8: The single-scatter-and-disappear model vs simple exponential function.

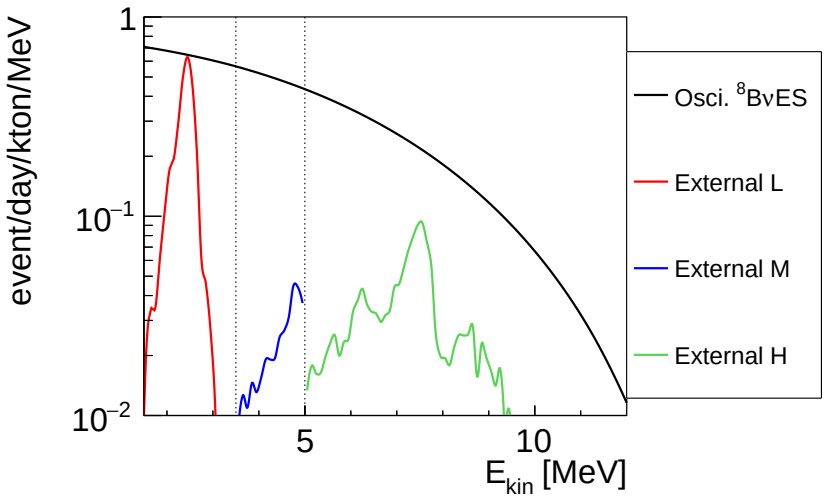

Figure 8.9: External γ-ray backgrounds in *SolarPhase*. Dotted lines show indicate different volume selections. $r < 2$ m ($E < 3.5$ MeV), $r < 3.5$ m ($3.5 < E < 5$ MeV), $r < 3$ m ($5 < E$ MeV).

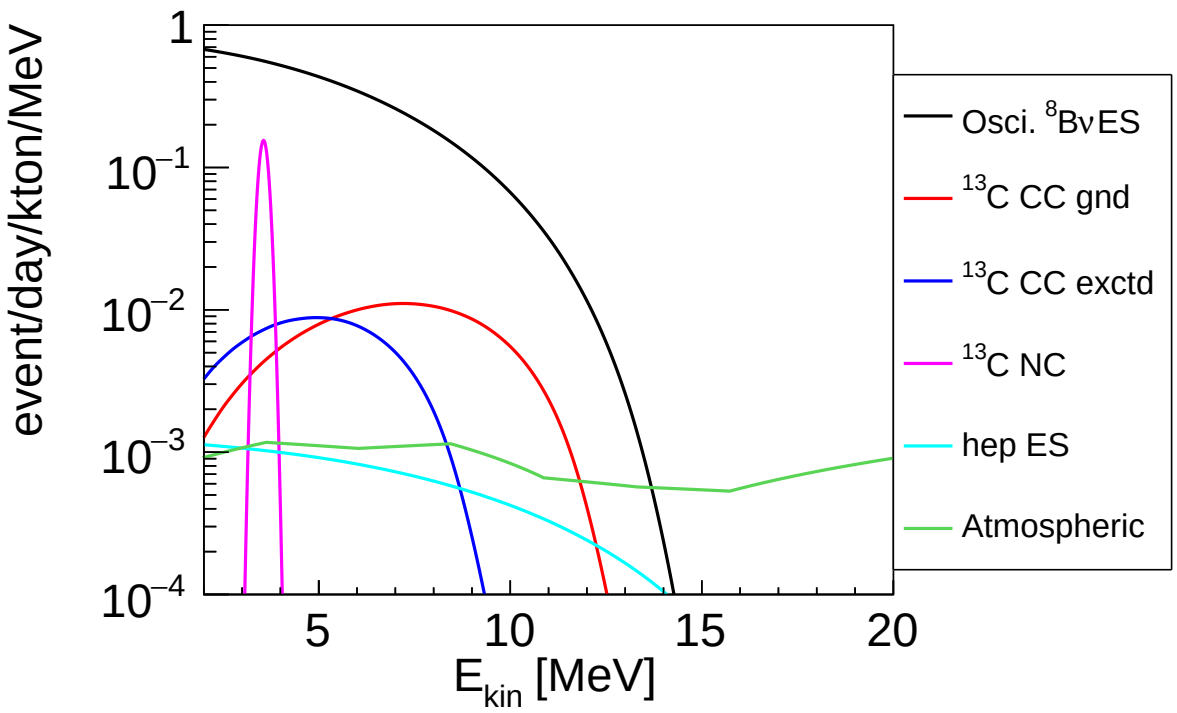

Figure 8.10: Energy spectra of ν-related backgrounds for ^{8}B ν ES measurement.

8.4 Neutrino Related Backgrounds

8.4.1 Solar Neutrino Events

Event rates of neutrino captures on ^{13}C (see Section 2.3.2) and *hep* ES are estimated with the following assumptions:

- the best-fit oscillation model ($\Delta m^2_{21} = 7.5 \times 10^{-5}$ eV^2, $\sin^2\theta_{12} = 0.306$) [38]
- total fluxes of BP2004 [103] ($\Phi_{\mathrm{B8}} = 5.82 \times 10^6$ /cm^2/s, $\Phi_{hep} = 7.88 \times 10^3$ /cm^2/s)
- ^{13}C reaction cross sections from Ref. [43]

8.4.2 Atmospheric Neutrinos

Single events from atmospheric ν's, mainly proton recoils (see Ref. [61, Sec. 9.2.6] for a general introduction), were estimated by an MC simulation.

Figure 8.10 shows the energy spectra of neutrino related backgrounds.

9 ^{8}B Solar Neutrino Analysis

In this chapter, I estimate the ^{8}B solar neutrino flux using the selected solar neutrino candidates. A rate-only analysis and a rate+shape (energy spectrum fitting) analysis are performed. The rate+shape analysis will be done with the following three types of ^{8}B solar neutrino spectra:

- Unoscillated spectrum (continuous over all energy)
- Unoscillated spectrum (divided into three regions [2–3, 3–5, 5–20 MeV])
- Oscillated spectrum (P_{ee} approximated with a quadratic function)

9.1 Expected Signal

The expected ^{8}B ν ES event rate is calculated assuming the following parameters:

- $\Delta m^2_{21} = 7.51 \times 10^{-5}$ eV^2, $\sin^2\theta_{12} = 0.306$ [38]
- Total flux: 5.25×10^6 /cm^2/s [19]

Figure 9.1 shows the expected spectrum in KamLAND. The rate in each energy region is as follows:

- 2–3 MeV: 0.64 /d/kt
- 3–5 MeV: 1.0 /d/kt
- 5–20 MeV: 1.2 /d/kt

Figure 9.2 shows the spectrum normalized by the unoscillated shape. The shape difference between the oscillated and unoscillated shapes in each energy region is as follows:

- 2–3 MeV: 2.6%
- 3–5 MeV: 4.5%
- 5–10 MeV: 6.5%

The scale difference between the best-fit oscillation and currently allowed flat P_{ee} model is $\sim 10\%$ at 2–5 MeV region.

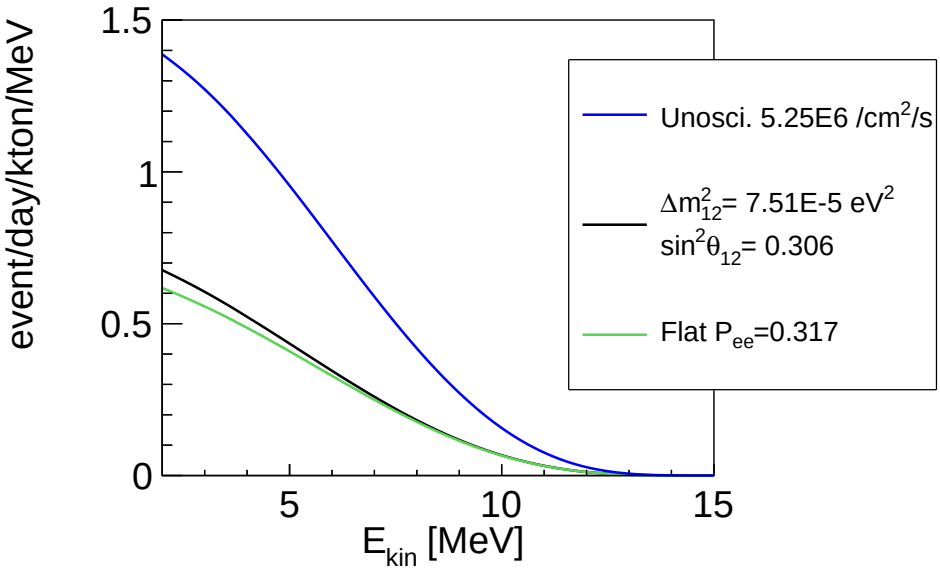

Figure 9.1: Expected ^{8}B ν ES spectrum in KamLAND.

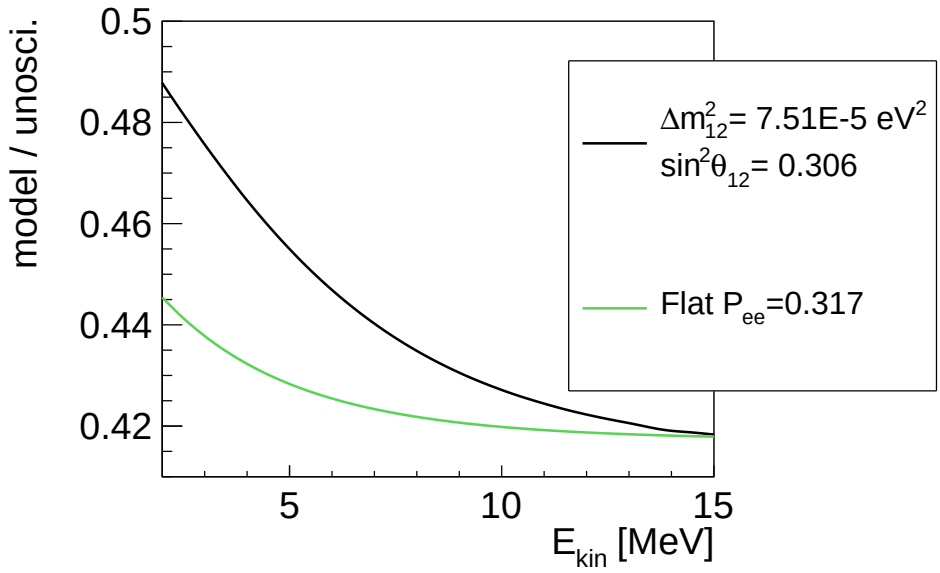

Figure 9.2: Expected ^{8}B ν ES spectrum in KamLAND normalized by the unoscillated shape.

Table 9.1: Number of observed events

Periods	2–3.5 MeV	3.5–5 MeV	5–20 MeV	Total
BeforePurif	-	-	183	183
SolarPhase	15	77	79	171
AfterZen	15	47	52	114
Total	30	124	314	468

9.2 Fiducial Volume and Livetime

- *BeforePuri*
  - $5 < E_{\mathrm{kin}} < 20$ MeV: $r < 3$ m, 88.2 ton, 1262 days (79% of runtime 1598 days)
- *SolarPhase*
  - $2 < E_{\mathrm{kin}} < 3.5$ MeV: $r < 2$ m, 29.4 ton, 447 days
  - $3.5 < E_{\mathrm{kin}} < 5$ MeV: $r < 3.5$ m, 153 ton, 441 days
  - $5 < E_{\mathrm{kin}} < 20$ MeV: $r < 3$ m, 88.2 ton, 443 days (70% of runtime 629 days)
- *AfterZen*
  - $2 < E_{\mathrm{kin}} < 3.5$ MeV: $r < 2$ m, 29.4 ton, 289 days
  - $3.5 < E_{\mathrm{kin}} < 5$ MeV: $r < 3.5$ m, 153 ton, 292 days
  - $5 < E_{\mathrm{kin}} < 20$ MeV: $r < 3$ m, 88.2 ton, 291 days (62% of runtime 467 days)[1]

9.3 Observed Events

Figure 9.3, 9.4, 9.5 show the observed events in each phase. Figure 9.6 shows the 3-phases combined histogram. It is just for visualization. The observed number of events are summarized in Table 9.1. In total, 468 events were observed in all energy and periods.

[1] MoGURA trouble periods are included to runtime and treated as deadtime.

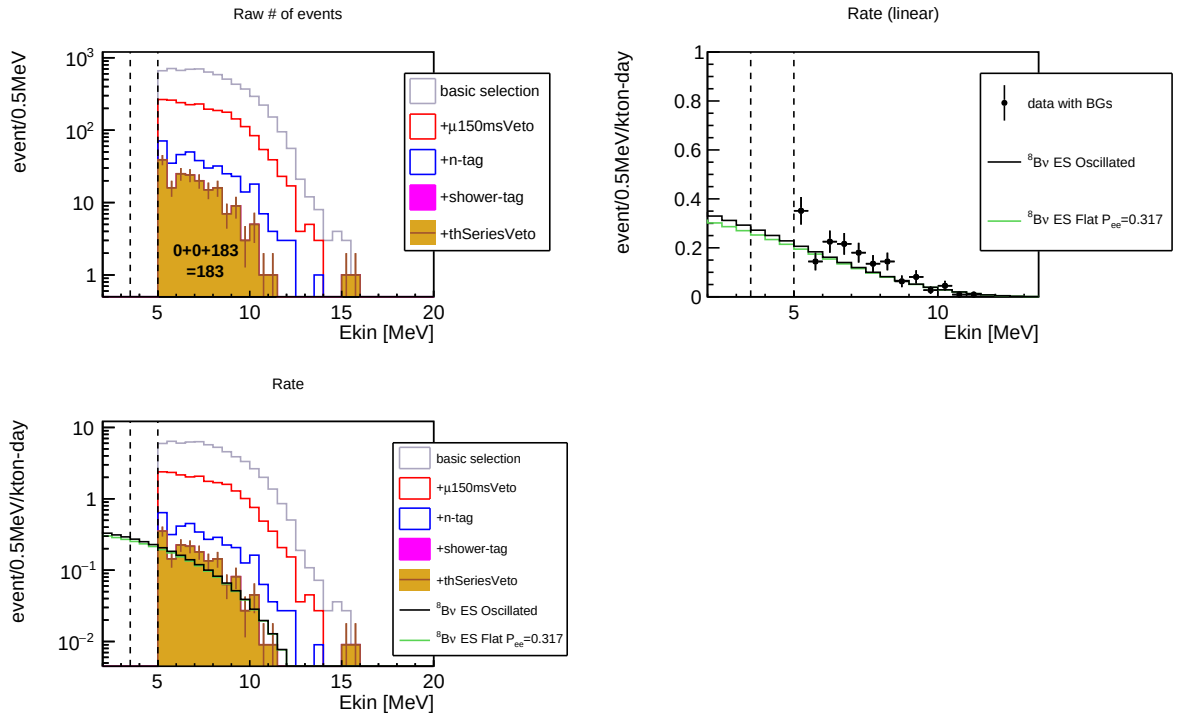

Figure 9.3: Event Reduction (*BeforePurif*).

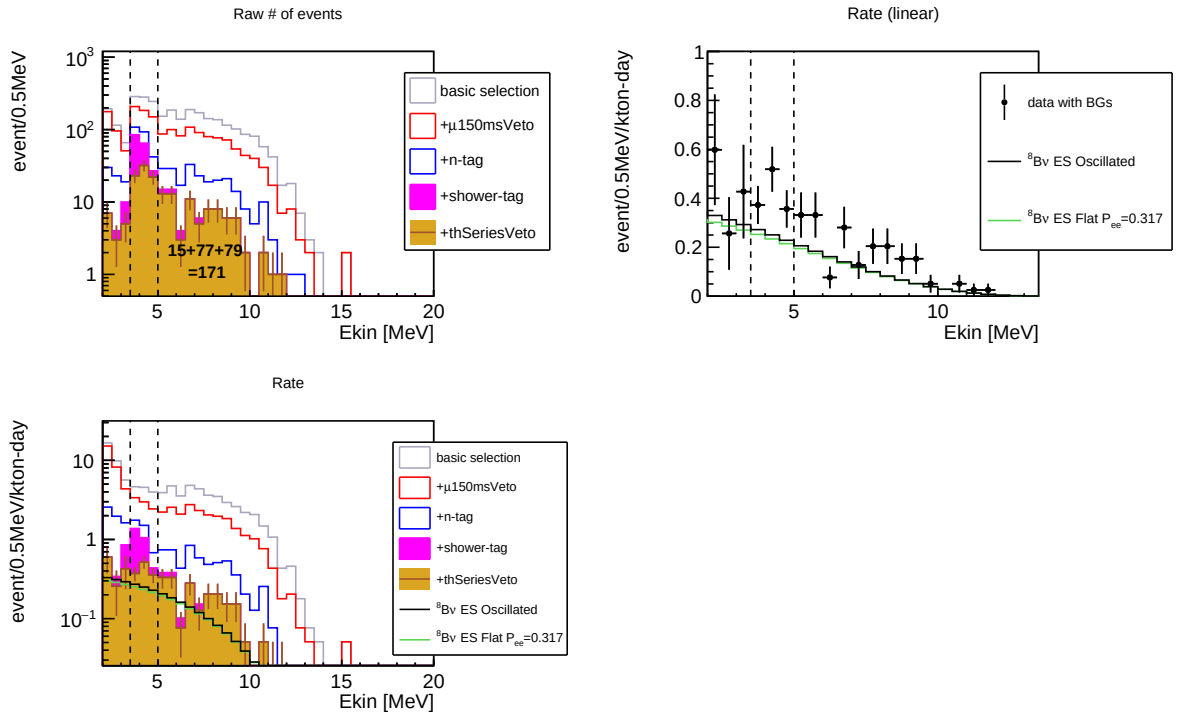

Figure 9.4: Event Reduction (*SolarPhase*).

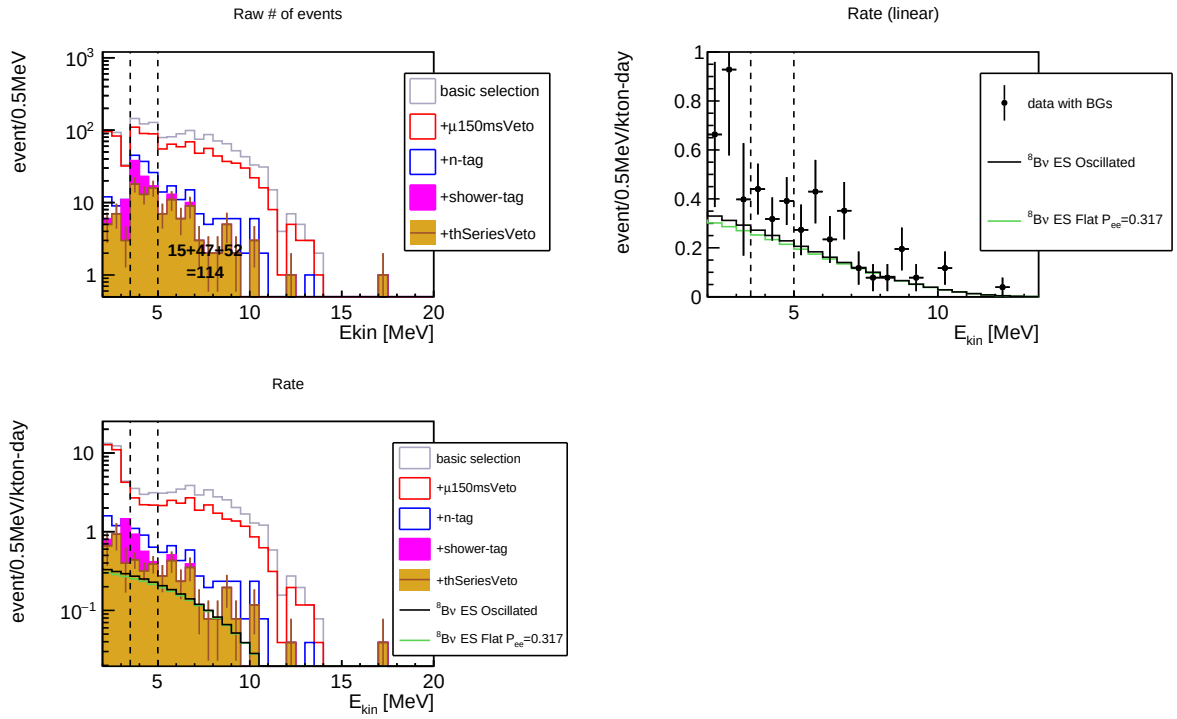

Figure 9.5: Event Reduction (*AfterZen*).

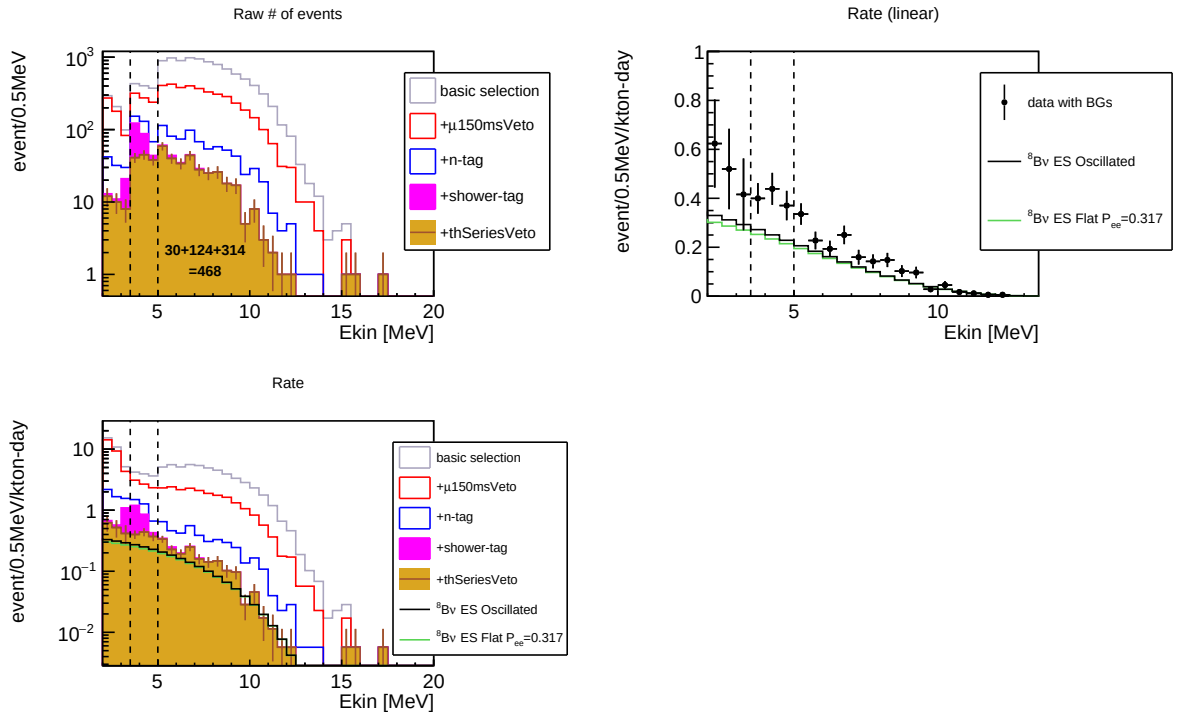

Figure 9.6: Event Reduction (3 phases combined).

9.4 Estimated Backgrounds

Table 9.2, 9.3, 9.4 show the summary of estimated backgrounds in each phase. Here *Ext* is the external γ BG, *Alpha* is the linear energy scale parameter and FV is the fiducial volume scale parameter.

Table 9.2: BG estimation (*BeforePurif*)

BGs	Estimation				
				unit	in fitting
Ext	1.00E+00	±	5.50E-01	(relative)	floated
Tl208	4.27E+01	±	1.93E+00	/day/kt	floated
SpaN12	4.50E-07	±	3.90E-07	/day/kt	fixed
SpaB12	9.85E-03	±	7.85E-04	/day/kt	fixed
SpaHe8	2.89E-03	±	4.33E-03	/day/kt	fixed
SpaC9	1.05E-02	±	7.57E-03	/day/kt	fixed
SpaLi9	2.78E-02	±	8.27E-03	/day/kt	fixed
SpaB8	1.24E-02	±	2.93E-02	/day/kt	floated
SpaLi8	0.00E+00	±	1.50E-01	/day/kt	floated
SpaBe11	9.00E-02	±	5.00E-02	/day/kt	floated
C13CCG	1.00E+00	±	0.00E+00	(relative)	fixed
C13CCE	1.00E+00	±	0.00E+00	(relative)	fixed
AtmNu	1.00E+00	±	3.00E-01	(relative)	floated
hepES	1.00E+00	±	1.60E-01	(relative)	floated
Alpha	1.00E+00	±	4.30E-02	(relative)	floated
FV0	1.00E+00	±	3.00E-02	(relative)	floated

Table 9.3: BG estimation (*SolarPhase*)

BGs	Estimation				
				unit	in fitting
ExtL	1.00E+00	±	2.00E-01	(relative)	floated
ExtM	1.00E+00	±	8.00E-01	(relative)	floated
ExtH	1.00E+00	±	6.00E-01	(relative)	floated
Tl208	4.30E-02	±	3.72E-01	/day/kt	floated
SpaN12	2.54E-07	±	5.38E-07	/day/kt	fixed
SpaB12	6.30E-03	±	8.09E-03	/day/kt	fixed
SpaHe8	1.00E-08	±	5.35E-03	/day/kt	fixed
SpaC9	8.67E-04	±	1.05E-02	/day/kt	fixed
SpaLi9	1.69E-02	±	2.49E-02	/day/kt	fixed
SpaB8	1.25E-02	±	4.21E-02	/day/kt	floated
SpaLi8	3.63E-01	±	3.74E-01	/day/kt	floated
SpaBe11	4.86E-02	±	5.87E-02	/day/kt	floated
SpaC10	9.30E-01	±	1.04E+00	/day/kt	floated
SpaHe6	1.65E-01	±	2.09E-01	/day/kt	floated
C13CCG	1.00E+00	±	0.00E+00	(relative)	fixed
C13CCE	1.00E+00	±	0.00E+00	(relative)	fixed
C13NC	1.00E+00	±	4.00E-01	(relative)	floated
C11	9.80E+02	±	1.18E+02	/day/kt	floated
AtmNu	1.00E+00	±	3.00E-01	(relative)	floated
hepES	1.00E+00	±	1.60E-01	(relative)	floated
Pa234	1.00E-08	±	2.80E+01	/day/kt	floated
Ac228	2.11E+01	±	4.47E+01	/day/kt	floated
Alpha	1.00E+00	±	4.30E-02	(relative)	floated
FV0	1.00E+00	±	7.70E-02	(relative)	floated
FV1	1.00E+00	±	4.30E-02	(relative)	floated
FV2	1.00E+00	±	5.10E-02	(relative)	floated

Table 9.4: BG estimation (*AfterZen*)

BGs	Estimation				
				unit	in fitting
ExtL	1.00E+00	±	2.00E-01	(relative)	floated
ExtM	1.00E+00	±	8.00E-01	(relative)	floated
ExtH	1.00E+00	±	6.00E-01	(relative)	floated
Tl208	7.61E-01	±	4.32E-01	/day/kt	floated
SpaN12	1.00E-08	±	2.99E-06	/day/kt	fixed
SpaB12	7.88E-03	±	1.44E-02	/day/kt	fixed
SpaHe8	1.00E-08	±	1.62E-02	/day/kt	fixed
SpaC9	1.00E-08	±	1.12E-02	/day/kt	fixed
SpaLi9	1.56E-02	±	3.21E-02	/day/kt	fixed
SpaB8	1.00E-08	±	8.62E-02	/day/kt	floated
SpaLi8	3.47E-01	±	3.41E-01	/day/kt	floated
SpaBe11	2.53E-02	±	5.17E-02	/day/kt	floated
SpaC10	1.00E-08	±	9.83E-02	/day/kt	floated
SpaHe6	1.32E-01	±	2.34E-01	/day/kt	floated
C13CCG	1.00E+00	±	0.00E+00	(relative)	fixed
C13CCE	1.00E+00	±	0.00E+00	(relative)	fixed
C13NC	1.00E+00	±	4.00E-01	(relative)	floated
C11	1.07E+03	±	1.58E+02	/day/kt	floated
AtmNu	1.00E+00	±	3.00E-01	(relative)	floated
hepES	1.00E+00	±	1.60E-01	(relative)	floated
Pa234	2.49E+01	±	4.29E+01	/day/kt	floated
Ac228	1.00E-08	±	7.94E+01	/day/kt	floated
Alpha	1.00E+00	±	4.30E-02	(relative)	floated
FV0	1.00E+00	±	1.05E-01	(relative)	floated
FV1	1.00E+00	±	5.90E-02	(relative)	floated
FV2	1.00E+00	±	6.90E-02	(relative)	floated

9.5 Rate Analysis

Table 9.5, 9.6, 9.7 show the expected and observed numbers of events in each phase. They are also expressed in figures. See Figure 9.7, 9.9, and 9.11, respectively. Figure 9.8, 9.10, 9.12 show the background-subtracted histograms. Figure 9.13 shows the combined histogram. It is just for visualization. The subtracted number of events in each phase was compared with the expectation from the unoscillated case, where the total ^{8}B solar ν flux of $(5.25 \pm 0.21) \times 10^6$ /cm^2/s [19] was assumed. The results were as follows (see Figure 9.14) :

- (2–3 MeV): 0.46 ± 0.35
- 2–3.5 MeV: 0.42 ± 0.26
- 3.5–5 MeV: 0.49 ± 0.14
- 5–20 MeV: 0.507 ± 0.059

They are consistent with the expectations from the best-fit oscillation parameters [38] and a flat P_{ee} model [18].

Table 9.5: Expected vs observed number of events (*BeforePurif*)

BGs	5–20 MeV		
Ext	14.92	±	8.21
Tl208	0.00	±	0.00
SpaN12	0.00	±	0.00
SpaB12	0.71	±	0.06
SpaHe8	0.14	±	0.22
SpaC9	0.65	±	0.47
SpaLi9	1.02	±	0.30
SpaB8	0.97	±	2.30
SpaLi8	0.00	±	9.51
SpaBe11	6.15	±	3.42
C13CCG	5.86	±	0.00
C13CCE	2.14	±	0.00
AtmNu	1.41	±	0.42
hepES	0.50	±	0.08
BGTotal	34.48	±	13.24
Observed	183		
Subtracted	148.52	±	18.93
Unoscillated	309.33	±	27.88
Sub/Unosc	0.48	±	0.07
Flux(1e6/cm2/s)	2.52	±	0.33

Table 9.6: Expected vs observed number of events (*SolarPhase*)

BGs	(2–3 MeV)			2–3.5 MeV			3.5–5 MeV			5–20 MeV		
ExtL	3.04	±	0.61	3.05	±	0.61	0.00	±	0.00	0.00	±	0.00
ExtM	0.00	±	0.00	0.00	±	0.00	2.10	±	1.68	0.00	±	0.00
ExtH	0.00	±	0.00	0.00	±	0.00	0.00	±	0.00	5.78	±	3.47
Tl208	0.01	±	0.09	0.15	±	1.27	1.77	±	15.32	0.00	±	0.00
SpaN12	0.00	±	0.00	0.00	±	0.00	0.00	±	0.00	0.00	±	0.00
SpaB12	0.00	±	0.01	0.01	±	0.01	0.06	±	0.08	0.17	±	0.21
SpaHe8	0.00	±	0.00	0.00	±	0.01	0.00	±	0.07	0.00	±	0.10
SpaC9	0.00	±	0.00	0.00	±	0.00	0.00	±	0.05	0.02	±	0.24
SpaLi9	0.01	±	0.01	0.01	±	0.01	0.08	±	0.12	0.23	±	0.33
SpaB8	0.01	±	0.02	0.01	±	0.04	0.11	±	0.37	0.36	±	1.22
SpaLi8	0.33	±	0.34	0.55	±	0.57	4.22	±	4.35	8.44	±	8.69
SpaBe11	0.03	±	0.04	0.05	±	0.06	0.50	±	0.61	1.22	±	1.47
SpaC10	7.03	±	7.86	7.46	±	8.34	0.00	±	0.01	0.00	±	0.00
SpaHe6	0.51	±	0.65	0.55	±	0.69	0.00	±	0.00	0.00	±	0.00
C13CCG	0.02	±	0.00	0.05	±	0.00	0.56	±	0.00	2.06	±	0.00
C13CCE	0.05	±	0.00	0.09	±	0.00	0.77	±	0.00	0.76	±	0.00
C13NC	0.00	±	0.00	0.19	±	0.07	2.09	±	0.84	0.00	±	0.00
C11	0.05	±	0.01	0.05	±	0.01	0.00	±	0.00	0.00	±	0.00
AtmNu	0.01	±	0.00	0.02	±	0.01	0.11	±	0.03	0.46	±	0.14
hepES	0.01	±	0.00	0.02	±	0.00	0.09	±	0.01	0.18	±	0.03
Pa234	0.00	±	2.44	0.00	±	2.44	0.00	±	0.00	0.00	±	0.00
Ac228	0.36	±	0.75	0.36	±	0.75	0.00	±	0.00	0.00	±	0.00
BgTotal	11.48	±	8.32	12.60	±	8.88	12.47	±	16.05	19.66	±	9.56
Observed	10			15			77			79		
Subtracted	-1.48	±	8.90	2.40	±	9.69	64.53	±	18.29	59.34	±	13.05
Unoscillated	15.54	±	1.44	22.76	±	2.10	100.21	±	6.06	108.65	±	10.76
Sub/Unosci	-0.10	±	0.57	0.11	±	0.43	0.64	±	0.19	0.55	±	0.13
Flux(10^6/cm^2/s)	-0.50	±	3.01	0.55	±	2.23	3.38	±	0.97	2.87	±	0.65

Table 9.7: Expected vs observed number of events (*AfterZen*)

BGs	(2–3 MeV)	2–3.5 MeV	3.5–5 MeV	5–20 MeV
ExtL	1.96 ± 0.39	2.00 ± 0.40	0.00 ± 0.00	0.00 ± 0.00
ExtM	0.00 ± 0.00	0.00 ± 0.00	1.41 ± 1.13	0.00 ± 0.00
ExtH	0.00 ± 0.00	0.00 ± 0.00	0.00 ± 0.00	3.83 ± 2.30
Tl208	0.11 ± 0.07	1.67 ± 0.95	20.73 ± 11.78	0.00 ± 0.00
SpaN12	0.00 ± 0.00	0.00 ± 0.00	0.00 ± 0.00	0.00 ± 0.00
SpaB12	0.00 ± 0.01	0.01 ± 0.01	0.05 ± 0.09	0.14 ± 0.25
SpaHe8	0.00 ± 0.01	0.00 ± 0.01	0.00 ± 0.13	0.00 ± 0.20
SpaC9	0.00 ± 0.00	0.00 ± 0.00	0.00 ± 0.03	0.00 ± 0.17
SpaLi9	0.00 ± 0.01	0.01 ± 0.01	0.05 ± 0.10	0.14 ± 0.28
SpaB8	0.00 ± 0.03	0.00 ± 0.05	0.00 ± 0.50	0.00 ± 1.63
SpaLi8	0.21 ± 0.20	0.34 ± 0.34	2.67 ± 2.63	5.29 ± 5.21
SpaBe11	0.01 ± 0.02	0.02 ± 0.04	0.17 ± 0.35	0.42 ± 0.85
SpaC10	0.00 ± 0.48	0.00 ± 0.51	0.00 ± 0.00	0.00 ± 0.00
SpaHe6	0.26 ± 0.47	0.28 ± 0.50	0.00 ± 0.00	0.00 ± 0.00
C13CCG	0.02 ± 0.00	0.03 ± 0.00	0.37 ± 0.00	1.35 ± 0.00
C13CCE	0.03 ± 0.00	0.06 ± 0.00	0.51 ± 0.00	0.50 ± 0.00
C13NC	0.00 ± 0.00	0.12 ± 0.05	1.39 ± 0.55	0.00 ± 0.00
C11	0.03 ± 0.01	0.03 ± 0.01	0.00 ± 0.00	0.00 ± 0.00
AtmNu	0.01 ± 0.00	0.01 ± 0.00	0.06 ± 0.02	0.30 ± 0.09
hepES	0.01 ± 0.00	0.01 ± 0.00	0.06 ± 0.01	0.12 ± 0.02
Pa234	1.40 ± 2.41	1.40 ± 2.41	0.00 ± 0.00	0.00 ± 0.00
Ac228	0.00 ± 0.86	0.00 ± 0.86	0.00 ± 0.00	0.00 ± 0.00
BgTotal	4.07 ± 2.69	6.00 ± 2.87	27.47 ± 12.15	12.07 ± 6.00
Observed	12	15	47	52
Subtracted	7.93 ± 4.38	9.00 ± 4.82	19.53 ± 13.95	39.93 ± 9.38
Unoscillated	10.04 ± 1.18	14.70 ± 1.72	66.34 ± 4.83	71.32 ± 7.80
Sub/Unosci	0.79 ± 0.45	0.61 ± 0.34	0.29 ± 0.21	0.56 ± 0.15
Flux(1e6/cm2/s)	4.15 ± 2.33	3.21 ± 1.75	1.55 ± 1.11	2.94 ± 0.72

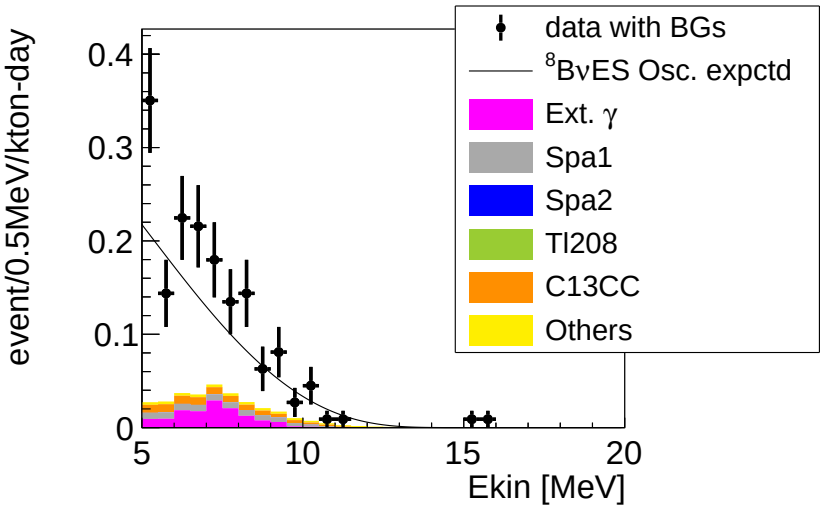

Figure 9.7: Observed events vs expected BGs (Rate only) (*BeforePurif*).

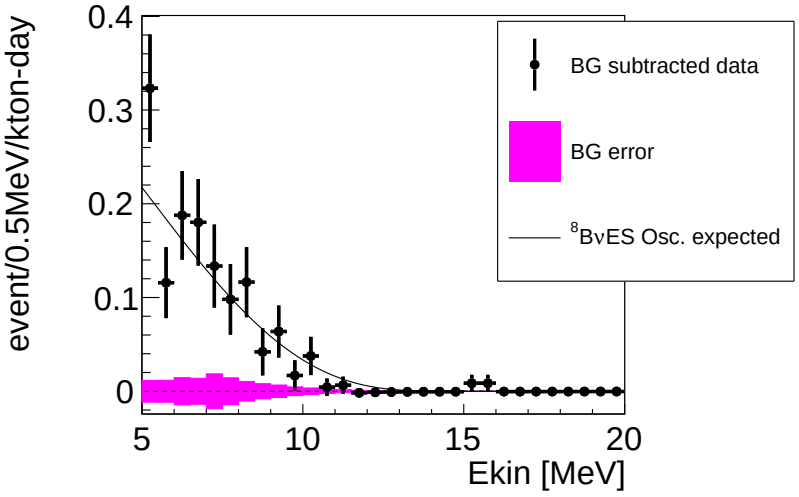

Figure 9.8: BG subtracted spectrum (Rate only) (*BeforePurif*).

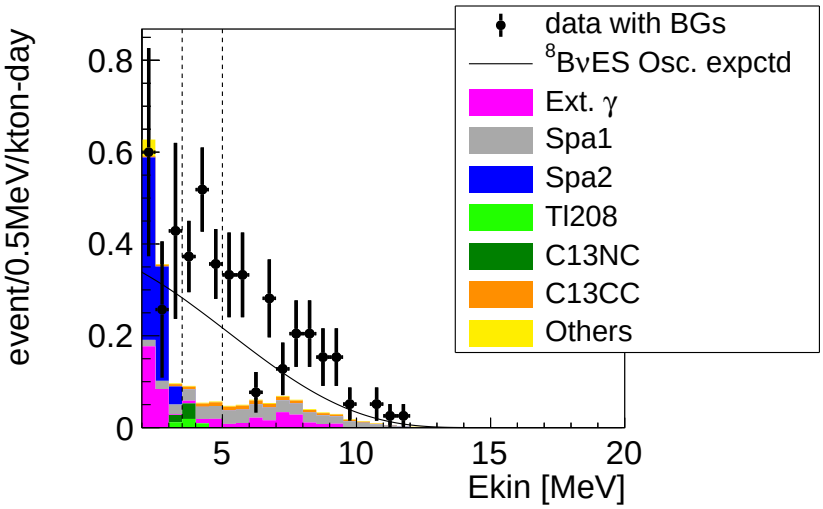

Figure 9.9: Observed events vs expected BGs (Rate only) (*SolarPhase*).

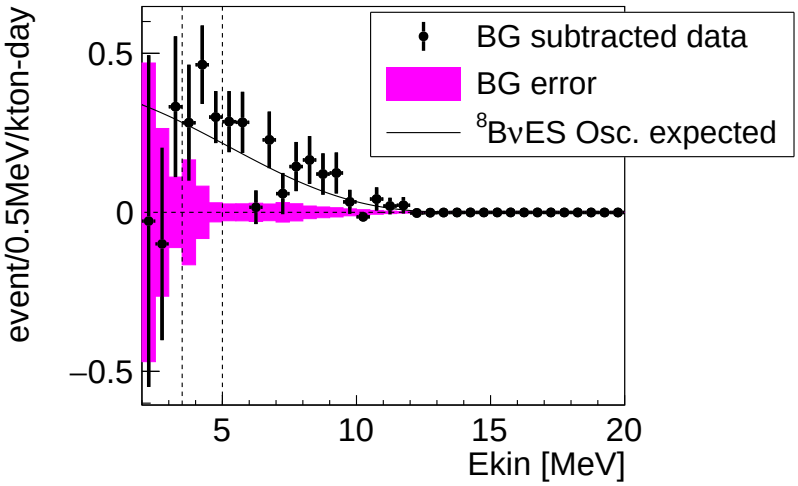

Figure 9.10: BG subtracted spectrum (Rate only) (*SolarPhase*).

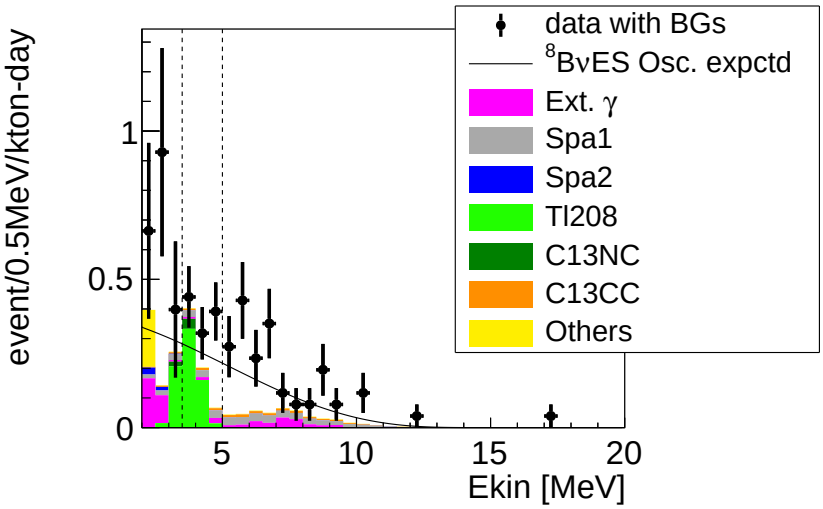

Figure 9.11: Observed events vs expected BGs (Rate only) (*AfterZen*).

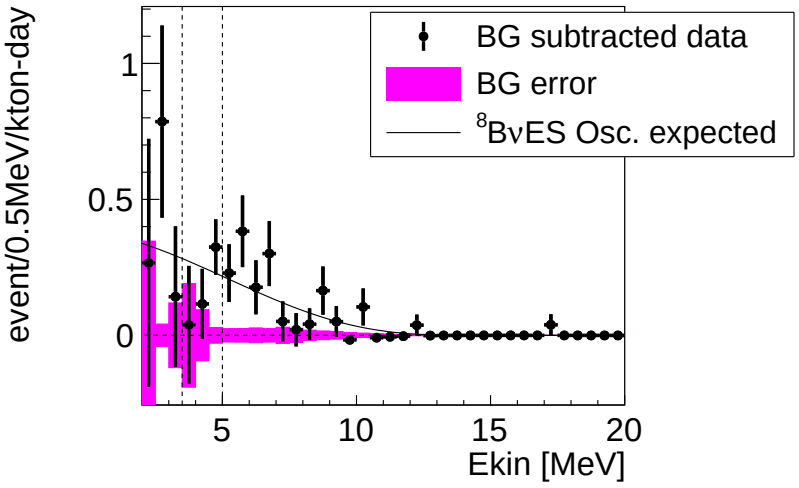

Figure 9.12: BG subtracted spectrum (Rate only) (*AfterZen*).

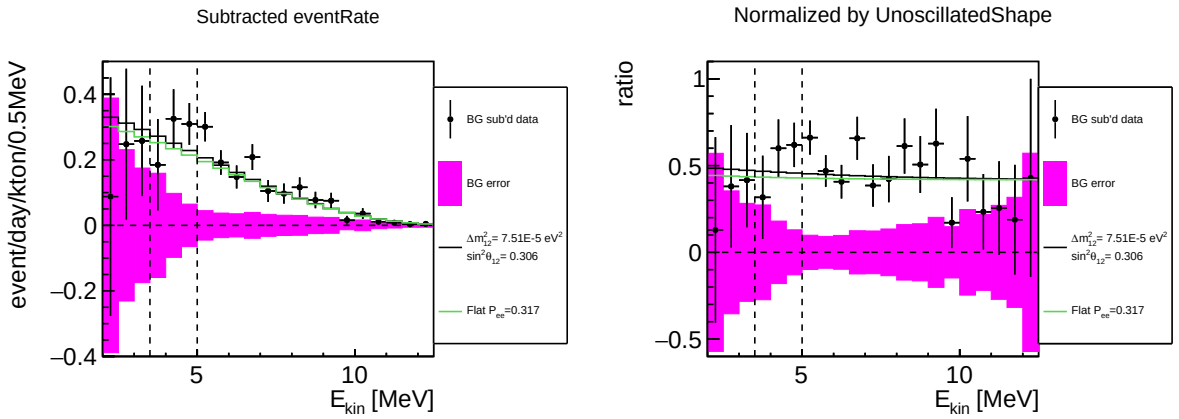

Figure 9.13: BG subtracted spectrum (Rate only) (3 phases combined). Just for visualization.

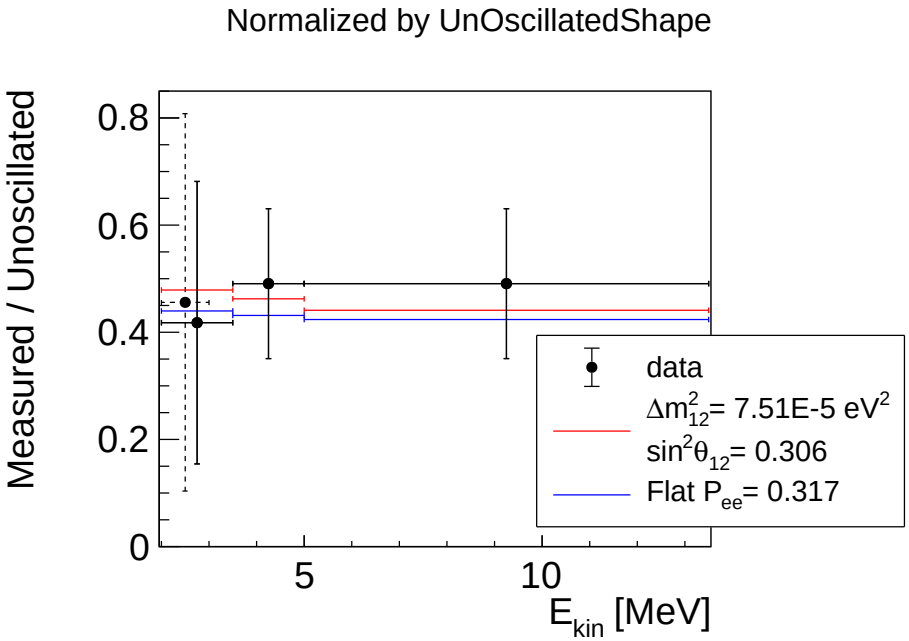

Figure 9.14: Flux (Rate only) (3 phases combined).

9.6 Rate+Shape Analysis (Unoscillatad Shape)

9.6.1 Binned Maixmum Likelihood

Energy spectrum fittings are performed with a binned maximum likelihood method whose χ^2 is defined as

$$\chi^2_{\text{final}} = \chi^2_{\text{energy}} + \chi^2_{\text{penalty}}, \tag{9.90}$$

$$\chi^2_{\text{energy}} = \begin{cases} 2\sum_i \left[-(n_i - f_i)\right] & (n_i = 0) \\ 2\sum_i \left[-(n_i - f_i) + n_i \log \frac{n_i}{f_i}\right] & (n_i > 0) \end{cases}, \tag{9.91}$$

where

- i denotes i-th energy bin.
- n_i is the number of event observed in i-th energy bin.
- f_i is the number of event expected in i-th energy bin.

$$\chi^2_{\text{penalty}} = \sum_j \frac{(m_j - \mu_j)^2}{\sigma_j^2}, \tag{9.92}$$

where

- j denotes j-th constrained parameter.
- m_j is the estimated parameter from the energy spectrum fitting.
- μ_j is the mean value of j-the parameter in the external estimation.
- σ_j is the uncertainty of the external estimation.

9.6.2 Fit with Unoscillated Shape (Continuous)

A fit with a continuous shape over energy is useful to grasp the situation of remaining backgrounds. Figure 9.15 9.16, 9.17 show the energy spectra fitted with the unosillated ^{8}B solar ν spectrum. The best-fit parameters and the number of events are summarized in:

- *BeforePuri*: Table 9.8 ,9.9
- *SolarPhase*: Table 9.10 ,9.11
- *AfterZen*: Table 9.12 ,9.13

^{208}Tl in *SolarPhase* and *AfterZen* and spallation products (^{10}C, ^{6}He, ^{8}B) in *SolarPhase* were well determined in the energy spectrum fitting. Based on these results, the estimations of rejection efficiencies are improved as follows:

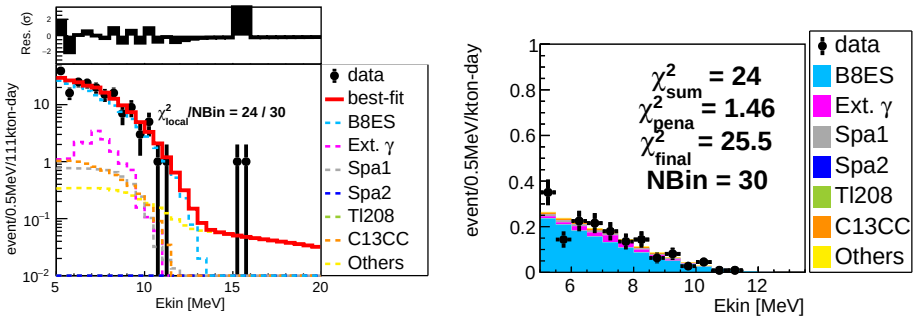

Figure 9.15: Fit with unoscillated shape (*BeforePurif*).

- ^{208}Tl
  - *SolarPhase*: $(98 \pm 19)\% \rightarrow (92 \pm 11)\%$
  - *AfterZen*: $(63 \pm 16)\% \rightarrow (87 \pm 12)\%$
- ^{10}C
  - *SolarPhase*: $(95.0 \pm 4.5)\% \rightarrow (100 \pm 2.2)\%$

Figure 9.18 shows the $\Delta\chi^2$ distributions for the measured flux in each phase. The estimated fluxes were:

- *BeforePurif*: $(2.73^{+0.36}_{-0.35}) \times 10^6/\mathrm{cm}^2/\mathrm{s}$
- *SolarPhase*: $(2.92^{+0.50}_{-0.50}) \times 10^6/\mathrm{cm}^2/\mathrm{s}$
- *AfterZen*: $(3.00^{+0.55}_{-0.52}) \times 10^6/\mathrm{cm}^2/\mathrm{s}$
- 3-phases combined: $(2.84^{+0.26}_{-0.25}) \times 10^6/\mathrm{cm}^2/\mathrm{s}$

The combined result agrees with the SK's result [38], $(2.35 \pm 0.04) \times 10^6/\mathrm{cm}^2/\mathrm{s}$, within 2σ.

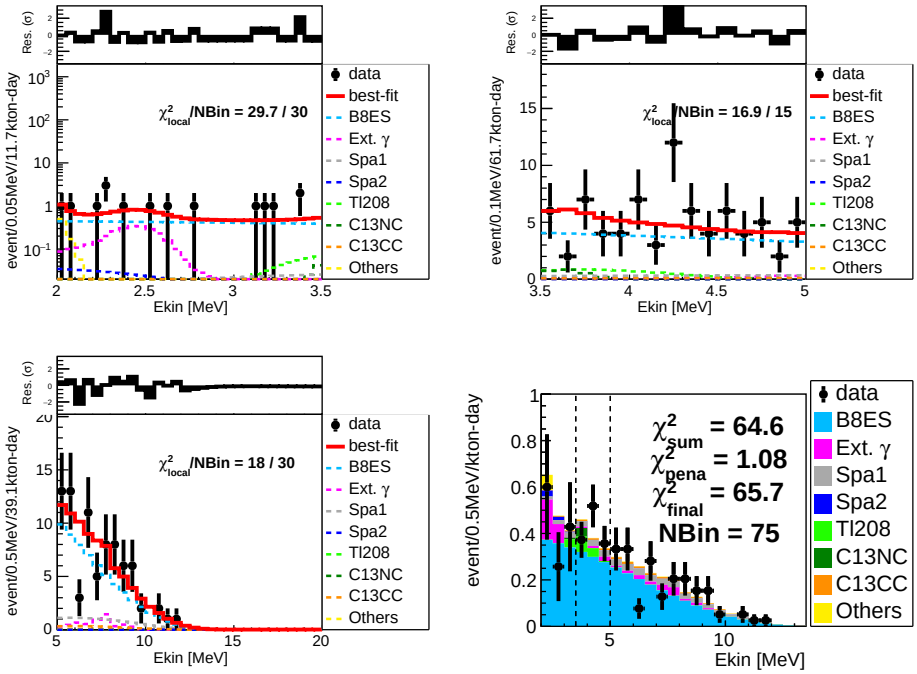

Figure 9.16: Fit with unoscillated shape (*SolarPhase*).

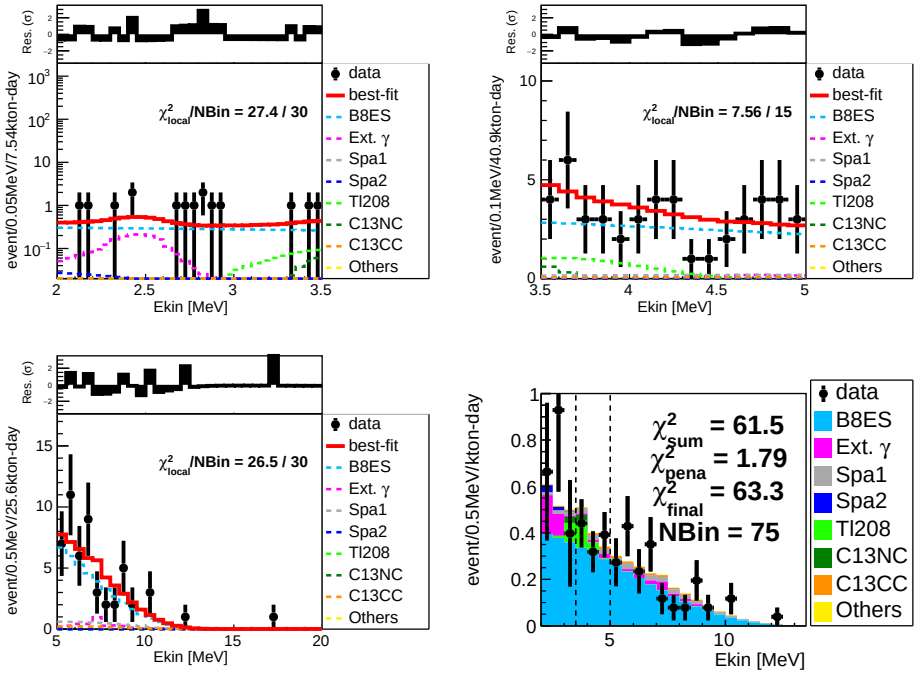

Figure 9.17: Fit with unoscillated shape (*AfterZen*).

Table 9.8: Estimation vs best-fit parameters (Unoscillated shape fit) (*BeforePurif*)

Parameters	Unit	Condition	Estimation (Constraint)			Best-fit		
B8NuES	1e6/cm2/s	floated				2.74E+00	±	3.29E-01
Ext	(relative)	floated	1.00E+00	±	5.50E-01	1.07E+00	±	5.17E-01
Tl208	/day/kt	floated	4.27E+01	±	1.93E+00	4.27E+01	±	1.93E+00
SpaN12	/day/kt	fixed	4.50E-07	±	3.90E-07	4.50E-07	±	fixed
SpaB12	/day/kt	fixed	9.85E-03	±	7.85E-04	9.85E-03	±	fixed
SpaHe8	/day/kt	fixed	2.89E-03	±	4.33E-03	2.89E-03	±	fixed
SpaC9	/day/kt	fixed	1.05E-02	±	7.57E-03	1.05E-02	±	fixed
SpaLi9	/day/kt	fixed	2.78E-02	±	8.27E-03	2.78E-02	±	fixed
SpaB8	/day/kt	floated	1.24E-02	±	2.93E-02	8.67E-03	±	2.92E-02
SpaLi8	/day/kt	floated	0.00E+00	±	1.50E-01	0.00E+00	±	1.40E-01
SpaBe11	/day/kt	floated	9.00E-02	±	5.00E-02	9.08E-02	±	4.98E-02
C13CCG	(relative)	fixed	1.00E+00	±	0.00E+00	1.00E+00	±	fixed
C13CCE	(relative)	fixed	1.00E+00	±	0.00E+00	1.00E+00	±	fixed
AtmNu	(relative)	floated	1.00E+00	±	3.00E-01	1.10E+00	±	2.81E-01
hepES	(relative)	floated	1.00E+00	±	1.60E-01	1.00E+00	±	1.60E-01
Alpha	(relative)	floated	1.00E+00	±	4.30E-02	9.50E-01	±	1.92E-02
FV0	(relative)	floated	1.00E+00	±	3.00E-02	1.00E+00	±	3.00E-02

Table 9.9: Best-fit number of events (Unoscillated shape fit) (*BeforePurif*).

BGs	5–20 MeV		
B8NuES	147.10	±	17.66
Ext	15.90	±	7.71
Tl208	0.00	±	0.00
SpaN12	0.00	±	fixed
SpaB12	0.68	±	fixed
SpaHe8	0.13	±	fixed
SpaC9	0.63	±	fixed
SpaLi9	0.97	±	fixed
SpaB8	0.65	±	2.19
SpaLi8	0.00	±	8.35
SpaBe11	5.87	±	3.22
C13CCG	5.63	±	fixed
C13CCE	1.89	±	fixed
AtmNu	1.58	±	0.40
hepES	0.48	±	0.08
BestFitTotal	181.49	±	21.36
Observed	183		

Table 9.10: Estimation vs best-fit parameters (Continuous unoscillated shape fit) (*SolarPhase*)

Parameters	Unit	Condition	Estimation (Constraint)			Best-fit		
Nu	$10^6/cm^2/s$	floated				2.92E+00	±	5.05E-01
ExtL	(relative)	floated	1.00E+00	±	2.00E-01	9.79E-01	±	1.92E-01
ExtM	(relative)	floated	1.00E+00	±	8.00E-01	1.09E+00	±	7.64E-01
ExtH	(relative)	floated	1.00E+00	±	6.00E-01	9.26E-01	±	5.41E-01
Tl208	/day/kt	floated	4.30E-02	±	3.72E-01	1.51E-01	±	2.07E-01
SpaN12	/day/kt	fixed	2.54E-07	±	5.38E-07	2.54E-07	±	fixed
SpaB12	/day/kt	fixed	6.30E-03	±	8.09E-03	6.30E-03	±	fixed
SpaHe8	/day/kt	fixed	1.00E-08	±	5.35E-03	1.00E-08	±	fixed
SpaC9	/day/kt	fixed	8.67E-04	±	1.05E-02	8.67E-04	±	fixed
SpaLi9	/day/kt	fixed	1.69E-02	±	2.49E-02	1.69E-02	±	fixed
SpaB8	/day/kt	floated	1.25E-02	±	4.21E-02	1.01E-02	±	2.69E-02
SpaLi8	/day/kt	floated	3.63E-01	±	3.74E-01	3.66E-01	±	3.35E-01
SpaBe11	/day/kt	floated	4.86E-02	±	5.87E-02	4.99E-02	±	5.94E-02
SpaC10	/day/kt	floated	9.30E-01	±	1.04E+00	4.76E-05	±	3.88E-01
SpaHe6	/day/kt	floated	1.65E-01	±	2.09E-01	1.43E-01	±	1.79E-01
C13CCG	(relative)	fixed	1.00E+00	±	0.00E+00	1.00E+00	±	fixed
C13CCE	(relative)	fixed	1.00E+00	±	0.00E+00	1.00E+00	±	fixed
C13NC	(relative)	floated	1.00E+00	±	4.00E-01	9.02E-01	±	3.68E-01
C11	/day/kt	floated	9.80E+02	±	1.18E+02	9.80E+02	±	1.18E+02
AtmNu	(relative)	floated	1.00E+00	±	3.00E-01	9.83E-01	±	2.96E-01
hepES	(relative)	floated	1.00E+00	±	1.60E-01	1.00E+00	±	1.62E-01
Pa234	/day/kt	floated	1.00E-08	±	2.80E+01	2.65E-08	±	1.83E+01
Ac228	/day/kt	floated	2.11E+01	±	4.47E+01	1.73E+01	±	3.38E+01
Alpha	(relative)	floated	1.00E+00	±	4.30E-02	1.02E+00	±	1.15E-02
FV0	(relative)	floated	1.00E+00	±	7.70E-02	9.84E-01	±	7.47E-02
FV1	(relative)	floated	1.00E+00	±	4.30E-02	1.01E+00	±	3.96E-02
FV2	(relative)	floated	1.00E+00	±	5.10E-02	9.94E-01	±	4.73E-02

Table 9.11: Best-fit number of events (Continuous unoscillated shape fit) (*SolarPhase*)

BGs	2–3.5 MeV			3.5–5 MeV			5–20 MeV		
B8νES	12.48	±	2.16	55.31	±	9.58	62.13	±	10.76
ExtL	2.99	±	0.59	0.00	±	0.00	0.00	±	0.00
ExtM	0.00	±	0.00	2.11	±	1.48	0.00	±	0.00
ExtH	0.00	±	0.00	0.00	±	0.00	5.55	±	3.24
Tl208	0.42	±	0.58	6.69	±	9.18	0.00	±	0.00
SpaN12	0.00	±	fixed	0.00	±	fixed	0.00	±	fixed
SpaB12	0.01	±	fixed	0.06	±	fixed	0.17	±	fixed
SpaHe8	0.00	±	fixed	0.00	±	fixed	0.00	±	fixed
SpaC9	0.00	±	fixed	0.00	±	fixed	0.02	±	fixed
SpaLi9	0.01	±	fixed	0.08	±	fixed	0.23	±	fixed
SpaB8	0.01	±	0.02	0.09	±	0.23	0.29	±	0.79
SpaLi8	0.54	±	0.49	4.14	±	3.79	8.68	±	7.94
SpaBe11	0.05	±	0.06	0.50	±	0.59	1.27	±	1.51
SpaC10	0.00	±	3.23	0.00	±	0.01	0.00	±	0.00
SpaHe6	0.50	±	0.62	0.00	±	0.01	0.00	±	0.00
C13CCG	0.04	±	fixed	0.53	±	fixed	2.09	±	fixed
C13CCE	0.09	±	fixed	0.74	±	fixed	0.79	±	fixed
C13NC	0.09	±	0.04	2.30	±	0.94	0.00	±	0.00
C11	0.18	±	0.02	0.00	±	0.00	0.00	±	0.00
AtmNu	0.02	±	0.01	0.10	±	0.03	0.45	±	0.14
hepES	0.02	±	0.00	0.09	±	0.01	0.18	±	0.03
Pa234	0.00	±	1.89	0.00	±	0.00	0.00	±	0.00
Ac228	0.56	±	1.10	0.00	±	0.00	0.00	±	0.00
Total	18.01	±	4.61	72.75	±	13.92	81.84	±	13.87
Observed	15			77			79		

Table 9.12: Estimation vs best-fit parameters (Continuous unoscillated shape fit) (*AfterZen*)

Parameters	Unit	Condition	Estimation (Constraint)			Best-fit		
B8NuES	1e6/cm2/s	floated				3.01E+00	±	5.38E-01
ExtL	(relative)	floated	1.00E+00	±	2.00E-01	1.00E+00	±	1.98E-01
ExtM	(relative)	floated	1.00E+00	±	8.00E-01	9.97E-01	±	7.90E-01
ExtH	(relative)	floated	1.00E+00	±	6.00E-01	9.03E-01	±	5.84E-01
Tl208	/day/kt	floated	7.61E-01	±	4.32E-01	2.68E-01	±	2.43E-01
SpaN12	/day/kt	fixed	1.00E-08	±	2.99E-06	1.00E-08	±	fixed
SpaB12	/day/kt	fixed	7.88E-03	±	1.44E-02	7.88E-03	±	fixed
SpaHe8	/day/kt	fixed	1.00E-08	±	1.62E-02	1.00E-08	±	fixed
SpaC9	/day/kt	fixed	1.00E-08	±	1.12E-02	1.00E-08	±	fixed
SpaLi9	/day/kt	fixed	1.56E-02	±	3.21E-02	1.56E-02	±	fixed
SpaB8	/day/kt	floated	1.00E-08	±	8.62E-02	5.12E-04	±	8.40E-02
SpaLi8	/day/kt	floated	3.47E-01	±	3.41E-01	3.09E-01	±	3.32E-01
SpaBe11	/day/kt	floated	2.53E-02	±	5.17E-02	2.41E-02	±	5.16E-02
SpaC10	/day/kt	floated	1.00E-08	±	9.83E-02	1.11E-02	±	2.13E-01
SpaHe6	/day/kt	floated	1.32E-01	±	2.34E-01	1.52E-01	±	2.32E-01
C13CCG	(relative)	fixed	1.00E+00	±	0.00E+00	1.00E+00	±	fixed
C13CCE	(relative)	fixed	1.00E+00	±	0.00E+00	1.00E+00	±	fixed
C13NC	(relative)	floated	1.00E+00	±	4.00E-01	1.02E+00	±	3.98E-01
C11	/day/kt	floated	1.07E+03	±	1.58E+02	1.07E+03	±	1.57E+02
AtmNu	(relative)	floated	1.00E+00	±	3.00E-01	1.07E+00	±	2.89E-01
hepES	(relative)	floated	1.00E+00	±	1.60E-01	1.00E+00	±	1.60E-01
Pa234	/day/kt	floated	2.49E+01	±	4.29E+01	1.81E-05	±	3.07E+01
Ac228	/day/kt	floated	1.00E-08	±	7.94E+01	3.94E-04	±	6.16E+01
Alpha	(relative)	floated	1.00E+00	±	4.30E-02	9.83E-01	±	2.62E-02
FV0	(relative)	floated	1.00E+00	±	1.05E-01	1.03E+00	±	9.87E-02
FV1	(relative)	floated	1.00E+00	±	5.90E-02	9.88E-01	±	5.78E-02
FV2	(relative)	floated	1.00E+00	±	6.90E-02	1.01E+00	±	6.62E-02

Table 9.13: Best-fit number of events (Continuous unoscillated shape fit)(*AfterZen*)

BGs	2–3.5 MeV			3.5–5 MeV			5–20 MeV		
B8NuES	8.53	±	1.53	38.24	±	6.84	39.60	±	7.08
ExtL	2.01	±	0.40	0.00	±	0.00	0.00	±	0.00
ExtM	0.00	±	0.00	1.52	±	1.21	0.00	±	0.00
ExtH	0.00	±	0.00	0.00	±	0.00	3.31	±	2.14
Tl208	0.70	±	0.64	6.71	±	6.07	0.00	±	0.00
SpaN12	0.00	±	fixed	0.00	±	fixed	0.00	±	fixed
SpaB12	0.01	±	fixed	0.05	±	fixed	0.13	±	fixed
SpaHe8	0.00	±	fixed	0.00	±	fixed	0.00	±	fixed
SpaC9	0.00	±	fixed	0.00	±	fixed	0.00	±	fixed
SpaLi9	0.01	±	fixed	0.05	±	fixed	0.13	±	fixed
SpaB8	0.00	±	0.05	0.00	±	0.51	0.01	±	1.57
SpaLi8	0.32	±	0.34	2.44	±	2.63	4.62	±	4.96
SpaBe11	0.02	±	0.04	0.17	±	0.37	0.39	±	0.83
SpaC10	0.06	±	1.06	0.00	±	0.00	0.00	±	0.00
SpaHe6	0.31	±	0.47	0.00	±	0.00	0.00	±	0.00
C13CCG	0.03	±	fixed	0.39	±	fixed	1.33	±	fixed
C13CCE	0.06	±	fixed	0.52	±	fixed	0.48	±	fixed
C13NC	0.19	±	0.08	1.02	±	0.40	0.00	±	0.00
C11	0.01	±	0.00	0.00	±	0.00	0.00	±	0.00
AtmNu	0.01	±	0.00	0.07	±	0.02	0.33	±	0.09
hepES	0.01	±	0.00	0.06	±	0.01	0.11	±	0.02
Pa234	0.00	±	1.24	0.00	±	0.00	0.00	±	0.00
Ac228	0.00	±	0.32	0.00	±	0.00	0.00	±	0.00
BestFitTotal	12.28	±	2.45	51.24	±	9.62	50.44	±	9.09
Observed	15			47			52		

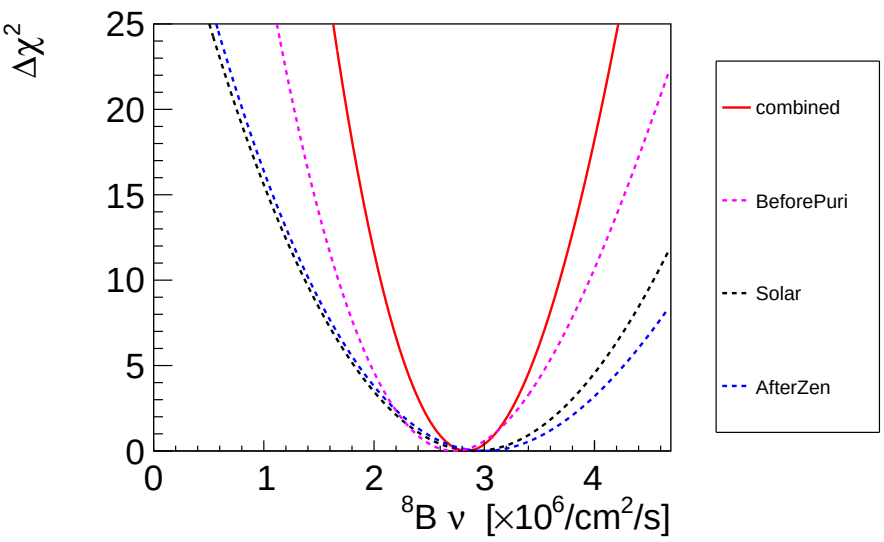

Figure 9.18: Flux measured with the unoscillated spectrum.

9.6.3 Fit with Unoscillated Shape (Divided)

Ultimately the difference of the flux between lower and higher energy regions is expected to be seen. The data below 5 MeV is new for KamLAND and that below 3 MeV is new in the world. Therefore I divided the unoscillated spectrum into three parts, 2–3 MeV, 3–5 MeV and 5–20 MeV, and fitted the data with them.

The analysis for *BeforePurif* uses only one energy region above 5 MeV and the result has already been shown in Figure 9.15, Table 9.8, 9.9. The results for *SolarPhase* and *AfterZen* are shown in Figure 9.19, Table 9.14, 9.15 and Figure 9.20, Table 9.16, 9.17, respectively.

Figure 9.21, 9.22, 9.23 show the $\Delta\chi^2$ distributions for the flux. The 3-phases combined measured fluxes were:

- $2 < E_{\rm kin} < 3$ MeV: $(3.25^{+1.11}_{-1.03}) \times 10^6$ /cm^2/s
- $3 < E_{\rm kin} < 5$ MeV: $(2.93^{+0.52}_{-0.51}) \times 10^6$ /cm^2/s
- $5 < E_{\rm kin} < 20$ MeV: $(2.81^{+0.29}_{-0.28}) \times 10^6$ /cm^2/s

They correspond to the ratios to the unoscillated expectations of:

- $2 < E_{\rm kin} < 3$ MeV: $(0.62^{+0.21}_{-0.20})$
- $3 < E_{\rm kin} < 5$ MeV: $(0.56^{+0.10}_{-0.10})$
- $5 < E_{\rm kin} < 20$ MeV: $(0.535^{+0.060}_{-0.058})$

In the 2–3 MeV case, the significance of the null-rejection is $\Delta\chi^2 = 11.5$ (3.4σ).

Figure 9.24 shows the measured ratios and expected ratios from models. The results favors slightly higher values than both the best-fit oscillation and the flat expectations. The tensions (χ^2) are 4.0 for the best-fit oscillation and 6.1 for the flat expectations, where uncertainties on the models are not considered. The tension between the models is not so significant ($\Delta\chi^2 = 2.1$).

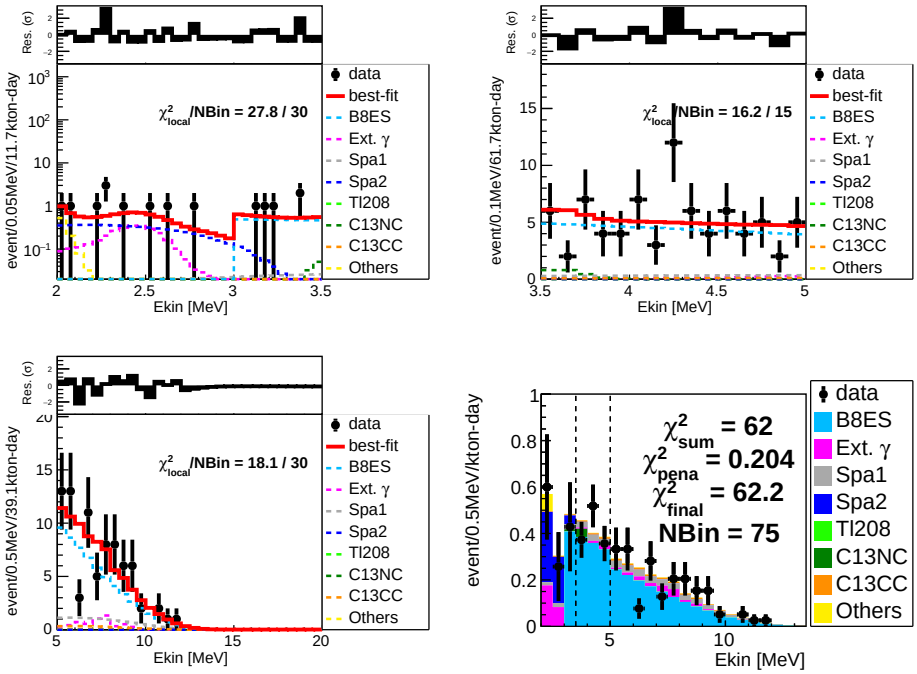

Figure 9.19: Fit with unoscillated shape with energy regions divided (*SolarPhase*).

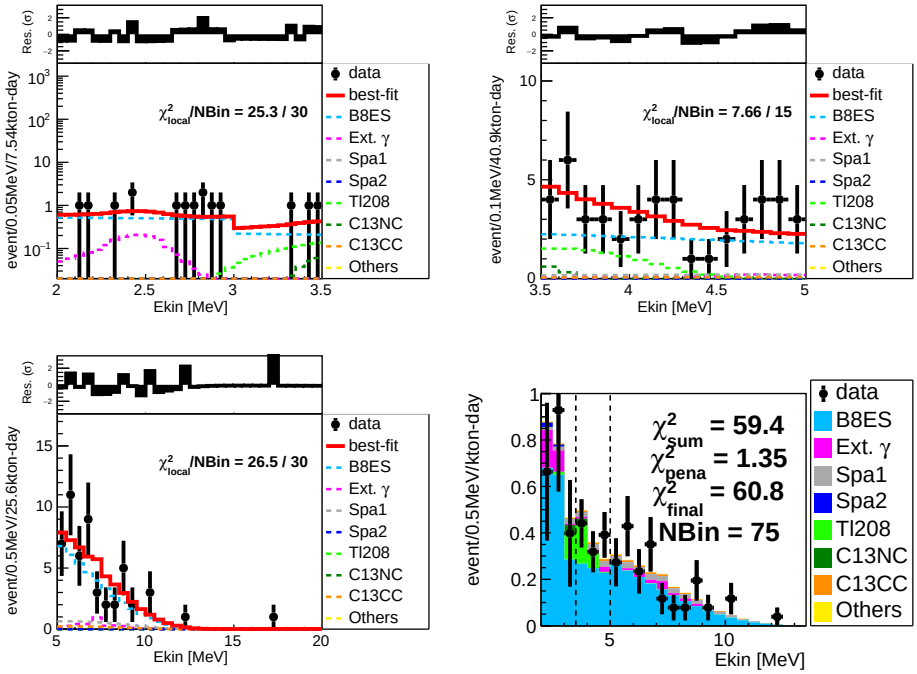

Figure 9.20: Fit with unoscillated shape with energy regions divided (*AfterZen*).

Table 9.14: Estimation vs best-fit parmeters (Divided unoscillated shape fit) (*SolarPhase*)

Parameters	Unit	Condition	Estimation (Constraint)			Best-fit		
^{8}BνES2–3	10^6/cm^2/s	floated				4.30E-05	±	1.82E+00
^{8}BνES3–5	10^6/cm^2/s	floated				3.50E+00	±	5.31E-01
^{8}BνES5–20	10^6/cm^2/s	floated				2.84E+00	±	6.47E-01
ExtL	(relative)	floated	1.00E+00	±	2.00E-01	9.97E-01	±	1.99E-01
ExtM	(relative)	floated	1.00E+00	±	8.00E-01	9.79E-01	±	7.97E-01
ExtH	(relative)	floated	1.00E+00	±	6.00E-01	9.50E-01	±	5.91E-01
Tl208	/day/kt	floated	4.30E-02	±	3.72E-01	2.43E-05	±	2.30E-01
SpaN12	/day/kt	fixed	2.54E-07	±	5.38E-07	2.54E-07	±	fixed
SpaB12	/day/kt	fixed	6.30E-03	±	8.09E-03	6.30E-03	±	fixed
SpaHe8	/day/kt	fixed	1.00E-08	±	5.35E-03	1.00E-08	±	fixed
SpaC9	/day/kt	fixed	8.67E-04	±	1.05E-02	8.67E-04	±	fixed
SpaLi9	/day/kt	fixed	1.69E-02	±	2.49E-02	1.69E-02	±	fixed
SpaB8	/day/kt	floated	1.25E-02	±	4.21E-02	1.09E-02	±	4.18E-02
SpaLi8	/day/kt	floated	3.63E-01	±	3.74E-01	3.64E-01	±	3.64E-01
SpaBe11	/day/kt	floated	4.86E-02	±	5.87E-02	5.02E-02	±	5.85E-02
SpaC10	/day/kt	floated	9.30E-01	±	1.04E+00	6.94E-01	±	4.37E-01
SpaHe6	/day/kt	floated	1.65E-01	±	2.09E-01	1.66E-01	±	2.08E-01
C13CCG	(relative)	fixed	1.00E+00	±	0.00E+00	1.00E+00	±	fixed
C13CCE	(relative)	fixed	1.00E+00	±	0.00E+00	1.00E+00	±	fixed
C13NC	(relative)	floated	1.00E+00	±	4.00E-01	9.11E-01	±	3.94E-01
C11	/day/kt	floated	9.80E+02	±	1.18E+02	9.80E+02	±	1.18E+02
AtmNu	(relative)	floated	1.00E+00	±	3.00E-01	9.84E-01	±	3.00E-01
hepES	(relative)	floated	1.00E+00	±	1.60E-01	1.00E+00	±	1.60E-01
Pa234	/day/kt	floated	1.00E-08	±	2.80E+01	1.47E+00	±	5.46E+01
Ac228	/day/kt	floated	2.11E+01	±	4.47E+01	2.26E+01	±	4.00E+01
Alpha	(relative)	floated	1.00E+00	±	4.30E-02	1.01E+00	±	3.21E-02
FV0	(relative)	floated	1.00E+00	±	7.70E-02	9.95E-01	±	7.59E-02
FV1	(relative)	floated	1.00E+00	±	4.30E-02	1.00E+00	±	4.28E-02
FV2	(relative)	floated	1.00E+00	±	5.10E-02	9.99E-01	±	5.10E-02

Table 9.15: Best-fit number of events (Divided unoscillated shape fit) (*SolarPhase*)

BGs	2–3.5 MeV			3.5–5 MeV			5–20 MeV		
^{8}BνES2–3	0.00	±	5.34	0.00	±	0.00	0.00	±	0.00
^{8}BνES3–5	4.77	±	0.73	66.46	±	10.10	0.00	±	0.00
^{8}BνES5–20	0.00	±	0.00	0.00	±	0.00	59.84	±	13.66
ExtL	3.04	±	0.61	0.00	±	0.00	0.00	±	0.00
ExtM	0.00	±	0.00	1.95	±	1.59	0.00	±	0.00
ExtH	0.00	±	0.00	0.00	±	0.00	5.62	±	3.50
Tl208	0.00	±	0.69	0.00	±	9.97	0.00	±	0.00
SpaN12	0.00	±	fixed	0.00	±	fixed	0.00	±	fixed
SpaB12	0.01	±	fixed	0.06	±	fixed	0.17	±	fixed
SpaHe8	0.00	±	fixed	0.00	±	fixed	0.00	±	fixed
SpaC9	0.00	±	fixed	0.00	±	fixed	0.02	±	fixed
SpaLi9	0.01	±	fixed	0.08	±	fixed	0.23	±	fixed
SpaB8	0.01	±	0.03	0.09	±	0.36	0.32	±	1.22
SpaLi8	0.54	±	0.54	4.15	±	4.15	8.58	±	8.57
SpaBe11	0.05	±	0.06	0.51	±	0.59	1.27	±	1.48
SpaC10	5.72	±	3.60	0.01	±	0.01	0.00	±	0.00
SpaHe6	0.57	±	0.71	0.00	±	0.01	0.00	±	0.00
C13CCG	0.04	±	fixed	0.54	±	fixed	2.08	±	fixed
C13CCE	0.09	±	fixed	0.75	±	fixed	0.78	±	fixed
C13NC	0.11	±	0.05	2.21	±	0.96	0.00	±	0.00
C11	0.12	±	0.01	0.00	±	0.00	0.00	±	0.00
AtmNu	0.02	±	0.01	0.10	±	0.03	0.45	±	0.14
hepES	0.02	±	0.00	0.09	±	0.01	0.18	±	0.03
Pa234	0.16	±	5.83	0.00	±	0.00	0.00	±	0.00
Ac228	0.60	±	1.07	0.00	±	0.00	0.00	±	0.00
BestFitTotal	15.88	±	8.87	77.01	±	14.92	79.53	±	16.62
Observed	15			77			79		

Table 9.16: Estimations vs best-fit parameters (Divided unoscillated fit) (*AfterZen*)

Parameters	Unit	Condition	Estimation (Constraint)			Best-fit		
^{8}BνES2–3	10^6/cm^2/s	floated				5.17E+00	±	1.83E+00
^{8}BνES3–5	10^6/cm^2/s	floated				2.39E+00	±	6.59E-01
^{8}BνES5–20	10^6/cm^2/s	floated				3.06E+00	±	6.06E-01
ExtL	(relative)	floated	1.00E+00	±	2.00E-01	9.81E-01	±	1.94E-01
ExtM	(relative)	floated	1.00E+00	±	8.00E-01	1.12E+00	±	7.93E-01
ExtH	(relative)	floated	1.00E+00	±	6.00E-01	8.84E-01	±	5.25E-01
Tl208	/day/kt	floated	7.61E-01	±	4.32E-01	3.92E-01	±	2.13E-01
SpaN12	/day/kt	fixed	1.00E-08	±	2.99E-06	0.00E+00	±	fixed
SpaB12	/day/kt	fixed	7.88E-03	±	1.44E-02	7.88E-03	±	fixed
SpaHe8	/day/kt	fixed	1.00E-08	±	1.62E-02	0.00E+00	±	fixed
SpaC9	/day/kt	fixed	1.00E-08	±	1.12E-02	0.00E+00	±	fixed
SpaLi9	/day/kt	fixed	1.56E-02	±	3.21E-02	1.56E-02	±	fixed
SpaB8	/day/kt	floated	1.00E-08	±	8.62E-02	2.65E-04	±	8.56E-02
SpaLi8	/day/kt	floated	3.47E-01	±	3.41E-01	3.34E-01	±	2.92E-01
SpaBe11	/day/kt	floated	2.53E-02	±	5.17E-02	2.48E-02	±	5.20E-02
SpaC10	/day/kt	floated	1.00E-08	±	9.83E-02	5.99E-09	±	9.13E-02
SpaHe6	/day/kt	floated	1.32E-01	±	2.34E-01	1.12E-01	±	2.21E-01
C13CCG	(relative)	fixed	1.00E+00	±	0.00E+00	1.00E+00	±	fixed
C13CCE	(relative)	fixed	1.00E+00	±	0.00E+00	1.00E+00	±	fixed
C13NC	(relative)	floated	1.00E+00	±	4.00E-01	1.02E+00	±	4.06E-01
C11	/day/kt	floated	1.07E+03	±	1.58E+02	1.07E+03	±	1.57E+02
AtmNu	(relative)	floated	1.00E+00	±	3.00E-01	1.07E+00	±	2.95E-01
hepES	(relative)	floated	1.00E+00	±	1.60E-01	1.00E+00	±	1.62E-01
Pa234	/day/kt	floated	2.49E+01	±	4.29E+01	5.69E-05	±	3.07E+01
Ac228	/day/kt	floated	1.00E-08	±	7.94E+01	4.27E-08	±	6.08E+01
Alpha	(relative)	floated	1.00E+00	±	4.30E-02	9.83E-01	±	2.16E-02
FV0	(relative)	floated	1.00E+00	±	1.05E-01	9.90E-01	±	9.82E-02
FV1	(relative)	floated	1.00E+00	±	5.90E-02	1.00E+00	±	5.61E-02
FV2	(relative)	floated	1.00E+00	±	6.90E-02	1.00E+00	±	6.02E-02

Table 9.17: Best-fit number of events (Divided unoscillated shape fit)(*AfterZen*)

BGs	2–3.5 MeV			3.5–5 MeV			5–20 MeV		
^{8}BνES2–3	10.02	±	3.55	0.00	±	0.00	0.00	±	0.00
^{8}BνES3–5	2.15	±	0.59	30.38	±	8.37	0.00	±	0.00
^{8}BνES5–20	0.00	±	0.00	0.00	±	0.00	40.35	±	7.99
ExtL	1.96	±	0.39	0.00	±	0.00	0.00	±	0.00
ExtM	0.00	±	0.00	1.71	±	1.21	0.00	±	0.00
ExtH	0.00	±	0.00	0.00	±	0.00	3.24	±	1.92
Tl208	1.02	±	0.56	9.81	±	5.33	0.00	±	0.00
SpaN12	0.00	±	fixed	0.00	±	fixed	0.00	±	fixed
SpaB12	0.01	±	fixed	0.05	±	fixed	0.13	±	fixed
SpaHe8	0.00	±	fixed	0.00	±	fixed	0.00	±	fixed
SpaC9	0.00	±	fixed	0.00	±	fixed	0.00	±	fixed
SpaLi9	0.01	±	fixed	0.05	±	fixed	0.13	±	fixed
SpaB8	0.00	±	0.05	0.00	±	0.52	0.00	±	1.60
SpaLi8	0.34	±	0.30	2.64	±	2.31	5.00	±	4.37
SpaBe11	0.02	±	0.04	0.18	±	0.37	0.40	±	0.84
SpaC10	0.00	±	0.45	0.00	±	0.00	0.00	±	0.00
SpaHe6	0.23	±	0.45	0.00	±	0.00	0.00	±	0.00
C13CCG	0.03	±	fixed	0.39	±	fixed	1.33	±	fixed
C13CCE	0.06	±	fixed	0.52	±	fixed	0.48	±	fixed
C13NC	0.19	±	0.08	1.03	±	0.41	0.00	±	0.00
C11	0.01	±	0.00	0.00	±	0.00	0.00	±	0.00
AtmNu	0.01	±	0.00	0.07	±	0.02	0.33	±	0.09
hepES	0.01	±	0.00	0.06	±	0.01	0.11	±	0.02
Pa234	0.00	±	1.25	0.00	±	0.00	0.00	±	0.00
Ac228	0.00	±	0.32	0.00	±	0.00	0.00	±	0.00
BestFitTotal	16.07	±	3.95	46.88	±	10.29	51.50	±	9.48
Observed	15			47			52		

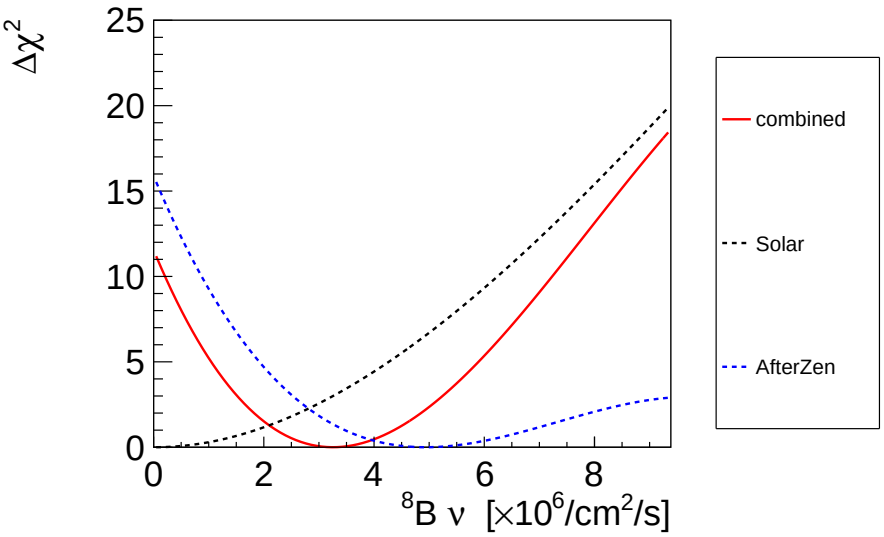

Figure 9.21: 2–3 MeV flux.

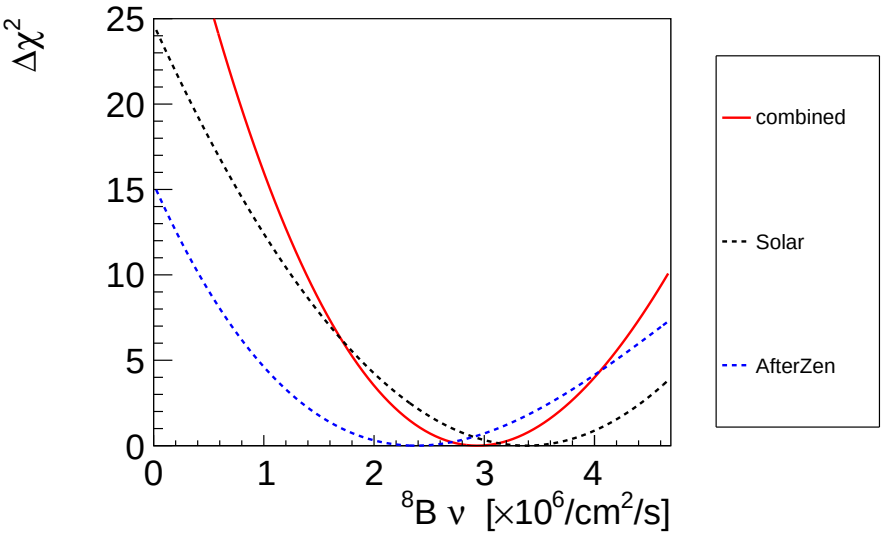

Figure 9.22: 3–5 MeV flux.

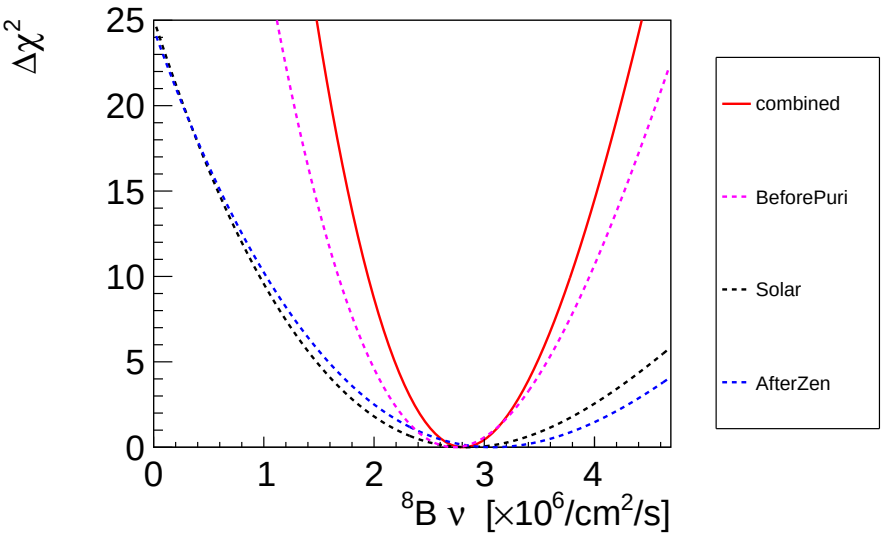

Figure 9.23: > 5 MeV flux.

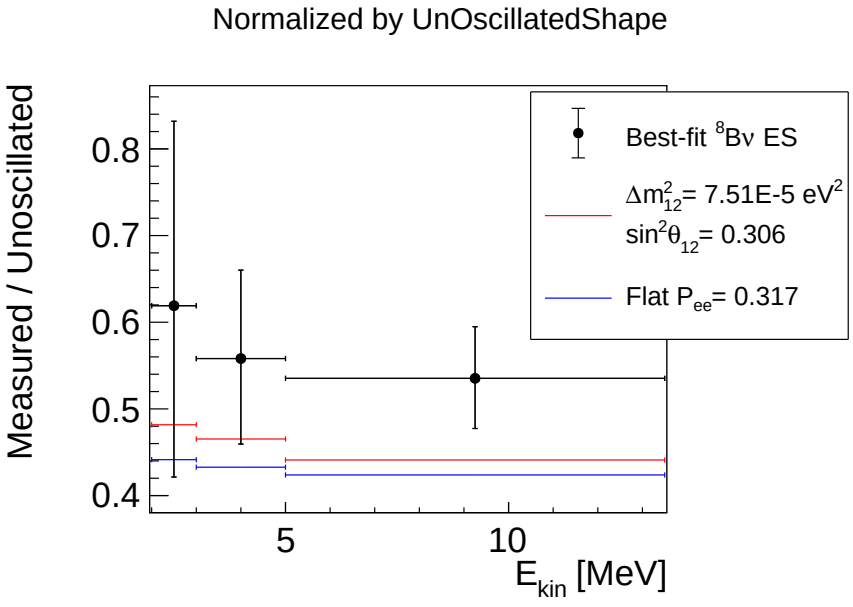

Figure 9.24: Measured flux in each energy region.

9.7 Rate+Shape Analysis (P_{ee} Approximation)

In Ref. [19], SNO modeled their CC+NC+ES combined data with six parameters as

$$\Phi_{\rm obs}(E_\nu;\Phi_{\rm total},c_0,c_1,c_2,a_0,a_1)=\Phi_{\rm total}P_{ee}(E_\nu), \tag{9.93}$$

$$P_{ee}(E_\nu)=R_DP_{ee}^D+R_NP_{ee}^N, \tag{9.94}$$

where

- $\Phi_{\rm total}$: ^{8}B solar ν total flux
- R_D: day-livetime ratio
- R_N: night-livetime ratio
- P_{ee}^D: day-time survival probability
- P_{ee}^N: night-time survival probability

P_{ee}^D was approximated with a quadratic function

$$P_{ee}^D\sim c_0+c_1(E_\nu/{\rm MeV}-10)+c_2(E_\nu/{\rm MeV}-10)^2. \tag{9.95}$$

The day/night asymmetry was modeled with a linear function

$$A_{DN}\equiv\frac{P_{ee}^N-P_{ee}^D}{(P_{ee}^N+P_{ee}^D)/2}\sim a_0+a_1(E_\nu/{\rm MeV}-10). \tag{9.96}$$

Therefore P_{ee} can be expressed with $P_{ee}^D(c_0,c_1,c_2)$ and $A_{DN}(a_0,a_1)$

$$P_{ee}(c_0,c_1,c_2,a_0,a_1)=(R_D+R_N\frac{2+A_{DN}}{2-A_{DN}})P_{ee}^D. \tag{9.97}$$

SK followed the same way with SNO and derived constraints on (c_0,c_1,c_2) using their ES data [18]. Therefore, by following the same way, it is possible to combined our data with SNO's and SK's ones.

Figure 9.25 shows the P_{ee} expected from the best-fit oscillation parameters ($\Delta m^2_{12}=7.15\times10^{-5}$ eV^2, $\sin^2(\theta_{12})=0.306$, $\sin^2(\theta_{13})=0.0219$) [38] and its approximation with a quadratic function ($c_0=0.321$, $c_1=-0.00790$, $c_2=0.00143$).

9.7.1 Day/Night Asymmetry Correction

In Ref. [18], SK corrected SNO's 6D result with their day/night asymmetry result. However there was a relatively huge change in the value of reported day/night asymmetry recently:

- $(-3.6\pm1.7)\%$ [18] $\rightarrow$ $(-2.1\pm1.1)\%$ [38]

Figure 9.26 shows the comparison of the day/night asymmetry effects expected in SNO with the following setups:

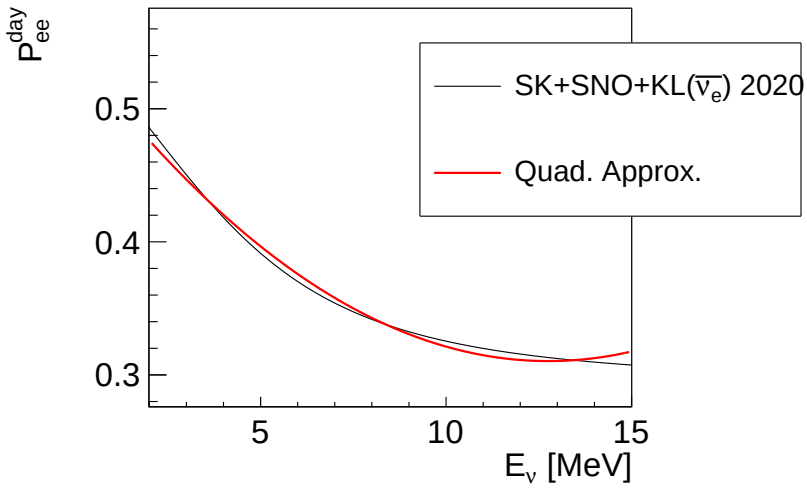

Figure 9.25: P_{ee} best-fit oscillation vs approximation

- SK2020+SNO2013+KamLAND($\bar{\nu}_e$) (global2020):
  $\Delta m^2_{12} = 7.15 \times 10^{-5}$ eV^2, $\sin^2(\theta_{12}) = 0.306$, $\sin^2(\theta_{13}) = 0.0219$
- SK2020+SNO (solar2020):
  $\Delta m^2_{12} = 6.1 \times 10^{-5}$ eV^2, $\sin^2(\theta_{12}) = 0.306$, $\sin^2(\theta_{13}) = 0.0219$
- SK2016+SNO (solar2016):
  $\Delta m^2_{12} = 4.8 \times 10^{-5}$ eV^2, $\sin^2(\theta_{12}) = 0.310$, $\sin^2(\theta_{13}) = 0.0219$

From the solar2020 case, I obtained the day/night asymmetry parameters as follows:

- $a_0 = 0.04657$
- $a_1 = 0.00654$

These values can be used for the new correction reflecting the result of Ref. [38]. Figure 9.27 shows the comparison of P^D_{ee} among three conditions, the original SNO 6-dimensional result, one with the old correction and one with the new correction. The impact of the change of the correction is more significant in SK+SNO combined results[2], see Figure 9.28. The old correction overly corrected the *downturn*-feature of the day/night asymmetry. It gave more *upturn*-like shape of P^D_{ee}.

[2]For SK's (c_0, c_1, c_2), reported values in Ref. [18] were just used. They are affected by the old D/N correction.

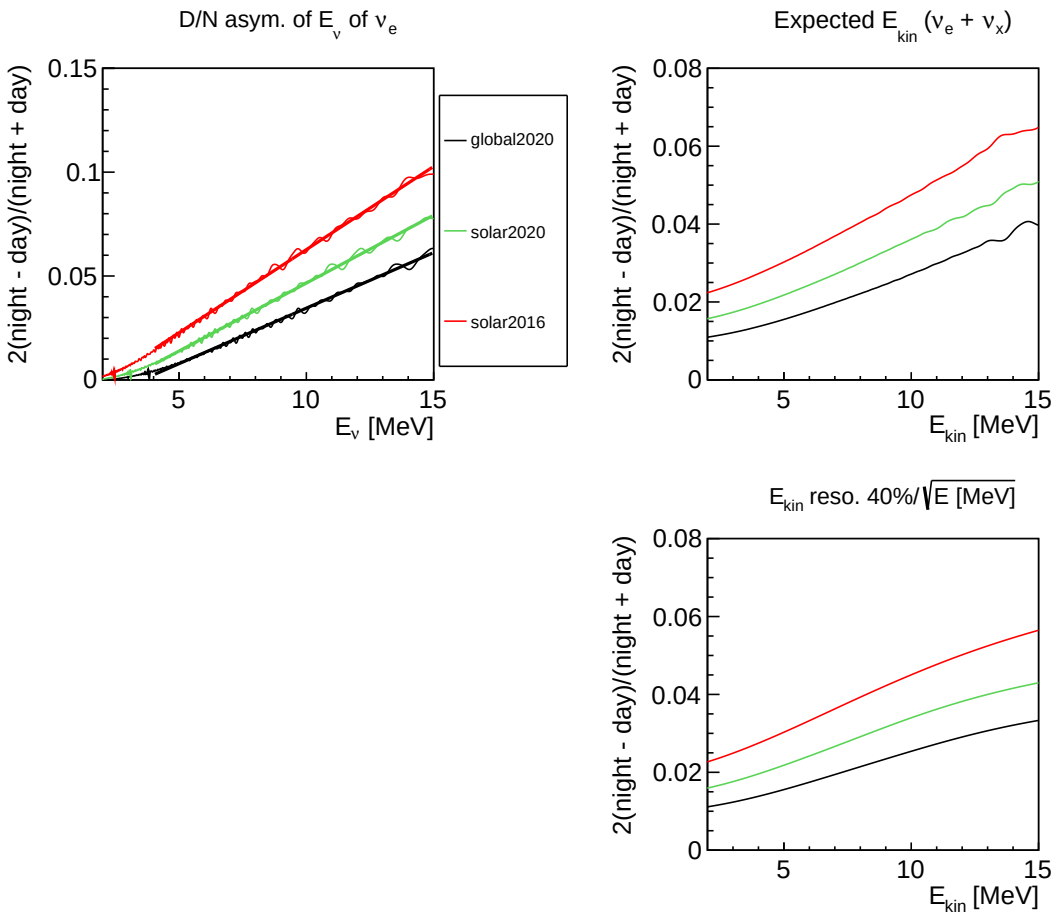

Figure 9.26: Day night asymmetry at SNO

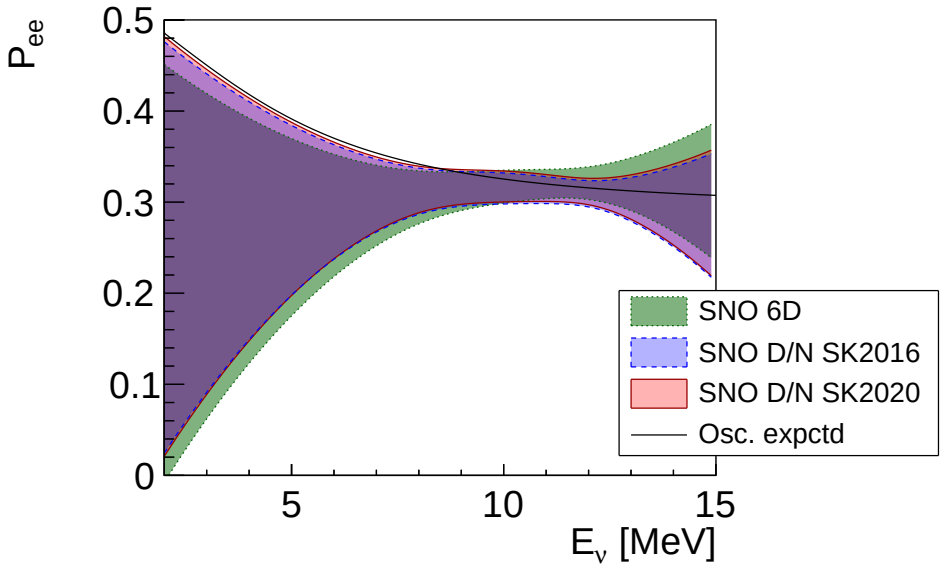

Figure 9.27: P_{ee} SNO 1σ band

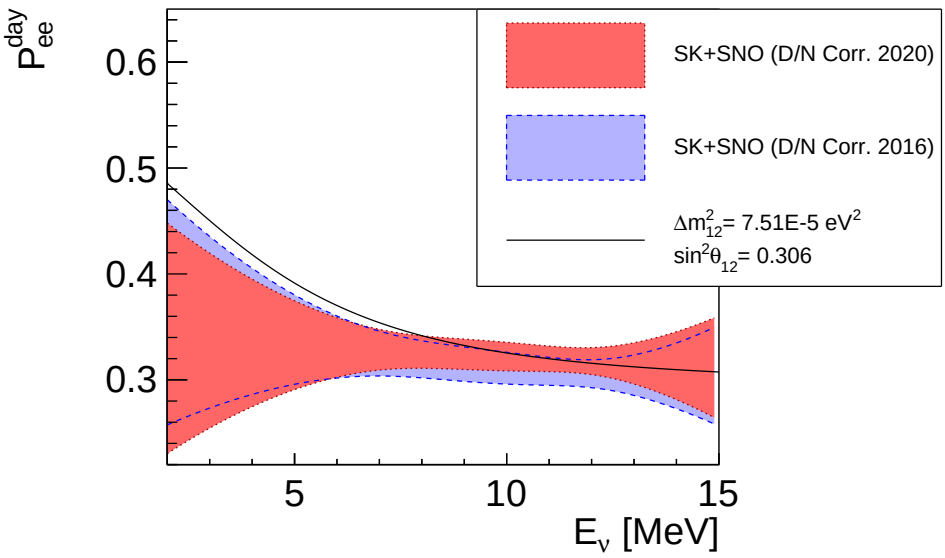

Figure 9.28: P_{ee} SK+SNO 1σ band

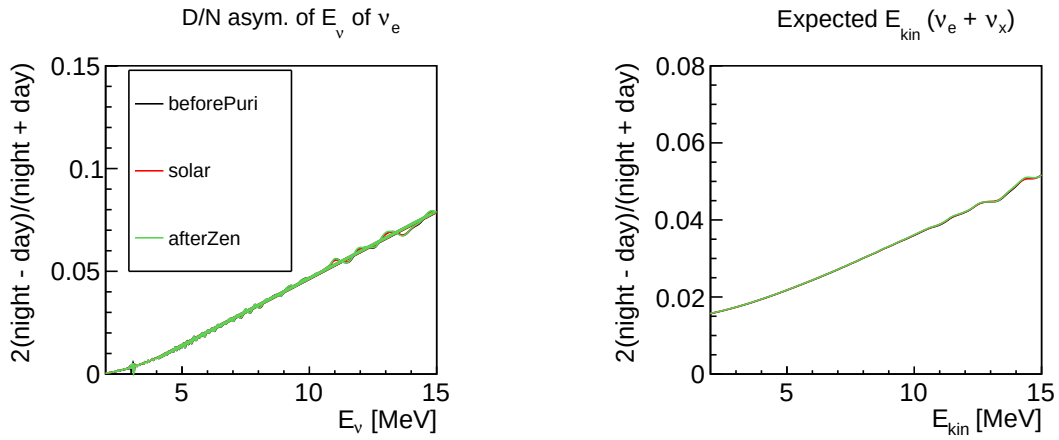

Figure 9.29: Day night asymmetry at KamLAND

The day/night asymmetry in KamLAND in each phase was also studied assuming solar2020 condition, see Figure 9.29. The difference among periods was small. Therefore I use the fit result of *BeforePurif* for the correction of all phases:

- $a_0 = 0.0464818$
- $a_1 = 0.00651602$

These are almost same as the ones for SNO.

The night-time livetime ratios were estimated as follows:

- *BeforePurif*: 0.536
- *SolarPhase*: 0.5106
- *AfterZen*: 0.5121

9.7.2 Spectrum Fitting

I fitted the energy spectrum of each phase replacing the ^{8}B ν ES spectrum with the P_{ee}-approximated one. The total flux of 5.25×10^6 /cm^2/s was assumed. Figure 9.30, 9.31, 9.32 show the best-fit spectra. The best-fit parameters (c_0, c_1, c_2) are summarized in Table 9.18. Figure 9.36 shows the corresponding P_{ee} curves.

Table 9.18: Summary of P_{ee} approximated fit results

Period	c_0			c_1			c_2		
BeforePurif	0.392	±	0.070	-0.120	±	0.030	-0.024	±	0.018
SolarPhase	0.518	±	0.105	-0.080	±	0.050	-0.030	±	0.019
AfterZen	0.392	±	0.112	-0.020	±	0.050	0.005	±	0.018

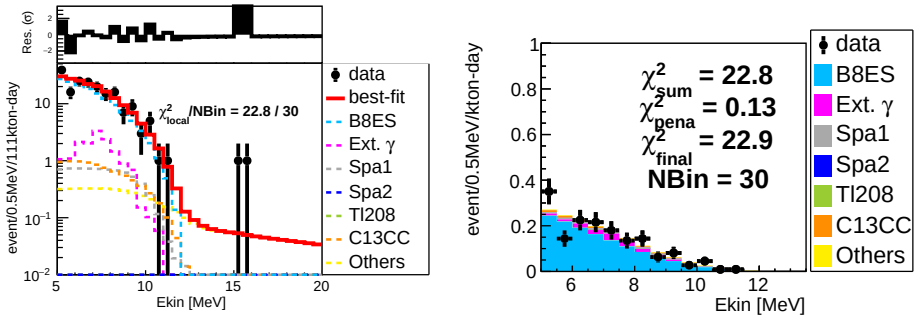

Figure 9.30: Fit with quadratic approximation (*BeforePurif*). Best-fit energy scale = 1.005.

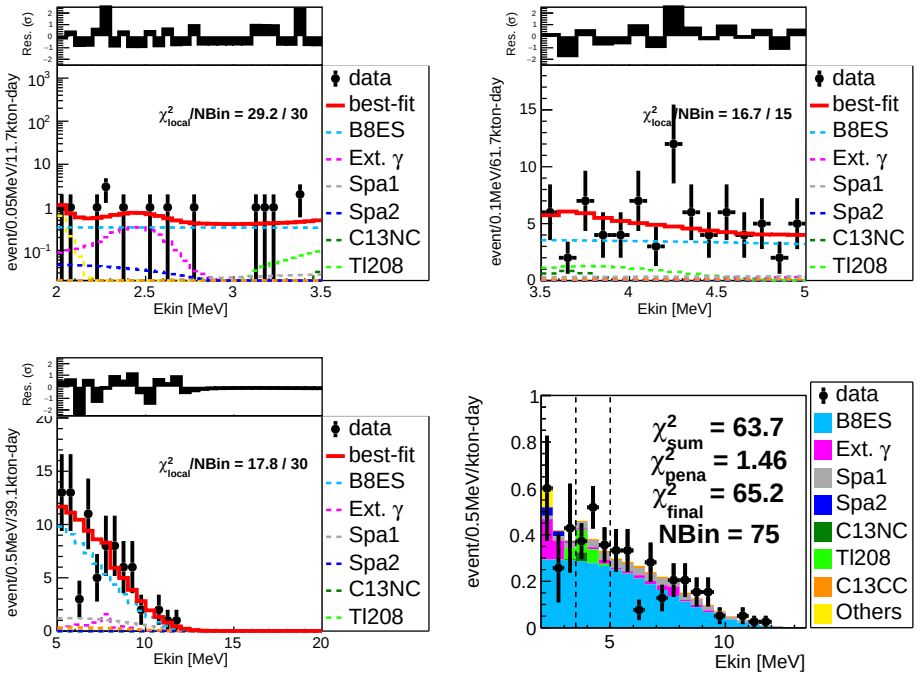

Figure 9.31: Fit with quadratic approximation (*SolarPhase*). Best-fit energy scale = 1.026.

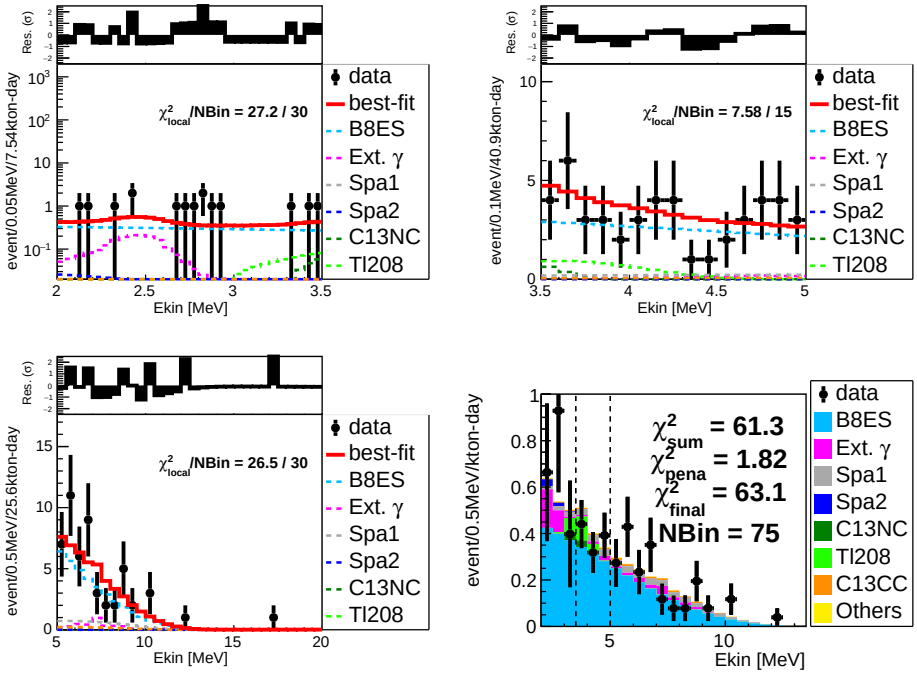

Figure 9.32: Fit with quadratic approximation (*AfterZen*). Best-fit energy scale = 0.987.

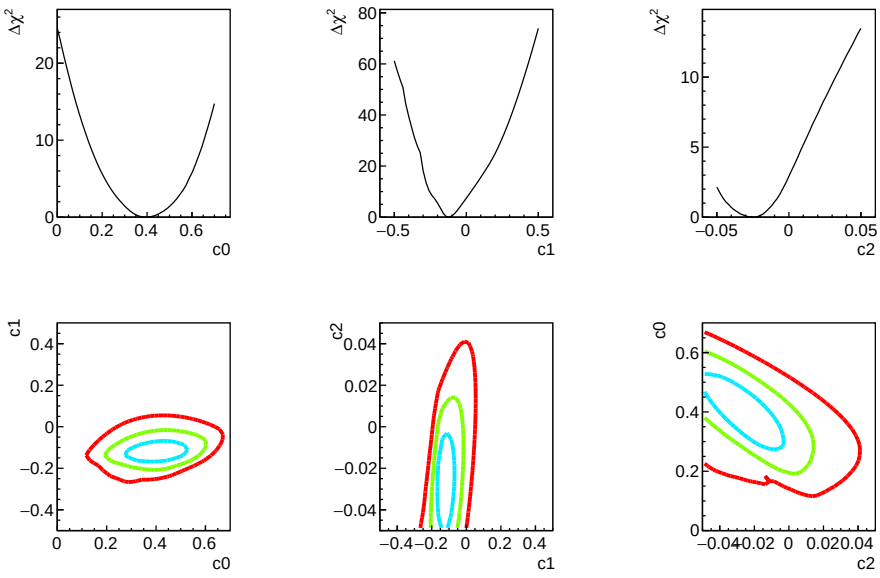

Figure 9.33: Constraints on (c_0, c_1, c_2) (*BeforePurif*) (2D d.o.f, 1,2,3σ)

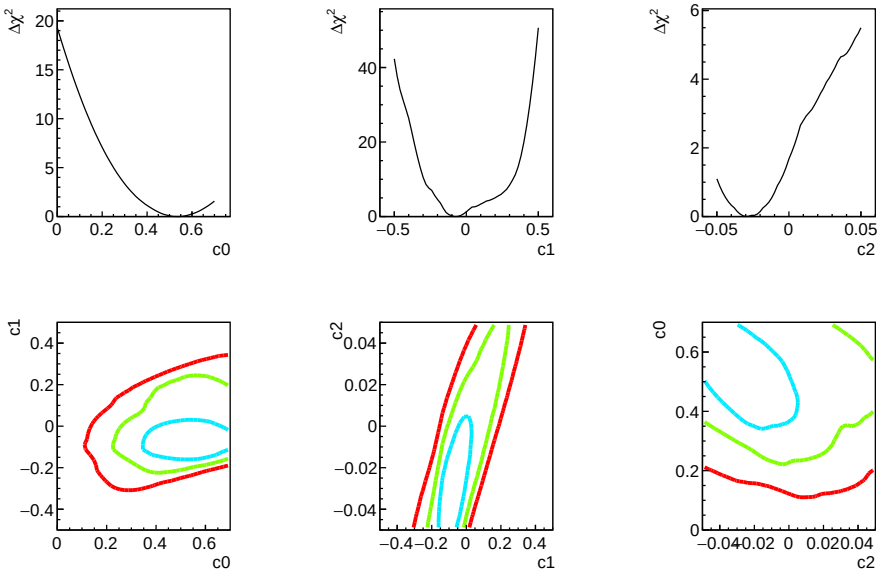

Figure 9.34: Constraints on (c_0, c_1, c_2) (*SolarPhase*) (2D d.o.f, 1,2,3σ)

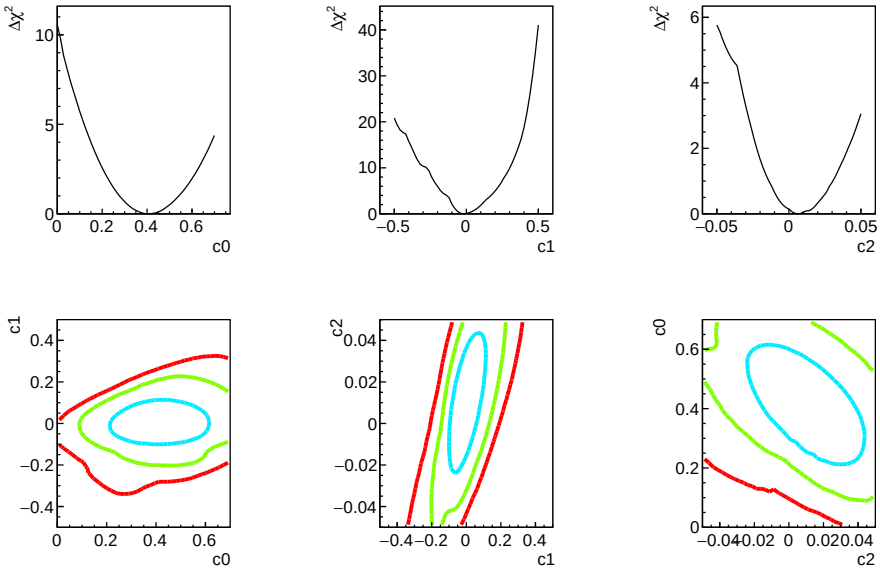

Figure 9.35: Constraints on (c_0, c_1, c_2) (*AfterZen*) (2D d.o.f, 1,2,3σ)

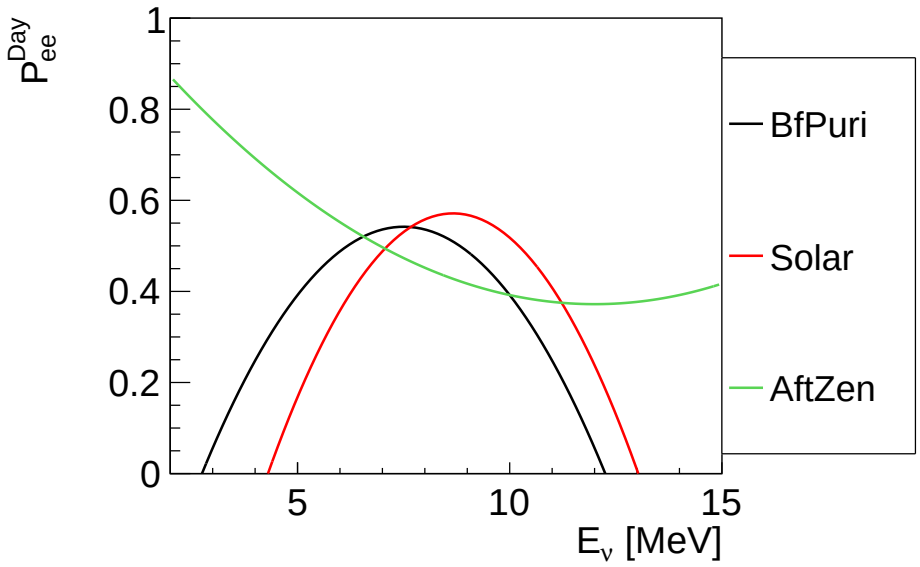

Figure 9.36: Best-fit P_{ee} of each phase

3-phases Combined Result

Figure 9.37 shows the 3-phases combined constraints on (c_0, c_1, c_2). Figure 9.38 shows the corresponding P_{ee} bands. The following are the measured parameters:

- $c_0 = 0.427 \pm 0.099$
- $c_1 = -0.0827 \pm 0.0600$
- $c_2 = -0.0182 \pm 0.0212$
- c_0-c_1 corr. $= 0.107$
- c_1-c_2 corr. $= 0.669$
- c_2-c_0 corr. $= -0.575$

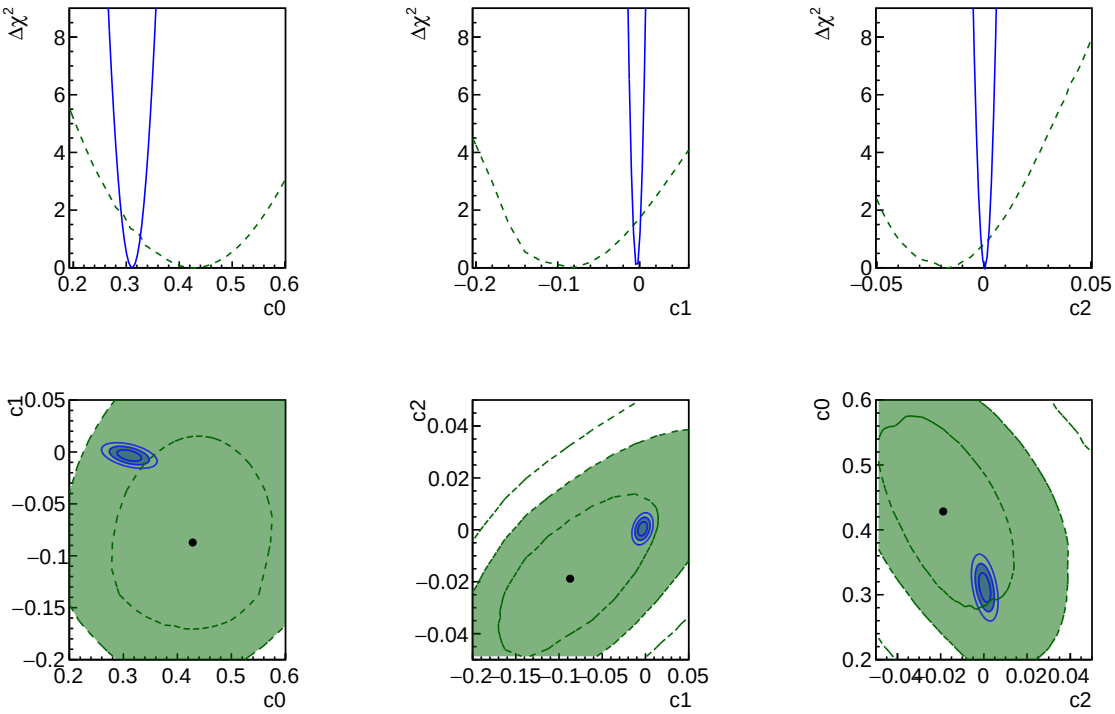

Figure 9.37: Constraints on (c_0, c_1, c_2). (2 d.o.f 1,2,3σ) Green is KamLAND. Blue is SK+SNO.

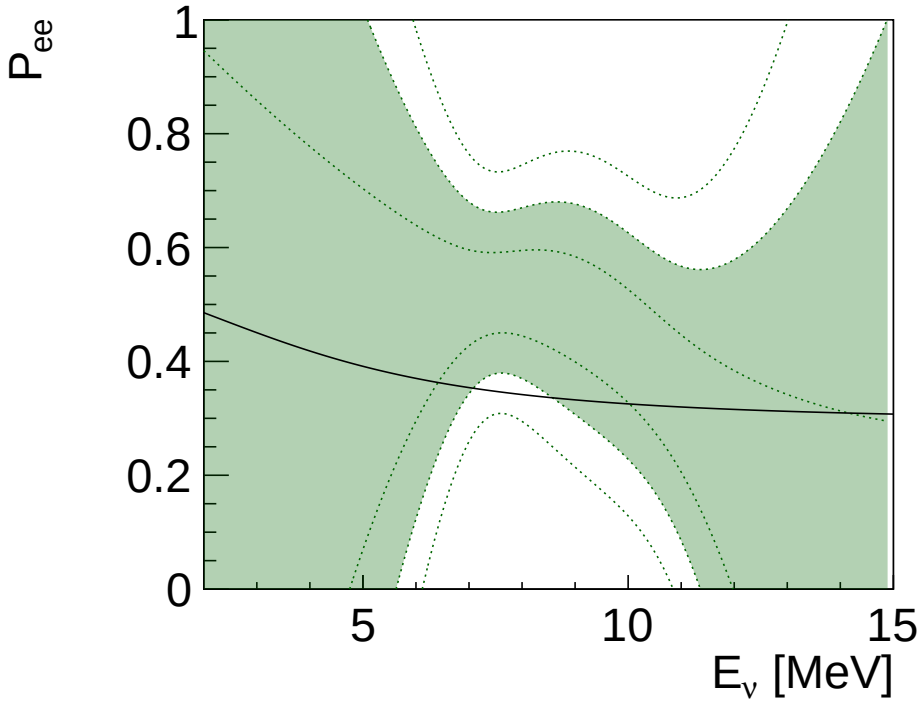

Figure 9.38: KamLAND constraints on P_{ee}. 1, 2, 3σ bands.

9.7.3 Combination with SK and SNO

Figure 9.39 shows the SK+SNO+KamLAND(this work) combined constraints on (c_0, c_1, c_2). Figure (1σ), (1, 2, 3σ) show the corresponding P_{ee} bands. The obtained constraints on the parameters are summarized in Table 9.19. The addition of the KamLAND result pulled up P_{ee} at lower energy towards the direction expected from the best-fit oscillation model. $\Delta\chi^2$ (p-value) for the flat model ($c_1 = c_2 = 0$) was slightly increased (decreased) from 0.35 (84%) (SK+SNO) to 0.89 (64%) (SK+SNO+KamLAND).

Table 9.19: Summary of constraints on (c_0, c_1, c_2)

Parameter	SK+SNO	SK+SNO+KamaLAND(this work)	Osci. expected
c_0	0.3220 ± 0.0135	0.3274 ± 0.0130	0.321
c_1	-0.0021 ± 0.0038	-0.0033 ± 0.0037	-0.00790
c_2	0.0000 ± 0.0019	0.0001 ± 0.0018	0.00143
c_0-c_1 corr.	-0.337	-0.323	
c_1-c_2 corr.	0.285	0.295	
c_2-c_0 corr.	-0.474	-0.489	

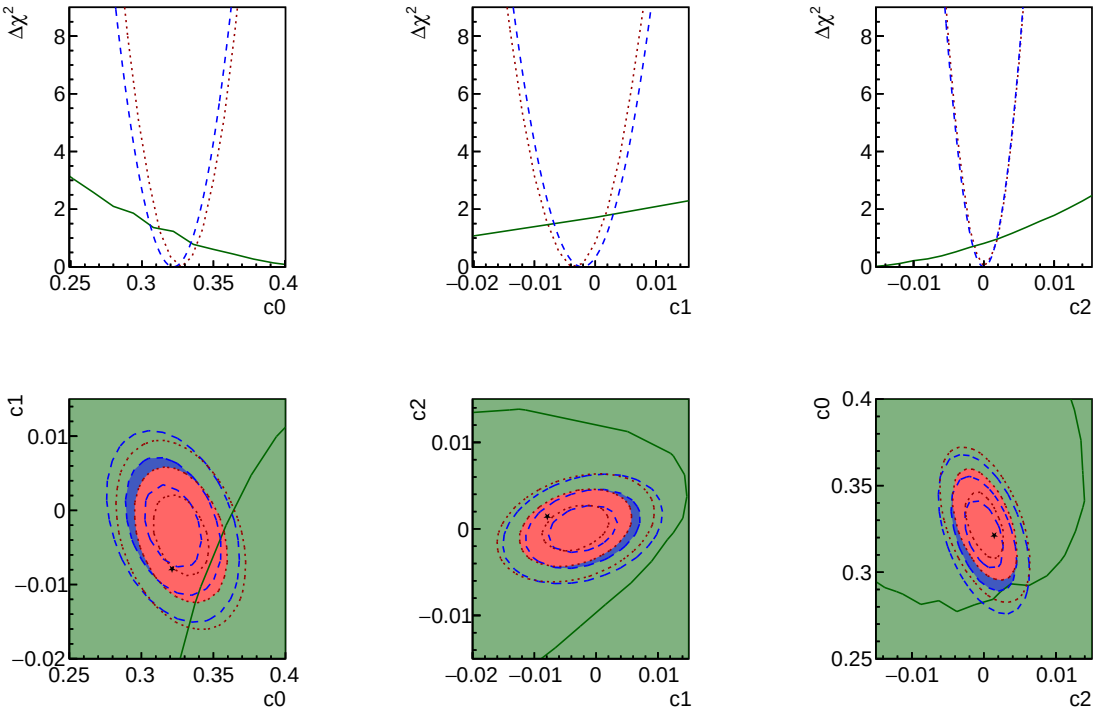

Figure 9.39: Combined constraints on (c_0, c_1, c_2). Green is KamLAND, blue is SK+SNO and red is SK+SNO+KamLAND. Contours correspond to 1, 2 and 3σ. Black point is the best-approximation of the best-fit oscillation model.

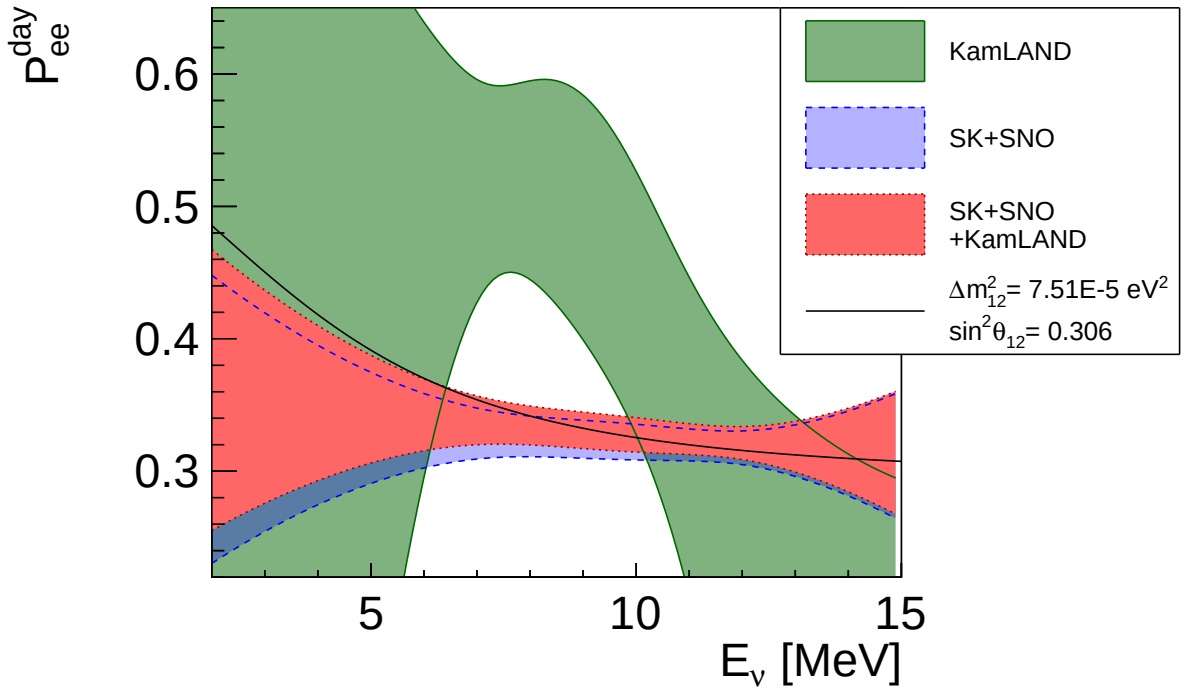

Figure 9.40: P_{ee} 1 σ bands.

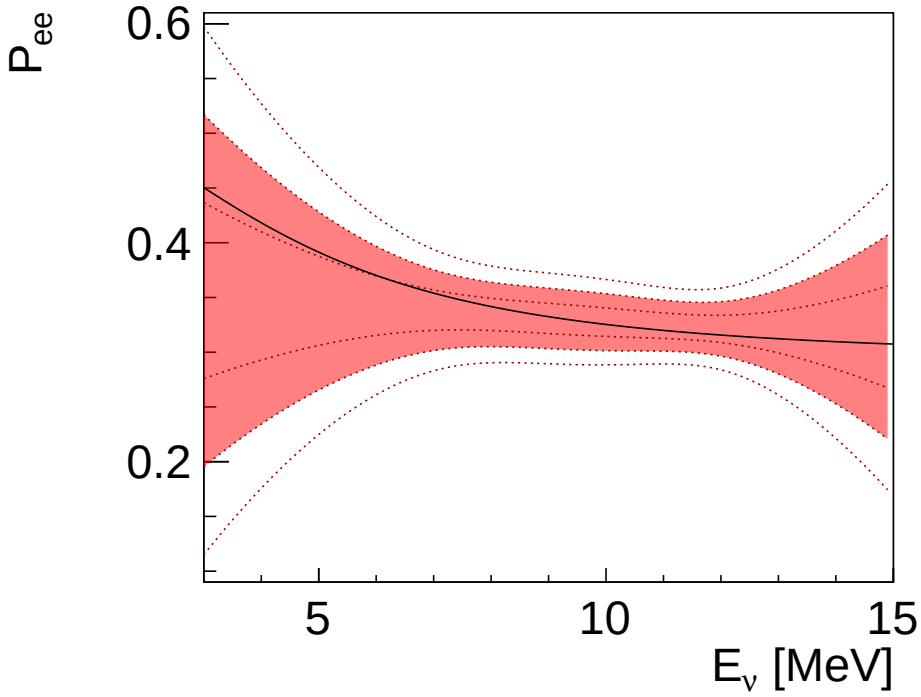

Figure 9.41: SK+SNO+KamLAND combined P_{ee} 1,2, 3σ bands.

10 Discussion

10.1 Uncertainties

The total uncertainty on the measured flux, normalized by 2.35×10^6 /cm^2/s [38], in each energy region is as follows:

- 2–3 MeV: 47%
- 3–5 MeV: 22%
- 5–20 MeV: 12%

10.1.1 Impact of the Energy Scale Uncertainty

In this study, a linear energy scale uncertainty of 4.3% is applied to all phases. The following are impacts of the uncertainty on the unoscillated ^{8}B solar ν ES flux:

- 2–3 MeV: 3.4%
- (2–3.5 MeV): 3.2%
- (3.5–5 MeV): 1.6%
- 5–20 MeV: 7.5%

10.1.2 Impact of the Fiducial Volume Uncertainty

Fiducial volume uncertainties in each phase were described in Section 4.3.3. The following are the recap:

- 2–3.5 MeV ($r < 2$ m): 7.7–10.5%
- 3.5–5 MeV ($r < 3.5$ m): 4.3–5.9%
- 5–20 MeV ($r < 3$ m): 3% (*BeforePurif*)

10.1.3 Summary on Uncertainties

The uncertainties were basically dominated by statistical ones. Thus better accuracy is expected simply with more exposure. Background estimations of ^{208}Tl and spallation products may also be improved with it. The 4.3% energy scale uncertainty is getting significant at 5–20 MeV analysis. It mainly comes from the uncertainty of the energy model, which can also be studied further with more statistics using spallation ^{12}B events.

10.2 Prospects for Future LS Experiments

As can be seen from Figure 9.24, the expected ES flux difference at 2–5 MeV region between the best-fit oscillation model and the flat model is around 10%. That is, we have to measure the flux at that energy region at a few % uncertainty to detect the *upturn*. Given the expected event rate ~ 2 /d/kt (2–5 MeV), 5000 d-kt exposure is needed for 1% statistical error. It's, roughly speaking, a two-year-measurement with a 10 kt detector assuming a $\sim 70\%$ livetime.

A 20-kt LS detector, JUNO [104, 105], is currently being constructed. After a spatial cut for external backgrounds, it is expected that its target mass will be 12.2 kt (7.9 kt) at 3–5 MeV (2–3 MeV).

Its experimental site is shallower than KamLAND. Resulting cosmic muon flux is 2.5 times higher than that of KamLAND. Backgrounds from spallation products won't be so serious with the background reduction performance shown in this thesis. A simulation in Ref. [104] adopted *n-tag* and a 3-m cylinder cut along muon tracks. The cylinder cut yielded 40% deadtime. This can be reduced with a replacement of the cut with *shower-tag*.

The level of the LS-intrinsic background, ^{208}Tl, cannot be known until the commissioning. *Day-scale* tag (and BiTl tag) can loosen the acceptable ^{232}Th concentration in LS from $\mathcal{O}(10^{-17})$ g/g to $\mathcal{O}(10^{-16})$ g/g.

No unexpected backgrounds were observed in my study. Therefore their simulation result, $> 7\sigma$ level rejection of the flat model with 10 years of data acquisition, looks promising if the desired fiducial volume uncertainty ($< 1\%$) and energy scale uncertainty ($< 0.3\%$) are achieved.

10.3 Implications for Double-beta Decay Experiments

(Neutrino-less) double-beta ($(0\nu)\beta\beta$) decay experiments often search for signals at 2–3 MeV energy region. No unexpected backgrounds were observed in my study in that energy region. This fact is complemental for $\beta\beta$ experiments especially using LS like KamLAND-Zen and SNO+.

As a direct contribution, the combination of spallation background reduction, *shower-tag* and *n-tag*, was used in the KamLAND-Zen 800 result [7].

10.4 ν_x + ^{13}C Neutral Current

A signal from the ν_x + ^{13}C neutral current (NC) interaction is 3.685 MeV mono-energetic γ. The expected rate from ^{8}B solar ν is ~ 0.05 /d/kt. Given the livetime of *SolarPhase* (441 days) and *AfterZen* (292 days) and 140 ton fiducial mass, the expected number of events is 5.1.

KamLAND-Zen periods are also available for this signal search with a different fiducial volume selection, $3 < r < 3.5$ m. The target mass in this case is 52 ton. The following are the runtime of each period:

- *Zen400 1st*: 210 days
- *Zen400 2nd*: 690 days

- *Zen800*: 1400 days

Assuming 70% livetime-ratio, the total livetime becomes 1600 days. The expected number of events is 4.2.

In total 9.3 events are expected. With more study on the external backgrounds, enlargement of fiducial radius up to $r = 4$ m may be possible. In this case, statistics of *SolarPhase* and *AfterZen* are increased by a factor of 1.5. The factor for KamLAND-Zen periods is 2.3. Then total expected number of events will be 17. Moreover, *Zen800* is still accumulating data.

ES signal is the primary background for this NC search. A particle identification tool, KamNET, has been developed recently [106]. It yielded $\beta\beta$ acceptance of 90% while suppressing ^{214}Bi ($\beta\gamma$) acceptance to 70%. The NC signal is pure γ. Therefore a higher discrimination performance is expected in the ES (β) vs NC (γ) case. The NC energy region is higher than the $\beta\beta$ study case (2–3 MeV) and higher photon statistics would also provide better performance. The directional information from the Cherenkov photons might also be available[1]. If, roughly saying, 50% NC acceptance is achieved while suppressing ES acceptance to 10%, the detection significance is expected to be 1.5σ (2σ) for the 3.5-m analysis (4-m analysis)[2].

In this NC search, after the application of the particle identification tool, the ultimate background will be ^{208}Tl ($\beta\gamma$). *Day-scale* tag and BiTl tag play crucial roles here.

[1] 3.5 MeV visible energy corresponds to $\sim$ 1000 p.e. A few percent of that (10–30 p.e.) comes from direct Cherenkov photons. An enrichment is available with an early timing selection in some level.

[2] Assumptions: Energy ROI $\pm$0.25 MeV around 3.69 MeV. Expected ES rate is 0.27 /d/kt.

11 Conclusion

In this study, novel methods were introduced to reduce single event backgrounds from muon spallation products and LS-intrinsic ^{208}Tl. More than 90% rejection efficiency of the spallation products above 2 MeV in all analysis periods and 80–90% rejection efficiency of ^{208}Tl in *SolarPhase* and *AfterZen* were achieved. Remaining events with 2–15 MeV energy after the cuts are dominated by ^{8}B solar ν ES events.

A rate + shape analysis yielded the world first measurement of the ^{8}B solar ν flux with ES at the 2–3 MeV $E_{\rm kin}$ region as

$$(3.25^{+1.11}_{-1.03}) \times 10^6 \ /\mathrm{cm}^2/\mathrm{s},$$

which was $0.62^{+0.21}_{-0.20}$ of the expectation from the unoscillated flux. The null-rejection significance was 3.4σ. Fluxes (ratios to the unoscillated expectations) measured at other energy regions were:

- 3–5 MeV: $(2.93^{+0.52}_{-0.51}) \times 10^6$ /cm^2/s $(0.56^{+0.10}_{-0.10})$
- 5–20 MeV: $(2.81^{+0.29}_{-0.28}) \times 10^6$ /cm^2/s $(0.535^{+0.060}_{-0.058})$

No significant differences from the result of SK, $(2.35 \pm 0.04) \times 10^6$ /cm^2/s [38], were observed.

The energy dependence of the day-time survival probability of ^{8}B solar ν_e on the Earth, P^D_{ee}, was approximated with a quadratic function to test *upturn*. In a combined analysis, p-value for the flat model (no *upturn* model) decreased from 84% (SK+SNO) to 64% (SK+SNO+KamLAND).

No unknown backgrounds were observed in 2–3 MeV region. This fact may be helpful for future LS experiments and $0\nu\beta\beta$ experiments.

Bibliography

[1] K. S. Hirata *et al.*, Observation of ^{8}B solar neutrinos in the Kamiokande-II detector, Phys. Rev. Lett. **63** (1989) 16–19. doi:10.1103/PhysRevLett.63.16.
URL https://link.aps.org/doi/10.1103/PhysRevLett.63.16

[2] S. Fukuda *et al.*, Solar ^8B and hep Neutrino Measurements from 1258 Days of Super-Kamiokande Data, Phys. Rev. Lett. **86** (2001) 5651–5655. doi:10.1103/PhysRevLett.86.5651.
URL https://link.aps.org/doi/10.1103/PhysRevLett.86.5651

[3] Q. R. Ahmad *et al.*, Measurement of the Rate of $\nu_e + d \rightarrow p + p + e^-$ Interactions Produced by ^8B Solar Neutrinos at the Sudbury Neutrino Observatory, Phys. Rev. Lett. **87** (2001) 071301. doi:10.1103/PhysRevLett.87.071301.
URL https://link.aps.org/doi/10.1103/PhysRevLett.87.071301

[4] K. Eguchi *et al.*, First Results from KamLAND: Evidence for Reactor Antineutrino Disappearance (Jan 2003). doi:10.1103/PhysRevLett.90.021802.
URL https://link.aps.org/doi/10.1103/PhysRevLett.90.021802

[5] S. Petcov, M. Piai, The LMA MSW solution of the solar neutrino problem, inverted neutrino mass hierarchy and reactor neutrino experiments, Physics Letters B **533** (2002) 94–106. doi:https://doi.org/10.1016/S0370-2693(02)01591-5.
URL https://www.sciencedirect.com/science/article/pii/S0370269302015915

[6] A. Gando *et al.*, Search for Majorana Neutrinos Near the Inverted Mass Hierarchy Region with KamLAND-Zen, Phys. Rev. Lett. **117** (2016) 082503. doi:10.1103/PhysRevLett.117.082503.
URL https://link.aps.org/doi/10.1103/PhysRevLett.117.082503

[7] KamLAND-Zen Collaboration, First Search for the Majorana Nature of Neutrinos in the Inverted Mass Ordering Region with KamLAND-Zen (2022). doi:10.48550/ARXIV.2203.02139.
URL https://arxiv.org/abs/2203.02139

[8] T. S. collaboration *et al.*, The SNO+ experiment, Journal of Instrumentation **16** (2021) P08059. doi:10.1088/1748-0221/16/08/P08059.
URL https://dx.doi.org/10.1088/1748-0221/16/08/P08059

[9] J. N. Bahcall, Neutrino astrophysics, Cambridge University Press, 1989.

[10] N. Vinyoles *et al.*, A New Generation of Standard Solar Models, The Astrophysical Journal **835** (2017) 202. doi:10.3847/1538-4357/835/2/202.
URL https://dx.doi.org/10.3847/1538-4357/835/2/202

[11] N. Grevesse, A. J. Sauval, Standard Solar Composition, Space Science Reviews **85** (1998) 161–174. doi:10.1023/A:1005161325181.
URL https://doi.org/10.1023/A:1005161325181

[12] M. Asplund *et al.*, The Chemical Composition of the Sun, Annual Review of Astronomy and Astrophysics **47** (2009) 481–522. arXiv:https://doi.org/10.1146/annurev.astro.46.060407.145222, doi:10.1146/annurev.astro.46.060407.145222.
URL https://doi.org/10.1146/annurev.astro.46.060407.145222

[13] X.-J. Xu, Z. Wang, S. Chen, Solar neutrino physics (2022). doi:10.48550/ARXIV.2209.14832.
URL https://arxiv.org/abs/2209.14832

[14] B. Pontecorvo, Inverse beta processes and nonconservation of lepton charge, Zh. Eksp. Teor. Fiz. **34** (1957) 247.

[15] Z. Maki, M. Nakagawa, S. Sakata, Remarks on the Unified Model of Elementary Particles, Progress of Theoretical Physics **28** (1962) 870–880. arXiv:https://academic.oup.com/ptp/article-pdf/28/5/870/5258750/28-5-870.pdf, doi:10.1143/PTP.28.870.
URL https://doi.org/10.1143/PTP.28.870

[16] T. Araki *et al.*, Measurement of Neutrino Oscillation with KamLAND: Evidence of Spectral Distortion, Phys. Rev. Lett. **94** (2005) 081801. doi:10.1103/PhysRevLett.94.081801.
URL https://link.aps.org/doi/10.1103/PhysRevLett.94.081801

[17] Y. Fukuda *et al.*, Evidence for Oscillation of Atmospheric Neutrinos, Phys. Rev. Lett. **81** (1998) 1562–1567. doi:10.1103/PhysRevLett.81.1562.
URL https://link.aps.org/doi/10.1103/PhysRevLett.81.1562

[18] K. Abe *et al.*, Solar neutrino measurements in Super-Kamiokande-IV, Phys. Rev. D **94** (2016) 052010. doi:10.1103/PhysRevD.94.052010.
URL https://link.aps.org/doi/10.1103/PhysRevD.94.052010

[19] B. Aharmim *et al.*, Combined analysis of all three phases of solar neutrino data from the Sudbury Neutrino Observatory, Phys. Rev. C **88** (2013) 025501. doi:10.1103/PhysRevC.88.025501.
URL https://link.aps.org/doi/10.1103/PhysRevC.88.025501

[20] G. Bellini *et al.*, Precision Measurement of the ^{7}Be Solar Neutrino Interaction Rate in Borexino, Phys. Rev. Lett. **107** (2011) 141302. doi:10.1103/PhysRevLett.107.141302.
URL https://link.aps.org/doi/10.1103/PhysRevLett.107.141302

[21] M. G. Aartsen *et al.*, Determining neutrino oscillation parameters from atmospheric muon neutrino disappearance with three years of IceCube DeepCore data, Phys. Rev. D **91** (2015) 072004. doi:10.1103/PhysRevD.91.072004.
URL https://link.aps.org/doi/10.1103/PhysRevD.91.072004

[22] K. Abe *et al.*, Atmospheric neutrino oscillation analysis with external constraints in Super-Kamiokande I-IV, Phys. Rev. D **97** (2018) 072001. doi:10.1103/PhysRevD.97.072001.
URL https://link.aps.org/doi/10.1103/PhysRevD.97.072001

[23] A. Gando *et al.*, Reactor on-off antineutrino measurement with KamLAND, Phys. Rev. D **88** (2013) 033001. doi:10.1103/PhysRevD.88.033001.
URL https://link.aps.org/doi/10.1103/PhysRevD.88.033001

[24] Y. Abe *et al.*, Measurement of $\theta 13$ in Double Chooz using neutron captures on hydrogen with novel background rejection techniques, Journal of High Energy Physics **2016** (2016) 163. doi:10.1007/JHEP01(2016)163.
URL https://doi.org/10.1007/JHEP01(2016)163

[25] F. P. An *et al.*, Improved measurement of the reactor antineutrino flux and spectrum at Daya Bay*, Chinese Physics C **41** (2017) 013002. doi:10.1088/1674-1137/41/1/013002.
URL https://dx.doi.org/10.1088/1674-1137/41/1/013002

[26] J. K. Ahn *et al.*, Observation of Reactor Electron Antineutrinos Disappearance in the RENO Experiment, Phys. Rev. Lett. **108** (2012) 191802. doi:10.1103/PhysRevLett.108.191802.
URL https://link.aps.org/doi/10.1103/PhysRevLett.108.191802

[27] P. Adamson *et al.*, Measurement of Neutrino and Antineutrino Oscillations Using Beam and Atmospheric Data in MINOS, Phys. Rev. Lett. **110** (2013) 251801. doi:10.1103/PhysRevLett.110.251801.
URL https://link.aps.org/doi/10.1103/PhysRevLett.110.251801

[28] K. Abe *et al.*, Search for Electron Antineutrino Appearance in a Long-Baseline Muon Antineutrino Beam, Phys. Rev. Lett. **124** (2020) 161802. doi:10.1103/PhysRevLett.124.161802.
URL https://link.aps.org/doi/10.1103/PhysRevLett.124.161802

[29] M. A. Acero *et al.*, Improved measurement of neutrino oscillation parameters by the NOvA experiment, Phys. Rev. D **106** (2022) 032004. doi:10.1103/PhysRevD.106.032004.
URL https://link.aps.org/doi/10.1103/PhysRevD.106.032004

[30] I. Esteban *et al.*, The fate of hints: updated global analysis of three-flavor neutrino oscillations, Journal of High Energy Physics **2020** (sep 2020). doi:10.1007/jhep09(2020)178.
URL https://doi.org/10.1007%2Fjhep09%282020%29178

[31] NuFIT 5.1 (2021).
URL http://www.nu-fit.org/

[32] L. Wolfenstein, Neutrino oscillations in matter, Phys. Rev. D **17** (1978) 2369–2374. doi:10.1103/PhysRevD.17.2369.
URL https://link.aps.org/doi/10.1103/PhysRevD.17.2369

[33] S. P. Mikheyev, A. Y. Smirnov, Resonance Amplification of Oscillations in Matter and Spectroscopy of Solar Neutrinos, Sov. J. Nucl. Phys. **42** (1985) 913–917.

[34] X. Shi, D. N. Schramm, J. N. Bahcall, Monte Carlo exploration of Mikheyev-Smirnov-Wolfenstein solutions to the solar neutrino problem, Phys. Rev. Lett. **69** (1992) 717–720. doi:10.1103/PhysRevLett.69.717.
URL https://link.aps.org/doi/10.1103/PhysRevLett.69.717

[35] G. D. Orebi Gann *et al.*, The Future of Solar Neutrinos, Annual Review of Nuclear and Particle Science **71** (2021) 491–528. arXiv:https://doi.org/10.1146/annurev-nucl-011921-061243, doi:10.1146/annurev-nucl-011921-061243.
URL https://doi.org/10.1146/annurev-nucl-011921-061243

[36] A. N. Ioannisian, A. Y. Smirnov, Neutrino Oscillations in Low Density Medium, Phys. Rev. Lett. **93** (2004) 241801. doi:10.1103/PhysRevLett.93.241801.
URL https://link.aps.org/doi/10.1103/PhysRevLett.93.241801

[37] M. Blennow, T. Ohlsson, H. Snellman, Day-night effect in solar neutrino oscillations with three flavors, Phys. Rev. D **69** (2004) 073006. doi:10.1103/PhysRevD.69.073006.
URL https://link.aps.org/doi/10.1103/PhysRevD.69.073006

[38] Y. Nakajima, Recent results and future prospects from Super- Kamiokande (Jun. 2020). doi:10.5281/zenodo.3959640.
URL https://doi.org/10.5281/zenodo.3959640

[39] J. N. Bahcall, M. Kamionkowski, A. Sirlin, Solar neutrinos: Radiative corrections in neutrino-electron scattering experiments, Phys. Rev. D **51** (1995) 6146–6158. doi:10.1103/PhysRevD.51.6146.
URL https://link.aps.org/doi/10.1103/PhysRevD.51.6146

[40] A. Bellerive *et al.*, The Sudbury Neutrino Observatory, Nuclear Physics B **908** (2016) 30–51, neutrino Oscillations: Celebrating the Nobel Prize in Physics 2015. doi:https://doi.org/10.1016/j.nuclphysb.2016.04.035.
URL https://www.sciencedirect.com/science/article/pii/S0550321316300736

[41] J. Arafune *et al.*, ^{13}C as a solar neutrino detector, Physics Letters B **217** (1989) 186–190. doi:https://doi.org/10.1016/0370-2693(89)91540-2.
URL https://www.sciencedirect.com/science/article/pii/0370269389915402

[42] M. Fukugita *et al.*, Reaction cross sections for ν $^{13}e^-$ ^{13}N and ν $^{13}\nu$, ^{13}C* for low energy neutrinos, Phys. Rev. C **41** (1990) 1359–1364. doi:10.1103/PhysRevC.41.1359.
URL https://link.aps.org/doi/10.1103/PhysRevC.41.1359

[43] T. Suzuki, A. B. Balantekin, T. Kajino, Neutrino capture on ^{13}C, Phys. Rev. C **86** (2012) 015502. doi:10.1103/PhysRevC.86.015502.
URL https://link.aps.org/doi/10.1103/PhysRevC.86.015502

[44] T. Suzuki *et al.*, Neutrino-13C cross sections at supernova neutrino energies, Journal of Physics G: Nuclear and Particle Physics **46** (2019) 075103. doi:10.1088/1361-6471/ab1c11.
URL https://dx.doi.org/10.1088/1361-6471/ab1c11

[45] M. Anderson *et al.*, Measurement of the ^{8}B solar neutrino flux in SNO+ with very low backgrounds, Phys. Rev. D **99** (2019) 012012. doi:10.1103/PhysRevD.99.012012.
URL https://link.aps.org/doi/10.1103/PhysRevD.99.012012

[46] G. Bellini *et al.*, Measurement of the solar ^{8}B neutrino rate with a liquid scintillator target and 3 MeV energy threshold in the Borexino detector, Phys. Rev. D **82** (2010) 033006. doi:10.1103/PhysRevD.82.033006.
URL https://link.aps.org/doi/10.1103/PhysRevD.82.033006

[47] M. Agostini *et al.*, Improved measurement of ^{8}B solar neutrinos with 1.5 kt $\cdot$ y of Borexino exposure, Phys. Rev. D **101** (2020) 062001. doi:10.1103/PhysRevD.101.062001.
URL https://link.aps.org/doi/10.1103/PhysRevD.101.062001

[48] S. Abe *et al.*, Measurement of the ^{8}B solar neutrino flux with the KamLAND liquid scintillator detector, Phys. Rev. C **84** (2011) 035804. doi:10.1103/PhysRevC.84.035804.
URL https://link.aps.org/doi/10.1103/PhysRevC.84.035804

[49] M. Buizza Avanzini, The ^{8}B Solar Neutrino Analysis in Borexino and Simulations of Muon Interaction Products in Borexino and Double Chooz, Ph.D. thesis, Milan U. (2012).

[50] S. Abe *et al.*, Abundances of Uranium and Thorium Elements in Earth Estimated by Geoneutrino Spectroscopy, Geophysical Research Letters **49** (2022) e2022GL099566, e2022GL099566 2022GL099566. arXiv:https://agupubs.onlinelibrary.wiley.com/doi/pdf/10.1029/2022GL099566, doi:https://doi.org/10.1029/2022GL099566.
URL https://agupubs.onlinelibrary.wiley.com/doi/abs/10.1029/2022GL099566

[51] A. Gando *et al.*, ^{7}Be solar neutrino measurement with KamLAND, Phys. Rev. C **92** (2015) 055808. doi:10.1103/PhysRevC.92.055808.
URL https://link.aps.org/doi/10.1103/PhysRevC.92.055808

[52] S. Abe *et al.*, Search for Low-energy Electron Antineutrinos in KamLAND Associated with Gravitational Wave Events, The Astrophysical Journal **909** (2021) 116. doi:10.3847/1538-4357/abd5bc.
URL https://doi.org/10.3847/1538-4357/abd5bc

[53] S. Abe *et al.*, Limits on Astrophysical Antineutrinos with the KamLAND Experiment, The Astrophysical Journal **925** (2022) 14. doi:10.3847/1538-4357/ac32c1.
URL https://doi.org/10.3847/1538-4357/ac32c1

[54] S. Abe *et al.*, A Search for Correlated Low-energy Electron Antineutrinos in KamLAND with Gamma-Ray Bursts, The Astrophysical Journal **927** (2022) 69. doi:10.3847/1538-4357/ac4e7e.
URL https://doi.org/10.3847/1538-4357/ac4e7e

[55] S. Abe *et al.*, Production of radioactive isotopes through cosmic muon spallation in KamLAND, Phys. Rev. C **81** (2010) 025807. doi:10.1103/PhysRevC.81.025807.
URL https://link.aps.org/doi/10.1103/PhysRevC.81.025807

[56] T. Iwamoto, Measurement of Reactor Anti-Neutrino Disappearance in KamLAND, Ph.D. thesis, Tohoku university (2003).
URL http://www.awa.tohoku.ac.jp/KamLAND/internal/ThesisFile_KamLAND/iwamoto_d.pdf

[57] Y. Takemoto, Observation of ^{7}Be Solar Neutrinos with KamLAND, Ph.D. thesis, Tohoku university (2014).
URL https://www.awa.tohoku.ac.jp/Thesis/ThesisFile/takemoto_yasuhiro_d.pdf

[58] O. Tajima, Measurement of Electron Anti-Neutrino Oscillation Parameters with a Large Volume Liquid Scintillator Detector, KamLAND, Ph.D. thesis, Tohoku university (2003).
URL http://www.awa.tohoku.ac.jp/KamLAND/internal/ThesisFile_KamLAND/tajima_osamu_d.pdf

[59] K. Oki, 高精度大口径光電子増倍管の開発研究 (Research and development of high-precision large-aperture photomultiplier tubes) (1999).
URL https://www.awa.tohoku.ac.jp/Thesis/ThesisFile/oki_kazuhiro_m.pdf

[60] K. Tagashira, 高精度17インチ光電子増倍管の性能計測研究 (Performance measurement study of high-precision 17-inch photomultiplier tubes) (2000).
URL https://www.awa.tohoku.ac.jp/Thesis/ThesisFile/tagashira_kenji_m.pdf

[61] L. A. Winslow, First Solar Neutrinos from KamLAND: A Measurement of the B-8 Solar Neutrino Flux, Ph.D. thesis, UC, Berkeley (2008).

[62] H. Ozaki, Refurbishment of KamLAND Outer Cherenkov Detector and Improvement in Performance (2017).
URL https://www.awa.tohoku.ac.jp/Thesis/ThesisFile/ozaki_hideyoshi_m.pdf

[63] Y. Gando *et al.*, The nylon balloon for xenon loaded liquid scintillator in KamLAND-Zen 800 neutrinoless double-beta decay search experiment, Journal of Instrumentation **16** (2021) P08023. doi:10.1088/1748-0221/16/08/p08023.
URL https://doi.org/10.1088/1748-0221/16/08/p08023

[64] K. Nakajima, First Results from ^{7}Be Solar Neutrino Observation with KamLAND, Ph.D. thesis, Tohoku university (2010).
URL https://www.awa.tohoku.ac.jp/KamLAND/internal/ThesisFile_KamLAND/nakajima_kyohei_d.pdf

[65] G. Keefer *et al.*, Laboratory studies on the removal of radon-born lead from KamLAND's organic liquid scintillator, Nuclear Instruments and Methods in Physics Research Section A: Accelerators, Spectrometers, Detectors and Associated Equipment **769** (2015) 79–87. doi:https://doi.org/10.1016/j.nima.2014.09.050.
URL https://www.sciencedirect.com/science/article/pii/S016890021401078X

[66] H. Watanabe, Comprehensive Study of Anti-neutrino Signals at KamLAND, Ph.D. thesis, Tohoku university (2012).
URL http://www.awa.tohoku.ac.jp/KamLAND/internal/ThesisFile_KamLAND/watanabe_hiroko_d.pdf

[67] S. Enomoto, Neutrino Geophysics and Observation of Geo-Neutrinos at KamLAND, Ph.D. thesis, Tohoku university (2005).
URL http://www.awa.tohoku.ac.jp/Thesis/ThesisFile/enomoto_sanshiro_d.pdf

[68] T. Hachiya, Delayed coincidence with a day-scale window for tagging ^{232}Th series isotopes in KamLAND, Journal of Physics: Conference Series **1468** (2020) 012257. doi:10.1088/1742-6596/1468/1/012257.
URL https://doi.org/10.1088/1742-6596/1468/1/012257

[69] A. Oki, 新トリガーによる KamLAND-Zen 実験での ^{10}C バックグラウンド除去 (^{10}C Background Reduction in KamLAND-Zen Using New Trigger) (2013).
URL https://www.awa.tohoku.ac.jp/Thesis/ThesisFile/oki_ayumu_m.pdf

[70] T. Banks *et al.*, A compact ultra-clean system for deploying radioactive sources inside the KamLAND detector, Nuclear Instruments and Methods in Physics Research Section A: Accelerators, Spectrometers, Detectors and Associated Equipment **769** (2015) 88–96. doi:https://doi.org/10.1016/j.nima.2014.09.068.
URL https://www.sciencedirect.com/science/article/pii/S0168900214011000

[71] B. E. Berger *et al.*, The KamLAND full-volume calibration system, Journal of Instrumentation **4** (2009) P04017–P04017. doi:10.1088/1748-0221/4/04/p04017.
URL https://doi.org/10.1088/1748-0221/4/04/p04017

[72] G. Keefer, Calibration ^{222}Rn Introduction During Z-Axis Calibrations , KamLAND Collaboration Meeting (Sep 2007).

[73] Private conversation with Prof. Tadao Mitsui (Jun 2022).

[74] Y. Kibe, PPO concentration of LS before and after distillation, KamLAND Collaboration Meeting (Sep 2007).

[75] ATOMIC WEIGHTS OF THE ELEMENTS 2015.
URL https://iupac.qmul.ac.uk/AtWt/AtWt15.html

[76] S. Enomoto, (α, n) Background Overview , KamLAND Collaboration Meeting (Oct 2004).

[77] Chemical Book.
URL https://www.chemicalbook.com/ProductMSDSDetailCB3693821_EN.htm

[78] Fisher Scientic.
URL https://www.fishersci.com/shop/products/2-5-diphenyloxazole-99-thermo-scientific/AAA1065414

[79] K. Ichimura, T. Ebihara, Transmission, light yield and gas chromatography of KamLAND LS , KamLAND Collaboration Meeting (Sep 2006).

[80] H. Watanabe *et al.*, PPO concentration of LS after distillation , KamLAND Collaboration Meeting (Mar 2009).

[81] S. Matsuda, Search for Neutrinoless Double-Beta Decay in ^{136}Xe after Intensive Background Reduction with KamLAND-Zen, Ph.D. thesis, Tohoku university (2016).
URL http://www.awa.tohoku.ac.jp/Thesis/ThesisFile/matsuda_sayuri_d.pdf

[82] S. Obara, A Search for Supernova Relic Neutrinos with KamLAND during Reactor-Off Period, Ph.D. thesis, Tohoku university (2018).
URL http://www.awa.tohoku.ac.jp/KamLAND/internal/ThesisFile_KamLAND/obara_shuhei_d.pdf

[83] M. Batygov, Combined Study of Reactor and Terrestrial Antineutrinos with KamLAND, Ph.D. thesis, University of Tennessee (2006).
URL https://trace.tennessee.edu/utk_graddiss/1918/

[84] K. Ichimura, Precise measurement of neutrino oscillation parameters with KamLAND, Ph.D. thesis, Tohoku university (2008).
URL http://www.awa.tohoku.ac.jp/KamLAND/internal/ThesisFile_KamLAND/ichimura_koichi_d.pdf

[85] K. Ichimura, 4-pi analysis , KamLAND Collaboration Meeting (Oct 2020).

[86] N. Kawada, Spectroscopic measurement of geoneutrinos from uranium and thorium with KamLAND, Ph.D. thesis, Tohoku university (2022).
URL https://www.awa.tohoku.ac.jp/Thesis/Doctor_Thesis.html

[87] M. Batygov, New Energy Fitter Development and Tests , KamLAND Collaboration Meeting (Oct 2005).

[88] I. Shimizu, Energy Tool Update , KamLAND Collaboration Meeting (Sep 2009).

[89] I. Shimizu, An Evidence for Spectral Distortion of Reactor Anti-Neutrinos and A Study of Three Flavor Neutrino Oscillation, Ph.D. thesis, Tohoku university (2005). URL http://www.awa.tohoku.ac.jp/KamLAND/internal/ThesisFile_KamLAND/shimizu_itaru_d.pdf

[90] Y. Shimizu, Observation of Geo-Neutrinos with KamLAND, Ph.D. thesis, Tohoku university (2010).
URL http://www.awa.tohoku.ac.jp/KamLAND/internal/ThesisFile_KamLAND/shimizu_yuri_d.pdf

[91] T. Mitsui, CPT-invariant Energy Scale , KamLAND Collaboration Meeting (Sep 2009).

[92] T. Mitsui, CPT-invariant Energy Scale II , KamLAND Collaboration Meeting (Mar 2010).

[93] T. Mitsui, - , KamLAND Collaboration Meeting (Somewhere 2003–2005).

[94] T. Björnstad *et al.*, The decay of ^{8}He, Nuclear Physics A **366** (1981) 461–468. doi:https://doi.org/10.1016/0375-9474(81)90522-4.
URL https://www.sciencedirect.com/science/article/pii/0375947481905224

[95] D. Tilley *et al.*, Energy levels of light nuclei A=8,9,10, Nuclear Physics A **745** (2004) 155–362. doi:https://doi.org/10.1016/j.nuclphysa.2004.09.059.
URL https://www.sciencedirect.com/science/article/pii/S0375947404010267

[96] Y. Karino, KamLAND-Zen 実験における宇宙線ミューオン起源のバックグラウンド除去効率の改善 (Improvement of Background Rejection for Cosmic Muon Spallation in KamLAND-Zen) (2017).
URL https://www.awa.tohoku.ac.jp/Thesis/ThesisFile/karino_yuki_m.pdf

[97] S. W. Li, J. F. Beacom, Tagging spallation backgrounds with showers in water Cherenkov detectors, Phys. Rev. D **92** (2015) 105033. doi:10.1103/PhysRevD.92.105033.
URL https://link.aps.org/doi/10.1103/PhysRevD.92.105033

[98] Y. Gando, First results of KamLAND-Zen 800, Journal of Physics: Conference Series **1468** (2020) 012142. doi:10.1088/1742-6596/1468/1/012142.
URL https://doi.org/10.1088/1742-6596/1468/1/012142

[99] S. Ieki, Summary page of FLUKA simulation (KamLAND internal) (2022).
URL https://www.awa.tohoku.ac.jp/KamLAND-Zen/internal/KamWiki/dokuwiki/doku.php?id=local:ieki:fluka

[100] H. Ozaki, High Sensitivity Search for Neutrinoless Double-Beta Decay in KamLAND-Zen with Double Amount of ^{136}Xe, Ph.D. thesis, Tohoku university (2020).
URL https://www.awa.tohoku.ac.jp/KamLAND-Zen/internal/ThesisFile_KamLAND-Zen/ozaki_hideyoshi_d.pdf

[101] Y. Kibe, Observation of ^{8}B Solar Neutrinos with KamLAND, Ph.D. thesis, Tohoku university (2010).
URL http://www.awa.tohoku.ac.jp/KamLAND/internal/ThesisFile_KamLAND/kibe_yoshiaki_d.pdf

[102] PSTAR.
URL https://physics.nist.gov/PhysRefData/Star/Text/PSTAR.html

[103] J. N. Bahcall, M. H. Pinsonneault, What do we (not) know theoretically about solar neutrino fluxes?, Phys. Rev. Lett. **92** (2004) 121301. doi:10.1103/PhysRevLett.92.121301.
URL https://link.aps.org/doi/10.1103/PhysRevLett.92.121301

[104] A. Abusleme *et al.*, Feasibility and physics potential of detecting 8B solar neutrinos at JUNO *, Chinese Physics C **45** (2021) 023004. doi:10.1088/1674-1137/abd92a.
URL https://dx.doi.org/10.1088/1674-1137/abd92a

[105] JUNO Collaboration *et al.*, Model Independent Approach of the JUNO ^{8}B Solar Neutrino Program (2022). doi:10.48550/ARXIV.2210.08437.
URL https://arxiv.org/abs/2210.08437

[106] A. Li *et al.*, KamNet: An Integrated Spatiotemporal Deep Neural Network for Rare Event Search in KamLAND-Zen (2022). doi:10.48550/ARXIV.2203.01870.
URL https://arxiv.org/abs/2203.01870